

Acoustofluidics 2016

Technical University
of Denmark

Acoustofluidics 2016

Thursday 22 – Friday 23 September 2016
Technical University of Denmark (DTU)

An international conference dedicated to the science
and technology of micro- and nanoscale acoustofluidics

Conference proceedings

www.fysik.dtu.dk/Acoustofluidics2016

Invited speakers

Philippe Marmottant, Université Grenoble Alpes: *Bubble-based acoustofluidics*

Erwin Peterman, Vrije Universiteit Amsterdam: *Acoustic force spectroscopy*

Michaël Baudoin, Université Lille 1: *SAW-based vortical acoustofluidics*

Per Augustsson, Lunds Universitet: *Iso-acoustophoresis*

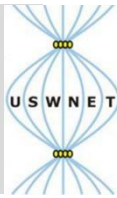
Exhibitors:



Scientific committee

Henrik Bruus, conference chair, DTU (DK)
Jürg Dual, ETH Zürich (CH)
Thomas Franke, University of Glasgow (GB)
James Friend, UC San Diego (US)
Peter Glynne-Jones, Univ Southampton (GB)
Martyn Hill, University of Southampton (GB)
Thomas Laurell, Lund University (SE)
Andreas Lenshof, Lund University (SE)
Adrian Neild, Monash University (AU)
Stefan Radel, TU Wien (AT)
Martin Wiklund, KTH Stockholm (SE)





Acoustofluidics 2016



Exhibitor



COMSOL Multiphysics® is an integrated software environment for creating physics-based models and simulation apps. A particular strength is its ability to account for coupled or multiphysics phenomena. Add-on products expand the simulation platform for electrical, mechanical, fluid flow, and chemical applications. Interfacing tools enable the integration of COMSOL Multiphysics® simulations with all major technical computing and CAD tools on the CAE market. Simulation experts rely on the COMSOL Server™ product to deploy apps to their design teams, manufacturing departments, test laboratories, and customers throughout the world. Stop by our booth during the poster session to learn more about the COMSOL software.

Links

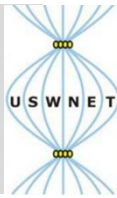
COMSOL.com

[COMSOL 5.2, Acoustics Module, Release Highlights](#)

[COMSOL Multiphysics, Acoustics Module](#)

[Acoustics Module Specification Chart](#)

[Follow the COMSOL Blogs](#)



Acoustofluidics 2016



Technical University
of Denmark

Exhibitor

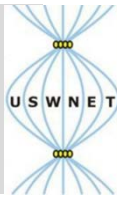


BelektroniG presents its High-End solution for driving surface acoustic wave (SAW) actuators or resonant devices. SAW actuators allow creating forces inside microfluidic systems e.g. droplet movement, mixing and pumping, cell sorting and even fluid atomization. On the other hand SAW actuators require special high-frequency electronics to be used. The BelektroniG Power SAW Generator integrates all required functionality for an easy access to acoustofluidic experiments. Main features are a network analyzer mode to detect and characterize connected SAW actuators, an automatic scanning mode, a multichannel output with adjustable phases for experiments with standing waves, as well as pulse modes and trigger in-/outputs. The Power SAW Generator comes with a convenient PC-Software allowing an easy access to all the functions and also to monitor your experiment and record data. BelektroniG will show some live experiments at its exhibition table.

Links

[BelektroniG website](#)

[BelektroniG Power SAW Generators](#)



Acoustofluidics
2016



Exhibitor



AcouSort AB develops continuous flow-based microfluidic systems for cell/particle separation, enrichment and handling technology. The core technology relies on acoustic standing wave forces integrated in microfluidic systems, which enable sorting and rapid processing of cell samples. AcouSort develops proprietary bioanalytical and clinical applications based on acoustophoresis and can also offer custom-developed acoustophoresis applications. The AcouTrap system is a new product that integrates acoustic cell trapping with a 96-well pipetting robot. This stand-alone system can be used to trap and hold cells, bacteria or microparticles while performing washing, enrichment, staining or other protocols.

Link

www.acousort.com

SAW-based vortical acoustofluidics

M. Baudoin¹, A. Riaud^{1,2}, J.-L. Thomas² and O. Bou Matar¹

¹ IEMN, LIA LEMAC/LICS, Université Lille 1, UMR CNRS 8520, Avenue Poincaré, 59652 Villeneuve d'Ascq, France

E-mail: michael.baudoin@univ-lille1.fr, URL: <http://films-lab.univ-lille1.fr/michael>

² Institut des NanoSciences de Paris (INSP), Université Pierre et Marie Curie, UMR CNRS 7588, 4 place Jussieu, 75252 Paris cedex 05, France

Introduction

Surface acoustic waves (SAWs) are versatile waves for the actuation of fluids at micrometric scales. In the literature, it has been shown that these waves can be used to displace, divide, merge and atomize sessile droplets, but also actuate fluids embedded in microchannels, manipulate collectively particles or sort them depending on their acoustic properties (see [1,2,3] for a review). The major advantages of SAW-based actuators compared to bulk acoustical transducers or other techniques are (i) the wide range of possibilities offered for microfluidic actuation, (ii) the compactness of the system and its easy integration in a lab on a chip, (iii) the simple fabrication with standard metal sputtering, photolithography and etching processes and (iv) the possibility to generate waves at frequencies ranging from a few MHz to a few GHz, thus allowing to manipulate fluids and particles from sub-micron to millimeter scales.

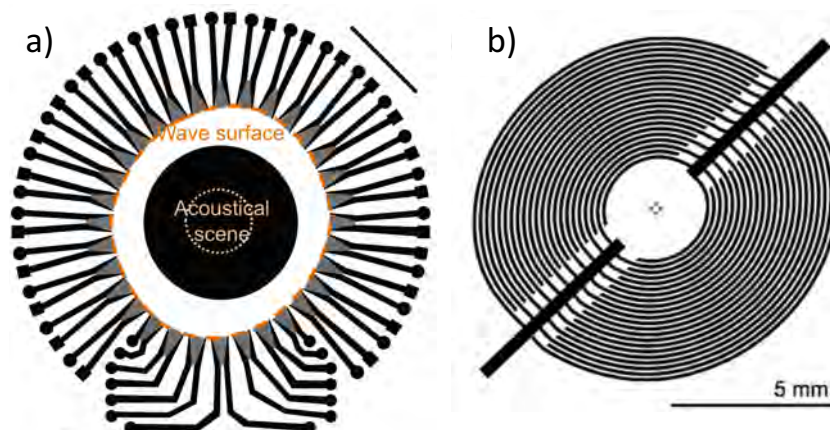


Figure 1: (a) Interdigitated transducers array used for the design of a SAW-based multifunction platform. (b) Single spiraling transducer enabling the synthesis of swirling surface acoustic wave.

Nevertheless, there are still some limitations for the development of a SAW-based microfluidic toolbox. First, most operations performed with SAWs require a specific design of the wave generation system, the so-called InterDigitated Transducers (IDTs). This limits the use of SAW actuators to one specific task. Second, there are still some operations which cannot be performed with the current systems such as the 3D selective manipulation of a single particle, independently of its neighbors. Indeed, in the case of acoustical tweezers based on standing waves, all particles with similar properties contained in a cavity are trapped either in the nodes or in the antinodes depending on their density and compressibility contrast with the surrounding medium. They will then move collectively when the standing wave nodes and antinodes are moved.

In this presentation, we will first show that it is possible to design a multifunction platform based on an IDT Array (IDTA), which enables to perform all the operations described in the literature. Second, we will demonstrate the possibilities offered by a new kind of surfaces acoustic waves named swirling SAWs for 3D selective particles trapping. We will finally show that swirling SAWs can be either synthesized with the IDTA or with a single IDT with a spiraling design, which opens prospects for submicron particles trapping.

Interdigitated transducers array and inverse filter for a multifunction platform

An IDT array based on a set of 32 IDTs was designed (see Fig. 1a) to create a versatile SAW-based microfluidic toolbox [4]. Each IDT is positioned along the wave surface around a central zone (called

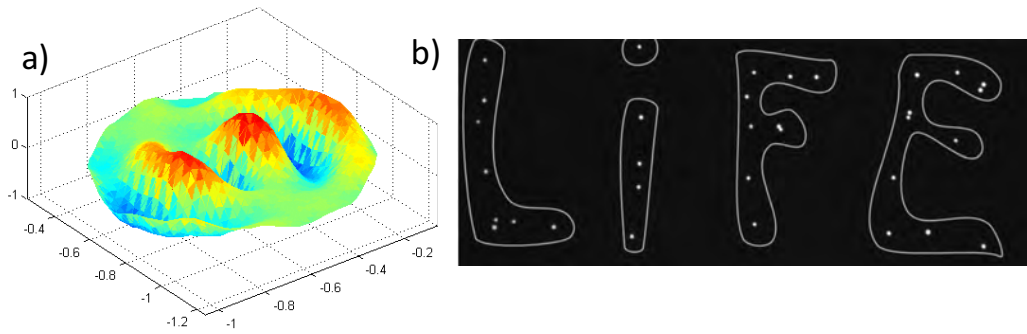


Figure 2: (a) Swirling SAW generated at the surface of a X-cut Niobate Lithium substrate and measured with a laser interferometer. (b) 30 microns particles initially randomly distributed in a microfluidic chamber and moved with the swirling SAW-based tweezer to form a prescribed pattern.

the acoustic scene) where we want to synthesize a prescribed acoustic field. The wave surface is not circular owing to the anisotropy of the piezoelectric X-cut Niobate Lithium substrate used to generate the wave. The wavelength of each IDT is adapted to each crystallographic direction since the wave speed depends on the direction of the wave vector. Each IDT is independently controlled with a programmable electronics (a FPGA) and the inverse filter technique is used to determine which signal imposing to each transducer to synthesize a targeted wavefield. With this system, we demonstrated in [5], that it is possible to synthesize any surface wave compatible with the wave equation in the substrate. As a proof of concept, we also showed that it is possible to move, divide, fusion and atomize droplets with a unique system [5].

Swirling SAWs and selective tweezers

We further demonstrated that is possible to generate a new kind of SAWs with this system named swirling SAWs (see Fig. 2b), which can be used as precursor wave to synthesize acoustical vortices (also named Bessel beams), in the bulk of a liquid sample [4,6]. It was shown recently that such acoustical vortices are particularly well suited for the 3D trapping of individual particles with the radiation pressure, thus enabling the design of selective single beam acoustical tweezers [7]. Contrary to plane standing waves, acoustical vortices are indeed highly localized waves, which create a strong localized trap at the center of the beam. With the IDTA, the swirling SAWs can be synthesized at different positions of the acoustical scene [6], thus enabling digital control of the trap position in the X and Y directions. But trapping in the third direction (orthogonal to the substrate) is also possible by taming the degeneracy of the swirling wave from the anisotropic piezoelectric substrate to the isotropic liquid [6].

Generating swirling SAWs with a single spiraling IDT

The IDT array is an extremely versatile toolbox, which enables selective particle trapping with swirling SAWs in addition to the other operations demonstrated in the literature. Nevertheless it remains limited to frequency under 100 MHz, since no FPGA can be found at higher frequencies. Moreover, the price of programmable electronics becomes prohibitive at high frequency. We showed recently that it is possible to synthesize swirling SAWs (and thus to trap and move particles) by using a single IDT with a specific spiraling design (See Fig. 1b). With this system we demonstrated selective particle trapping of 30 microns polystyrene particles in a microfluidic chamber (see Fig. 2b).

Conclusion

In this presentation, we will first demonstrate the possibilities offered by a multifunction platform based on a 32 IDTs array and the inverse filter technique to perform not only previous operations demonstrated in the literature but also the 3D selective particle trapping, with a new kind of surface acoustic waves named swirling SAWs. Then we will show that such selective tweezers can also be obtained with a single spiraling IDT.

References

- [1] J.R. Friend and L. Yeo. *Rev. Mod. Phys.* **83**, 647-704 (2011).
- [2] Ding, X. et al. *Lab Chip* **13**, 3626 (2013).
- [3] L.Y. Yeo, and J.R. Friend. *Annu. Rev. Fluid Mech.* **46**, 379-406 (2014).
- [4] A. Riaud et al. *Phys. Rev. Appl.* **4**, 034004 (2015).
- [5] A. Riaud et al. Accepted for publication in *IEEE T. Ultraso. Ferr.* (2016).
- [6] A. Riaud et al. *Phys. Rev. E* **92**, 063201 (2015).
- [7] D. Baresch, J.-L. Thomas and R. Marchiano *Phys. Rev. Lett.*, **116**: 024301 (2016).

Bubble-based acoustofluidics

Philippe Marmottant, Pierre Thibault, Thomas Combriat, Flore Mekki-Berrada, Nicolas Bertin, Olivier Stephan, Olivier Vincent, Alexandre Ponomarenko, Diane Bienaimé

Laboratoire Interdisciplinaire de Physique, CNRS and Université Grenoble
E-mail: philippe.marmottant@univ-grenoble-alpes.fr

Introduction

In this talk we will present unusual phenomena occurring in microfluidic devices and trees, linked to bubble vibrations.

Vibrations and streaming around bubble pairs in flat microchannels

First, we will present the vibration mode of bubbles flattened in microfluidic channel. Bubbles exhibit parametric shape modes that we can carefully investigate under ultrasound. A strong associated streaming occurs near vibrating bubbles, especially when bubbles are close to each other. This streaming would prove helpful to mix liquids. See Fig. 1 for an illustration of the streaming around two bubbles.

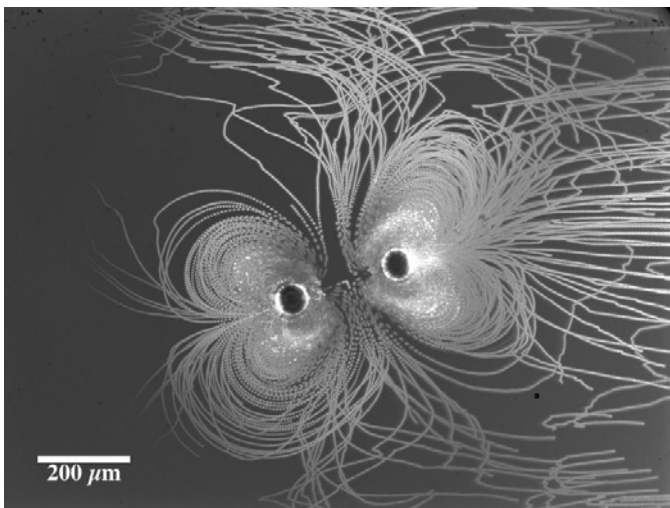


Figure 1: Streaming around two bubbles in flat microfluidic channels

Acoustic microswimmers

Acoustic microswimmers present great potential for microfluidic applications and targeted drug delivery. Here we introduce the concept of armoured microbubbles. Contained within the size range of 10-20 micrometers, they are made by three-dimensional microfabrication and each consist of a spherical capsule with an opening, which captures a bubble inside when submerged, see Fig 2a. In this armour the bubbles can last for hours even under forced oscillations. We found that the acoustic resonance of the armoured microbubble is dictated by capillary forces and not by gas volume, and its measurement agrees with a theoretical calculation. A strong propulsive jet reaching up to 100 $\mu\text{m/s}$ is observed in the fluid near the armour opening, see figure 2b. This is steady streaming caused by the non-linear response of the fluid, which we can predict. This jet is the basis for self-propulsion, or for pumping fluid around when the armoured bubble is attached to a substrate. A collection of armoured microbubbles can be fabricated and used inside microchannels for efficient mixing. Complex armour shapes, containing multiple bubbles, can also be created. A direct application of this is for multi-directional microswimmers, where each bubble has a different resonance frequency, which can be excited by scanning frequencies with a broadband acoustic source.

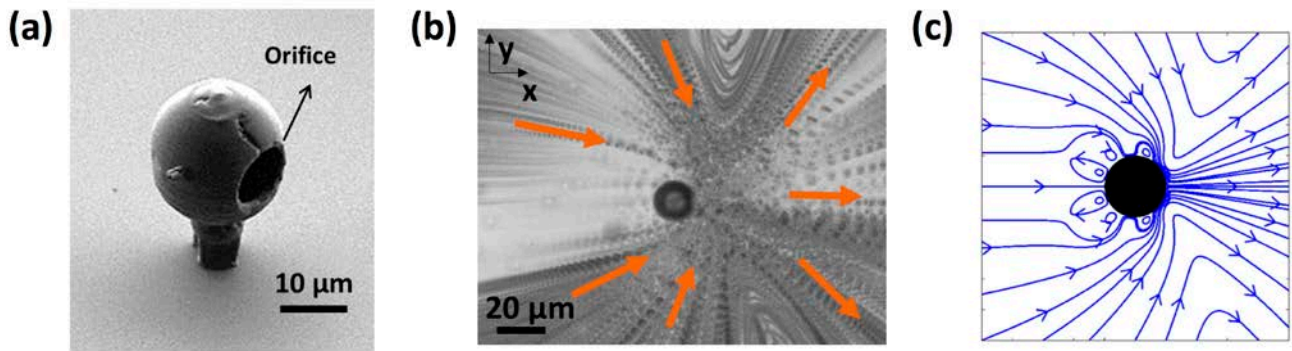


Figure 2: Acoustic microswimmer (a) SEM image of an armour protecting bubbles against dissolution, but letting the interface vibrate; (b) streamlines generated by the vibrating; (c) theoretical prediction.

Nucleation, vibration and growth of bubbles in "organic" tree channels

We will present our investigations on the nucleation of bubbles in natural micro-vessels, tree vessels, by showing experiments on wood and on leaves. Such explosive bubbles occur by cavitation, since the liquid sap in trees is under extreme negative pressure. They emit a characteristic sound and then form the start of an emboly that can affect the hydraulic circulation of sap, see figure 3.

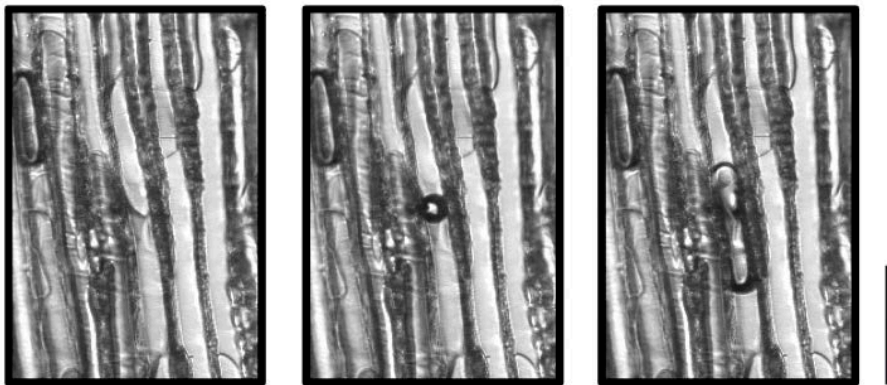


Figure 3: Bubble developing in wood conduits. The scale bar is 100 micrometers.

Conclusion

We are looking forward to presenting this work for the international acoustofluidics community at *Acoustofluidics 2016* at DTU, Kongens Lyngby, Denmark on 22 - 23 September 2016 !



Acoustic Force Spectroscopy

Erwin J.G. Peterman¹, Douwe Kamsma¹, Gerrit Sitters^{1,2} and Gijs J.L. Wuite¹

¹Department of Physics and Astronomy, Vrije Universiteit Amsterdam, Amsterdam, The Netherlands

E-mail: e.j.g.peterman@vu.nl, URL: www.nat.vu.nl/~erwinp

²LUMICKS B.V., Amsterdam, The Netherlands

Introduction

Over the last decades, several techniques have been developed to apply forces to biomolecules and to concomitantly detect their deformation, including optical tweezers, magnetic tweezers and scanning force microscopy [1]. We have recently developed another approach, Acoustic Force Spectroscopy (AFS), that makes use of acoustic forces to manipulate molecules [2]. In this presentation we will give an overview of the approach and discuss recent developments [3] and applications.

AFS

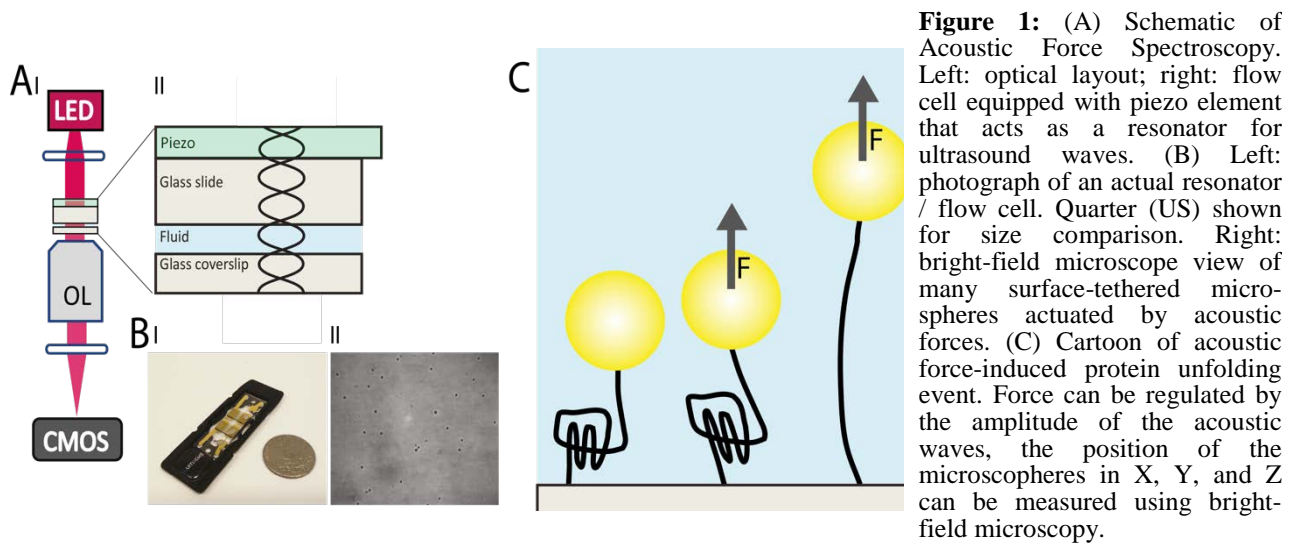
In AFS (Fig. 1), a standing acoustic wave is applied to a glass flow cell using a piezo element [2]. Micrometer-sized particles, such as polystyrene microspheres, with different density and acoustic properties as the water surrounding them will be pushed to the nodes of these standing waves. When the microspheres are tethered to the glass walls of the flow cell using a DNA molecule or a protein, well-controlled forces can be applied to the tethered molecules. The position of the microspheres can be tracked in three dimensions and in this way, the mechanical properties of DNA can be studied or the energetics of antigen-antibody interactions. The key advantage of AFS is that it is a highly parallel approach allowing simultaneous detection and manipulation of many biomolecules in one field of view at the same time. Another advantage is that the forces are applied by a piezo element driven by a standard function generator, that can be controlled at will and instantaneously.

New developments

Since our original publication [2] we have implemented several technical improvements to AFS that make the technique applicable to a wider range of applications. First, we now use transparent piezo elements, which allows implementation in a trans-illuminated bright-field microscope, substantially improving optical performance and improving compatibility with existing microscopes. Furthermore, we have developed a model to calculate forces in the sample, in order to optimize the dimensions of our acoustic flow cells. In addition, we discovered that a superposition of two standing waves can be applied, which allows modification of the force profile, for example to generate a more constant force. This allows transformation of AFS from a distance clamp to a force clamp by a simple electronic switch. Finally, we show that AFS is, in principle, compatible with high NA water or oil immersion objectives. This comes, however at the price of less high forces due to leakage of acoustic energy out of the resonator.

Conclusion

AFS is a promising new technique to apply forces to single-molecules. Many applications can be envisioned, including force-induced protein unfolding and cell mechanics. AFS's key advantage is its ability to measure many tethers simultaneously, greatly improving experimental throughput. Furthermore, it is a compact system that can be implemented in most microscopes, and it is relatively affordable. Commercial versions are available from Vrije Universiteit spin-off company LUMICKS B.V.



References

- [1] Woodside, M.T., and S.M. Block. *Annu Rev Biophys.* **43**, 19-39 (2014).
- [2] Sitters, G., D. Kamsma, G. Thalhammer, M. Ritsch-Martel, E.J. Peterman, and G.J. Wuite. *Nat Methods.* **12**, 47-50 (2015).
- [3] Kamsma, D., R. Creighton, G. Sitters, G.J. Wuite, and E.J. Peterman. *Methods* **105**, 26-33 (2016).

Iso-acoustophoresis

Per Augustsson

Department of Biomedical Engineering, Lund University, Lund, Sweden

E-mail: per.augustsson@bme.lth.se, URL: <http://bme.lth.se/staff/augustsson-per/per-augustsson/>

Introduction

Acoustophoresis, where flow and acoustic fields are used to separate suspended objects, is getting increasingly more attention for cell and bacteria-handling applications relating to medicine and biology. Major benefits are flexibility in design, gentleness to cells and that relatively large forces can be exerted on suspended objects enabling processing of several milliliters of sample per minute [1-3].

Two important features limit acoustophoresis. First, the strong size dependency hampers separation of cells based on the underlying properties density and compressibility. Second, the presence of acoustic streaming leads to a smallest size of objects that can be manipulated by primary radiation forces. To address these problems, in addition to our general curiosity, we have started to explore the action of acoustic fields on fluids of inhomogeneous acoustic properties. The work that I will present is primarily experimental, but, spurred by our observations, an interesting theoretical framework is evolving [4].

In brief, we show that cells and liquids re-organize themselves in a systematic way when exposed to an acoustic standing wave, and this enables size-insensitive phenotype-specific separation of cells based on their acoustic properties. Further we have found that acoustic streaming in the bulk can be reduced thousand-fold by the stabilizing forces that arise in liquids of inhomogeneous acoustic properties.

Principle of Iso-acoustic focusing (IAF)

In IAF, cells are deflected sideways by a half-wavelength resonant acoustic pressure field oriented orthogonal to the flow, in a laminar flow microchannel. Cells suspended in a standard cell-culture medium are injected near both side walls of the channel and cell-free liquid of higher acoustic impedance Z_{med} is injected in a central inlet to occupy the central part of the flow. The flow velocity of the channel is tailored such that an acoustic impedance gradient forms by way of molecular diffusion. Because the acoustic radiation force F_{rad} is governed by the difference in mass density ρ and adiabatic compressibility κ between the cell and the surrounding medium, there exists a medium condition for which the acoustic contrast Φ and force F_{rad} are zero, and thus the acoustically induced sideways velocity u_{rad} vanishes. This condition we refer to as the iso-acoustic point (IAP). To a good approximation the IAP is the location at which Z_{med} equals the effective acoustic impedance Z_{cell} of the cell[5].

Cells initially injected near a wall will migrate toward the channel center due to a positive acoustic contrast, (Fig. 1a). Upon traversing up the impedance gradient of the medium, the acoustic contrast eventually becomes zero at the IAP, preventing the cell from moving any further. If the cell instead starts out in the channel center, it will move out towards the walls, down the impedance gradient, until reaching the same IAP. At the end of the microfluidic channel, the sideways position of individual cells can be recorded and then translated to an effective cell acoustic impedance, since $Z_{cell} = Z_{med}$ at the IAP, (Fig. 1b).

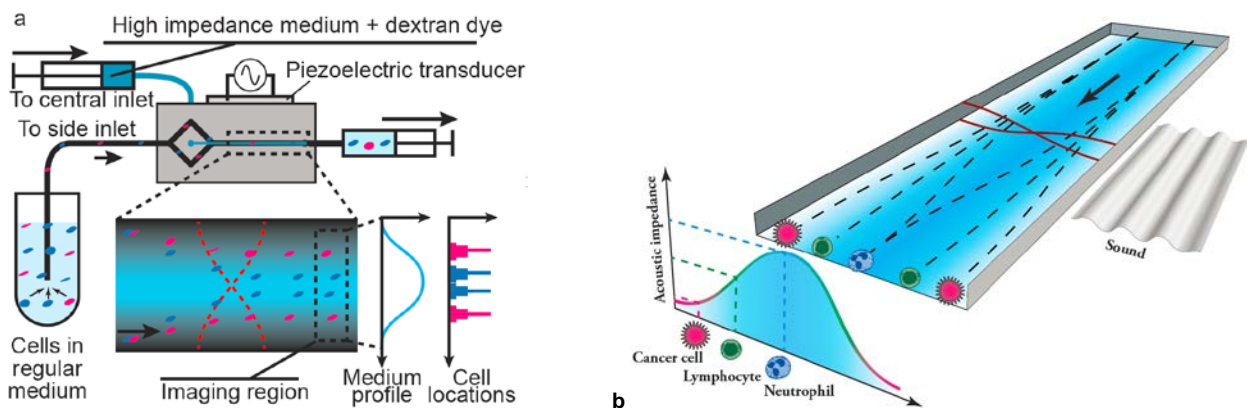


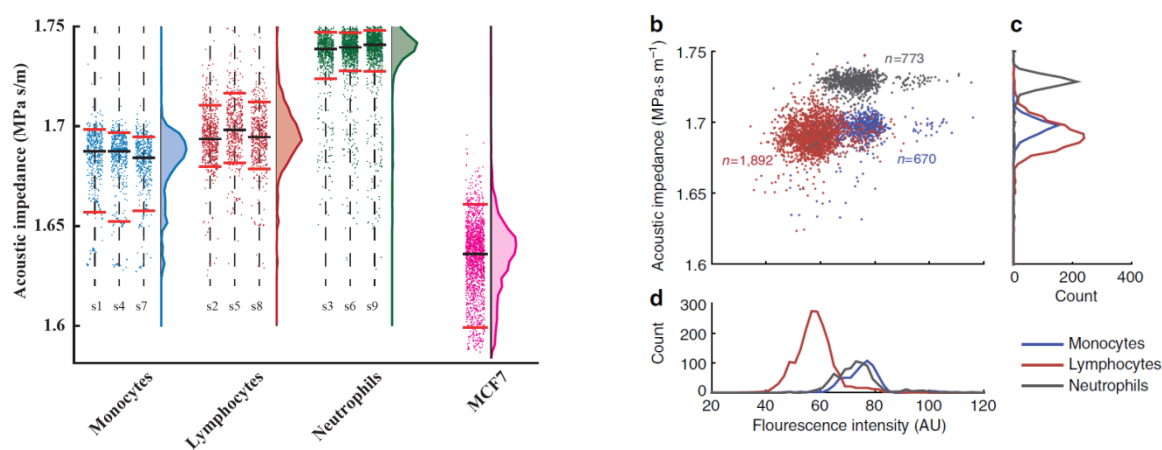
Figure 1: Schematic of (a) the system and (b) the principle of IAP-based, and thus size-insensitive, cell separation.

Cells flow through a channel and a sound field pushes them sideways into media of gradually increasing density. Near the end, the sideways position of each cell depends on its phenotype-specific acoustic impedance. Fig. (a) is from [5].

Results

To understand to what extent acoustic impedance can discriminate cells from mixed populations, we analyzed MCF7 breast cancer cells, primary human monocytes, lymphocytes and neutrophils purified from whole blood via negative selection (Fig. 2a). Lymphocytes (red) and monocytes (blue) have partly overlapping acoustic impedance distributions, whereas neutrophils (green) have substantially higher acoustic impedance. The results suggest that neutrophils can be distinguished from lymphocytes and monocytes purely based on their location in an acoustic impedance gradient. Since lymphocytes and monocytes have substantially different sizes ($\sim 7.5 \mu\text{m}$ and $\sim 9.0 \mu\text{m}$, respectively) but similar acoustic impedance ($\sim 1.69 \text{ MPa s m}^{-1}$), whereas neutrophils and monocytes have similar sizes ($\sim 9.0 \mu\text{m}$) but differing acoustic impedances ($\sim 1.73 \text{ MPa s m}^{-1}$ and $\sim 1.69 \text{ MPa s m}^{-1}$, respectively), these results clearly illustrate the size-independence of the IAF method. Notably, MCF7 cancer cells have lower acoustic impedance than all the investigated leukocytes which holds promise for efficient isolation of circulating tumor cells from liquid biopsies from cancer patients.

To highlight how acoustic properties combined with optical measurements can form a two-parameter classification analogous to flow cytometry, without using cell type-specific labels, we point to the scatter plot and the associated distributions in Fig. 3 of the effective acoustic impedance vs the total cell fluorescence intensity. Even though the total intensity is not a true measure of cell volume, the scatter plot allows us to distinguish monocytes from lymphocytes based on an optical measurement, while the assessment of the effective acoustic impedance enables identification of neutrophils.



a

Figure 2: (a) Scatter plots containing 9050 data points of subsequent measurements of pre-enriched monocytes (blue), lymphocytes (red) and neutrophils (green). Labels s1 to s12 indicate the order of the sample analysis. (b) Scatter plots of the measured effective acoustic impedance vs fluorescence intensity of pre-enriched monocytes, lymphocytes and neutrophils (gray) from a second donor, and the distributions of (c) the effective acoustic impedance and (d) fluorescence intensity. (Data is from [5]).

Conclusion

Our results show that, in IAF, stratified liquids and suspended cells arrange themselves in a way that can be predicted from their effective acoustic impedances. This rearrangement and process is analogous to another well-established equilibrium method, density gradient centrifugation, but IAF has the benefit of being straightforwardly implemented in microfluidic systems. The precise spatiotemporal control offered by microfluidics leads us to envision that the IAF method can be developed into a tunable cell profiling method as well as a new tool for size-insensitive label-free cell separation.

References

- [1] Adams, J.D., C.L. Ebbesen, R. Barnkob, A.H.J. Yang, H.T. Soh, and H. Bruus, *Journal of Micromechanics and Microengineering*, **22**(7), (2012).
- [2] Chen, Y., M. Wu, L. Ren, J. Liu, P.H. Whitley, L. Wang, and T.J. Huang, *Lab on a Chip*, **16**(18), 3466-3472 (2016).
- [3] Hawkes, J.J., R.W. Barber, D.R. Emerson, and W.T. Coakley, *Lab on a Chip*, **4**(5), 446-452 (2004).
- [4] Karlsen, J.T., P. Augustsson, and H. Bruus, *Physical Review Letters* **117**, 114504 (2016)..
- [5] Augustsson, P., J.T. Karlsen, H.-W. Su, H. Bruus, and J. Voldman, *Nat Commun*, **7** (2016).



Generation of acoustic vortices using standing surface acoustic waves in a microfluidic device

Pierre Thibault, Ianis Bernard, Alexander A. Doinikov, Thomas Combriat, and Philippe Marmottant

CNRS, LIPhy UMR 5588, Université Grenoble-Alpes, Grenoble, 38401 France
E-mail: pierre.thibault@univ-grenoble-alpes.fr, URL: <http://www-liphy.univ-grenoble-alpes.fr>

Introduction

In the presence of boundaries, standing acoustic waves are known to generate acoustic streaming due to viscous effects. When two orthogonal standing acoustic waves at a same frequency are emitted in a plane parallel to such boundary, we have predicted that the presence of a phase lag leads to interference terms and consequently to some component of the vorticity of the streaming velocity normal to the boundary. Using a microfluidic device associating a PDMS cavity and a LiNbO₃ substrate emitting surface acoustic waves at 37 MHz seeded with micron size particles as tracers, we could indeed observe such vortices forming a pattern with alternate clockwise and anti-clockwise rotation. In addition, we uncovered complex 3D trajectories between levitation planes that built normal to the channel plane. Since our aim was to manipulate fluids and particles at small scale, we developed a theoretical framework including radiation, streaming forces and torques to mimic the observed velocities and trajectories.

Prediction

In 1958 [1], Nyborg published its calculation of the streaming velocity near a rigid wall oriented along the direction of a standing wave, as is the case in Kundt's tube experiment. He found alternate positive and then negative limiting velocities, *i.e.* at a distance corresponding to the viscous boundary layer thickness δ , every quarter of a wavelength. We show here that when two such perpendicular waves are emitted from two pairs of sources, as sketched in Fig. 1a, with some phase lag φ , the presence of interference terms leads to elliptical trajectories of the fluid particles, and therefore to vorticity of the velocity field in a direction perpendicular to the walls. We illustrate this phenomenon on Fig. 1b where we have represented the velocity field obtained from our calculations in the xy plane, according to the approach proposed in ref.[2].

Materials and methods

To test this prediction, we have built an experimental cell adapted from a previous design developed for acoustic tweezers[3]. A X-cut LiNbO₃ wafer was assembled to a PDMS cavity (1 mm×1 mm and approx. 110 μm high) into which the liquid was introduced. For the experiment, sound was emitted from four interdigitated structures arranged as a square and excited at a same frequency of 37 MHz (see Fig. 1a). Due to the anisotropy of the sound velocities of the material, the pitches of the IDTs pairs 2-4 along \mathbf{e}_x (crystal Y-axis) and 1-3 along \mathbf{e}_y (crystal Z-axis) were made to be 100.0 μm and 94.5 μm in order to resonate at the same frequency. The top part of the acoustic cavity was made of a glass coverslip to create a high acoustic impedance interface.

For each experiment, water plus 1- μm polystyrene microbeads used as tracers were introduced into the cavity through a microchannel. The cross-standing waves were then obtained from 4 synchronized AC generators which excited surface acoustic waves which further leaked into the acoustic cavity. The velocity measurements were then performed using a high speed camera at some given altitude in the channel since while, due to the nature of the sources, a standing wave with several pressure nodes and antinodes built in the channel height.

Results and interpretation

Fig. 1c shows some typical trajectories of the fluid obtained from PTV when the phase lag φ between S3-S1 and S2-S4 is equal to $\pi/2$. We observe a pattern of 4 vortices with alternate left-right vorticity in each unit cell of dimensions $\lambda_x \times \lambda_y$. This corresponds to a period of the vortices that is twice that of the acoustic standing wave. We also compare in Fig. 1d and 1e the velocity profiles obtained along the two directions indicated by the purple and red stripes of Fig. 1c with our model. Provided the

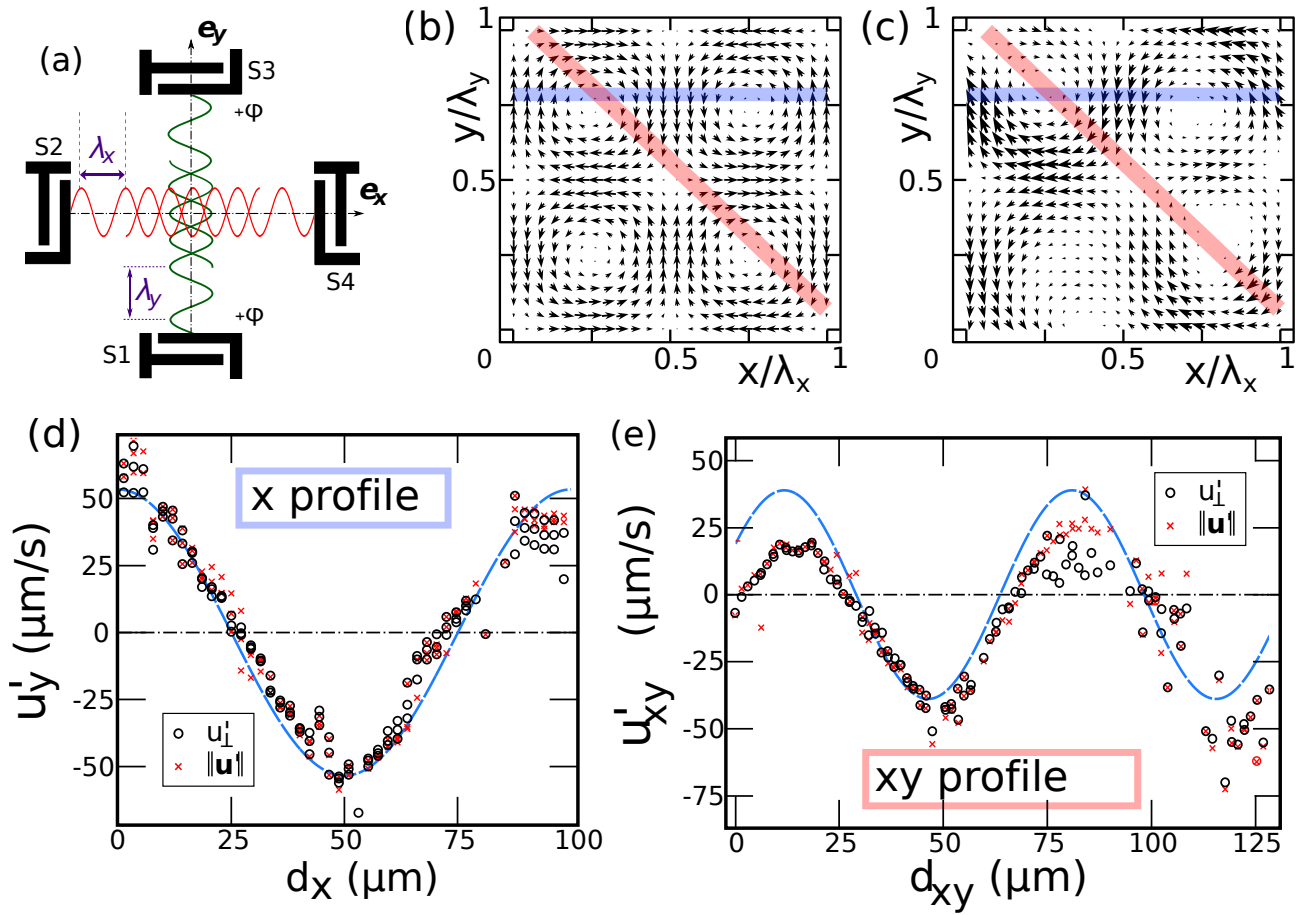


Figure 1: (a) Scheme of interferences of two orthogonal waves with some phase lag φ . (b) Prediction for velocity field in the xy plane at a distance from the rigid walls which is a multiple of $\lambda_z/2$. (c) Measured velocity field obtained from particle tracking. The wavelengths are respectively $\lambda_x = 100.0 \mu\text{m}$ and $\lambda_y = 94.5 \mu\text{m}$. (d) Velocity profile following the purple stripe shown on (c), with d_x in abscissa the distance. Black circles correspond to the velocity u'_\perp perpendicular to x -axis and red crosses to the norm of the 2D velocity $\|\mathbf{u}'\|$. The blue line is a fit assuming a streaming velocity of $53 \mu\text{m.s}^{-1}$. (e) Same as (d) along the red stripe oriented at -45° from x -axis with d_{xy} the distance. u'_\perp represents the component of the velocity projected on an axis at $+45^\circ$ from x -axis.

velocity scale for the acoustic streaming is of order of $53 \mu\text{m.s}^{-1}$, which is typical of our experiments, we obtain an excellent agreement, even if the data are slightly biased due to some additional large scale streaming that developed in the experimental cell, perpendicular to the the xy direction.

Conclusion

We have proven theoretically and experimentally the possibility of creating vortices from acoustic streaming in a high frequency microfluidic device using surface acoustic waves as sources. They differ from the usually observed vortices since their vorticity is perpendicular to the wall from which they originate. Due to this property, they open to a whole set of new possibilities, including fluid mixing, or orienting. From a theoretical point of view, they constitute a modern extension of the pioneering work by Wang *et al.* on the acoustic rotation of spherical objects[4].

This work received support from European Community's Seventh Framework Programme (FP7/2007-2013) ERC Grant Agreement Bubbleboost no. 614655.

References

- [1] W. L.Nyborg. The Journal of the Acoustical Society of America **30**, 329-339 (1958).
- [2] J. Vanneste, J and O. Bühler. Proceedings of the Royal Society A **467**, 1779-1800 (2011).
- [3] S. B. Q. Tran, P. Marmottant, and P. Thibault. Applied Physics Letters **101**, 114103 (2012).
- [4] F.H. Busse, and T.G. Wang. The Journal of the Acoustical Society of America **6**, 1634-1638 (1981).

Particle Sorting using a Combination of Travelling and Standing Surface Acoustic Waves

Adrian Neild¹, Jia Wei Ng¹, Citsabehsan Devendran¹, Ye Ai² and David J. Collins²

¹Laboratory for Micro Systems, Department of Mechanical and Aerospace Engineering, Monash University, Clayton, Australia. E-mail: adrian.neild@monash.edu

²Pillar of Engineering Product Development, Singapore University of Technology and Design, Singapore

Introduction

Acoustic fields offer a versatile and non-contact method widely used for particle and cell manipulation. Excitation is usually achieved through resonance of the fluid body using bulk acoustic waves, or resonance of certain modes in the substrate causing surface acoustic waves (SAW). In order to generate an ultrasonic standing wave using SAW, two counter propagating travelling waves are usually used, in this work, we make show that over the width of a wide channel, such an approach actually gives rise to a sound field which is dominated by travelling wave effects at each edge and a standing field at the center, due to the leaky way in which energy is lost from the substrate into the fluid. We show that using that this feature of the field can be used to achieve deterministic particle sorting, in which particles are migrated by the travelling wave into certain size dependent locations within the standing wave field. Unlike other acoustic sorting systems [1-3], the end location of each particle size is stable rather than time of exposure dependent, as it is a balance of travelling and standing wave forces. In this way 5.1 μm , 6.1 μm and 7.0 μm are accurately sorted.

The System and Operating Principle

Figure 1 shows a schematic of the system, it can be seen that a set of IDTs is positioned on either side of the channel. Due to the coupling of energy from the substrate to the fluid, the strength of the surface acoustic wave diminishes as it propagates from the IDT, as such at the edges of the channel, where the path length is considerable further for one IDT than the other, there is an imbalance in amplitude, and as such, if the width is substantial then there will be a region near the channel edges in which the behavior is dominated by the travelling wave from the nearest IDT set. Whilst in the middle of the channel, the path length and so amplitudes are approximately equal, so a standing wave will be created.

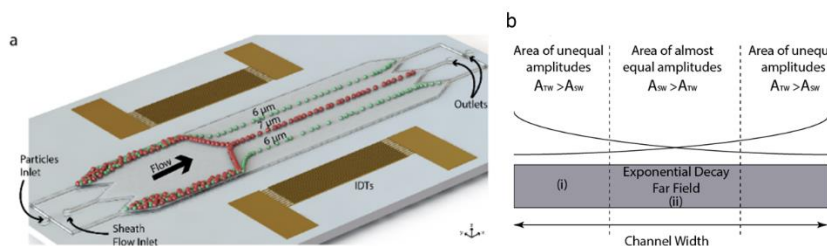


Figure 1: (a) a schematic of the system, particles are introduced at the edge of the channel either side of a central buffer, the sound field is dominated by travelling wave effects at the edges and a standing wave centrally (b), so that particles will migrate until reaching a stable location in the standing wave.

Calculated Force Field

To demonstrate the effect of the forces generated in this hybrid travelling and standing wave field, a simplified system has been modelled numerically. In the model, two counter propagating travelling waves are produced at each end of the model and attenuated as per the leaking of energy into the fluid in a SAW system, which has been characterized as $9.24 \lambda_{\text{SAW}}^{-1}$ Nepers/m [4]. The forces acting on a particle located within this field is then calculated numerically [5]. Figure 2 shows the forces acting on a particle in a purely travelling wave, and a pure standing wave, and compares this with a hybrid field. As the forces arising in a travelling wave are related to the radius to the sixth power, whilst those in a pure standing wave are to the third power, the relative strength of forces differs based on particle size. As such, when a hybrid field exists the location at which the force becomes zero, as the particle migrates inwards from the edge of the channel, differs as a function of size. Once this region is reached, however, the particle's location is stable, so the time of exposure does not play a role in the particle sorting. This means that it is expected that particles of different sizes will emerge along different streamlines from the field, and that even whilst still within the field, these streamlines should be parallel to the direction of fluid flow (indicating a stable location has been reached), this latter feature differs from other particle sorting systems presented in the literature.

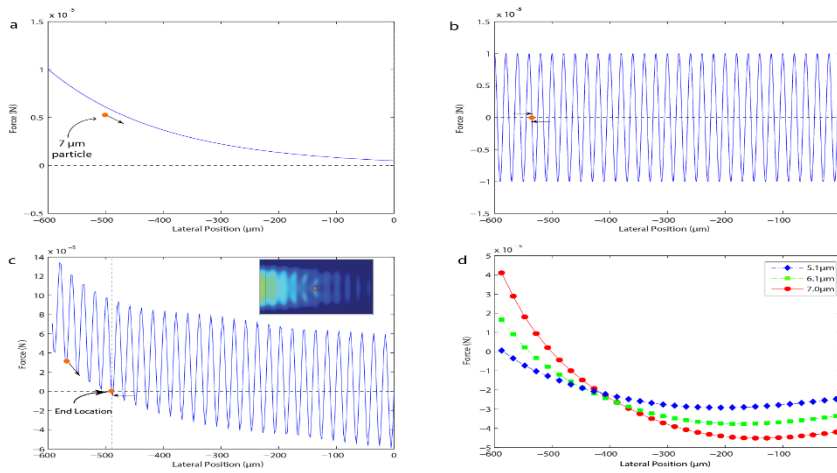


Figure 2: (a) the force due to a pure travelling wave, and that due to a pure standing wave (b) are well known. However, when a hybrid field exists displaying components of both in spatially varying proportions, the force field also displays a mixture of characteristics (c). The first point at which the force becomes zero, as labelled, represents a stable end location for the particle, it will not migrate further across the channel width. By plotting each successive minima in the force for different particle sizes it can be seen that the location of the zero crossing is size dependent (d).

Results

Figure 3 shows the trajectory of different particle sizes as they migrate (left to right) through the sound field, it can be seen that in each case a stable location is reached after which the trajectory is parallel to the flow direction. When particles of different sizes are passed through the system highly specific size-based sorting is achieved as these stable locations are size dependent.

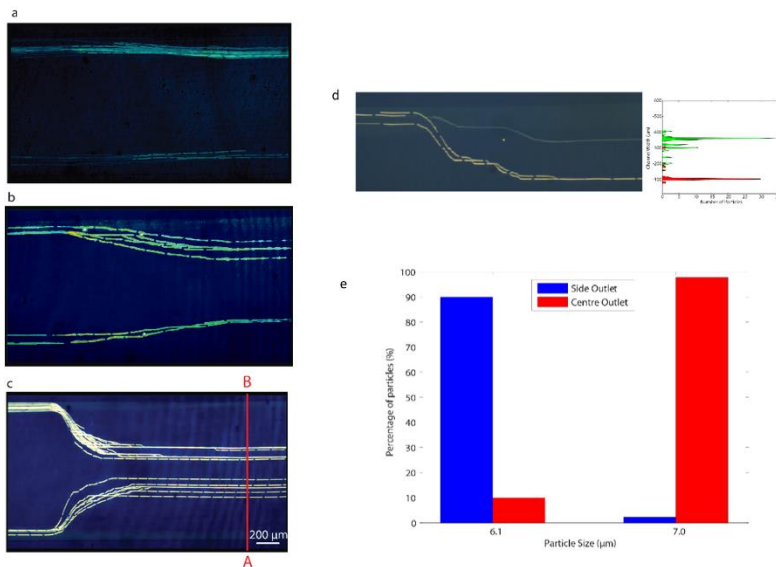


Figure 3: (a-c) the trajectories of 5.1, 6.1 and 7.0 μm particles are shown as they flow through the force field from left to right. The trajectories are characterized by a migration inwards in the travelling wave dominated part of the field, to a stable end location in the standing wave dominated part of the field in which they move through the field along fluid streamlines with no further lateral deviation. When a mixed population is passed through the system the difference in the end locations are clearly seen (d), and accurate sorting can be achieved between 6.1 and 7.0 μm particles (e).

Conclusion

Through the accurate description of the sound field generated by two IDTs, a scenario which is nominally termed a standing surface acoustic wave, we have shown that the field is more complex consisting of travelling and standing wave effects. This complexity gives rise to the possibility of deterministic sorting based on size, with lateral migration to stable end locations dictated by particle size.

References (Times New Roman 10 pt)

- [1] D. J. Collins, T. Alan, and A. Neild. Lab on a chip **14**, 1595-1603 (2014).
- [2] G. Destgeer, B. H. Ha, J. H. Jung, and H. J. Sung. Lab on a chip **14**, 4665-4672 (2014).
- [3] X. Ding, S. C. Lin, M. I. Lapsley, S. Li, X. Guo, C. Y. Chan, I. K. Chiang, L. Wang, J. P. McCoy, and T. J. Huang. Lab on a chip **12**, 4228-4231 (2012).
- [4] S. Shiokawa, Y. Matsui, and T. Ueda T. Proceedings Ultrasonics Symposium, IEEE **641**, 643-646 (1989).
- [5] J. Dual, P. Hahn, I. Leibacher, D. Moller, T. Schwarz, and J. Wang. Lab on a chip **12**, 4010-4021 (2012).

Multi-purpose SAW-based device for comprehensive cell behavior studies

Christine Faust¹, Erik Angermann¹, Andreas Winkler¹, and Hagen Schmidt¹

¹SAWLab Saxony, Leibniz FW Dresden, Dresden, Germany
E-mail: c.faust@ifw-dresden.de, URL: <http://www.sawlab-saxony.de/>

Introduction

The use of surface acoustic waves (SAW) in microfluidics has become a powerful tool for the manipulation of fluids (e.g. mixing and pumping) as well as for manipulation of particles and cells (e.g. focusing and trapping) in fluidic systems [1]. When using a symmetric array of opposing interdigital transducers (IDT) a standing wave field in a fluid is generated with nodal points at half wavelength. There cells can be trapped, while culture medium can flow through the chamber preventing a critical shortage of nutrients [2]. By altering the phase of the excited SAWs the position of the nodal points (and by this the position of the cells) can be changed within the acoustic path inside the microfluidic chamber [3]. At the same time, the SAW-induced pressure waves generate streaming of the fluid which causes mixing and the development of a concentration gradient if different fluids are used.

The objective of the experimental work presented here is the SAW-controlled manipulation and placement of cells and other specimens within a well-defined gradient field of active agents in a microfluidic chamber. We introduce a SAW-based microfluidic device which enables the adjustment of concentration gradients, the trapping of cells and their defined movement via phase shift of the opposing SAW to expose the cells to different concentrations of nutrient substances, active agents and analytic solutions. The successful application of such a device is a major goal in cell analytics and biological research.

With the described SAW-device we successfully isolated cells of *Saccharomyces cerevisiae* out of a flow of culture medium, exposed them to different concentrations within a gradient field of methylene blue and nutrient solution by defined shifting of the nodal points and were able to perform an online live-dead-staining.

Results

With the presented setup it was possible to trap cells out of a flow of nutrient solution and to hold them at a specific position independent of flow conditions inside the chamber. At the same time the device enabled the movement of the cell pattern around the microchamber by phase-shifting of the driver signals fed to the IDT pairs to expose the trapped cells to different concentrations of a specific substance as depicted in Fig. 1. Trapped cells were observed during alteration of medium and a long-term observation allowed to document the process of dying of a cell due to a long exposure to methylene blue (Fig. 1). Using staining times that cause no cell death, a classical live-dead-differentiation was performed.

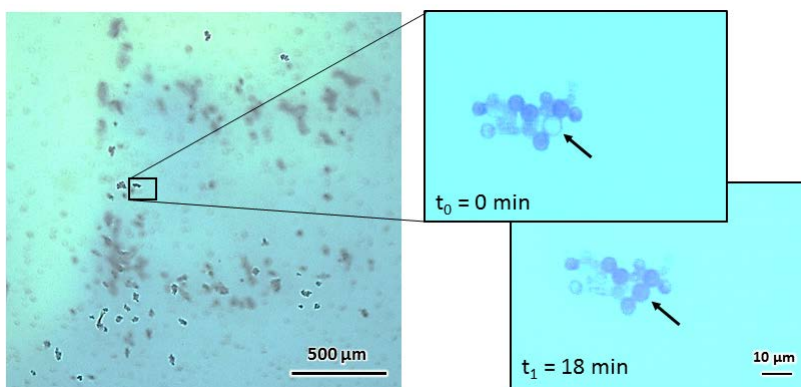


Figure 1: Cells of *Saccharomyces cerevisiae* trapped in the SAW induced pressure field in the microfluidic chamber. Caused by the height of the chamber the trapping occurs in a stack of several planes. The enlarged viewing traced the focused cells over time when exposed to methylene blue solution. The arrow indicates a cell whose process of death was monitored.

One of the benefits of the device is its independency of a certain concentration of cells. Especially for low cell densities the trapping allows to get enough cells for statistic reliable analysis without long enrichment steps. The trapping of cells has been successfully executed over a wide range of flow rates and acoustic energies enabling the use of a parameter set according to a specific task: Low acoustic power levels combined with low flow rates are an ideal combination for long term cell observation, as the acting forces on the cells are so low that they do not influence the cells and the slight flow of culture medium provides fresh nutrients to the cells

and removes waste products. When applying higher energies naturally there are higher forces acting on the cells which can be used to figure out effective physical properties of cells.

Experiment

All experiments were conducted with a setup as depicted in Fig. 2. IDTs consisting of 5 nm Ti and 295 nm highly-textured Al with a wavelength of $\lambda=150\ \mu\text{m}$ were patterned on a $128^\circ\text{YX-LiNbO}_3$ substrate with a propagation direction of 0° , 54° and 90° with regard to the crystallographic X-direction, as for these directions Rayleigh type waves undergo no beam steering. The aperture of the IDTs was 2 mm and the overlap of the SAW paths defined the manipulation area of 2 mm x 2 mm. For the experiments only the IDTs in X-direction and $X+90^\circ$ were used. The different phase velocities in X and $X+90^\circ$ -direction resulted in frequencies for Rayleigh wave excitation of about 24.3 MHz and 25.8 MHz, respectively. The electrical characterization by network analyzer (Agilent 5071C, Agilent Technologies) showed an S_{11} of 0.2 for the X-direction as well as for the $X+90^\circ$ -direction when using a matching circuit [4].

The surface of the SAW-chips was passivated with a 1 μm thick layer of sputtered SiO_2 to prevent electrode corrosion and to ensure biocompatibility of the device.

A microfluidic chamber made of Polydimethylsiloxane (PDMS, Sylgard 184, Dow Corning, mixing ratio 1:10) via replica molding was mounted to the SAW-chip surface by UV-ozone activation of PDMS and chip surface, manual alignment and subsequent curing at 80°C for 30 min. The area of the PDMS-chamber was 3 mm x 3 mm, which was larger than the overlapping area of crossing SAW paths to prevent unpredictable influences of chamber walls on the wave field. Fluidic connection was achieved by punching holes in the PDMS and tubing with syringe pump (neMESYS, cetoni GmbH) or waste outlet.

The organism used in these studies was baker's yeast *Saccharomyces cerevisiae* cultivated in minimal medium consisting of 20 g/l glucose and 9 g/l NaCl dissolved in water. The online staining was performed with methylene blue (0.05 % in water).

Pre-cultured (overnight) yeast cells were diluted in fresh medium to get a cell density of around 10^7 cells per liter and injected in the microfluidic chamber via a syringe pump with a flow rate of 0,5 $\mu\text{l/s}$. Once the chamber was filled with cell containing medium, the IDTs were activated by about 100 mW for each IDT (PowerSAW, Belektronik GmbH) to trap the cells at the nodal points. When a sufficient number of cells was trapped, the cell containing medium flow was stopped and changed to culture medium. At the same time the flow of staining solution was started so that the sum of both inflows result again in a flow rate of 0.5 $\mu\text{l/s}$.

The trapped cells were now moved by shifting the phase of SAWs around in the chamber to expose them to different concentrations of culture medium and staining solution. The observation of the cells was done with a digital microscope (Keyence VHX2000).

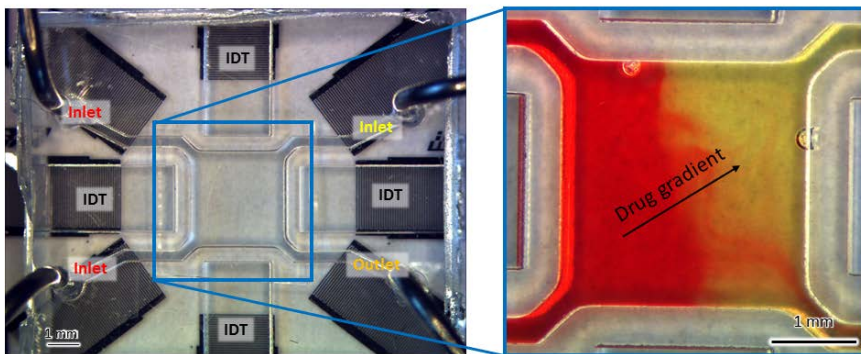


Figure 2: Experimental setup with SAW-induced gradient of two different fluids dyed with red or yellow ink for better visualization.

Conclusion

With the introduced SAW-device we performed a two dimensional trapping of yeast cells as well as a defined movement of the trapped cells in the manipulation area. By using different inflow solutions the acoustic streaming force generated a gradient which allows us to expose the cells to different concentrations of a staining solution and observe their reaction. The device offers high functionality and indicates a promising path forward to a broad range in cell research.

References

- [1] X. Ding, P. Li, S. Lin, Z. Stratton, N. Nama, F. Guo, D. Slotcavage, X. Mao, J. Shi, F. Costanzo, and T. Huang. Lab on a Chip **13**, 3626-3649 (2013)
- [2] D. Collins, B. Morahan, J. Garcia-Bustos, C. Doerig, M. Plebanski, and A. Neild. Nature Communications **6**, (2015)
- [3] L. Meng, F. Cai, Z. Zhang, L. Niu, Q. Jin, F. Yan, J. Wu, Z. Wang, and H. Zheng. Biomicrofluidics **5**, (2011)
- [4] A. Winkler, R. Brünig, C. Faust, R. Weser, and H. Schmidt. Sensors and Actuators A: Physical, accepted for publication (06/2016)

Radiation-dominated microparticle motion in a PDMS microchannel driven by a standing surface acoustic wave

Rune Barnkob¹, N. Nama², L. Ren², F. Costanzo², T. J. Huang², and C. J. Kähler¹

¹Institute of Fluid Mechanics and Aerodynamics, Bundeswehr University Munich, Germany
E-mail: barnkob@unibw.de

²Department of Engineering Science and Mechanics, The Pennsylvania State University, PA, USA

Introduction

Acoustofluidics systems, driven by surface acoustic waves (SAWs), are receiving a growing interest due to their abilities to manipulate particles and liquids in a controlled manner [1]. In such systems, the acoustic radiation force is often responsible for the motion of suspended particles. However, the exact oscillatory acoustic fields and the resulting radiation-force-driven particle motion are usually unknown, especially the motion perpendicular to the actuated substrate which is typically parallel to the direction of observation. In this work we present full three-dimensional measurements of microparticle acoustophoresis in PDMS microchannels driven by standing SAWs. The aim is to validate and improve our existing numerical model [2] and to investigate the role of microchannel height. The model agrees qualitatively well with the measurements of radiation-dominated 5- and 8- μm particles, both for different substrate displacement node positions, microchannel widths, and for thin and thick PDMS wall widths. We confirm that our model includes the most relevant elements for understanding radiation-dominated particle manipulation via SAWs.

Experiments

The experimental system is shown in Fig. 1. It consists of a liquid-filled PDMS microchannel bonded on a lithium niobate (LiNbO_3) piezoelectric substrate acoustically-actuated by two interdigital transducers (IDTs). When acoustically actuated, the IDTs create two counter-propagating SAWs (or Rayleigh waves) which result in a standing SAW of wavelength $\lambda = 600 \mu\text{m}$ at the substrate/microchannel interface. The standing SAW propagates into the microchannel liquid and creates an oscillating pressure field which generates a steady acoustic streaming field as well as an acoustic radiation force on suspended particles. Microchannels of cross-sections $600 \times 125 \mu\text{m}^2$ and $310 \times 94 \mu\text{m}^2$ were studied. To investigate the effect of wall thickness, we examined microchannels of different PDMS wall widths W (300 μm and 5 mm). The PDMS top wall thickness H was in all cases 5 mm or more. The actuation was done at frequencies $f \sim 6 \text{ MHz}$ and peak-peak voltages $U_{\text{pp}} \sim 40 \text{ V}$.

We studied 5- and 8- μm fluorescent polystyrene particles in a 20:80 w/w glycerol-water mixture and we recorded the three-dimensional particle motion using the General Defocusing Particle Tracking (GDPT) [3]. The measured sedimentation rates of the suspended particles were less than 0.1 $\mu\text{m/s}$, which is negligible in comparison with the acoustically-driven velocities of around 10-30 $\mu\text{m/s}$. In order to obtain several particle trajectories while maintaining a low particle concentration (to neglect particle interactions), we used a fully automated acquisition system similar to the work by Augustsson et al. [4]. The measurement volume covered the entire microchannel cross-section along 1.4 mm.

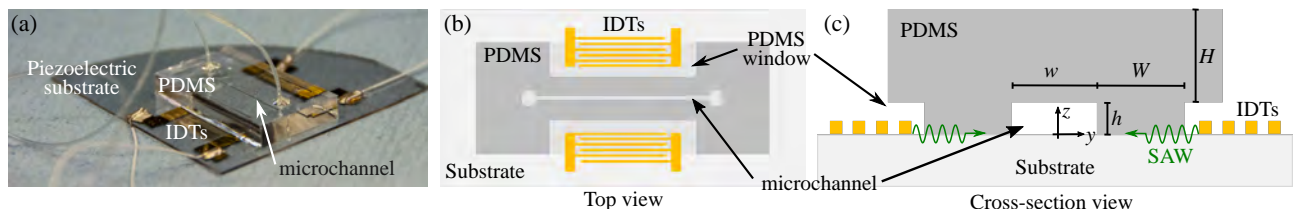


Figure 1: (a) Standing SAW microchip. Schematic of (b) the top view and (c) the cross-section view.

Results

A small representation of the results is shown in Fig. 2 and 3. All figures show the motion of 5- μm particles in the yz -cross-section and the first result to report is the translational invariance of the yz -motion along the x -direction. It is thus reasonable to compare to our 2D FEM model of the particle

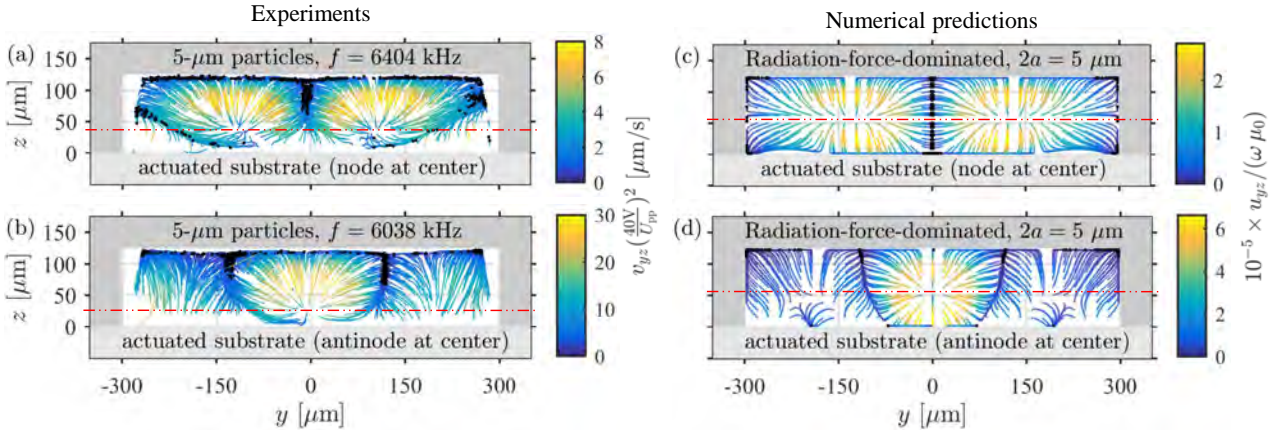
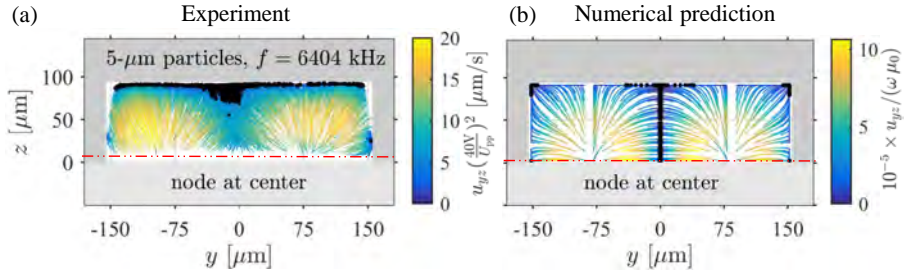


Figure 2: 5- μm particle trajectories in the cross-section in a microchannel of width $w = 600 \mu\text{m}$, height $h = 125 \mu\text{m}$, and thick wall width $W = 5 \text{mm}$. The velocity magnitude u_{yz} is shown as colors. Panels (a) and (b) each show more than 900 experimental trajectories measured using the GDPT technique for 3D particle tracking [3], while panels (c) and (d) show the numerical FEM predictions for pure radiation-force-dominated single-particle motion [2]. Note that the velocity magnitudes cannot be compared between experiments and numerics as the substrate actuation velocity $\omega\mu_0$ is not known experimentally.

Figure 3: 5- μm particle trajectories with velocity magnitude u_{yz} as colors in a microchannel of width $w = 310 \mu\text{m}$, height $h = 94 \mu\text{m}$, and thin wall width $W = 300 \mu\text{m}$. A total of 2376 experimental trajectories are displayed.



motion in the yz -cross-section [2]. Furthermore, the motion is clearly dominated by the radiation force and 8- μm particles show same behavior (velocity amplitude scales as expected with particle size squared). Figure 2 shows the results for a microchannel of cross-section $600 \times 125 \mu\text{m}^2$ and thick walls $W = 5 \text{mm}$, while Figure 3 shows the results for a microchannel of cross-section $310 \times 94 \mu\text{m}^2$ and thin walls $W = 300 \mu\text{m}$. In both cases, the model match the experiment qualitatively quite well. This is despite the fact that the model assumes the PDMS wall width to be larger than 2 mm and that no waves can enter the channel through the PDMS walls (for more details see [5]). As expected from the damping of the SAW by the PDMS walls, experimentally we have larger particle velocities for the 300- μm channel with thin walls compared to the 600- μm channel with thick walls. The velocity amplitude of the numerical prediction in Fig. 3 cannot be compared to the ones in Fig. 2.

The dashed red lines indicate the approximate vertical z -position of the horizontal antifocus xy -plane from which the particles are pushed away vertically. Comparing experiments with numerics, the z -position of the antifocus plane differ $\sim 20\%$ for the 600- μm -wide channel and match well for the 300- μm -wide channel. Clearly the z -position of the antifocus plane depends on the height-to-wavelength aspect ratio h/λ (as h decreases for $\lambda = 600 \mu\text{m}$, the z -position of the antifocus plane decreases too). Using numerical predictions to increase h , we observe that the z -position of the antifocus plane increases as well and as h reaches $\sim 175 \mu\text{m}$, a set of a new focus plane and antifocus plane appears.

Conclusions

We present three-dimensional measurements of particles undergoing radiation-dominated single-particle acoustophoresis in a PDMS microchannel acoustically actuated by a standing SAW. The numerical predictions agree qualitatively well with the measurements for channels of different widths, heights, and wall widths. Furthermore, we show that the vertical position of horizontal focus- and antifocus planes depends on the channel height-to-wavelength aspect ratio. Further work will outline the exact radiation-dominated vertical focusing conditions as well as focus on the role of acoustic streaming.

References

- [1] G. Destgeer and H. J. Sung. Lab Chip **15**, 2722-2738 (2015).
- [2] N. Nama, R. Barnkob, Z. Mao, C. J. Kähler, F. Costanzo, and T. J. Huang. Lab Chip **15**, 2700-2709 (2015).
- [3] R. Barnkob, C. J. Kähler, and M. Rossi. Lab Chip **15**, 3556-3560 (2015). <https://www.unibw.de/lrt7/gdpt>
- [4] P. Augustsson, R. Barnkob, S. T. Wereley, H. Bruus, and T. Laurell. Lab Chip **11**, 4152-4164 (2011).
- [5] A. Darinskii, M. Weihnacht, and H. Schmidt. Lab Chip, DOI: 10.1039/C6LC00390G (2016).

Sub-micron particle manipulation with acoustic streaming driven by highly focused surface acoustic waves

David Collins¹, Zhichao Ma¹, and Ye Ai¹

¹Engineering Product Design Pillar, Singapore University of Technology and Design, Singapore. Email: david_collins@sutd.edu.sg, ye_ai@sutd.edu.sg. URL: http://people.sutd.edu.sg/~ye_ai/

Introduction

Manipulation of micron-scale objects is a common goal of microfluidic systems, in which particles and cells are redirected, concentrated or sorted for a variety of diagnostic and biomedical research purposes. Acoustic forces have demonstrated the ability to perform these manipulations in a non-contact, biocompatible and on-demand manner, though have typically been limited to $\sim 10 \mu\text{m}$ scale objects with the application of pure travelling or standing acoustic waves. Many next-generation processes, however, including those using exosomes to catalytic nanoparticles, require the ability to reliably manipulate objects on a smaller scale. While often treated as a side-effect and safely ignored in many systems, acoustic streaming has the ability to help circumvent these size limitations when explicitly utilized. In this work we use highly focused surface acoustic waves (SAW) and the resulting strong combined acoustic streaming and acoustic radiation force to demonstrate both static and continuous manipulation of particle diameters between 300-2000 nm.

System principles

Particle manipulation in an acoustofluidic system is influenced by the combined and competing influences of acoustic forces, arising from directional scattering and radiation pressure and fluid drag that resists the translation of these particles through a viscous fluid. Acoustic streaming, resulting from the attenuation and transfer of acoustic energy into bulk fluid motion in the direction of a propagating plane wave, influences particle motion by perturbing the fluid flow profile and thus redirecting entrained particles. Because the magnitude of the fluid drag arising from streaming is usually secondary to the primary acoustic forces and a lateral, continuous flow component, and because the streaming field is oriented non-uniformly across microfluidic channels, acoustic streaming is often either a secondary consideration, a nuisance, or ignored entirely. The effects of acoustic streaming that usually hinder particle manipulation [2], however can be nullified; Antfolk et al. recently cleverly generated circular rather than periodic streamlines to focus sub-micron particles in a standing wave node [3], though this methodology necessitates the use of phase-synced transducers and is effective over only a single half-wavelength. In contrast, in this work we explicitly maximize the effects of acoustic streaming to achieve rapid particle concentration through the imposition of a highly focused acoustic field generated by surface acoustic waves (SAW). SAW is a developing microfluidic actuation technology that permits the generation of acoustic fields in defined channel regions by applying an AC signal to interdigital transducers (IDTs) patterned on a piezoelectric substrate. Utilizing a focusing IDT structure, acoustic beams on the order of ~ 10 's of microns can be generated [4]; because streaming is generated by body force gradients, streaming velocities are maximized in the case of a focused

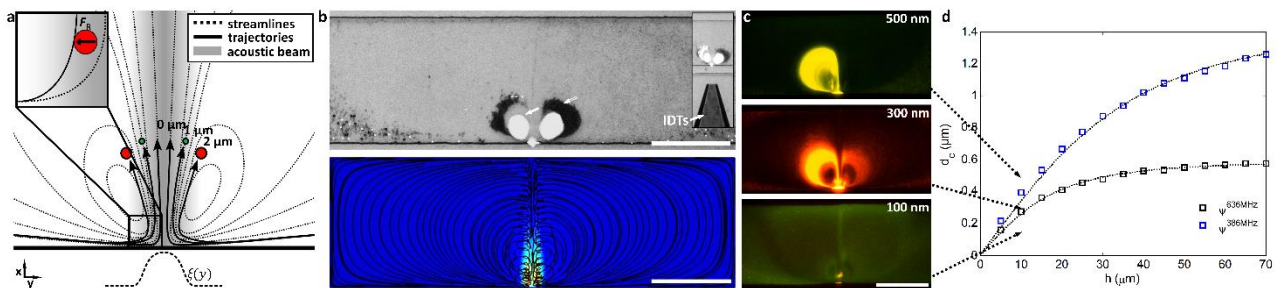


Figure 1: Particle manipulation with highly focused acoustic fields driven by SAW. (a) Mechanism of particle aggregation, where particles are differentially deflected into inner streamlines by the acoustic radiation force at the edge of the acoustic beam. (b) $1 \mu\text{m}$ (black) and $2 \mu\text{m}$ (white) particles aggregate (top image – inset shows position of IDTs relative to channel) in vortex focal points on either side of the maximum displacement regions (bottom image). (c) The particle dimensions that can be manipulated are a function of the beam width (and therefore force gradient), here showing the aggregation of 500 nm, 300 nm but not 100 nm particles, in line with the predictions in (d) for the 636 MHz device used. (d) Shows the simulated critical diameter (d_c) for a given channel height, above which the acoustic radiation pressure overcomes counteracting drag forces. Scale bars are $100 \mu\text{m}$. Adapted from figures in [1].

transducer that generates large substrate displacement gradients. Moreover, these large gradients are also ideal for particle manipulation, where a suspended particle denser than the surrounding medium will translate from regions of high acoustic energy density to a lower density one. The manipulation principle is shown in Figure 1a, where a suspended particle is displaced relative to the fluid streamlines arising from acoustic streaming by the acoustic force potential gradient on either side of the focused beam. Importantly, particles are concentrated from a fluid volume whose length scale spans multiple acoustic wavelengths (indeed it extends to infinity in a static flow condition).

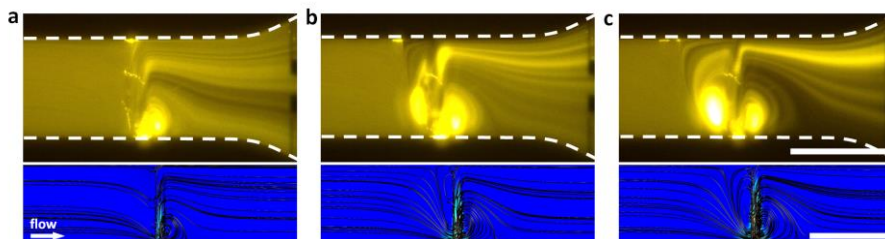


Figure 2: Continuous particle focusing. (a-c) A continuous solution of 500 nm particles is focused through the application of a focused 636 MHz SAW normal to the channel (top images). Observed particle trajectories correspond the simulated streamlines (bottom images). Scale bars are 100 μm .

Results and discussion

In line with the concept diagram in Figure 1a, Figure 1b shows the aggregation of 1 μm (black) and 2 μm particles (white) in the inner streamlines near the focused acoustic beam (inset in Figure 1b shows the location of the SAW IDTs relative to the channel). Owing to the larger acoustic forces imparted on the larger 2 μm particles, these are preferentially focused in the innermost streamlines of the rapidly rotating vortices, here in a 20 μm high channel. Figure 2c demonstrates the limits of size-based concentration, using a 636 MHz, 6 μm transducer with a 14 μm terminal aperture, 500 nm and 300 nm but not 100 nm particles are concentrated (here in a 10 μm high channel). This corresponds to simulation results in Figure 2d, where particles are acoustically focused only where the acoustic radiation force exceeds that of counteracting fluid drag, especially in the lateral y -direction; only particles larger than the predicted critical diameter d_c are dominated by the acoustic radiation force and successfully concentrated. See ref. [1] for more information on the setup of the boundary conditions and acoustic forces necessary to simulate acoustic forces and coupled acoustic streaming.

Streaming-influenced particle manipulation is also feasible in the presence of a continuous lateral flow, which produces an asymmetric flow profile on either side of the focused beam. In typical SAW-based separation, streaming is a secondary effect that has insubstantial effects on particle motion, where the lateral flow velocity is orders of magnitude greater than that of the streaming induced one [4, 5]. However, by utilizing streaming-maximizing focused SAW devices and substantial applied power densities, streaming velocities can approach those of microfluidic channel flow to generate vortical behavior that extends the channel width even with the application of a lateral flow. While the resulting streamlines in this case are not all closed, where continuity requires a path from the channel entrance to its exit, this sets up an interesting case where the incoming streamlines are all focused and pass through the same focused acoustic beam region at sufficient applied power. The resulting effect is that incoming particles are all exposed to similar acoustic forces regardless of their starting positions. Figure 2(a-c) shows the resulting focusing behavior in a continuous flow at 63, 126 and 251 mW (from left to right, respectively, with a lateral flow rate of 0.4 $\mu\text{l}/\text{min}$) and the corresponding simulation results (bottom images) that show the development of force-equalizing and focusing vortices at sufficient levels of applied power. In the near term we will explore and characterize this focusing behavior.

Conclusion

While acoustic fields, and travelling plane wave ones in particular, have had difficulty manipulating sub-micron particles, we show that the coopting of acoustic streaming effects that are usually ignored or avoided can result in concentration and focusing of particles with diameters on the order of 100's of nanometers. This is performed with a highly focused, high frequency SAW device, which maximizes both the magnitude of acoustic streaming velocities and the acoustic radiation force at the edges of the focused acoustic field. These combined effects serve to convectively transport and aggregate suspended sub-micron objects over distances much greater than the acoustic wavelength for consistent manipulation by the acoustic radiation force, resulting in concentration or particle focusing in static or continuous flow conditions. Given its tunable, low-clogging risk nature compared to hydrodynamic methods, this method is ideally suited to many emerging applications that require the manipulation of sub-micron specimens.

References

- [1] D. J. Collins, Z. Ma, and Y. Ai. *Analytical chemistry* **88**, 5513-5522, (2016).
- [2] P. B. Muller, R. Barnkob, M. J. H. Jensen, and H. Bruus. *Lab on a Chip* **12**, 4617-4627, (2012).
- [3] M. Antfolk, P. B. Muller, P. Augustsson, H. Bruus, and T. Laurell. *Lab on a Chip* **14**, 2791-2799, (2014).
- [4] D. J. Collins, A. Neild, and Y. Ai. *Lab on a Chip* **16**, 471-479, (2015).
- [5] G. Destgeer, B. H. Ha, J. H. Jung, and H. J. Sung. *Lab on a Chip* **14**, 4665-4672, (2014).

Proteomic analysis of acoustically trapped extracellular vesicles

Mikael Evander¹, Melinda Rezeli¹, Olof Gidlöf², Paulina Bryl-Górecka², Ramasri Sathanoori², Patrik Gilje², Krzysztof Pawłowski³, Péter Horvatovich⁴, David Erlinge², György Marko-Varga^{1,5}, Thomas Laurell^{1,5,6}

¹Department of Biomedical Engineering, Lund University, Lund, Sweden

E-mail: Mikael.evander@bme.lth.se, URL: <http://www.bme.lth.se>

²Department of Cardiology, Clinical Sciences, Lund University, Lund, Sweden

³Department of Experimental Design and Bioinformatics, Faculty of Agriculture and Biology, Warsaw University of Life Sciences, Warsaw, Poland

⁴Analytical Biochemistry, Department of Pharmacy, University of Groningen, Groningen, The Netherlands

⁵Centre of Excellence in Biological and Medical Mass Spectrometry, Lund University, Lund, Sweden

⁶Department of Biomedical Engineering, Dongguk University, Seoul, Korea

Introduction

Extracellular vesicles (ECVs) are sub-micron membrane particles released by cells in response to stress, activation and apoptosis. Circulating ECVs have been shown to reflect pathobiological processes, e.g. various forms of cardiovascular disease, and are believed to be a source of clinically useful biomarkers. ECVs are typically isolated from blood using a series of centrifugation steps, suspected to affect ECV integrity and create experimental artefacts [1]. Acoustic seed trapping of ECVs was recently shown as an alternative technique [2]. In this work we compare the ECV proteome in a set of clinically relevant samples prepared either by acoustic trapping or a standard centrifugation technique. We show that the proteomic profiles of ECVs isolated by acoustic trapping and standard centrifugation are highly similar and that the ECV proteome of myocardial infarction patients are enriched in proteins linked to known cardiovascular disease pathways, supporting the notion that ECVs are a useful source of blood biomarkers.

Method

We isolated ECVs from healthy controls and ST-elevation myocardial infarction (STEMI) patients (n=10 in each group) using either acoustic trapping or centrifugation. Platelet free plasma (PFP) was prepared by centrifugation of whole blood twice at 1600xg for 15 minutes. For acoustic trapping, an AcouTrap system from AcouSort AB was used, see figure 1. It combines an XYZ- pipetting stage with an acoustic trapping unit based on a 2 x 0.2 mm² glass capillary and a 4 MHz Pz26 transducer. Polystyrene seed particles (12 µm diameter) were trapped after which 150 µl of PFP diluted 1:2 with PBS was aspirated at 30 µl/min. The ECVs were trapped in the seed cluster, washed with PBS and released in 30 µl of PBS. For isolation of ECVs by standard centrifugation, PFP was spun at 20000xg for 1 hour. Isolated ECVs were lysed in RIPA buffer, the extracted proteins were digested using trypsin and finally subjected to proteomic profiling by label-free nano LC-MS/MS. The analysis was performed on a Orbitrap Fusion Mass Spectrometer equipped with an Easy n-LC 1000 pump. MS/MS spectra were searched using the SEQUEST HT search engine in the Proteome Discoverer Software v 1.4 using the UniProt Human Database (June 2015 release). Label-free quantification was performed with MaxQuant Software v 1.5.2.8. Protein annotation and enrichment analysis was performed using Panther Classification System (<http://pantherdb.org>) and DAVID system (Database for Annotation, Visualization and Integrated Discovery).

Results

We identified 251 and 280 “core” proteins in ECVs prepared by standard centrifugation from controls and STEMI patients, respectively. The corresponding number of proteins detected in the trapped samples was 242 and 250. 75% of these of proteins overlapped between the four groups, see figure 2. Functional classification of ECV proteins using gene ontology analysis revealed an enrichment of biological process annotations such as blood coagulation (36 proteins, $p < 1 \times 10^{-32}$), inflammatory response (80 proteins, $p < 1 \times 10^{-35}$), cell adhesion (37 proteins, $p < 1 \times 10^{-5}$) and lipid transport (22 proteins, $p < 1 \times 10^{-11}$). 13 proteins were detected only in trapped samples and 69 were found exclusively in samples prepared by centrifugation, while 80 % of the proteins were detected with both preparation techniques. Membrane associated proteins were overrepresented in centrifuged ECV samples relative to trapped samples (6 % vs. 3 %), while the proportion of extracellular proteins was slightly higher in trapped samples compared to centrifuged samples (34 % vs. 30 %). With regards to biological processes and molecular functions there was no difference between the ECV preparation methods. Proteins enriched in centrifuged samples included several apolipoproteins, whereas numerous immunoglobulins were enriched in trapped samples.

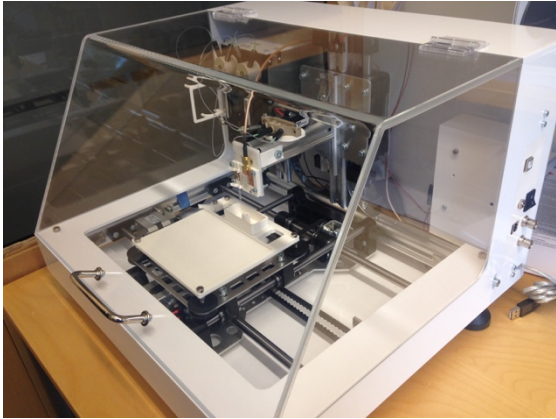


Figure 1: The AcouTrap (AcouSort AB, Lund, Sweden) was used for trapping, washing and dispensing extracellular vesicles from plasma samples. The instrument consists of a robotic stage that couples a 96-well plate to an acoustic trapping chip. Two syringe pumps and three valves are used to dispense and aspirate samples between different wells. The instrument is fully automated and is controlled through user-defined scripts in a LabVIEW program.

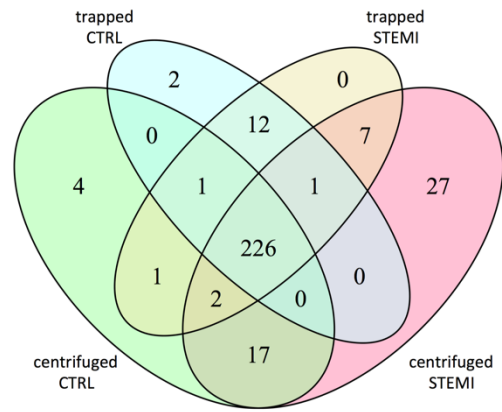


Figure 2: Venn diagram of the “core” proteins detected in at least 50% of the samples from the four different ECV sample groups.

24 proteins were found to be differentially expressed in STEMI versus control samples, of which 8 were found significant with both isolation techniques, 10 were found significant only with trapping and 6 were found significant exclusively in centrifuged samples, see figure 3. The majority of these proteins e.g. myoglobin, creatine kinase M-type, zyxin and actin, have previously been linked to cardiovascular disease, but their association with ECVs has not been shown before.

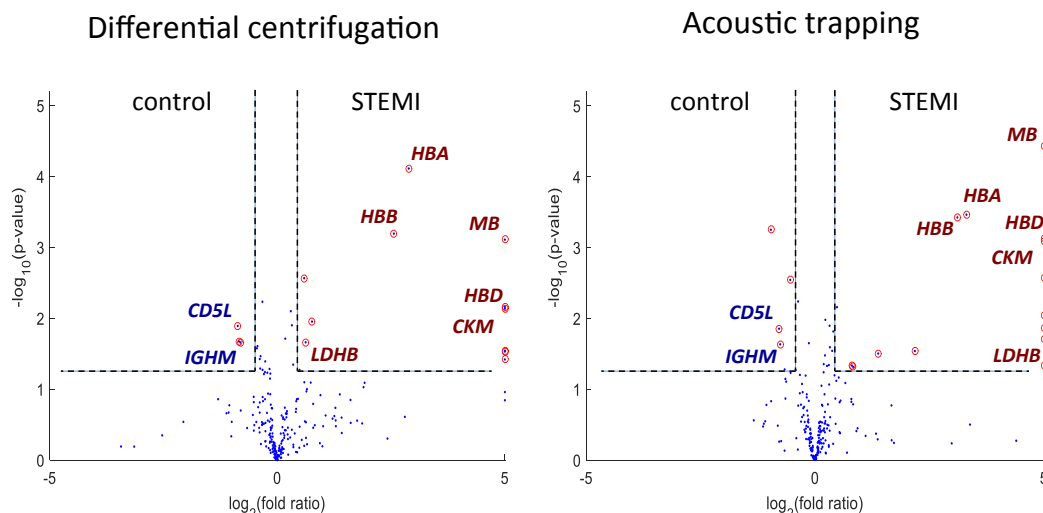


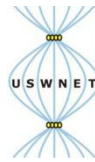
Figure 3: Protein \log_2 fold changes (on the x axis) and the corresponding adjusted \log_{10} p-values (on the y axis) are summarized in volcano plots for ECV samples isolated by acoustic trapping or differential centrifugation. The dots marked in red represent a p-value lower than 0.05 and an absolute \log_2 fold change higher than 0.5.

Conclusion

The proteomic profiles of ECVs isolated by acoustic trapping and standard centrifugation were highly similar, and there was an enrichment of proteins related to coagulation and inflammation, consistent with previous reports on ECV biology. There was an overrepresentation of proteins with known links to cardiovascular disease among differentially expressed proteins in STEMI patients, supporting the notion that ECVs are a source of blood biomarkers.

References

- [1] Lacroix, R.; Judicone, C.; Poncelet, P.; Robert, S.; Arnaud, L.; Sampol, J.; Dignat-George, F. *Journal of Thrombosis and Haemostasis* 2012, 10, 437-446
- [2] Evander, M.; Gidlof, O.; Olde, B.; Erlinge, D.; Laurell, T. *Lab on a Chip* 2015, 15, 2588- 2596.



Biomechanical Influence of the Acoustic Environment for Engineering Cartilage

U.S. Jonnalagadda¹, P. Glynn-Jones², R.O.C. Oreffo³, M. Hill², R.S. Tare^{1,3}

¹Bioengineering Science, Faculty of Engineering and the Environment, University of Southampton, UK

² Mechatronics, Faculty of Engineering and the Environment, University of Southampton, UK

³Center for Human Development, Stem Cells & Regeneration, Faculty of Medicine, University of Southampton, UK

Introduction

Previously, we have shown the potential of long-term tissue development with an acoustofluidic perfusion bioreactor [1]. In the present research, we investigated the role of the acoustic environment in stimulating the cells to developing hyaline-like cartilage. To this end, we create an acoustofluidic bioreactor to allow high throughput tissue development with electronically modulated shear stresses. The system was used to develop cartilaginous tissue following 21 days of levitated chondrogenic culture within a hypoxic environment (5% CO₂, 5% O₂, 37°C) in a humidified atmosphere. The driving parameters were also observed to influence the tissue composition, which lead to characterization of the acoustic environment to determine its influence on tissue development.

Device Fabrication

Layered resonators were fabricated by coupling piezoelectric transducers (PZ26) to 1.0 mm thick glass slides, which functioned as the carrier and also reflector layers. Polycarbonate film functioned as a spacer material and adhered to the carrier and reflector using poly(dimethyl siloxane) (PDMS). A numerical model was used to validate the presence of the half-wave mode for the given resonator dimensions.

Bioreactor Culture

Primary human articular chondrocytes (HACs) were used in 21 day cultures within the bioreactor under hypoxic conditions (5% CO₂, 5% O₂, and 37°C). The resulting tissue constructs were extracted from the resonators and chemically fixed to section and staining for cartilage-specific markers, such as SOX9, proteoglycans, and collagen type II. The present results suggest changes in matrix composition as the sweep time is increased, showing more cartilage-specific matrix production at 2 Hz relative to 50 Hz (Figure 1).

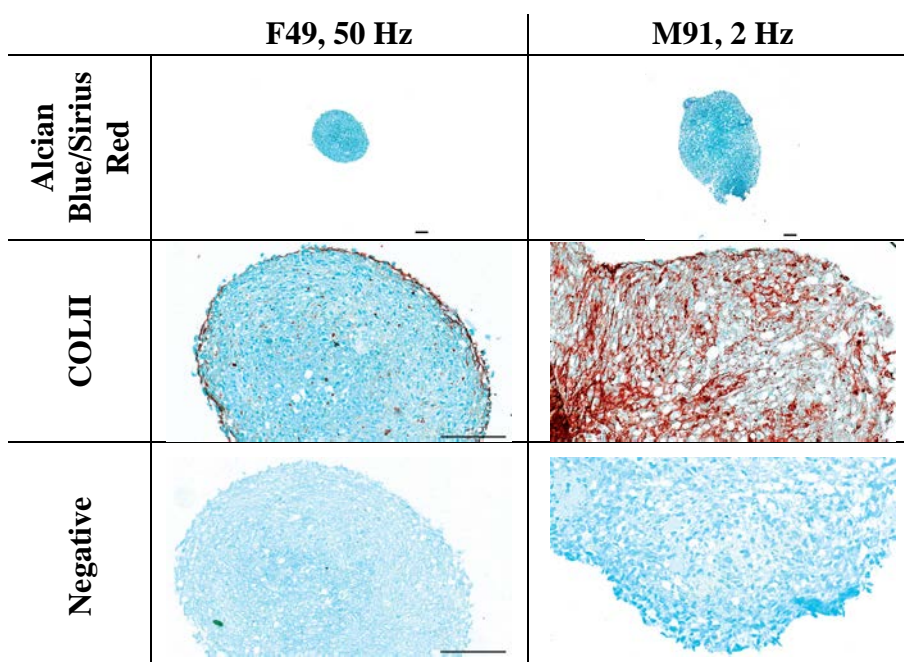


Figure 1: Cartilage tissue constructs following 21 days of culture within acoustic devices at 50 Hz (left) and 2 Hz (right), where the latter sweep rate resulted in more matrix production and cartilage specific markers, specifically type-II collagen. Scale bar = 100 micrometre

Investigation of the cell response to different sweep rates was accomplished through time-lapse imaging of levitating aggregates. From the time-lapse imaging, it was observed that the cells experience fluidic shear stresses resulting from lateral oscillations which depend on the frequency sweep rate.

To further quantify the lateral displacement of the cells, murine chondrocytes (ATDC5) were used to form aggregates at different driving parameters to determine the mechanical shear being applied onto the cells. The mean lateral displacement of the cells was computed via image cross-correlation and inputted into a finite element model to determine the fluid shear stress applied onto the cells.

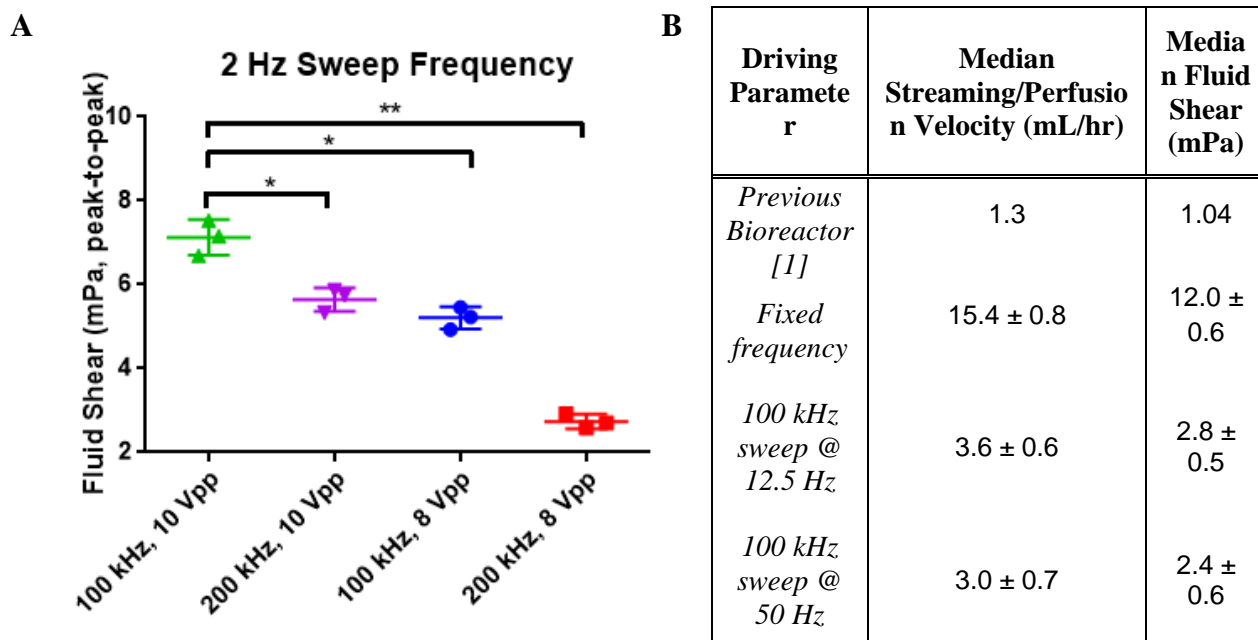


Figure 2: (A) The stress magnitude was quantified at different driving voltages and frequency sweeps at 2 Hz to show the fluid shear applied onto the cells can be altered through the sweep range and driving frequency. (B) Fluid shear due to streaming within the previous system and the present bioreactor. For the current bioreactor design, fluid shear measurements were derived from visualizing 1 micron particles within the trap at the resonant frequency of the resonator (fixed frequency), 100 kHz sweep at 12.5 and 50 Hz sweep rate. All data points were constructed from n = 3 (mean ± SD), *P < 0.001, **P << 0.001

The shear magnitude was quantified at different driving forces to understand how the fluid shear changes with the sweep rate, frequency sweep, and driving voltage (Figure 2A). The fluid shear magnitude decreased as the frequency sweep range widen and as the driving voltage decreased. In addition to the lateral forces, the acoustic environment was further characterized for fluid velocity from acoustic streaming. This was analyzed via micro-particle image velocimetry, to show how streaming velocities change with the sweep rate and compared to driving at a fixed frequency (Figure 2B). Due to limitations of the signal generator used, the acoustic streaming velocities at 50 Hz and 12.5 Hz were compared. The velocity measurements between 12.5 Hz and 50 Hz were assessed statistically to find no significant different. Additionally, these measurements were found to be significantly more than the perfusion flow rate reported previously. To this extent, the fluid flow, whether due to streaming or perfusion, may provide a complex signal to the cells in order to promote differentiation.

Conclusion

Present literature has shown how particles are influenced by the acoustic radiation and streaming forces, including their effects on cell viability [1-4]. The present experimental results furthers these findings and show that the mechanical environment within the resonator plays a crucial role in the development of robust hyaline-like cartilage.

References

- [1] S. Li, P. Glynne-Jones, O.G. Andriotis, K.Y. Ching, U.S. Jonnalagadda, R.O.C. Oreffo, M. Hill, and R.S. Tare., Lab on a Chip, **14**, 4475-4485 (2014).
- [2] A. Garbin, I. Leibacher, P. Hahn, H. Le Ferrand, A. Studart, and J. Dual, The Journal of the Acoustical Society of America, **138**, 2759-2769 (2015).
- [3] M. Ohlin, I. Iranmanesh, A.E. Christakou and M. Wiklund, Lab on a Chip, **15**, 3341-3349 (2015)
- [4] P. Hahn, I. Leibacher, T. Baasch, and J. Dual, Lab on a Chip, **15**, 4302-4313 (2015).

Acoustophoretic Handling of *C. elegans* in microfluidic channels

Peter Reichert¹, Thierry Baasch¹, Stefan Lakämper, Gamuret Hack¹, Nadia Vertti Quintero², Xavier Casadevall i Solvas², Andrew deMello², Gunawan Rudiyanto², Jürg Dual¹

¹Department of Mechanical and Process Engineering, Institute for Mechanical Systems, Swiss Federal Institute of Technology Zurich, Zurich, Switzerland

E-mail: reichert@imes.mavt.ethz.ch, URL: www.zfm.ethz.ch/e/exp-dyn

²Chemical and Biological Systems Engineering Laboratory, Swiss Federal Institute of Technology Zurich, Zurich, Switzerland

Introduction

Caenorhabditis elegans (*C. elegans*) is a model organism for research in the field of molecular and developmental biology. Microfluidic chips have improved the handling capabilities and have made high-resolution imaging and fluorescent scanning of *C. elegans* possible. The controlled handling of *C. elegans* is still a challenging task due to their active behaviour (swimming, bending and rolling) and special geometries, cooling, gasses or anesthetics have been used for the necessary immobilization [1],[3]. Bulk acoustic wave (BAW) acoustophoresis is proposed to be a new contactless handling tool for un-anesthetized *C. elegans* with ultrasound. *C. elegans* can be immobilized by focussing them in the pressure nodal line of a standing acoustic wave. Switching between two fluid resonance modes is used to sort *C. elegans* in separate outlets. To understand the effect of the acoustic field on the *C. elegans* the compressibility is estimated by evaluating *C. elegans* trajectories in the acoustic field and numerical simulations.

Experimental setup and simulation

The experimental setup shown in fig. 1(a) consists of a silicon/glass chip with microfluidic channels and a high-speed camera. Syringe pumps are used to inject wildtype *C. elegans* in a M9 buffer carrier fluid into the chip. For acoustophoresis, a piezoelectric transducer for the excitation of harmonic bulk acoustic waves is glued to the back side of the device. The transducer is excited by a function generator and an amplifier at the frequency of a fluid resonance inside the channel.

To understand the physical principles of the observed phenomena in the experiment, a device characterization and a scattering simulation with the FEM software Comsol Multiphysics is conducted. For the device characterization experiments with polystyrene particles of known material properties are used to evaluate the pressure distribution in the channel [4]. The acoustic radiation force on a *C. elegans* model at the experimentally evaluated pressure is extracted from time stepping the simulations in fig. 1(b) and (c). Together with a simulated drag coefficient it is possible to simulate the trajectories for a *C. elegans* model. A comparison of the simulated trajectories and an experimentally evaluated *C. elegans* trajectory allows to estimate a speed of sound for the *C. elegans* of about 1460 m/s.

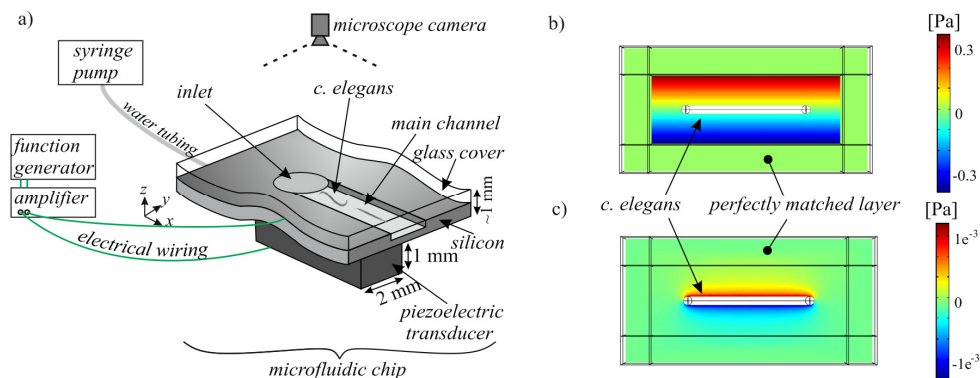


Figure 1. Sketch of the experimental setup, the microfluidic device and the simulated device. In (a) the main channel has a depth of 90 μm , a length of >8 mm and a width of 700 μm or 200 μm . A piezoelectric transducer Pz26 (Ferroperm) is mounted to the back side of the chip. Part (b) shows the acoustic background field bordered by perfectly matched layers (PML) for $\lambda/2 = 700\mu\text{m}$ around a cylindrically modelled *C. elegans* in the pressure node. The scattered pressure field of the *C. elegans* model is shown in (c).

Results

Immobilization of a *C. elegans* is shown in the image sequence from a high-speed recording in fig. 2. An adult *C. elegans* flows in a bent state through the microfluidic chip. After a visual detection ultrasound is switched on and the *C. elegans* is straightened and focussed in the middle of the channel. In this position e.g. a laser can detect fluorescence along the length or a motion detection software can be used for a length measurement. After a duration of 60 ms the ultrasound is switched off and the *C. elegans* bends again which shows its viability.

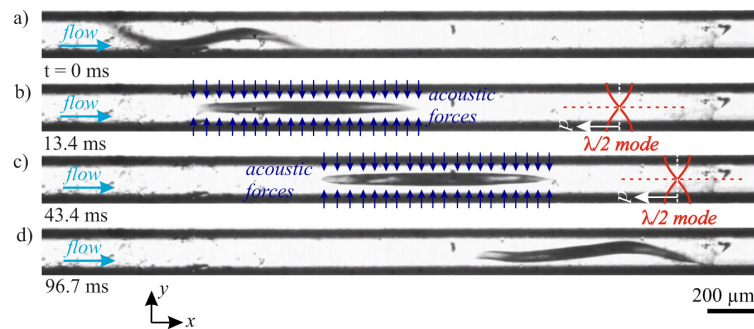


Figure 2: Straightening and immobilization of an adult *C. elegans* for optical scanning purposes. a) No ultrasound, a moving *C. elegans* flows with a speed of 25 mm/s. In b) and c) an excitation pulse at a frequency of 3.56 MHz at an amplitude of 34.7 Vpp straightens the *C. elegans* in the pressure node of the half wavelength ($\lambda/2$) fluid resonance mode in the channel middle. The *C. elegans* is slowed down to 9 mm/s due to acoustic forces in x- direction. In d) the negative control without ultrasound shows the bent *C. elegans*.

Sorting in fig. 3 is performed by switching between two fluid resonance modes and guiding the *C. elegans* either in the middle outlet or in one of the remaining outlets of the trifurcation (outlet 1.1 or outlet 1.2). Dependent on the size, the viability (image analysis) or a detected fluorescent threshold it is possible to sort *C. elegans* into two categories.

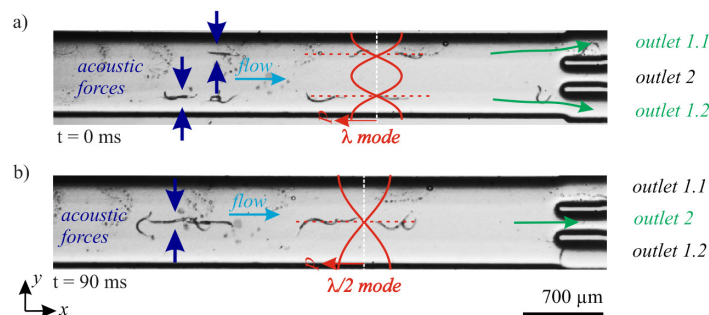


Figure 3: Sorting of *C. elegans* with an average length of 350 μm (L 3 stage) at a flow speed of 1.6 mm/s. (a) Excitation at 2.165 MHz generates a λ mode, which deflects *C. elegans* to the upper or bottom outlet. (b) In a next time step, the piezoelectric transducer is excited at a frequency of 970 kHz ($\lambda/2$), *C. elegans* are moved to the channel middle and are sorted to the outlet in the middle of the trifurcation. An amplitude of 25.3 Vpp is used. By switching between the λ - and $\lambda/2$ resonance mode sorting in two different outlets becomes possible.

Conclusion

The microfluidic handling tool BAW acoustophoresis enables immobilization and sorting of living *C. elegans*. With this method contactless and un-anesthetized handling of *C. elegans* at low flow rates in wide channels becomes possible. In the high kHz frequency range an acoustic actuation is harmless for living organisms. Acoustophoresis is seen as a handling tool for biological researchers which is harmless, versatile (immobilization and sorting), with a simple chip fabrication and is applicable for *C. elegans* in every stage of its life cycle. Furthermore, new experimental ideas become possible, e.g. the evaluation of the strength of a *C. elegans* (comparing simulation and experiment) or the imaging at low flow rates.

References

- [1] A. San-Miguel, et al. *Microfluidics as a tool for C. elegans research*. WormBook, www.wormbook.org, (2013).
- [2] H. Bruus, et al. *Forthcoming Lab on a Chip tutorial series on acoustofluidics: Acoustofluidics—exploiting ultrasonic standing wave forces and acoustic streaming in microfluidic systems for cell and particle manipulation*. Lab on a Chip 11(21), p. 3579-3580 (2011).
- [3] Y. Yan, et al. *A continuous-flow C. elegans sorting system with integrated optical fiber detection and laminar flow switching*. Lab on a Chip 14(20), p. 4000-4006 (2014).
- [4] R. Barnkob, et al. *Measuring the local pressure amplitude in microchannel acoustophoresis*. Lab on a Chip 10, p. 563-570 (2010).

Influence of protein repellent polymer coating on ultrasonic spheroid production in a multi-well microplate

K. Olofsson¹, V. Carannate², K. Kushiro³, M. Takai³, B. Önfelt^{1,2} and M. Wiklund¹

E-mail: karl.oloofsson@biox.kth.se, URL: <https://www.aphys.kth.se/groups/biox>

¹Department of Applied Physics, KTH Royal Institute of Technology, Stockholm, SWEDEN

²Department of Microbiology, Tumor and Cellbiology, Karolinska Institute, Stockholm, SWEDEN

³Department of Bioengineering, The University of Tokyo, Tokyo, JAPAN

SUMMARY

In this paper we demonstrate an improved tissue micro-engineering method producing 100 three-dimensional (3D) HepG2 cell structures in parallel based on a combination of ultrasonic actuation and polymer coating in a multi-well microplate made out of silicon and glass. By the use of a polymer coating in the microplates, the method creates non-adherent tumor models of controlled size and shape which introduces both a more flexible 3D culture system as well as improved quality of the 3D tumor structures relative to previous studies [1]. It is also shown by μ PIV that the polymer coating increases the acoustic energy density in the microplate relative to previous studies [2].

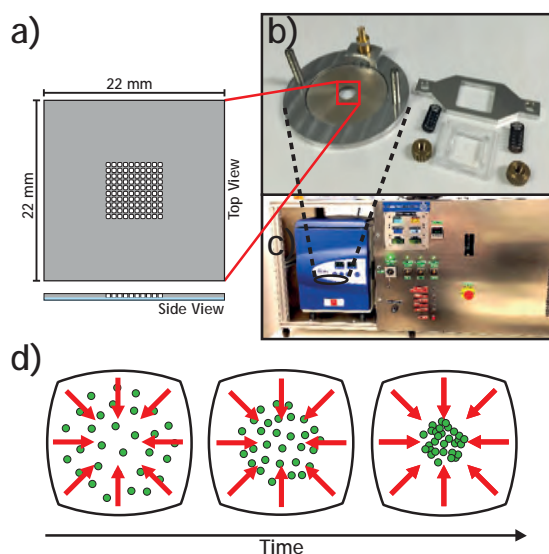


Figure 1: The silicon multi-well microplate etched with 100 micro-wells ($350 \mu\text{m} \times 350 \mu\text{m}$) (a) is bonded to a glass plate and mounted on the round piezo transducer (b) and actuated with an AC voltage. To produce micro-tumors, cells are seeded into the wells and incubated in an in-house built temperature control and incubator system (c). When actuated at the resonance frequency at 2.46 MHz, the seeded cells in the micro-well are pushed towards the center of each well by the ultrasonic radiation force (d).

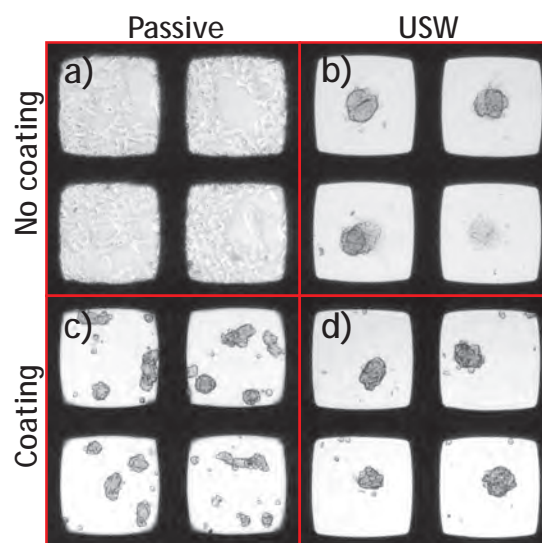


Figure 2: Bright field microscopy images of the four experimental combinations of HepG2 cells incubated in a microplate; two days of passive (no ultrasound) culture without coating (a), 24 hours active (ultrasound on) + 24 hours passive culture without coating (b), 2 days of passive culture with coating (c) and 24 hours active + 24 hours passive culture with coating (d). The micro-wells are $350 \mu\text{m}$ wide and 4 out of 100 wells are showed for each experimental case.

Motivation

Tissue micro-engineering is important for modelling 3D biological structures in cellular and pharmaceutical research. Cells within tissue interact with other cells, the extracellular matrix and soluble factors in a 3D communication network that governs cell behavior and tissue function [3]. The micro-environment of 3D cultures is different from the one present in standard 2D cell cultures. Therefore, 3D culture methods can be used to bridge the gap between in vitro and in vivo models. 3D cul-

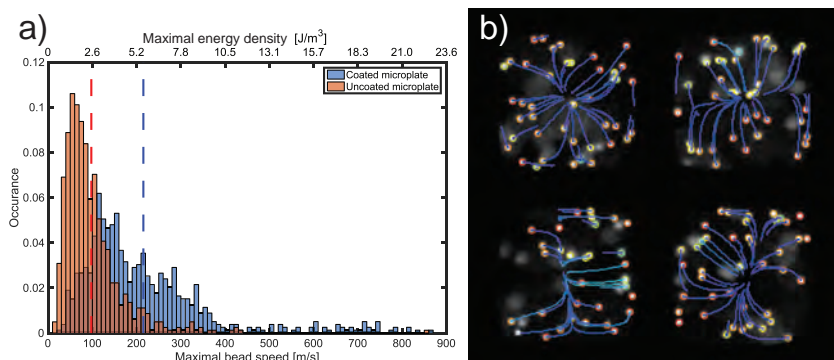


Figure 3: To investigate the maximal acoustic energy density, the maximum velocity of $10\ \mu\text{m}$ fluorescent beads was acquired during the initial aggregation in a microplate with and without polymer coating during frequency modulation ($2.46\ \text{MHz} \pm 50\ \text{kHz}$ at $1\ \text{kHz}$) and $15\ \text{V}_{\text{pp}}$. The maximum bead speed distribution (a) is higher for the beads in the coated microplate (mean = $215\ \mu\text{m/s}$, $N = 792$) compared to the uncoated microplate (mean = $98\ \mu\text{m/s}$, $N = 811$). The automatic μPIV analysis was performed in TrackMate (ImageJ plug-in) and a representative example is shown in (b)

ture methods are either anchorage-dependent (e.g., scaffolds) or anchorage-independent (e.g., hanging drop, coatings) [4].

Spheroid fabrication

We have earlier demonstrated an anchorage-dependent ultrasonic 3D culture method for the production of micro-tumors used for immunotherapy research [1] but in this paper we combine the method with a protein repelling polymer coating (described in [5] and briefly below) that introduces more flexibility and opens up new analysis approaches since the tumors are not anchored and can be extracted from the wells while retaining the compatibility with any type of optical microscopy. Briefly, a layer of the polymer coating was distributed over the entire multi-well microplate before cell seeding. The microplate is then coupled to the transducer which is driven at the resonance frequency inside an in-house built incubator with a novel integrated temperature regulation system (Figure 1).

Protein repellent polymer coating

The protein repellent coating consists of a random copolymer of groups that both physically and chemically binds to the silicon and glass bottom in the microplate. The polymer chains crosslink to each other with strong silane couplings and the total polymer layer is approximately $30\ \text{nm}$ thick [6].

Un-anchored spheroids

3D HepG2 tumors are successfully formed in the coated microplate after 24 hours of active culture (ultrasound on) followed by 24 hours of passive culture (ultrasound off). We compare these results with micro-tumors formed in an uncoated microplate (same culture scheme), two days of passive culture in a coated microplate and two days of passive culture without coating (Figure 2).

μPIV analysis

To investigate the influence of the polymer coating on the acoustic properties of the microplate, μPIV analysis was performed with $10\ \mu\text{m}$ fluorescent beads during the initial aggregation with and without coating in the same microplate. The results indicate that the acoustic energy density is higher with the polymer coating than without (Figure 3).

Conclusion

We have found that the addition of a protein repellent polymer coating in our 3D-culture method produces un-anchored spheroids of higher quality within less time, compared to an ultrasonic 3D culture without coating. Furthermore, the coated microplate generates higher acoustic energy density, which is somewhat surprising since the polymer material is less suitable for supporting acoustic resonances relative silicon and glass.

References

- [1] A. E. Christakou, M. Ohlin, B. Önfelt and M. Wiklund. *Lab Chip* **15**, 3222-3231 (2015).
- [2] M. Ohlin, A. E. Christakou, T. Frisk, B. Önfelt and M. Wiklund. *J. Micromech. Microeng.* **23**, 035008 (11pp) (2013).
- [3] C. J. Lovitt, T. B. Shelper and V. M. Avery. *Biology* **3**, 345-367 (2014).
- [4] S. Nath and G. R. Navi, *Pharmacology & Therapeutics* **163**, 94-108 (2016)
- [5] K. Nagahashi, Y. Teramura, M. Takai. *Colloids Surf B Biointerfaces* **134**, 384-391 (2015).

Spontaneous ultrasonic assembly of chemically encoded and responsive two-dimensional coacervate droplet arrays

Liangfei Tian¹, Nicolas Martin¹, Philip G. Bassindale^{2,3}, Avinash J. Patil¹, Mei Li¹, Adrian Barnes³, Bruce W. Drinkwater², Stephen Mann¹

¹Centre for Protolife Research and Centre for Organized Matter Chemistry, School of Chemistry, University of Bristol, Bristol BS8 1TS, UK, E-mail: liangfei.tian@bristol.ac.uk

²Faculty of Engineering, Queens Building, University of Bristol, Bristol BS8 1TR, UK, E-mail: b.drinkwater@bristol.ac.uk

³School of Physics, HH Wills Physics Laboratory, University of Bristol, Bristol BS8 1TL, UK

Introduction

Miniaturization of fluid compartments in the form of liquid micro-droplets is important in diverse scientific areas [1] such as chemical and biochemical analysis, protein crystallization and micro-reactor technology. Many of these applications require high-throughput analyses of spatially addressable arrays of liquid droplets over a range of timescales and chemical/physical environments. Typically, arrays of droplets with a uniform size have been prepared by microfluidics, microfabrication, printing, and by application of electrical or magnetic fields. The droplets are stabilized by immersion in an appropriate continuous phase (water droplets in oil for example) or exposure on a dry surface, which lead to patterns of physically isolated droplets. On the other hand, isolation of the droplets within the arrays is not compatible with dynamical interactions such as triggering chemical signals between the droplets or enabling the droplets to communicate with and respond to time-dependent changes in their external environment. To achieve these dynamical interactions, new technologies are required that provide high-throughput production and organization of liquid micro-droplets with similar polarity to the associated continuous phase, such as the formation and patterning of water-rich droplets in a continuous aqueous phase. Such systems are characterized by a relatively low surface tension between the droplets and continuous phase, and remain technically challenging.

Results and discussions

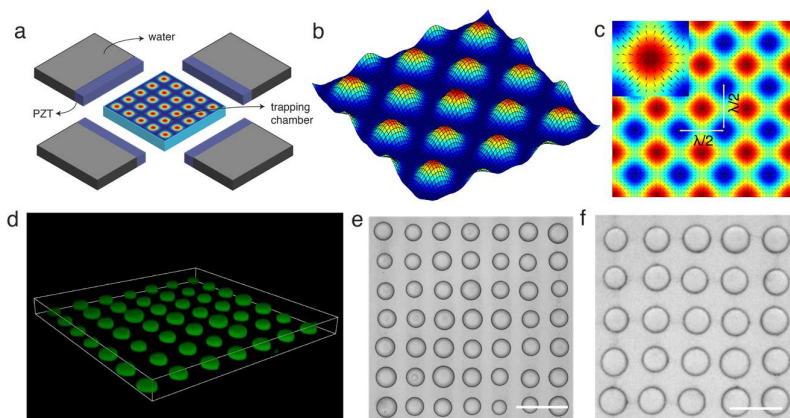


Figure 1: (a) Schematic representation of the acoustic trapping device. (b,c) Simulation of acoustic pressure distribution (b) and Gor'kov potential distribution (c) in the acoustic trapping device as shown in (a); high pressure (red), low pressure (blue). (d) 3D confocal microscopy image of acoustically trapped droplets. (e,f) Optical microscopy images of droplets produced using the device at different acoustic wavelengths. Depending on the wavelength, the centre-to-centre spacings of the droplets were determined by half of the acoustic wavelength. Scale bars = 200 μm .

Here, we demonstrate the spontaneous assembly and spatial organization of water-rich molecularly crowded micro-droplets to form 2D arrays in aqueous media. Droplet assembly is achieved by a spontaneous process of complex coacervation [2], which is a liquid-liquid phase separation phenomenon driven by electrostatic and entropic interactions usually between counter-charged polyelectrolytes. The resultant micron-sized coacervate droplets comprise a dense, component-enriched viscoelastic phase, dispersed in a chemically deficient aqueous continuous phase. Coacervate droplets have been used for storage of food additives, drug delivery, protein purification, and more recently, exploited as membrane-free protocells [3] capable of enhanced enzymatic activity, electric field-induced energization, and in vitro gene expression. Herein, we show that the in situ generation of femtolitre-sized coacervate micro-droplets and their spatial organization into 2D periodic lattices in water can be achieved without direct contact by acoustic trapping methods [4]. Acoustic radiation forces depend on the acoustic contrast generated by compositional differences between media [5], and although acoustic beams and standing waves have been exploited for multi-dimensional

trapping, patterning and manipulation of micron-sized particles and intact cells, generating defect-free uniform patterns with a single particle positioned at each acoustic pressure node has only been achieved at a highly specific ratio of particle size to acoustic standing wavelength [6]. Significantly, acoustic trapping has not been used to generate arrays of water-rich droplets dispersed in an aqueous medium, principally because of the minimal acoustic contrast and low interfacial tension of the system.

Using an acoustic standing wave trap, we demonstrate the spontaneous assembly and organization of droplets into defect-free arrays with controllable lattice spacing and droplet size (Figure 1). We show that individual droplets of near uniform size, typically 50-100 μm in diameter, are produced in the acoustic field by in situ coalescence of primary droplets that aggregate specifically at the Gor'kov potential minima (which correspond to acoustic pressure nodes) of the standing wave in the early stages of pattern formation. Significantly, coalescence between the initially very small primary droplets can be curtailed by adjusting the composition of the droplets such that localized aggregates of closely packed droplets are produced at each node in the acoustic pressure field. The localized clusters exhibit collective responses to modulations in the acoustic standing wave to produce arrays with reversible dynamical properties based on transformations in droplet shape and exchange of matter between adjacent nodes in the acoustic field.

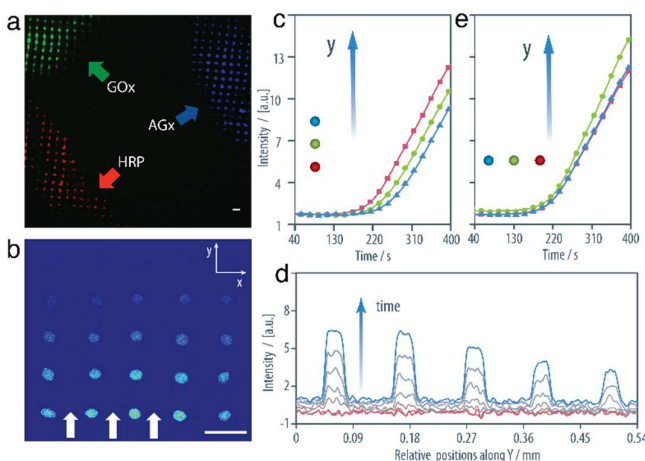


Figure 2: (a) Fluorescence microscopy image showing three spatially positioned domains of enzyme-containing droplet arrays with three different enzymes (see arrows). (b) Fluorescence microscopy image of an acoustically patterned 2D array of enzyme-containing coacervate droplets recorded 250 s after diffusion of the substrate along the y direction (arrows). Scale bars = 100 μm . (c) Plots of changes in fluorescence mean intensity associated with droplets along a single row aligned parallel to the direction of diffusion (y axis). (d) Fluorescence line intensity profiles recorded across a row of droplets aligned along the direction of diffusion (y axis) 50, 100, 150, 200, 225, 250, 275 and 300 s after injection of the substrates. (e) Similar plots as in (c) but for three droplets positioned at alternate lattice points in a row lying perpendicular to the diffusion front at a given time.

Our methodology is applicable to a wide range of complex coacervate systems involving biomolecules and synthetic polyelectrolytes. Moreover, periodic arrays of chemically encoded single droplets containing sequestered dye molecules, proteins, enzymes, nanoparticles or microparticles can be readily produced in situ during droplet assembly or partitioned into the patterned arrays post-assembly. By adjusting the ratio of the chemical for the coacervate formation we demonstrate that acoustically patterned populations of coacervate droplets containing different chemical information can be spatially positioned within the sample chamber of the trapping device (Figure 2a). Finally, we show that it is possible to transit a reaction wave-front through an array of acoustically trapped enzyme-containing coacervate micro-droplets by establishing an appropriate chemical gradient within the sample chamber of the device (Figures 2b-e).

Conclusion

Our results indicate that structured acoustic radiation forces are a powerful, versatile and inexpensive tool to manipulate the spatial assembly of uniform-sized coacervate micro-droplets in aqueous media to produce functional water-based molecularly crowded liquid droplet periodic arrays comprising selective chemicals, biomolecules and catalysts. Defect-free arrays of single coacervate droplets or droplet aggregates arranged in 2D lattices with controllable spacing, variable surface-attachment properties and reversible dynamical behavior have been achieved by combining an ASW force field with in situ complex coacervation. The final size of the droplets can be controlled by changes in the chemical concentrations or by quenching coalescence of the primary droplets to produce 2D arrays with fixed spacing and geometry but variable droplet size. A key advantage of the described methodology is associated with the high sequestration potential of the molecularly crowded coacervate droplets, which enables the selective uptake and storage of a wide range of functional components capable of operating in a continuous aqueous media, and it should be possible to develop devices capable of sustaining chemical signals between the droplets as well as enabling spatial and temporal responses to changing conditions in the external environment.

References

- [1] A. Huebner *et al.*, *Lab Chip* **8**, 1244-1254 (2008).
- [2] E. Kizilay, A. B. Kayitmazer and P. L. Dubin, *Adv. Colloid Interface Sci.* **167**, 24-37 (2011).
- [3] S. Koga, D. S. Williams, A. W. Perriman and S. Mann, *Nat. Chem.* **3**, 720-724 (2011).
- [4] C. R. P. Courtney *et al.*, *Proc. R. Soc. A* **468**, 337-360 (2011).
- [5] H. Bruus, *Lab Chip* **12**, 1014-1021 (2012).
- [6] D. J. Collins *et al.*, *Nat. Commun.* **6**, 8686 (2015).

Particle enrichment in two-phase microfluidic systems using acoustophoresis

Anna Fornell¹, Johan Nilsson¹, Linus Jonsson¹, Prem Kumar Periyannan Rajeswari², Haakan N. Joensson² and Maria Tenje^{1,3}

¹Dept. Biomedical Engineering, Lund University, Lund, Sweden
E-mail: anna.fornell@bme.lth.se

²Div. Proteomics and Nanobiotechnology, Science for Life Laboratory, KTH Royal Institute of Technology, Stockholm, Sweden

³Engineering Sciences, Science for Life Laboratory, Uppsala University, Uppsala, Sweden

Introduction

Droplet microfluidics provides a tool to create confined and discrete reaction chambers for biological and chemical experiments at high throughput [1]. The method has attracted special interest for single-cell studies since it is possible to encapsulate single cells inside droplets. This makes it possible to create more sensitive analysis of cells since the results arise from a particular cell and is not the average response of thousands of cells [2]. To miniaturize biological assays using droplets the same processes and steps performed in standard protocols have to be integrated on microfluidic chips. Here, we present a method to concentrate particles in droplets by combing acoustic particle focusing inside droplets with a trident shaped droplet split, and we report ten times higher concentration of particles in the center daughter droplets compared with the side daughter droplets when ultrasound is applied [3].

Experimental

An illustration of the developed concept for particle enrichment inside droplets and a photograph of the fabricated acoustofluidic device are shown in figure 1. The microfluidic channels were wet-etched on a silicon wafer and sealed by anodic bonding of a 1.1 mm thick glass lid. Aqueous droplets with polystyrene microparticles (5 μm) were generated in a continuous organic phase (olive oil). All liquid flows were controlled by syringe pumps. A piezoelectric transducer was glued on the silicon side of the chip. To achieve particle focusing inside the droplets the transducer was actuated with a frequency matched to create $\lambda/2$ -resonance in the main channel. After the particle focusing step each droplet was split into three daughter droplets in a trifurcation. The performance of the system was evaluated by measuring the concentration of particles in the center and side daughter droplets using a Coulter Counter. To demonstrate the possibility to manipulate cells inside droplets and show the suitability of the system for biological applications, red blood cells were encapsulated and manipulated inside the droplets.

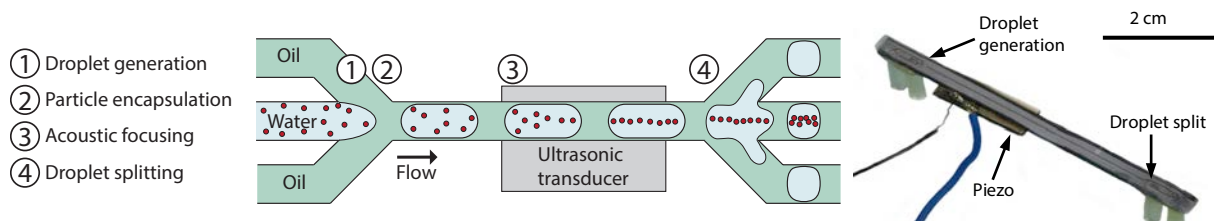


Figure 1: Left: Illustration of the concept for acoustic particle enrichment inside droplets. Aqueous droplets containing particles are generated. The applied acoustic field moves the particles to the pressure node in the center of the droplets, and finally each droplet is split into three daughter droplets at a trifurcation. Right: Photograph of the microfluidic chip for particle enrichment in droplets. Channel width \times channel height 435 μm \times 165 μm .

Results

At $\lambda/2$ -resonance (1.8 MHz, 25 V_{pk-pk}) the particles inside the droplets were moved to the center of the droplets. The droplets were transported downstream to a trifurcation where each droplet was split into three daughter droplets with approximately the same size (25-28 nl). When ultrasound was applied the majority of the particles were enriched in the center daughter droplets as seen in figure 2.

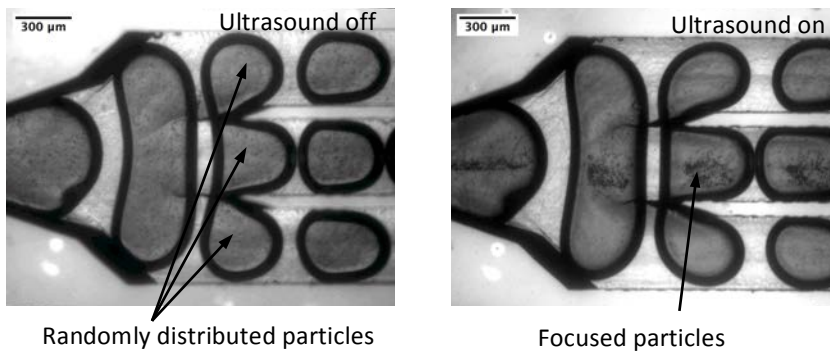


Figure 2: Particle enrichment in droplets. Without ultrasound (left photograph) the particles are positioned in the entire main droplet resulting in particles in all daughter droplets after the droplet split. When ultrasound is applied (right photograph) the particles are directed to the center daughter droplet during the splitting step resulting in particle enrichment.

The concentration of particles in the daughter droplets after the acoustic focusing step and the droplet split is presented in figure 3. When ultrasound was applied the concentration of particles in the center daughter droplets was more than ten times higher than in the side daughter droplets. In the control experiment without ultrasound only a small concentration difference was observed between the center and side daughter droplets.

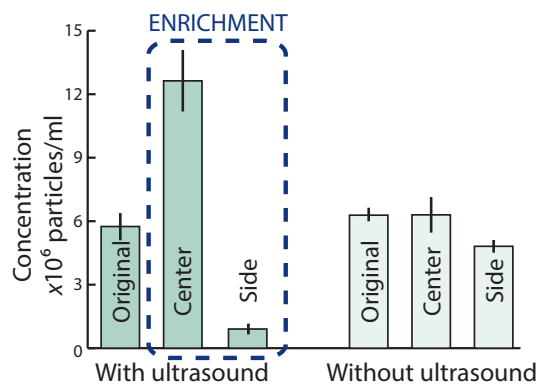


Figure 3: Concentration of particles with and without ultrasound during the droplet split. Experiments were performed three times (n=3) with data acquisition in triplicates. Error bars represent \pm standard deviation.

To investigate the possibility to use the described method for droplet based cell assays, red blood cells were encapsulated inside the droplets. When ultrasound was applied to the system the cells were found to be immediately moved to the center of the droplets, see figure 4.

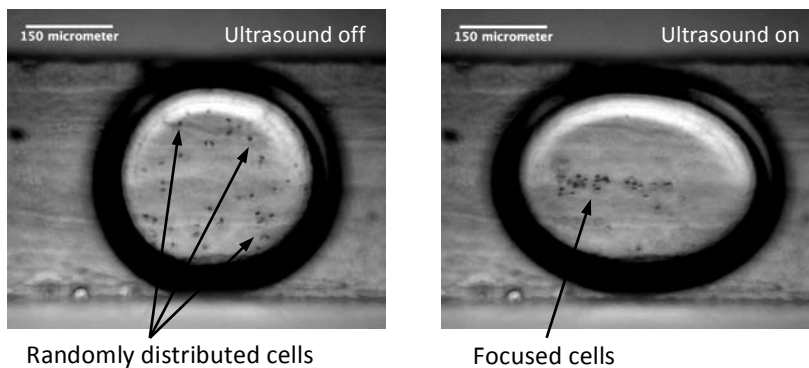


Figure 4: Acoustic focusing of red blood cells in droplets. At application of ultrasound the cells were positioned to the center of the droplet (right photo). It was also observed that the droplet interface was slightly deformed by the ultrasound.

Conclusion

We have developed a method to enrich particles inside droplets by combining acoustic focusing with a trident shaped droplet split. 89% of the particles were collected in the center daughter droplets when 2/3 of the original droplet volume was removed. It was also shown that the method can be used to manipulate red blood cells inside droplets. These results opens up for novel droplet based assays that are not possible to perform today.

References

- [1] R. Seemann, M. Brinkmann, T. Pfohl and S. Herminghaus, *Rep Prog Phys*, **75**, 16601 (2012).
- [2] D. Di Carlo and L. P. Lee, *Anal. Chem.*, **78**, 7918–7925 (2006).
- [3] A. Fornell, J. Nilsson, L. Jonsson, P. K. Periyannan Rajeswari, H. N. Joensson and M. Tenje, *Anal. Chem.*, **87**, 10521–10526 (2015).

2D acoustophoretic positioning of microparticles inside droplets

Mathias Ohlin¹, Anna Fornell², and Maria Tenje^{1,2,3}

¹Department of Engineering Sciences, Uppsala University, Sweden
E-mail: mathias.ohlin@angstrom.uu.se, URL: <http://www.teknik.uu.se/>

²Department of Biomedical Engineering, Lund University, Sweden

³Science for Life Laboratory, Uppsala University, Sweden

Introduction

We present a silicon-glass droplet-based microfluidic system with integrated two-dimensional (2D) acoustophoresis of microparticles (10 μm) for improved particle positioning within spherical droplets. We have previously reported on lateral positioning of microparticles inside large droplets (“plugs”) by one-dimensional acoustophoresis [1]. In this paper, we implement 2D acoustophoresis [2, 3] of microparticles prior to droplet generation as well as continuously throughout the whole system to increase the particle centricity within small sub 100-micrometer-sized spherical droplets with as much as a factor of 4 compared to an unactuated system.

Experimental

An overview of the droplet-based microfluidic system implementing dual transducer technology for 2D acoustophoresis can be seen in fig. 1. The system consists of a silicon-glass chip fabricated in-house using photolithography and dry-etching technology [4]. A channel with a rectangular cross-sectional design enables independent acoustic focus control of both y- and z-direction by two different piezoelectric transducers optimized for the resonance frequencies in each direction. The two ultrasound transducers which are mounted to the chip with cyanoacrylate adhesive can be seen in fig. 1A (cf. PZT1 and PZT2). These transducers are equipped with optimized aluminum matching layers making them efficient enough to be driven purely by a function generator (10 V_{pp}) without the need of an expensive RF amplifier. Moreover, the transducers are equipped with metal-epoxy based backing layers enabling broadband frequency-modulation actuation resulting in a more robust acoustophoretic function.

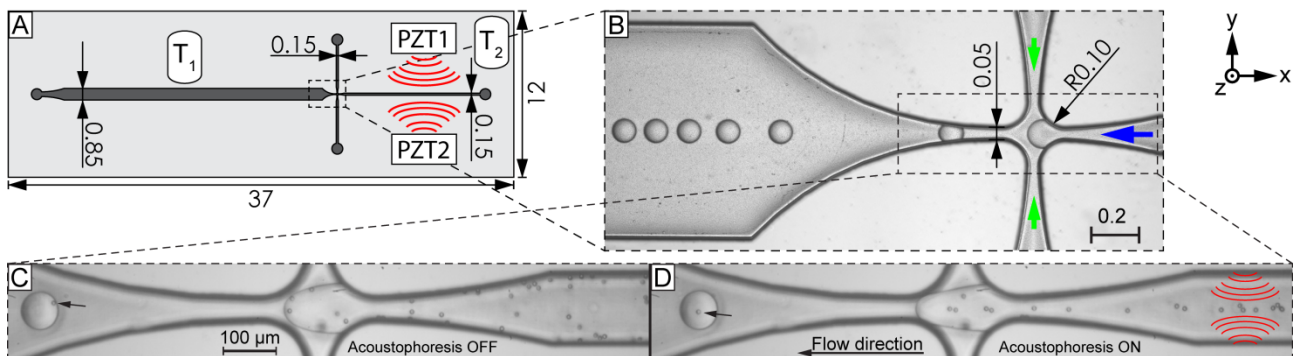


Figure 1: (A) Schematic drawing of the system. Here the two boxes PZT1 ($f_{\text{resonance}} = 7.7$ MHz, z-direction) and PZT2 ($f_{\text{resonance}} = 5.0$ MHz, y-direction) indicate the position of the two piezoelectric ultrasonic transducers used for the 2D acoustophoresis. To compensate for the small geometry variations the transducers are driven in frequency-modulation mode ($f_{\text{resonance}} \pm 100$ kHz @ 1 kHz) resulting in an approx. compensation ability of ± 3 μm . The boxes T1 and T2 mark the positions of the two K-type thermocouples used to monitor the temperatures. (B) A high-speed microscope photograph showing a snapshot of the droplet formation process at the cross junction. Green arrows indicate the direction of the continuous phase, fluorinated oil (Novec HFE-7500) with 2% Krytox pushed at a flow rate of 80 $\mu\text{l}/\text{min}$ (2×40 $\mu\text{l}/\text{min}$). The blue arrow indicates the direction of the dispersed phase, MQ-water with 0.1% Triton-X containing microparticles (10 μm polystyrene at a concentration of 2.3×10^6 particles/milliliter), pulled at a flow rate of 5 $\mu\text{l}/\text{min}$. Inserts (C) and (D) showing the cross junction are frames taken from high-speed microscope videos acquired at 2000 frames per second showing unactuated operation and 2D acoustophoresis, respectively. The black arrows point out typical results when encapsulating particles in spherical droplets with and without acoustophoresis. Unit is millimeter if not explicitly stated otherwise.

Results and discussion

At high droplet generation rates (hundreds of Hz), spherical droplets are exiting the droplet generation cross junction on a single line as can be seen in fig. 1B. The system can produce spherical droplets with volumes as small as $215 \text{ pl} \pm 22 \text{ pl}$ ($\phi = 74 \text{ } \mu\text{m} \pm 2 \text{ } \mu\text{m}$) at a rate as high as $298 \text{ Hz} \pm 85 \text{ Hz}$. For the unactuated control experiments (cf. fig. 1C) microparticles enter the cross junction almost randomly. However, with 2D acoustophoresis (cf. fig. 1D) all particles in the dispersed phase are focused at the center of the channel in both y- and z-direction before the droplet generator cross junction. Furthermore, since the spherical droplet has a dimension comparable to the channel height there is a continuous acoustophoretic effect within the droplet itself throughout the system. Typical results are indicated with black arrows in fig. 1C and 1D, i.e. for the unactuated operation particles tend to be closer to the droplet boundary compared to 2D acoustophoresis operation where particles tend to position themselves more centralized within the spherical droplet. We have chosen to focus on single-particle encapsulation with the aim for single-cell analysis and we note that the particle encapsulation process is stochastic for both unactuated operation and operation with 2D acoustophoresis. An analysis of droplets containing single particles is shown in fig. 2. The complete 2D-distribution of particles is depicted in fig. 1A and 1B which shows superposition of 1466 encapsulated single particles. Here the blue dots represent individual positions of single particles for the two operational modes (unactuated and 2D acoustophoresis). Using 2D acoustophoresis, 86% of the particles are focused to one of three locations (cf. fig. 2B) within the spherical droplet. For the unactuated control the same number is 48%. In particular, with 2D acoustophoresis the center location holds 44% of all particles compared to only 10% for the unactuated control. A boxplot of all particle positions measured from the droplet center is shown in fig. 2C. Similarly, the median particle distance from the droplet center is less for 2D acoustophoretic operation compared to unactuated operation of the microfluidic system.

The acquired fourfold increase of particles located in the central part of the droplet when implementing 2D acoustophoresis is favorable for single-cell analysis, e.g. minimizing optical aberrations for particles located close to the droplet boundary (cf. fig. 1C).

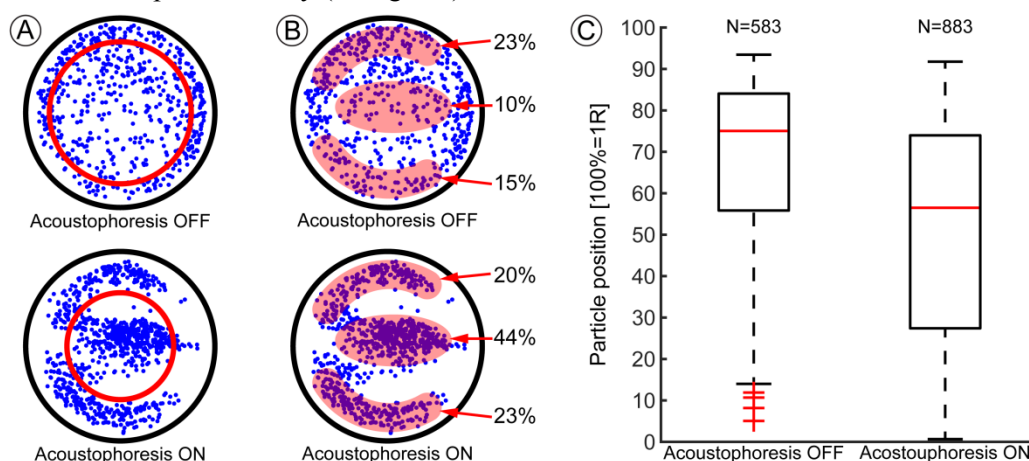


Figure 2: Particle position for the two operational modes – unactuated and 2D acoustophoresis. Particle positions are acquired approx. $500 \text{ } \mu\text{m}$ after the cross junction (cf. fig. 1) inside spherical droplets travelling with an estimated speed of 12 mm/s . (A) Superposition of all particle positions (blue dots) for the two operational modes. The red circle indicates the median particle distance from the droplet center. (B) Particle distribution divided into three regions here marked with red. The central region covers 15% of the total area whereas the two peripheral ones cover 14% each of the total area. The particle coverage percentages within the different regions are indicated by the red arrows with corresponding values. (C) A boxplot (whiskers represent minimum and maximum values, median is indicated by the red horizontal line in each box and outliers are indicated by red crosses) comparing relative particle position as a function of distance from droplet center. Here 100% corresponds to a particle positioned at droplet boundary resulting in a distance R (=droplet radius) from the droplet center and 0% indicates a particle positioned at the droplet center.

Conclusion

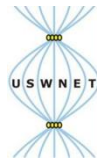
We have presented a silicon-glass two-phase droplet-based microfluidic system capable of producing sub 100-micrometer-sized spherical droplets at rates up to hundreds of droplets per second. Furthermore, we have implemented 2D acoustophoresis of microparticles increasing the centricity of encapsulated particles by as much as a factor of four making the system suitable for future single-cell analysis implementations.

Acknowledgements

Financial support is provided by Uppsala University, The Swedish Research Council and The Crafoord Foundation.

References

- [1] A. Fornell, *et al.*, *Analytical Chemistry*, vol. 87, pp. 10521-10526, 2015.
- [2] C. Grenvall, *et al.*, *Lab on a Chip*, vol. 14, pp. 4629-4637, 2014.
- [3] O. Manneberg, *et al.*, *Journal of Micromechanics and Microengineering*, vol. 18, 2008.
- [4] M. Ohlin, *et al.*, in *Micronano System Workshop 2016*, Lund, 17-18 May 2016.



An improved co-culture model of the mucosal airway enabled by acoustic trapping

Björn Hammarström¹, Hayden Foster², Donna E. Davies², Emily J. Swindle², Martyn Hill¹ and Peter Glynne-Jones¹

¹Engineering Sciences, Engineering and the Environment, Southampton University
E-mail: B.Hammarstrom@soton.ac.uk

²Academic Unit of Clinical and Experimental Science, Faculty of Medicine,
University of Southampton, UK

Introduction

The airway mucosa in the lung is composed of bronchial epithelial cells (BECs). The BECs create a protective barrier between the body and the external environment, and together with underlying fibroblast cells they maintain tissue homeostasis. Study of the mucosa is relevant in toxicology and drug screening [1] targeting a variety of respiratory conditions including asthma.

The acoustofluidic device presented here facilitates a novel *in vitro* model of the mucosa by making it possible to recreate the layered structure of two cell types found in the body. Non-contact acoustic trapping in a capillary tube [2] was used to form adherent-sheets of BECs from a single cell suspension. Releasing the BEC sheets on top of a confluent layer of fibroblasts enables the formation of a layered tissue construct comprised of the two cell types.

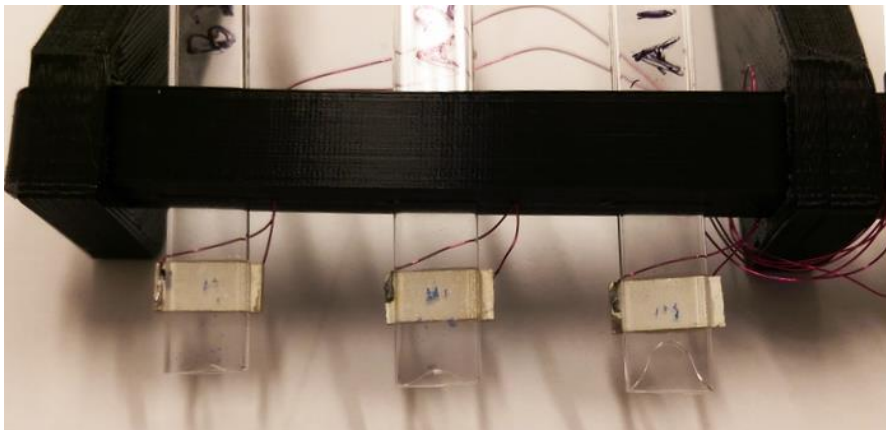


Figure 1; Acoustofluidic device for parallel cell-sheet generation. Three capillaries with piezoelectric elements are exited using a sweep. The cell sheets are formed close to the end of the capillary and can be released on top of structures of other cell types to generate co-culture tissue models.

Results & Discussion

The capillary device (**Figure 1**) permitted parallel production of three cell sheets per run, and the formation of adherens junctions between the trapped BECs (16HBE) was found to require two hours. During the incubation a slow perfusion flow (2 $\mu\text{l}/\text{min}$) was used to provide fresh nutrients, and maintaining a steady temperature of 37°C was found to be a critical for the adherens junctions to form. Due to the temperature sensitivity of the cells and the low perfusion rate a minimal operation voltage could be used. These settings were determined by evaluating cell-dissociation and viability after release from the acoustic trap.

In order to successfully co-culture BECs and fibroblasts as distinct cell layers it was found to be critically important to enable the BECs to form adherens junctions with each other prior to co-culture with fibroblasts. By contrast, direct deposition of BECs in suspension onto a confluent layer of fibroblasts did not allow the formation of distinct layers as the different cell types would compete with each other for contact with the culture well.

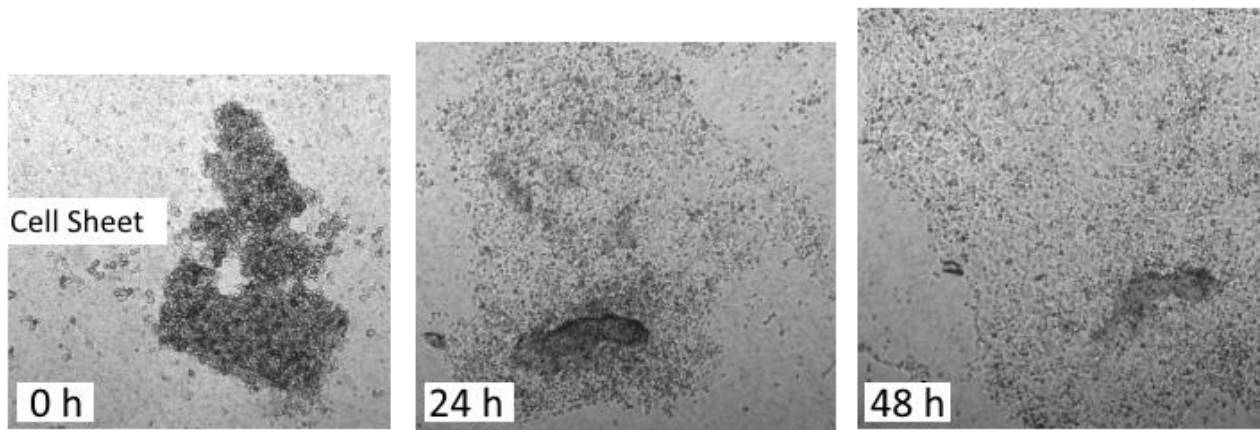


Figure 2: Cell culture on nanoporous membranes after epithelial cell sheet-formation in the acoustic trap. The BEC sheet can be seen spreading out to cover the surface of the membrane over time, demonstrating both viability and the absence of damage or contamination during extraction of the cells.

The design of the acoustic trap allows the cell sheets to be directly deposited onto nanoporous membranes (Corning Transwells) for long-term culture (**Figure 2**). The subsequent culture was done both directly on the nanoporous membranes and on top of confluent layers of fibroblasts. Locating the constructs on nanoporous membranes enables a direct contact *in vitro* co-culture model where the epithelial barrier is polarized and can be studied/stimulated from either side of the construct.

A primary advantage of this setup is the ability to gently extract the cell-sheets under laminar flow conditions. The platform also presents a scalable approach to generate these sheets by actuating the capillaries using a single source providing a frequency sweep and a single syringe pump utilizing a 10-port selection valve to access the capillaries.

Conclusion

The acoustofluidic method of generating epithelial cell-sheets demonstrates the potential to improve current *in vitro* models of the airway mucosa by placing epithelial cells in direct contact with fibroblasts. This allows an integrated multilayered cellular structure which more closely resembles the *in vivo* architecture of the airway. The resulting models may provide a useful tool for toxicological and pharmacological testing and investigations into cell-to-cell communication.

References

- [1] Swindle, E.J. et al., Expert Review of Respiratory Medicine, 5(6), 757-65 (2011)
- [2] B. Hammarstrom, et al., Lab on a Chip, 10 (17), 2251-2257 (2010).

Design considerations for acoustic modes in glass capillaries used in acoustic trapping devices

Mikkel W. H. Ley, and Henrik Bruus

Department of Physics, Technical University of Denmark, Kongens Lyngby, Denmark
E-mail: mley@fysik.dtu.dk, URL: <http://www.fysik.dtu.dk/microfluidics>

Introduction

In this work we present theoretical modeling to characterize the vibrational modes and the acoustic fields in a small water-filled glass capillary, see Fig. 1(a), which makes out a central part of a non-contact acoustic trapping device [1, 2]. This trapping technology is becoming increasingly used in microfluidic cell-handling [3-5], because its core component is a disposable, low-cost, and off-the-shelf glass capillary acting as a resonator for standing-wave trapping. However, a complete understanding of the combined acoustic field of fluid and solid, is lacking. We here provide a theoretical model of the combined acoustic resonance modes in the cross section of the capillary, a model which could prove useful in designing the next generation of acoustic trapping systems.

System

The acoustic trapping platform [1], sketched in Fig. 1, is composed of fluid-filled (water) cavity in a capillary of (Pyrex-)glass of width $W = 2000 \mu\text{m}$, height $H = 200 \mu\text{m}$, glass thickness $H_g = 140 \mu\text{m}$, and a few centimetres in length. The trap is actuated locally by a piezoelectric element with a frequency of around $f = 4 \text{ MHz}$. At resonance, the acoustic field can effectively trap particles above the piezoelectric actuator and retain them against the flow. However, because the volumes of the solid and of the fluid are of comparable size, the vibrations in these two domains are impacting each other to a great extent. This implies that to understand the acoustic field in the fluid, the full coupled system must be understood. To investigate the resulting acoustic field, we calculate the combined eigenmodes of the fluid and glass in the yz -cross section of the system.

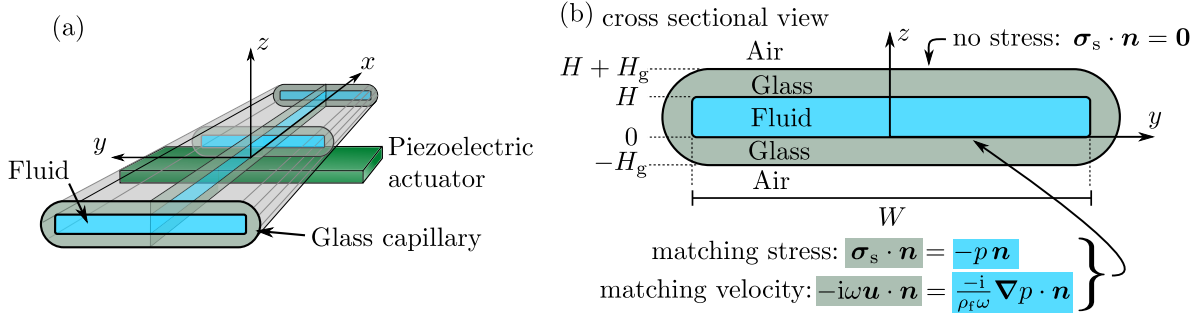


Figure 1: Sketch of the acoustic trapping device. (a) A section of the fluid-filled glass capillary. The capillary is actuated locally by a piezoelectric element, typically around 1 mm in width. (b) Sketch of yz -cross section of the capillary of width $W = 2000 \mu\text{m}$, height $H = 200 \mu\text{m}$, and glass thickness $H_g = 140 \mu\text{m}$

Theory

The dynamics of the glass capillary is modeled by the elastic displacement \mathbf{u} , stress σ_s , density ρ_s , Youngs modulus E , Poissons ratio ν , and angular eigenfrequency ω

$$-\rho_s \omega^2 \mathbf{u} = \nabla \cdot \sigma_s, \quad (1)$$

where σ_s is given by,

$$\sigma_s = \frac{E}{1 + \nu} \left[\frac{1}{2} (\nabla \mathbf{u} + (\nabla \mathbf{u})^T) + \frac{\nu}{1 - 2\nu} (\nabla \cdot \mathbf{u}) \mathbf{I} \right], \quad (2)$$

with \mathbf{I} being the unit tensor. The dynamics of the fluid (water) is modeled by the acoustic pressure

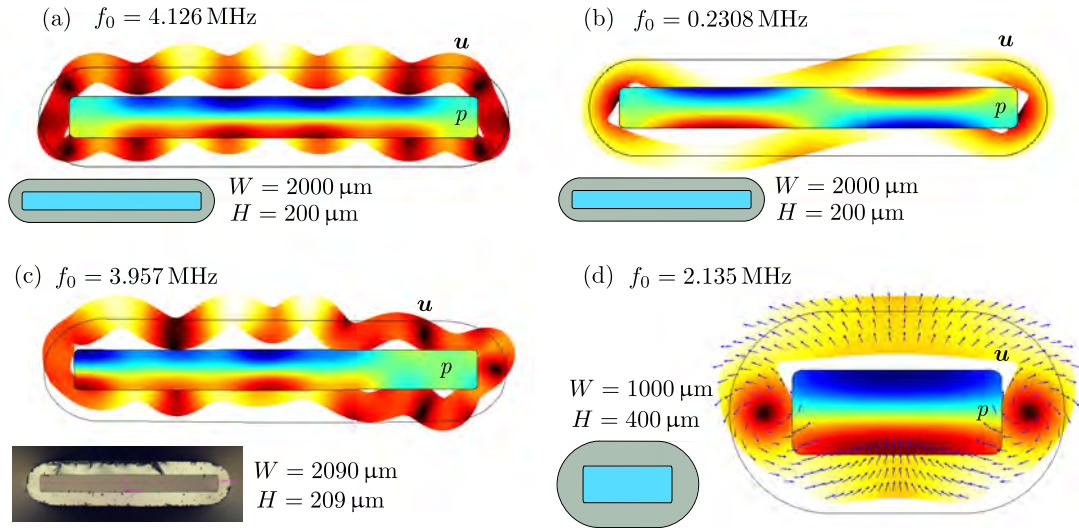


Figure 2: Eigenmodes of the system. The thumbnails below the respective plots denote the geometry used for the specific calculation. In (c), the geometry used in the simulation is the cross section shown in the thumbnail photograph of an actual capillary. The fluid pressure p and the magnitude $|\mathbf{u}|$ of the solid displacement are represented by the rainbow and the heat color schemes, respectively. The magnitude of the displacement have been exaggerated for clarity.

p , and density ρ_f ,

$$\nabla^2 p = -k_f^2 p, \quad \text{with } k_f = \frac{\omega}{c_f}. \quad (3)$$

At the solid-fluid boundaries, we impose continuous normal velocity $-\mathbf{i}\omega\mathbf{u} \cdot \mathbf{n} = \mathbf{v} \cdot \mathbf{n}$ and continuous stress $\boldsymbol{\sigma}_s \cdot \mathbf{n} = -p\mathbf{n}$. For the fluid, the velocity is derived from the pressure as $\mathbf{v} = \frac{-\mathbf{i}}{\rho_f\omega}\nabla p$. At the glass-air boundary, we impose a no-stress condition $\boldsymbol{\sigma}_s \cdot \mathbf{n} = \mathbf{0}$. Eqs. (1)-(3), are implemented and solved numerically in COMSOL Multiphysics v. 5.2.

Results and discussion

In Fig. 2 we show eigenmodes of the system at different eigenfrequencies f_0 . The fluid pressure p and the magnitude $|\mathbf{u}|$ of the solid displacement are represented by the rainbow and the heat color schemes, respectively. In Fig. 2(a), we plot the eigenmode most suited for acoustic trapping in the vicinity of $f \sim 4$ MHz. Note that at this frequency the solid appears to support a large number of oscillation wavelengths. In (b), at the much lower frequency of $f_0 = 0.23$ MHz, we find a more fundamental mode of the system, which also exhibits a favourable pressure pattern with two perpendicular pressure nodes at $y = 0$ and at $z = \frac{1}{2}H$. However, since this frequency is not a resonance frequency for the fluid alone, it is doubtful that this mode can produce significant pressure amplitudes in the fluid when actuated. To investigate the usual working mode around 4 MHz shown in (a), we have in (c) plotted the mode found in COMSOL by importing the actual geometry from the shown photograph of the capillary cross section. Though the change in geometry to slightly wavy in (c) is very small compared to the ideal and straight capillary geometry in (a), the mode changes significantly. This change is most likely due to the many wavelengths of the mode leading to an increased sensitivity to geometry perturbations. In contrast to the variations in the high-frequency modes around 4 MHz for the geometries shown in (a) and (c), the low-frequency modes from 0.1 - 0.5 MHz in the same geometries show much greater resemblance (plots not shown). We therefore investigate more narrow capillary geometries, for which the more stable fundamental modes also exists around 2 MHz instead of only the above mentioned 0.1-0.5 MHz. Altering the capillary slightly to $H = 400 \mu\text{m}$, $H_g = 280 \mu\text{m}$, and $W = 1000 \mu\text{m}$, shows promising results, see Fig. 2(d). With this geometry, an eigenmode composed of a one-wavelength solid displacement field and a favourable pressure pattern appears at a frequency of $f_0 = 2.1$ MHz, which is close to the simple standing half wave resonance of the fluid with frequency $f = \frac{c_f}{2H} = 1.87$ MHz. Such a mode could make it very suitable for use in the next generation acoustic trapping platforms.

References

- [1] B. Hammarström, T. Laurell and J. Nilsson. Lab Chip **12**, 4296-4304 (2012).
- [2] B. Hammarström, M. Evander, J. Wahlström and J. Nilsson. Lab Chip **14**, 1005-1013 (2014).
- [3] I. Gralinski, S. Raymond, T. Alan, and A. Neild. J Appl Phys **115**, 054505 (2014).
- [4] B. Hammarström, B. Nilson, T. Laurell, J. Nilsson and S. Ekström. Anal. Chem. **86**, 10560-10567 (2014),
- [5] E.S. Kim, M.-H. Lee, S.-H. Kim, I.-K. Hwang. J Korean Phys Soc **66**, 198-202 (2015).

The acoustic force density acting on inhomogeneous fluids with spatial variations in density and compressibility

Jonas T. Karlsen¹, Per Augustsson², and Henrik Bruus¹

¹Department of Physics, Technical University of Denmark, Kongens Lyngby, Denmark
E-mail: jonkar@fysik.dtu.dk, URL: <http://www.fysik.dtu.dk/microfluidics>

²Department of Biomedical Engineering, Lund University, Lund, Sweden

Introduction

To explain recent experimental findings on relocation and stabilization of density gradients in acoustofluidic devices [1, 2], we have developed a novel theory [3] for the acoustic force density acting on inhomogeneous fluids on time scales that are slow compared to the acoustic oscillation period. Our theory is an extension of fundamental work on the acoustic radiation force acting on particles [4–6] or immiscible fluid interfaces [7, 8] to include fluids with a continuous spatial variation in density and compressibility. A key prediction of our theory is that inhomogeneous configurations can be stabilized in the presence of destabilizing forces due to gravity or acoustic streaming flows. Experimental validation is obtained by confocal imaging of well-controlled inhomogeneous solutions of iodixanol in water in the glass-silicon microchip shown in Fig. 1.

Motivation

Building on the discovery of acoustic stabilization of inhomogeneous fluids [1], iso-acoustic focusing has been introduced as an equilibrium cell-handling method that overcomes the central issue of cell-size dependency in acoustophoresis [2]. The method can be considered a microfluidic analog to density gradient centrifugation, allowing spatial separation of different cell-types based on differences in their acousto-mechanical properties independent on size. To advance this technology, and potentially open up new routes to microscale handling of fluids and particles using acoustics, we here provide a theoretical explanation of the physics governing the acoustic forces acting on inhomogeneous fluids.

Theory

Briefly, we report here the general expression that we have derived for the force density \mathbf{f}_{ac} acting on a fluid of inhomogeneous compressibility κ_0 and density ρ_0 , dependent on the acoustic pressure p_1 and velocity \mathbf{v}_1 . For the cross-sectional half-wave resonance with wavenumber k sketched in Fig. 1(c), we further provide the simplified expression for the force density $\mathbf{f}_{ac}^{(1)}$ in the experimentally relevant and simplified case of a constant speed of sound c , and a weakly inhomogeneous density $\rho_0(\mathbf{r}) = [1 + \tilde{\rho}(\mathbf{r})]\rho_0^{(0)}$, where $\tilde{\rho}(\mathbf{r})$ is the relative deviation away from the reference density $\rho_0^{(0)}$,

$$\mathbf{f}_{ac} = -\frac{1}{4}|p_1|^2\nabla\kappa_0 - \frac{1}{4}|\mathbf{v}_1|^2\nabla\rho_0, \quad \text{and} \quad \mathbf{f}_{ac}^{(1)} = -\cos(2ky) E_{ac}^{(0)} \nabla\delta, \quad \text{for} \quad |\tilde{\rho}| \ll 1. \quad (1)$$

Here, $E_{ac}^{(0)}$ is the time-averaged acoustic energy density of zeroth order in $\tilde{\rho}$. Using $\mathbf{f}_{ac}^{(1)}$ as a body force in the Navier–Stokes equation coupled with the mass-continuity equation and the advection-diffusion equation for the iodixanol concentration, we simulate numerically the slow-time-scale dynamics resulting from the forces of gravity and acoustics.

Results

In Fig. 2 we compare the simulated and experimentally measured concentration fields after 17 s retention time for three acoustic energy densities E_{ac} , showing that the acoustic force density can stabilize a dense vertical fluid column against gravity, such that it broadens only by diffusion. Figure 3 shows time-resolved simulations obtained with $E_{ac} = 10 \text{ J/m}^3$ for (a) the stable initial configuration with the denser fluid at the center, (b) the unstable initial configuration with the denser fluid at the bottom, and (c) the unstable initial configuration with the denser fluid at the sides. While the stable initial configuration evolves only by diffusion, the unstable initial configurations evolve by complex advection patterns into essentially the same stable configuration with the denser fluid at the center. This fluid relocation is in full qualitative agreement with previously published experiments [1, 2].

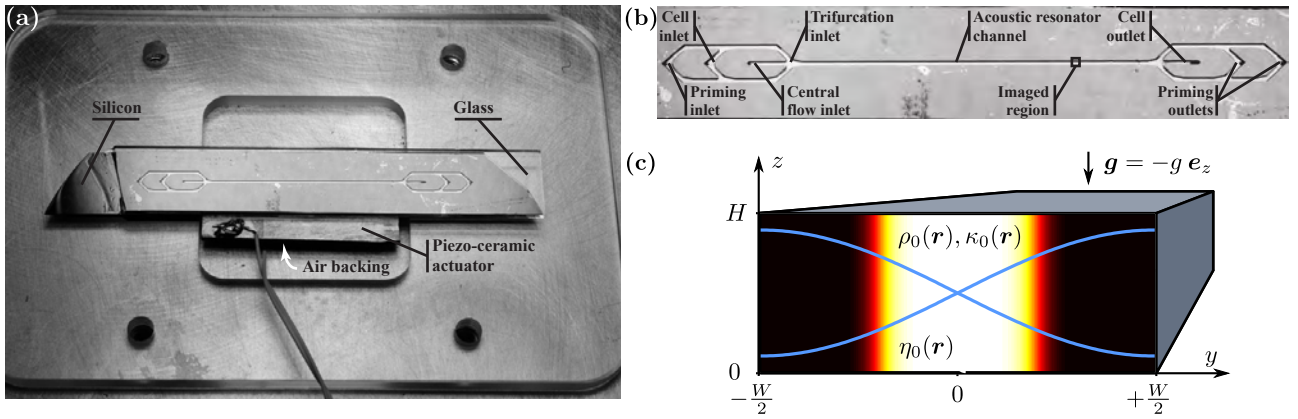


Figure 1: (a) Photo of the glass-silicon microchip in its holder with the piezo-transducer glued underneath. (b) Photo of the microchip showing the trifurcation inlet to the left and the outlet to the right. (c) Sketch of the microchannel cross section of width $W = 375 \mu\text{m}$ and height $H = 150 \mu\text{m}$ inside the microchip. The initial iodixanol concentration at the trifurcation inlet is 36% in the center (white) and 10% at the sides (black) leading to an inhomogeneous density $\rho_0(\mathbf{r})$, compressibility $\kappa_0(\mathbf{r})$, and dynamic viscosity $\eta_0(\mathbf{r})$. The gravitational acceleration is $\mathbf{g} = -g\mathbf{e}_z$. The fundamental half-wave acoustic pressure resonance is represented by the blue sinusoidal curves. Adapted from Refs. [2, 3].

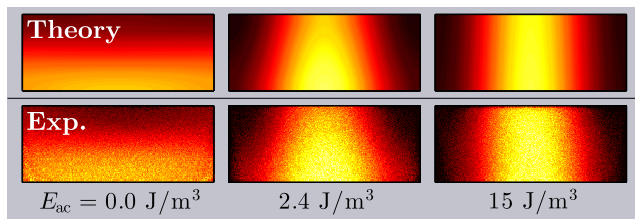


Figure 2: Simulation (top) and experimental confocal image (bottom) of the cross-sectional concentration of iodixanol after 17 s retention time for three acoustic energy densities E_{ac} . Initially, the denser fluorescently marked fluid (36% iodixanol, white) is in the center and the less dense fluid (10% iodixanol, black) is at the sides, see Fig. 1(c). The stable configurations confirm the observation in Ref. [2] that acoustic streaming is suppressed in inhomogeneous fluids. All parameters used in the simulation have been measured experimentally leaving no free fitting parameters. Adapted from Ref. [3].

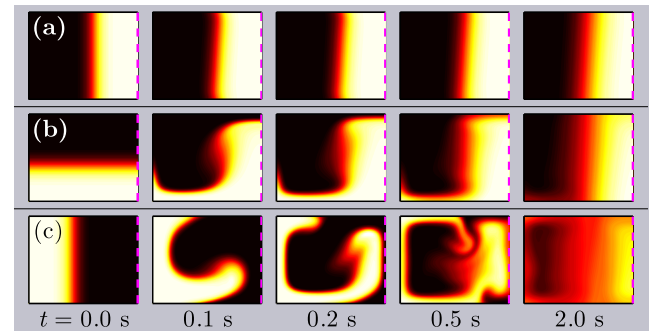


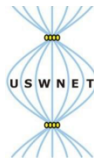
Figure 3: Simulation for $E_{ac} = 10 \text{ J/m}^3$ of the time-evolution of the iodixanol concentration profile in the vertical yz plane symmetric around $y = 0$ (dashed line), with only the left half $-\frac{1}{2}W \leq y \leq 0$ shown. Three different initial configurations of the dense (36% iodixanol, white) and less dense (10% iodixanol, black) solution give rise to different time evolutions. (a) A vertical slab of the dense fluid in the center. (b) A horizontal slab of the dense fluid at the bottom. (c) Two vertical slabs of the dense fluid at the sides. All configurations develop towards a stable configuration with the dense fluid located as a nearly vertical slab in the center in good agreement with previous experimental observations [1, 2]. Adapted from Ref. [3].

Conclusion

Our theory for the acoustic force density acting on an inhomogeneous fluid [3] explains recent experimental observations [1, 2], and agrees with our experimental validation without free parameters. The theoretical understanding of forces acting on inhomogeneous fluids opens up new avenues for designing acoustofluidic chips for microscale handling of fluids and particles.

References

- [1] S. Deshmukh, Z. Brzozka, T. Laurell, and P. Augustsson, *Lab Chip* **14**, 3394 (2014).
- [2] P. Augustsson, J. T. Karlsen, H.-W. Su, H. Bruus, and J. Voldman, *Nat. Commun.* **7**, 11556 (2016).
- [3] J. T. Karlsen, P. Augustsson, and H. Bruus, *Phys. Rev. Lett.* **117**, 114504 (2016).
- [4] L. V. King, *Proc. R. Soc. London, Ser. A* **147**, 212 (1934).
- [5] K. Yosioka and Y. Kawasima, *Acustica* **5**, 167 (1955).
- [6] J. T. Karlsen and H. Bruus, *Phys. Rev. E* **92**, 043010 (2015).
- [7] G. Hertz and H. Mende, *Z. Phys.* **114**, 354 (1939).
- [8] N. Bertin, H. Chraïbi, R. Wunenburger, J.-P. Delville, and E. Brasselet, *Phys. Rev. Lett.* **109**, 244304 (2012).



Acoustic and magnetic methods for the isolation and analysis of biomarkers in microfluidic platforms

C. Wyatt Shields IV,^{1,2} Korine A. Ohiri,^{2,3} Alice Li^{1,2} and Gabriel P. Lopez^{1,2,3,4}

¹NSF Research Triangle Material Research Science and Engineering Center, Durham, USA

²Department of Biomedical Engineering, Duke University, Durham, USA

³Department of Mechanical & Materials Science, Duke University, Durham, USA

⁴Department of Chemical & Biological Engineering, University of New Mexico, USA

Email: cws14@duke.edu and gplopez@unm.edu

Introduction

The early detection of cancer is vital to providing life-saving, therapeutic intervention [1]. However, current methods for detection (e.g., tissue biopsy, endoscopy and medical imaging) often suffer from low patient compliance and an elevated risk of complications, especially in elderly patients. As such, many are looking to “liquid biopsies” for clues into presence and status of cancer due to its minimal invasiveness and ability to provide rich information about the native tumor. In such liquid biopsies, peripheral blood is drawn from for detailed screenings of biomarkers via enumeration and analysis. A critical first step in performing these types of analyses is the separation, enrichment and/or isolation of the target biomarkers (e.g., cells or proteins), which can enable many diagnostic and therapeutic practices. In this presentation, we will provide an overview of a variety of acoustofluidic strategies developed by our group that may advance some of these processes. In particular, we will focus on the use of elastomeric particles in bioseparation assays. Further, we will describe extensions of this work to include acoustofluidic systems for rare cell isolation and analysis.

Monodisperse elastomeric particles

We have developed a facile method to synthesize large volumes of elastomeric particles made from silicone gels using a nucleation and growth process. Unlike cells and most synthetic particles that focus to the pressure node(s) of a standing wave (Fig. 1A), these particles display negative acoustic contrast by focusing to the pressure antinodes (Fig. 1B). We will show that these particles can be synthesized from a large variety of silicon alkoxide and alkoxy silane monomers for control over their chemical composition, and thus, mechanical properties (e.g., bulk modulus and density). Further, we can control the size of the particles from hundreds of nanometers to several micrometers [2].

Cell sequestration with elastomeric particles

Using the silicone gel particles, we show that we can capture living mammalian cells and sequester those cells to the pressure antinodes of a standing wave. This type of capture and isolation may hold promise for on-chip staining, analysis and potentially continuous sorting from cells without elastomeric particles bound to their surfaces for direct separation through positive or negative selection [3].

Biomarker isolation with elastomeric particles and elastin-like polypeptides

Using the elastomeric particles described above, we have developed a method that enables the rapid capture and isolation of small molecules from blood for their off-chip quantification. First, we used thermally responsive polypeptides (namely, elastin-like polypeptides (ELPs)) with binding ligands to capture biomarkers spiked in blood. Next, we added elastomeric particles with ELPs on

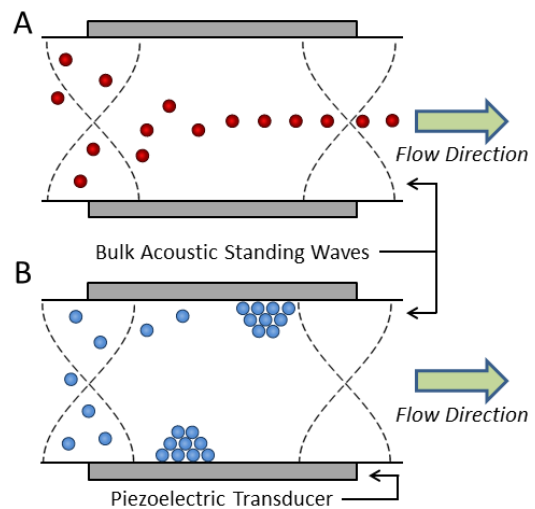


Figure 1. Particles with (A) positive acoustic contrast and (B) negative acoustic contrast in an acoustic standing wave. Image was adapted from [4].

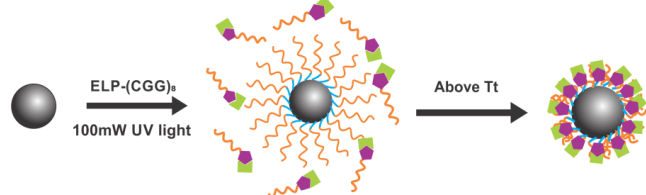


Figure 2. Elastomeric particles are functionalized with elastin-like polypeptides (ELPs) for capturing biomarkers via thermally induced co-aggregation of ELPs.

their surfaces to immobilize the captured biomarkers by increasing the temperature of the solution to co-aggregate the tethered and untethered polypeptides. The blood sample containing the biomarker-particle complexes was then diluted with warm buffer and injected into a microfluidic device supporting a half-wavelength bulk acoustic standing wave. The biomarker-particle complexes migrated to the pressure antinodes, whereas blood cells migrated to the pressure node, leading to a biased separation with efficiencies exceeding 90%. The biomarker-particle complexes were then analyzed via flow cytometry, where we achieved a detection limit of 0.75 nM for streptavidin in blood plasma. Finally, by reducing the temperature of the solution, greater than 75% of the biomarkers were released from the particles.

Synthesis of magnetoelastomeric particles

Building off of the work in the above-described topics, we have developed a new class of magnetic and elastomeric particles that exhibit positive magnetophoresis and negative acoustophoresis (i.e., negative acoustic contrast) in aqueous suspensions. These particles are comprised of polydimethylsiloxane (PDMS) with homogeneously distributed Fe₂O₃ nanoparticles. We show that we can synthesize these particles with capillary microfluidics, thus rendering the particles monodisperse, and we show that we can modify the surfaces of the particles for direct binding assays. Given their unique mechanical properties, we show these particles can enable a new form of acoustomagnetic separation for various bioanalytical applications.

Acoustically enhanced magnetic separation of cancer cells from blood for on-chip templating

Beyond cell or biomarker separation, there is a growing need for templating cells or particles after separation for automated analysis [5]. We have developed a set of microfluidic technologies that offer a unique set of strategies to focus, sort and template cells in independent microfluidic modules. The first module exploits ultrasonic standing waves to rapidly focus cells to the pressure node of a standing wave. The second module contains an off-chip magnet to impose a non-uniform magnetic field to separate cells with magnetic labels from unlabeled cells in a high throughput fashion via free-flow magnetophoresis. We show this module is capable of separating particles with efficiencies exceeding 90% at rates up to 2,000 events/sec. The third module uses a printed array of micromagnets to capture magnetically labeled cells into well-defined compartments, enabling on-chip staining and single cell analysis. Overall, this platform may enable facile processing of complex biological mixtures for direct single cell analysis.

Conclusion

Overall, we present a collection of microfluidic technologies designed to process complex biofluid mixtures for downstream analysis. These technologies can operate in standalone formats, or can be adapted to operate with established technologies, such as flow cytometry. A key advantage of these innovations is their ability to process inhomogeneous samples (e.g., processed blood) in a rapid, and thus high throughput, fashion [6]. We show that they can process fluids at a variety of concentrations and flow rates, target cells with various immunophenotypes and sort cells via positive (and potentially negative) selection. These technologies are chip-based, fabricated using standard clean room equipment, towards a disposable clinical tool. With further optimization in design and performance, these technologies might aid in the early detection, and potentially treatment, of cancer and various other physical ailments.

References

- [1] T. Zhang and A.J. Armstrong, *Curr Oncol Rep* **18**, 1-8 (2016).
- [2] C.W. Shields IV, *et al. Angew Chemie Int'l Ed* **53**, 8070-8073 (2014).
- [3] C.W. Shields IV, *et al. Langmuir* **30**, 3923-3927 (2014).
- [4] C.W. Shields IV, *et al. Lab Chip* **15**, 1230-1249 (2015).
- [5] S.H. Kim, *et al. Lab Chip* **15**, 4356-4363 (2015).
- [6] T. Laurell, F. Petersson, A. Nilsson. *Chem Soc Rev* **36**, 492-506 (2006).

Integration of acousto- and dielectrophoresis for tumor cell separation and concentration followed by single cell trapping

M. Antfolk¹, S. H. Kim², M. Kobayashi², L. Jonsson¹, K. Saori², S. Kaneda², T. Fujii², and T. Laurell¹

¹Department of Biomedical Engineering, Lund University, Lund, Sweden

E-mail: maria.antfolk@bme.lth.se

²Institute of Industrial Science, University of Tokyo, Tokyo, Japan

Introduction

Circulating tumor cells, shed from primary tumors and migrating into the blood, are considered a major cause of cancer metastasis. To detect these extremely rare CTCs (1 CTC in 10^9 blood cells), several groups have been developing microfluidic devices for continuous flow-based CTC separation [1]. A practical challenge of these systems is that the sorted cells should be collected for downstream analysis, which could cause severe loss of target cells. Recently, we developed a microfluidic system for rare cell analysis, combining an acoustofluidic chip for sample preconcentration and dielectrophoresis for subsequent single-cell trapping (Fig. 1 and 2).

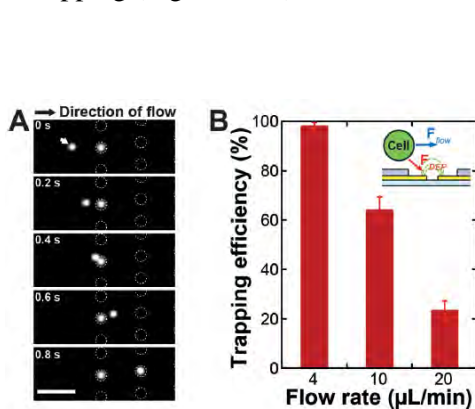


Figure 1: DEP trapping of DU145 cells (human prostate cancer cell line) without preconcentration. A) Fluorescent time lapse image of the microwell array during cell trapping. Scale bar is 100 μm. B) Cell trapping efficiency dependent on inflow rate in DEP chip alone. [2]

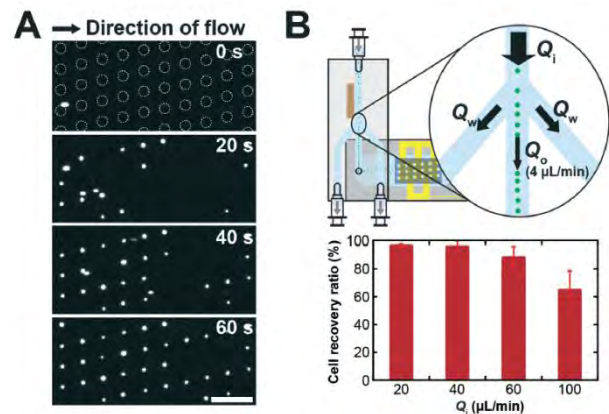


Figure 2: DEP trapping of DU145 cells (human prostate cancer cell line) after acoustophoresis preconcentration. A) Fluorescent time lapse image of the microwell array during cell trapping. Scale bar is 200 μm. B) Cell trapping efficiency depending on inflow rate into the acoustophoresis chip while flow rate to the DEP trapping chip was fixed at 4 μL/min. [2]

The system showed a 10 times improved sample throughput compared to trapping with the DEP chip alone, while maintaining a highly efficient cell recovery above 90% [2].

Here, we present a novel integrated device, combining an advanced acoustofluidic chip, which allows separation and concentration of the targeted cells, directly onto the dielectrophoresis trapping array to realize an automated single-cell CTC analysis system.

Results and discussion

The integration was achieved by directly bonding the sample outlet of the acoustofluidic chip (glass lid) with the inlet of the dielectrophoresis trapping chip (PDMS) (Fig. 3). A cell mixture was two-dimensionally pre-aligned to two positions before being separated and concentrated using acoustophoresis. Largely the cells are separated based on their size. The sample input flow rate was set to 80 μL/min.

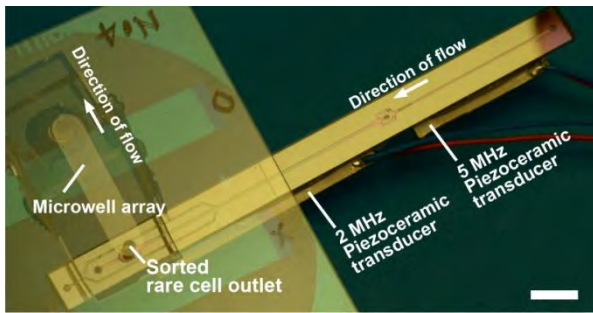


Figure 3: Photo of integrated device. For the integration of two original microfluidic devices, the sample outlet of the acoustofluidic chip was directly connected with the inlet of the DEP chip by bonding of the PDMS based DEP chip to the glass surface of the acoustofluidic chip.

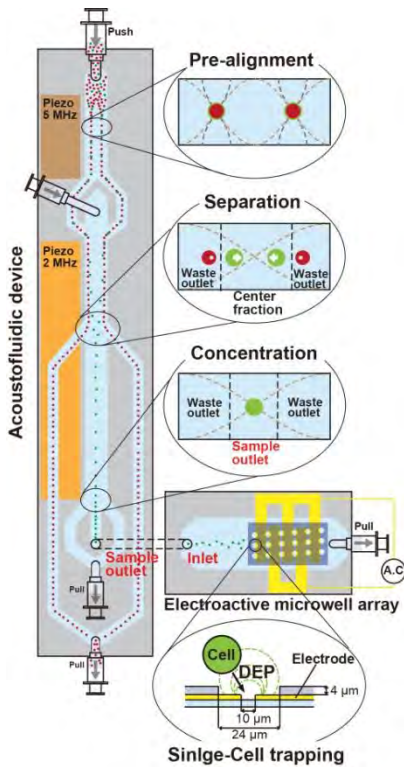


Figure 4: Schematic image of integration of acousto- and dielectrophoresis. A cell mixture was acoustically pre-aligned to two positions in the two-dimensional standing wave pressure nodes field. The aligned cells were separated, and concentrated at the end of the acoustofluidic chip. The sorted cells were arrayed into the DEP chip.

After the separation the collected fraction was then directly concentrated ~ 20 times. The concentrated central fraction, containing the target cells, then progressed into the dielectrophoresis single cell trapping array where they were trapped in individual wells allowing for the subsequent single-cell analysis (Fig. 4).

The optimal frequency for the acoustophoretic separation was tuned by running a mixture of $3.1\text{-}\mu\text{m}$ beads and $6\text{-}\mu\text{m}$ beads through the integrated device (Fig. 5 left). We demonstrated single-cell trapping after separation of DU145 (human prostate cancer cell line) from white blood cells (WBCs) with the integrated device, where the mean diameter of DU145 cells was larger than the WBCs. A mixture of DU145 and WBCs was sorted and concentrated, and then trapped in single-cell wells (Fig. 5 right). Subsequent on chip staining can also be performed (data not shown).

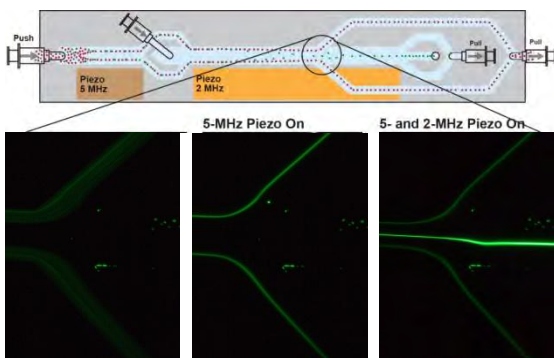


Figure 5: Left) Separation of μ beads. Mixture of $3.1\text{-}\mu\text{m}$ and $6\text{-}\mu\text{m}$ beads were introduced into the device and separated with the integrated device. Right) Trapped DU145 cells after separation.

Conclusion

We have successfully demonstrated an all integrated device for tumor cell separation and concentration with subsequent high efficiency single-cell arraying.

References

[1] Y. Chen, et al. *Lab Chip*, **14**, 626-645 (2014) [2] S. H. Kim, et al. *Lab Chip*, **15**, 4356-4363 (2015).



Acoustic streaming generated by a cylindrical bubble in a microfluidic channel

Alexander A. Doinikov¹, Thomas Combriat¹, Pierre Thibault¹, and Philippe Marmottant¹

¹LIPhy UMR 5588, CNRS/Université Grenoble-Alpes, Grenoble, France

E-mail: alexander.doinikov@univ-grenoble-alpes.fr, URL: <http://www.fysik.dtu.dk/Acoustofluidics2016>

Introduction

Acoustic excitation of cylindrical gas bubbles placed in a microfluidic channel gives rise to steady recirculating flows in a surrounding fluid. This nonlinear effect, known as acoustic streaming, is essential to a number of technologies, such as particle trapping, size-selective sorting and micromixing. The theoretical modeling of acoustic streaming in a microfluidic channel with elastic walls is a challenging problem because of specific features of the bubble dynamics. Under the above conditions, the bubble produces two types of scattered waves: (1) a bulk wave that propagates in the fluid gap with an ordinary sound speed and (2) Lamb-type surface waves that propagate at the fluid-wall interfaces with a much lower speed than that of the bulk wave [1,2]. In addition, the bubble undergoes translational oscillation caused by scattered waves from neighboring bubbles. Acoustic streaming produced by such a bubble results mainly from the interaction of the volume and translational modes of the bubble oscillations [1]. The aim of our study was to develop a theoretical model for acoustic streaming produced by a pulsating and translating cylindrical bubble confined between two elastic walls, taking into account the contributions of both bulk and surface waves. The model was then used for the calculation of streamlines, which revealed a dominant effect of the surface waves on the vortex orientation of streamline patterns. We have also checked the model against experimental data and found a good agreement between experimental and theoretical results.

Theoretical model

The derivation of the model includes two stages. At the first stage, the linear equations of fluid motion are solved. They include the continuity equation and the incompressible Navier-Stokes equation, which are applied to the fluid in the microfluidic channel. The solutions of the equations are based on a bubble model developed in our recent paper [2]. The above model describes the bulk scattered wave and the Lamb-type surface waves generated by the volume oscillation of a cylindrical bubble placed between two planar elastic walls. The linear solutions are used as input data for the equations of acoustic streaming.

The second stage consists in solving the equations of acoustic streaming [3]. As a result, we obtain the radial and the tangential components of the Lagrangian streaming velocity generated by the bubble, assuming that the translational motion of the bubble is caused by another bubble, which undergoes a similar acoustic action. The general streaming solutions are calculated with no restrictions on the ratio between the viscous penetration depth, δ_v , and the bubble radius, R_0 . However, in most cases of interest, the condition $\delta_v/R_0 \ll 1$ is valid. Therefore, it is appropriate to derive approximate equations for this limit. We provide such equations and use them in our numerical examples.

Predicted streamlines

In our calculations, we assume that the fluid in the microfluidic channel is water, the gas in bubbles is air, the channel walls are made of PDMS, and the channel height is $25 \mu\text{m}$. Figure 1 exemplifies calculated streamline patterns in the cases of (a) the absence and (b) the presence of surface waves. The calculation was made for two equal bubbles with radii $R_0 = 30 \mu\text{m}$, separated by a distance $d = 10R_0$ and excited at a frequency $f = 50 \text{ kHz}$. According to the terminology proposed by Rallabandi *et al.* [4], the vortex pattern in Fig. 1(a) is a streaming of the ‘fountain’ type, while that in Fig. 1(b) is a streaming of the ‘antifountain’ type. Thus, Fig. 1 reveals that the surface waves can reverse the vortex orientation.

Longuet-Higgins [5] has shown for a spherical bubble that the streaming velocity is proportional to $\sin(\Delta\phi)$, where $\Delta\phi$ is the phase shift between the radial and translational oscillations. As a consequence, the vortex orientation of streamlines is determined by the sign of $\sin(\Delta\phi)$ [1]. Our calculations reveal that, for a cylindrical bubble in a PDMS channel, the surface waves make the dependence on $\Delta\phi$ more complicated. According to our results, a ‘fountain’-type streaming usually occurs at $\sin(\Delta\phi) > 0$, while the ‘antifountain’ type is observed at $\sin(\Delta\phi) < 0$. However, this is not always the case. There are examples where the ‘fountain’ type occurs at $\sin(\Delta\phi) < 0$ and vice versa. Our calculations also show that the ‘fountain’ type is observed for smaller (with respect to the resonance size) bubbles, while for bigger bubbles, the vortex pattern changes to the ‘antifountain’ type. The streaming type is also changed with the interbubble distance. These results conform to experimental observations reported by Mekki-Berrada *et al.* [1].

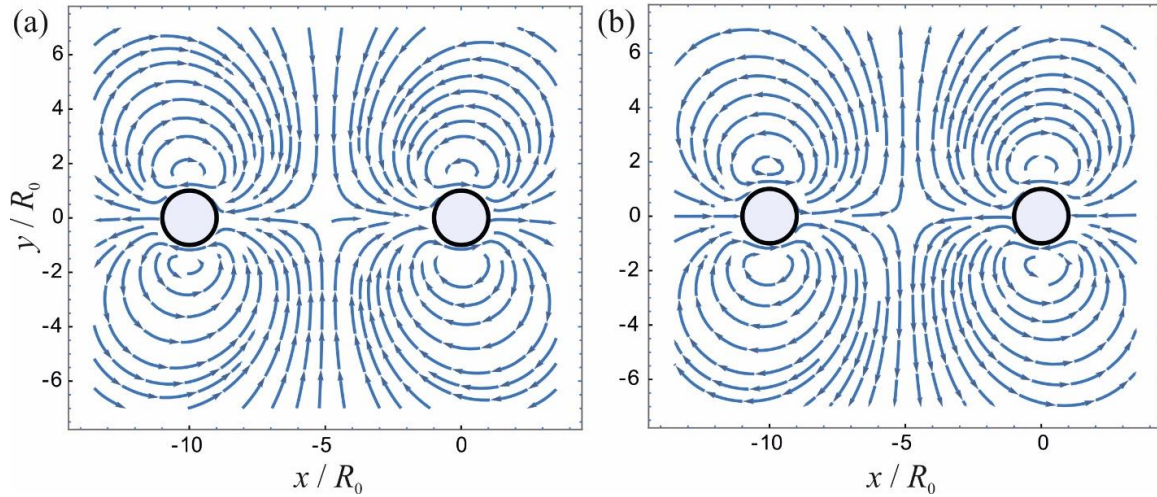


Figure 1: Theoretical streamline patterns for two cylindrical bubbles of equal sizes, undergoing radial and translational oscillations in a microfluidic channel. The bubble radii are $R_0 = 30 \mu\text{m}$, the interbubble distance is $d = 10R_0$, and the excitation frequency is $f = 50 \text{ kHz}$. (a) Surface waves are absent (‘fountain’-type streaming). (b) Surface waves are present (‘antifountain’-type streaming).

Experimental verification

Experimental and theoretical data are compared in Fig. 2. The experimental data are depicted by circles. They show the radial component V_r of the streaming velocity generated by two bubbles along the line of the bubble centers; see the insets. The value of V_r was measured versus distance r from the center of the right bubble. The data in Fig. 2(a) were obtained for bubbles with radii $38.3 \mu\text{m}$ and $33.6 \mu\text{m}$, separated by a distance $175 \mu\text{m}$, and excited at 40 kHz . The data in Fig. 2(b) were obtained for bubbles in contact, which had radii $30 \mu\text{m}$ and were excited at 80 kHz . The results given by our theoretical model are shown by the solid line. As one can see, in both cases, there is a good agreement between experiment and theory.

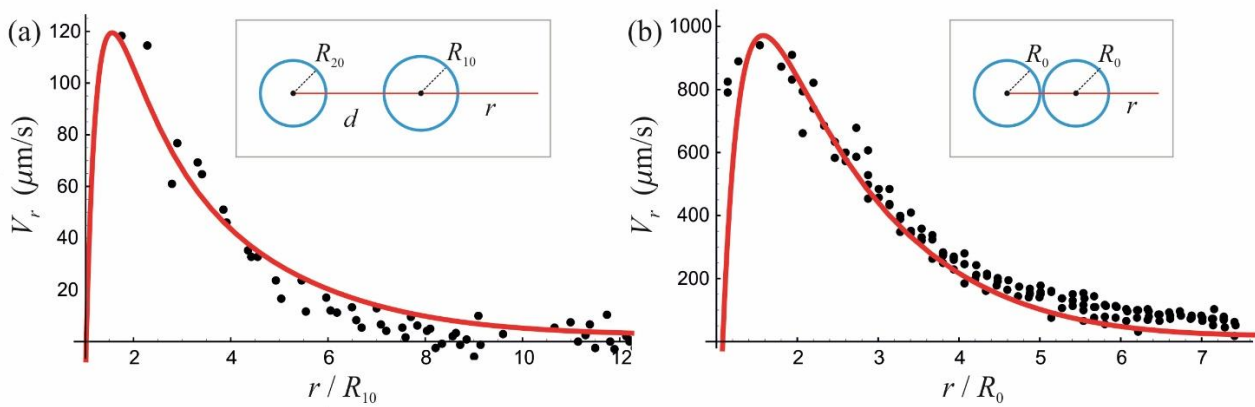


Figure 2: Comparison of experimental (circles) and theoretical (solid line) results. The radial component of the streaming velocity V_r versus distance r from the center of the right bubble. (a) Bubbles with radii $R_{10} = 33.6 \mu\text{m}$ and $R_{20} = 38.3 \mu\text{m}$, separated by a distance $d = 175 \mu\text{m}$, excited at 40 kHz . (b) Bubbles in contact, with radii $R_0 = 30 \mu\text{m}$, excited at 80 kHz .

Conclusion

A theoretical model has been developed for acoustic streaming generated by cylindrical bubbles in a microfluidic channel. The model first provides a rigorous analytical solution that allows for both bulk and surface waves produced by bubbles. Calculations reveal a dominant effect of the surface waves on streamline patterns. The model was validated experimentally.

The work received the ERC funding under the project “Bubbleboost” (ERC Grant agreement № 614655).

References

- [1] F. Mekki-Berrada, T. Combriat, P. Thibault, and P. Marmottant. *J. Fluid Mech.* **797**, 851-873 (2016).
- [2] A. A. Doinikov, F. Mekki-Berrada, P. Thibault, and P. Marmottant. *Proc. R. Soc. A* **472**, 20160031 (2016).
- [3] S. J. Lighthill. *J. Sound Vibr.* **61**, 391-418 (1978).
- [4] B. Rallabandi, C. Wang, and S. Hilgenfeldt. *J. Fluid Mech.* **739**, 57-71 (2014).
- [5] M. S. Longuet-Higgins. *Proc. R. Soc. Lond. A* **454**, 725-742 (1998).

Size Sorting of Particles in Microstreaming: Quantifying Lift Forces

Sascha Hilgenfeldt¹, Bhargav Rallabandi^{1,2}, Siddhansh Agarwal¹, and Raqeeb Thameem¹

¹Mechanical Science and Engineering, University of Illinois at Urbana-Champaign, Urbana, USA
E-mail: sascha@illinois.edu

²Department of Mechanical and Aerospace Engineering, Princeton University, Princeton, USA

Introduction: Bubble Microstreaming

Oscillating microbubbles excited by ultrasonic driving establish powerful steady flow fields, called bubble microstreaming [1, 2, 3]. The easily manufactured devices are versatile tools; previous experimental work in our group has established their usefulness for transport [4], force actuation on cells and vesicles [3], mixing [5], and particle sorting [6]. In parallel theoretical analysis, we have analytically described the flow fields in both the oscillatory and steady components [5, 7, 8].

Sorting of Particles by Size

Bubble microstreaming is achieved by manufacturing one or more blind side channels in a simple PDMS soft lithography device, which automatically retain air pockets upon filling. A piezo transducer drives bubble oscillations at low ultrasonic frequency ($\sim 20\text{kHz}$), resulting in a pair of steady vortices (Fig. 1a). When superimposed with a channel transport flow, the resulting flow field (Fig. 1b) guides suspended neutrally buoyant microparticles into close proximity of the oscillating bubble surface. Over very short time scales ($\sim 1\text{ms}$) and length scales ($\sim 10\mu\text{m}$), the particles suffer differential deflection, so that particles of different size can be collected at different microfluidic outlets (Fig. 1c). The sensitivity of the sorting is far greater than the smallest length scales of manufacture [6, 9].

A simple argument for quantifying this sorting uses the geometry of the flow only, assuming a contact interaction between particles and bubble interface [9]. However, high-speed photography reveals directly that there is no such contact, and that the particles get deflected gradually (Fig. 2a). Stroboscopic photography at the frequency of the driving measures the quantitative displacement of the sorted particles. Translated into an applied force, we observe a ms-long lift force action in the nN range, driving the particles across streamlines (Fig. 2b).

Modeling of Lift Force

To model the lift force quantitatively, we employ a version of the Maxey-Riley (MR) equation [10], which describes the motion of small spherical particles in low-Reynolds-number flow fields. The dominant factor in our case is not usually considered in this context: the interaction force between a particle and the nearby stress-free surface of the bubble. Employing a reciprocal theorem, we obtain a general expression of the force normal to the surface, for arbitrary distances.

The solution of the MR equation becomes relatively straightforward, as we know the flow fields explicitly. The results show particle dynamics in close agreement with experimental observation: a radial oscillatory motion is superimposed by not only a steady azimuthal transport, but a steady radial

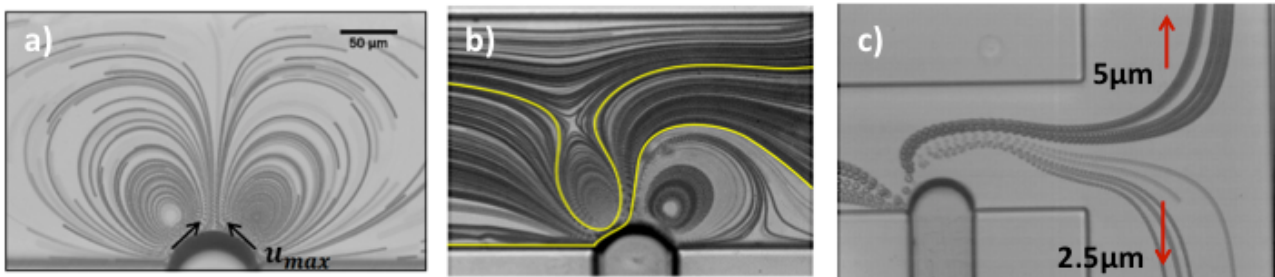


Figure 1: Microbubble streaming and sorting. (a) Vortex flow above a microbubble; (b) Flow field after superposition of transport flow; the yellow lines delineate the region in which sorting can occur; (c) Sorting experiment demonstrating complete separation of particles with radius $a_p = 2.5$ and $5\mu\text{m}$, respectively.

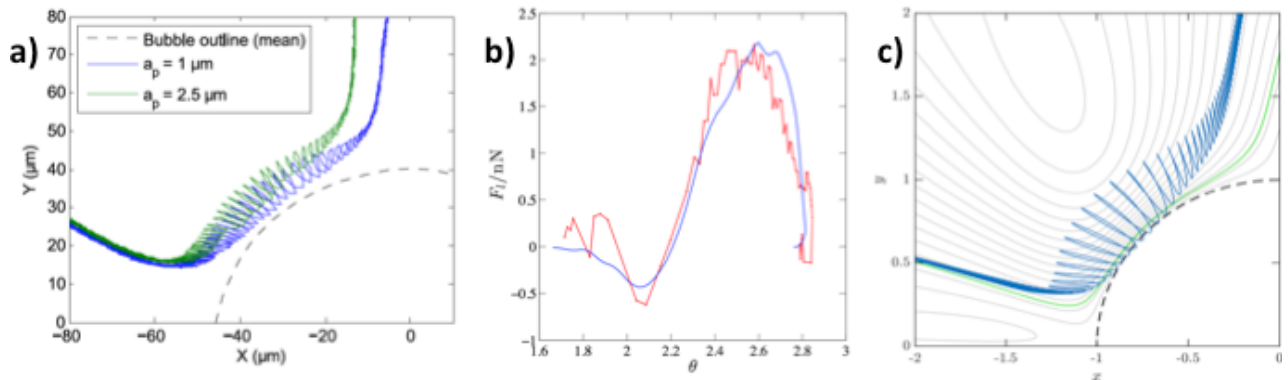


Figure 2: Lift on microparticles. (a) Examples of experimentally measured particle trajectories; (b) Lift forces as a function of azimuthal position, inferred from experiment (red) and computed from the model (blue); (c) Modeling of a particle trajectory (blue), indicating the rectification relative to a fluid element (green).

displacement relative to the fluid (Fig. 2c). The magnitude of displacement, and that of the inferred lift force, matches the experimental data with great accuracy, without any free parameters (Fig. 2b).

Further progress can be made using asymptotic expansions and a time scale separation between the fast oscillatory time scale and that of transport across the bubble. The analytical formalism shows that the steady radial force on the particle can be interpreted as a superposition of two effects: a dynamic rectification analogous to the rectification of fluid elements in streaming flow (but describing additional relative displacement between particle and fluid), and a contribution proportional to the density contrast between particle. This second contribution reduces to the well-known expression of the secondary radiation force [11] at large distances between bubble and particle, but is strongly modified near the surface.

Conclusion

We show here that the sorting forces acting on microparticles in streaming flows can be quantitatively understood and show features generalizing both the principles of streaming rectification and of secondary acoustic radiation force. Not only do these results explain the practically useful manipulation of micron-sized particles over very small length and time scales in bubble streaming flows, but they are readily generalized for a variety of other cases where small objects are exposed to oscillatory flow fields, whether these flows are caused by acoustic waves or not.

References

- [1] Samuel A. Elder. Cavitation microstreaming. *J. Acoust. Soc. Am.*, 31(1):54–64, 1959.
- [2] B. J. Davidson and N. Riley. Cavitation microstreaming. *J. Sound Vib.*, 15:217–233, 1971.
- [3] P. Marmottant and S. Hilgenfeldt. Controlled vesicle deformation and lysis by single oscillating bubbles. *Nature*, 423(6936):153–156, 2003.
- [4] P. Marmottant and S. Hilgenfeldt. A bubble-driven microfluidic transport element for bioengineering. *Proc. Natl. Acad. Sci. USA*, 101(26):9523–9527, 2004.
- [5] C. Wang, B. Rallabandi, and S. Hilgenfeldt. Frequency dependence and frequency control of microbubble streaming flows. *Phys. Fluids*, 25:022002, 2013.
- [6] C. Wang, S. V. Jalikop, and S. Hilgenfeldt. Size-sensitive sorting of microparticles through control of flow geometry. *Appl. Phys. Lett.*, 99(3):034101, 2011.
- [7] B. Rallabandi, C. Wang, and S. Hilgenfeldt. Two-dimensional streaming flows driven by sessile semicylindrical microbubbles. *J. Fluid Mech.*, 739:57–71, 2014.
- [8] Bhargav Rallabandi, Alvaro Marin, Massimiliano Rossi, Christian J Kähler, and Sascha Hilgenfeldt. Three-dimensional streaming flow in confined geometries. *J. Fluid Mech.*, 777:408–429, 2015.
- [9] Raqeeb Thameem, Bhargav Rallabandi, and Sascha Hilgenfeldt. Particle migration and sorting in microbubble streaming flows. *Biomicrofluidics*, 10(1):014124, 2016.
- [10] Martin R Maxey and James J Riley. Equation of motion for a small rigid sphere in a nonuniform flow. *Phys. Fluids*, 26(4):883–889, 1983.
- [11] Henrik Bruus. Acoustofluidics 7: The acoustic radiation force on small particles. *Lab on a Chip*, 12(6):1014–1021, 2012.

A sessile droplet of water carrying polystyrene microparticles meets with high frequency acoustic waves

Ghulam Destgeer, Jin Ho Jung, Jinsoo Park, Husnain Ahmed, Byung Hang Ha, and Hyung Jin Sung*

Flow Control Laboratory, Department of Mechanical Engineering, KAIST, Daejeon, 34141, South Korea.
Email: destgeer@kaist.ac.kr, hjsung@kaist.ac.kr, URL: <http://flow.kaist.ac.kr/>

Introduction

The concentration of targeted micro-objects, like solid particles and biological cells suspended in a fluid, has been achieved by using sound waves. However, the basic understanding of the underlying physics behind various concentration behaviors of the micro-objects was lacking. [1] We have recently been studying the interaction of acoustic waves, in the form of surface acoustic waves (SAWs) [2] and Lamb waves (LWs) [3], with a droplet of water carrying polystyrene particles of different diameters. The investigation reveals that the particle concentration depends on various parameters including particle diameters (d_p), acoustic wavelength in the fluid (λ_f), sound attenuation length, droplet volume, acoustic streaming flow (ASF) induced drag force, direct acoustic radiation force (ARF), etc. In this paper, we have presented the working mechanism behind the concentration behavior of the particles, and the experimental results achieved using SAWs and LWs (see Fig 1 and 2).

The SAW-based acoustofluidic device is composed of a piezoelectric substrate (lithium niobate, LN) and an interdigitated transducer (IDT) deposited on top. The SAWs interaction with a droplet of water, as shown in Fig. 1(A), produces a high velocity ASF, and exerts a strong ARF on the suspended particles. As a result of which, the suspended particles are concentrated into four distinct shapes, called regimes R1 – R4 of particles concentration. The concentration of particles at the center of the water droplet (termed as regime R1) is achieved when the attenuation length of SAW on the substrate surface (x_s) is greater than the droplet radius (r_d), and the $\kappa (= \pi d_p / \lambda_f)$ value is smaller than one. The particle concentration around the periphery of the droplet in the form of a ring (termed as regime R2) is achieved when $x_s < r_d$ and $\kappa < 1$. The particles are pushed to the side of the droplet in the form of an isolated island (termed as regime R3), when $x_s > r_d$ and $\kappa > 1$. The formation of a particle ring close to the center of the droplet (termed as regime R4) is associated with $x_s < r_d$ and $\kappa > 1$. These four distinct regimes R1 – R4 are produced under various combination of the ASF-based centrifugal force and drag force, and the standing or travelling SAW-based ARF. For the experimental demonstration as shown in Fig. 2(A), we have used a 5 μL droplet of water, which is actuated by 10, 20, 80, and 133 MHz frequency SAWs to concentrate polystyrene particles with diameters 1 – 30 μm .

The LW-based acoustofluidic device is composed of a LN substrate and a pair of L-shaped metal electrodes deposited on top as shown in Fig. 1(B). The LW-mode of LN substrate vibration is actuated when an appropriate resonant frequency AC signal is provided to the device. For a LN substrate with a 500 μm thickness, acoustic resonance occurs every ~ 3.5 MHz frequency interval. This feature of the LW-based device provides a vast range of possible device actuation frequencies. We have used the LW-based device to demonstrate that the concentration of polystyrene particles in the form of a ring strongly depends on the direct ARF and not the ASF alone. [4] For the experimental demonstration as shown in Fig. 2(B), we have used 45, 65.6, 114, and 224 MHz frequency LWs, and 1, 3, 6, and 10 μm diameter particles suspended in a 5 μL droplet of water.

Results

A summary of the experimental results, for particles manipulation inside a 5 μL sessile droplet of water using SAWs and LWs, is presented in Fig. 2. Sessile droplets of water carrying polystyrene particles with diameters 1, 3, 6, and 10 μm are separately exposed to SAWs with frequencies 10, 20, 80, and 133 MHz, such that sixteen different $d_p - f$ combinations arise (see Fig. 2(A)). For 10 and 20 MHz frequency SAWs, the attenuation length of sound waves (x_s) is larger than the droplet radius (r_d) on the substrate surface that leads to the formation of strong standing waves inside the droplet. For 80 and 133 MHz frequency SAWs, $x_s < r_d$ that leads to the dominance of the travelling waves inside the droplet. The cases corresponding to $\kappa < 1$, $\kappa > 1$, and regimes R1 – R4 are highlighted in different colors. Regime R1 corresponds to the concentration of particles at the center of the droplet as the acoustic radiation force (F_R) by the standing acoustic field dominates the particle motion. However, there are few exceptions to that: when smaller particles with diameter 1 μm are not influenced by the F_R , and move towards the periphery of the droplet (such a case is included in regime R2); and when larger particles with diameter 30 μm are dominated by the travelling waves F_R as $\kappa > 1$, and pushed to the side of the droplet (only case in regime R3). For regime R2, the particles are not influenced by the travelling or standing waves based F_R , and the centrifugal force drives them to the periphery of the droplet.

For regime R3, the larger particles are influenced by both of the travelling and standing waves based F_R ; however, the effect of the travelling waves dominates, and the particles are pushed to the side of the droplet and not captured in the center of the droplet. For regime R4, the particles are dominated by the travelling waves based F_R only, which battles against the centrifugal force acting outwardly; as a result, the particles form a smaller ring-like structure in the center of the droplet.

The interaction of LWs with 45, 65.6, 114, and 224 MHz frequencies with a sessile droplet of water carrying 1, 3, 6, and 10 μm diameter particles reveals the importance of F_R on the formation of particle rings (see Fig. 2(B)). Sixteen different cases are developed for various $f - d_p$ combinations, which are categorized based on the values of κ , and given different color codes. The particles motion inside the droplet is dominated by the travelling waves based F_R when $\kappa > 1$; as a result of which, the particles form a concentric ring. For all the other cases when $\kappa < 1$, the particles continue to flow with the ASF, and do not concentrate or agglomerate at a particular position.

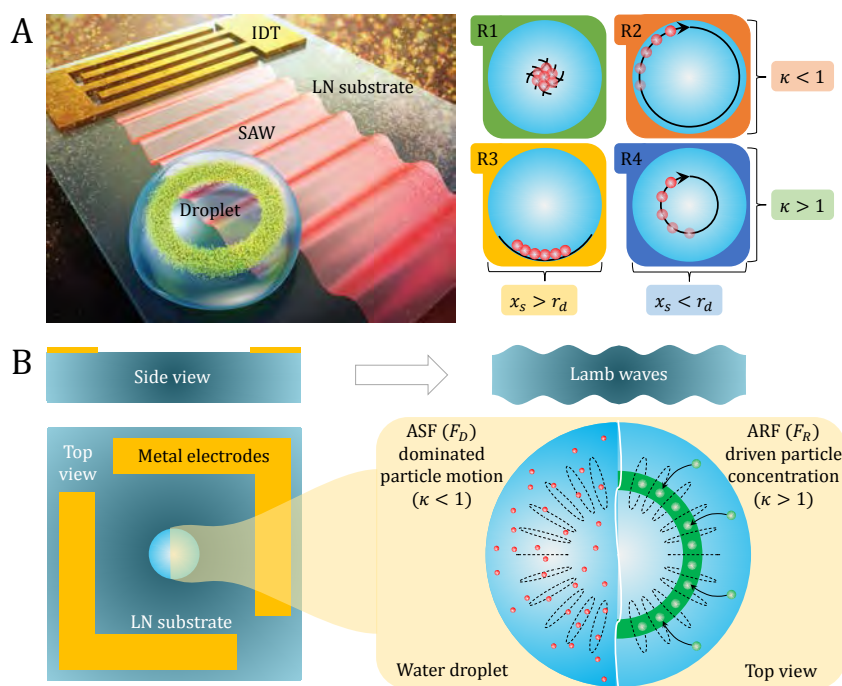


Figure 1: (A) A surface acoustic wave (SAW)-based acoustofluidic platform, composed of an interdigitated transducer (IDT) deposited on top of a piezoelectric substrate, is used to actuate a droplet of water. Four different regimes (R1-R4) of particle aggregation are realized. (Figure is adopted from Ref. 2) (B) A Lamb wave (LW)-based acoustofluidic device, composed of a pair of L-shaped metal electrodes deposited on top of a LN substrate, is used to manipulate particles suspended inside a water droplet. The smaller particles (with $\kappa < 1$) are only influenced by the F_D , and do not form a ring. The bigger particles (with $\kappa > 1$) are dominated by the F_R that concentrate the particles in the form of a concentric ring. (Figure is adopted from Ref. 3)

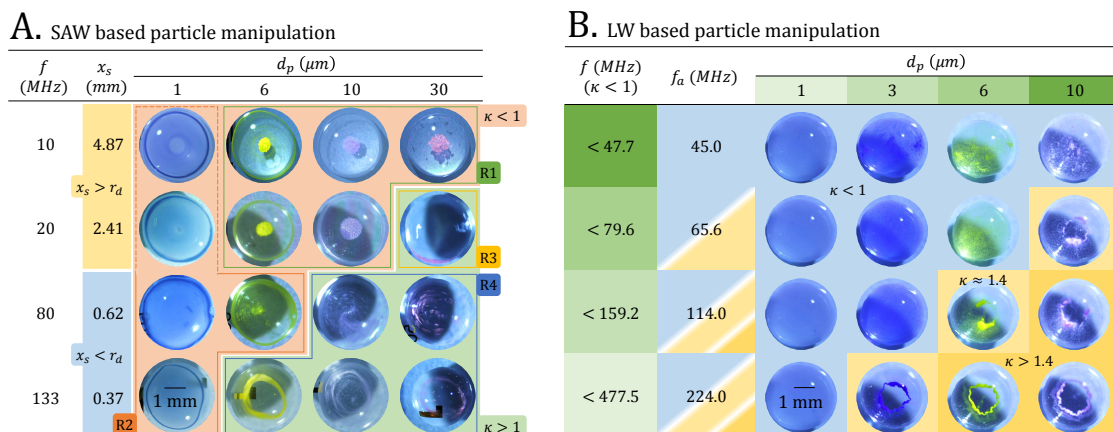


Figure 2: (A) Four different regimes R1 – R4 of particle concentration for various applied SAW frequencies (f), and particle diameters (d_p) are shown. (Figure is adopted from Ref. 2) (B) The LW-based particle manipulation is demonstrated. (Figure is adopted from Ref. 3)

Acknowledgements

This work was supported by the Creative Research Initiatives (no. 2016-004749) program of the National Research Foundation of Korea (MSIP) and the KUSTAR-KAIST Institute.

References

- [1] G. Destgeer, and H. J. Sung. Lab Chip **15**, 2722-2738 (2015).
- [2] G. Destgeer, H. Cho, B. H. Ha, J. H. Jung, J. Park, and H. J. Sung. Lab Chip **16**, 660-667 (2016).
- [3] G. Destgeer, B. Ha, J. Park, and H. J. Sung. Anal. Chem. **88**, 3976–3981 (2016).
- [4] A. R. Rezk, L. Y. Yeo, and J. R. Friend. Langmuir **30**, 11243–11247 (2014).



Acoustic droplet splitting in a micro fluidic channel by a slanted-finger interdigitated transducer

Jin Ho Jung, Ghulam Destgeer, Jinsoo Park, Byung Hang Ha, and Hyung Jin Sung*

¹Flow Control Laboratory, Department of Mechanical Engineering, KAIST, Daejeon, 34141, South Korea.
Email: jhjung11@kaist.ac.kr, hjsung@kaist.ac.kr, URL: <http://flow.kaist.ac.kr/>

Introduction

Recently, biologists, chemist, physicists, and engineers from numerous fields of researchers have co-worked together to demonstrate various microfluidic devices in an effort to scale benchtop experiments conducted in a modern lab to chip size platforms [1]. The miniaturization of experimental device has largely reduced reagent usage and the costs and time required to carry out the chemical assays. Recently, droplet-based microfluidic systems comprising intricately designed and precisely fabricated miniaturized micro channels have attracted much attention for their characteristic to isolate targeted reagents in picoliter volumes without worry of cross-contamination, evaporation, or experimental uncertainties. For this reason, the droplet handling techniques are highly demand. Among them, droplet splitting, categorized as passive or active splitting, is in demand for increasing throughput, reducing volumes after droplet production, sample washing, or generating two identical droplets [2-3]. In this study, we presented an active method to splitting droplets inside a straight PDMS channel using SAWs formed by a slanted-finger interdigitated transducer (SF-IDT). Previously, most SAW-based droplets handling techniques have used a transducer with a beam width much larger than the radius of droplet so that the droplet body is exposed to the acoustic beams to make lateral migration of the droplets without significantly deforming the water-oil interface. In this work, a narrow region of the SF-IDT is activated at a given resonant frequency to generate a narrow SAW beam that is order of the droplet diameter. The SF-IDT is adapted to partially expose the droplet to the acoustic waves, which deform the oil–water interface and splits the droplet into two daughter droplets. The droplet splitting ratio is determined by the applied SAW voltage and the flow rate of the continuous or dispersed fluid flow.

Results

The acousto fluidic droplet splitting system composed of a polydimethylsiloxane (PDMS) micro channel and an SF-IDT, as shown in Fig. 1(a). A water droplet with the oil phase carrier fluid, produced at a T-junction of the microchannel (see Fig. 1(b)), is exposed to a narrow acoustic beam, which generated from the SF-IDT and acts as an acoustic knife to split the droplet into two parts. Also, experimental images of droplet splitting using the 82 MHz frequency SAW are depicted in Fig. 1(c). At time was 0 ms, the daughter droplet on the right side was previously split and trapped by the acoustic radiation forces, whereas another mother droplet on the left flowed along the PDMS channel to the acoustic force region. As the mother droplet entered the SAW actuation region ($t = 0\text{--}39$ ms), it pushed the trapped droplet rightward to push it from the acoustic beam trap ($t = 39\text{--}70$ ms). The 82 MHz frequency SAW beam had an aperture width ($100\ \mu\text{m}$) that was similar with the droplet diameter ($150\text{--}200\ \mu\text{m}$), such that most of the acoustic beam was focused at the beam center to deform the water-oil interface. The surface of the droplet began to deform as soon as it passed the path of the acoustic wave ($t = 70\text{--}77$ ms). Within 10 ms of the SAW actuation, the surface was deformed from a linear to a concave shape that formed a short region across the droplet body ($t = 80$ ms). After a few ms, the droplet neck (short region) thinned more (81 ms) and finally broke up (82 ms) into two daughter droplets. The proposed acoustofluidic system could be used to control the droplet splitting ratio by varying the flow rate and the applied voltage. First, the droplet neck length (d_{neck}) was measured per each droplets to study the correlation between the SAW power and the droplet splitting speed (see Fig. 2(a)). Second, the droplet splitting ratio was observed under different SAW power and total flow rates (see Fig. 2(b)). The corresponding experimental cases are depicted in Fig. 2 (c). The droplet splitting ratio could be varied from 0.1 to 0.63 in the proposed system. We designed an acousto fluidic system comprised of the single SF-IDT and the simple PDMS micro channel for on-demand droplet splitting. The droplet could be easily split into two daughter droplets, and the droplet splitting ratio could be controlled between 0.1 and 0.63 by tuning the flow rate and the applied SAW voltage.

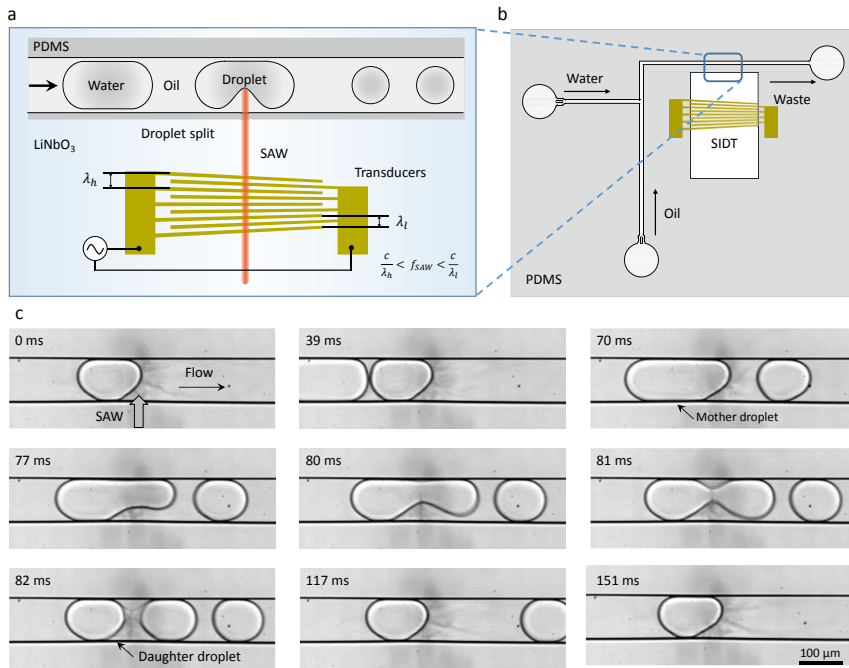


Fig. 1 (a) Schematic of the acousto fluidic droplet splitting system composed of a polydimethylsiloxane (PDMS) microchannel and a slanted-finger interdigitated transducer (SF-IDT). The SF-IDT can be used at a range of frequencies (f_{SAW}) to generate a narrow surface acoustic wave (SAW) beam capable of splitting a droplet into two daughter droplets. (b) A water droplet in an oil carrier fluid is produced at the T-junction of the PDMS microchannel and travelled to the SAW actuation region downstream for splitting. (c) Experimental images of the droplet splitting by the SF-IDT. The SAW, with an 82 MHz frequency, is directed from bottom towards top, and the droplets are transported from left to right. The droplet is split into two parts. The flow rate was 100 $\mu\text{L/hr}$ and the SAW voltage was 2.19 V.

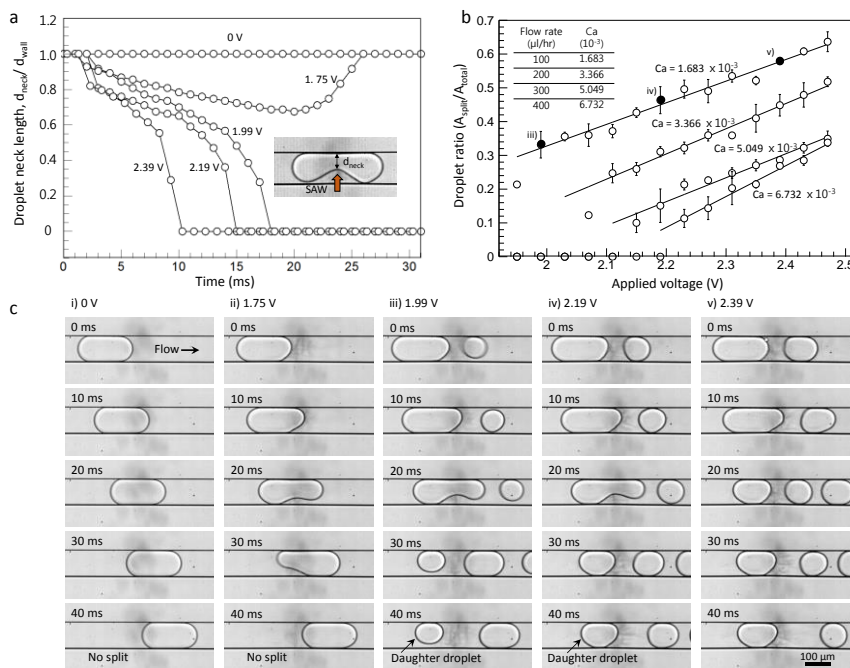


Fig. 2 Droplet splitting device performance. (a) The droplet neck length (d_{neck}), as shown in the inset, measured during the splitting process, was normalized against the micro channel width (d_{wall}), and was drawn against time for varying the SAW power and a flow rate of 100 $\mu\text{L/hr}$. (b) The droplet splitting ratio (area of the split left side droplet A_{split} divided by the total area of the mother droplet (A_{total})) was tuned by the flow rate and the applied voltage. The droplet splitting ratio was controlled from 0.1 to 0.63 in the device. The black markers represent the corresponding experimental cases in (c). (c) Experimental images of the droplet splitting process at a flow rate of 100 $\mu\text{L/hr}$ ($Ca = 1.683 \times 10^{-3}$).

Acknowledgements

This work was supported by the Creative Research Initiatives (no. 2016-004749) program of the National Research Foundation of Korea (MSIP) and the KUSTAR-KAIST Institute.

References

- [1] G. M. Whitesides, *Nature*, **442**, 368-373 (2006).
- [2] A. Pit, M. Duits and F. Mugele, *Micromachines*, **6**, 1768-1793 (2015).
- [3] M. Sesen, T. Alan and A. Neild, *Lab chip*, **15**, 3030-3038 (2015).

Interparticle Force in Acoustofluidic Devices

Kian-Meng Lim¹, Felix Bob Wijaya¹, and Shahrokh Sepehrirahnama¹

¹Department of Mechanical Engineering, National University of Singapore, Singapore
E-mail: limkm@nus.edu.sg

Introduction

When micro-particles are subjected to an acoustic standing wave, it is well-known that a primary radiation force acts on the particles, moving them towards either the pressure node or antinode depending on the acoustic contrast factor. As the particles arrive at the pressure node or antinode, they tend to agglomerate due to interparticle force, also known as the secondary radiation force, due to the re-scattering of the acoustic field. Recently, the multipole expansion method [1] has been used to calculate the interparticle force acting on two spheres. To address the interparticle force between non-spherical particles, a hybrid method, combining the boundary element method and multipole translation, is proposed in this work.

Methodology

A present method uses the boundary element method (BEM) to solve the wave scattering problem and the multipole translation method to obtain multipole and local coefficients of the scattered fields to calculate the interparticle radiation force (Figure 1). **Step 1:** The boundary integral equation is formulated to solve for the wave scattering problem in the presence of two particles. **Step 2:** The strength of monopole and dipole sources on each particle surface are then transformed to the particle center to obtain a multipole representation of the scattered field. The multipole coefficients are calculated using the multipole-to-multipole (M2M) translation and rotation operators [2]. **Step 3:** The scattered field from one particle (say Spheroid 2) is then re-expanded as a local expansion at the center of the other particle (Spheroid 1 in this case) by using the multipole-to-local (M2L) translation operator [2]. **Step 4:** The interparticle force acting on Spheroid 1 is calculated by substituting the local expansion coefficients (due to the scattered field of Spheroid 2 – **Step 3**) and the multipole coefficients (due to the scattered field of Spheroid 1 – **Step 2**) into the general expressions for radiation force, as derived by Silva [3]. In the following section, the interparticle radiation force \mathbf{F}_{ss} will be presented in the non-dimensional form $\mathbf{Y}_{ss} = \mathbf{F}_{ss}/(\pi E_0 a^2)$ [3], where E_0 is the energy density of the incident field, and a is the characteristic length of the particle, such as the radius of sphere.

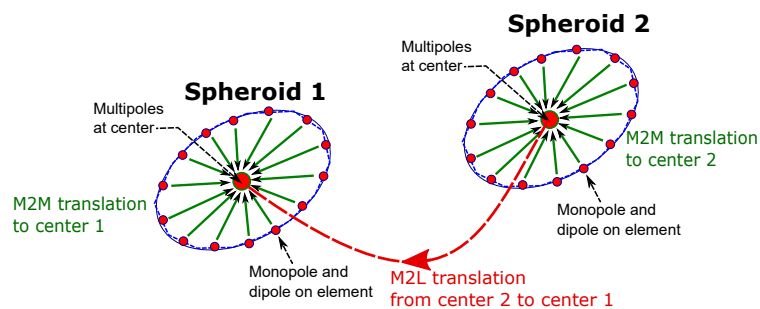


Figure 1: Multipole transformation for calculation of interparticle force.

Results

The above methodology is used to calculate interparticle forces acting on spheres and spheroids in a standing wave. Figure 2 (a) illustrates the case of two rigid spheres subjected to a standing wave $\phi_{in}(z)$. The distance between the center of the two spheres and the incident angle are denoted by L and θ , respectively. The size of each sphere is given by $ka = 0.0628$ where k is the wavenumber and a the radius of the spheres. By using the proposed method, the interparticle force acting on each sphere was calculated for different values of L and θ . The results (using multipoles up to order 6) are in good agreement with those obtained from the multipole expansion method [1], Figure 2 (b) and

(c). Figure 2 (b) shows the radial component of the interparticle force (\mathbf{e}_r) acting on Sphere 1, which can be seen to decrease with distance L . Moreover, as the incident angle θ changes from 0^0 to 90^0 , the radial component changes from repulsive (-) to attractive (+). Figure 2 (c) shows the tangential component of the interparticle force (\mathbf{e}_θ). This tangential component is zero at $\theta = 0^0$ and $\theta = 90^0$; for angles between, the tangential component pushes Sphere 1 towards the pressure nodal line.

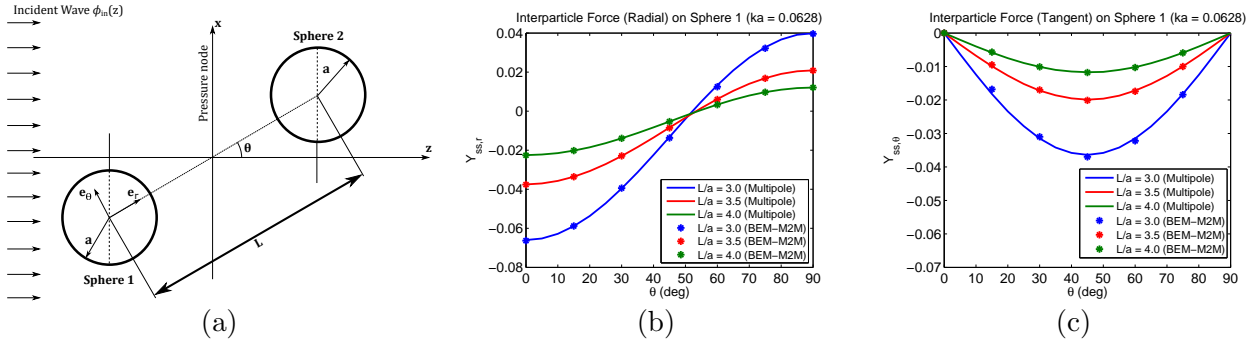


Figure 2: (a) Schematic of the problem setup for two rigid spheres with center-to-center distance L and incident angle θ . The spheres are placed symmetrically with respect to the pressure nodal line. The interparticle force, (b) radial component and (c) tangential component, acting on the Sphere 1 are calculated for different values of L and θ .

Next, the shape of the particle is changed to spheroidal shape, as shown in Figure 3(a), with the angle between the two spheroids and the wave direction kept at zero. The aspect ratio ϵ of the spheroids is varied while keeping the volume the same as a sphere with $ka = 0.0628$. From Figure 3(b), it can be seen that the interparticle force is repulsive and decreases with distance L , which is consistent with the previous result of two spheres when $\theta = 0^0$. It is observed that the change in aspect ratio has considerable effect on the magnitude of the interparticle force when L is small. It can be seen that the oblate spheroids ($\epsilon = 1/2$ and $\epsilon = 2/3$) experience a larger force than that on the prolate spheroid ($\epsilon = 3/2$), which might be due to the larger projected area perpendicular to the wave direction.

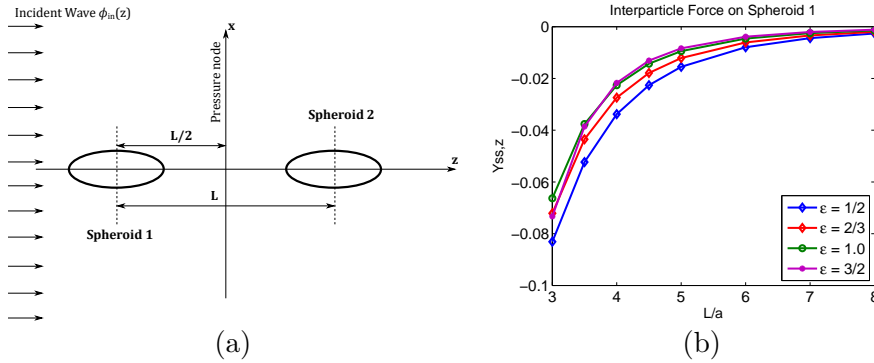


Figure 3: (a) Schematic of the problem setup for two rigid spheroids with center-to-center distance L . The spheroids are placed symmetrically with respect to the pressure nodal line; (b) Interparticle force acting on the Spheroid 1 calculated for different values of L .

Conclusion

Interparticle force on two particles subjected to an acoustic standing wave was calculated by using a hybrid method that combines the boundary element method with multipole translation. For the case of two spheres, the calculation results showed that the interparticle force is either repulsive or attractive depending on the incident angle, consistent with previous studies. For spheroids, it was found that the change in the aspect ratio has a considerable effect on the magnitude of the interparticle force when the distance between the center of two spheroids is small. In the future, the proposed hybrid method would be used to calculate the interparticle torque acting on non-spherical particles.

References

- [1] S. Sepehrirahnama, K.M. Lim, and F.S. Chau. J. Acoust. Soc. Am. **137** (5), 26142622 (2015).
- [2] N.A. Gumerov, R. Duraiswami. *Fast multipole methods for the Helmholtz equation in three dimensions*, Elsevier (USA 2005).
- [3] G.T. Silva. J. Acoust. Soc. Am. **130** (6), 3541-3544 (2011).



Particle pearl-chain formation, an experimental and numerical study

Thierry Baasch¹, Ivo Leibacher¹, and Jürg Dual¹

¹Department of Mechanical Engineering, Institute for Mechanical Systems, ETH Zurich, Zurich, Switzerland
E-mail: baasch@imes.mavt.ethz.ch

Introduction

Acoustic standing waves are used for the contactless manipulation of particles, cells and organisms. Driven by the acoustic radiation force, particles, depending on their respective contrast factor, accumulate in the pressure nodes or antinodes. In one dimensional standing waves, an interesting phenomenon can be observed with micrometer sized glass particles close to the nodal lines. The particles accumulate in chains parallel to the nodal lines, as expected by the Gor'kov theory. However, most interestingly, inter-chain repulsion occurs. This prevents different chains from touching and gives rise to a striped pattern in the particle positions. Acoustic inter-particle forces are thought to be responsible for this sort of pattern formation and a theoretical investigation was presented by Nyborg [1]. To our knowledge no one has analyzed this phenomenology using multibody trajectory simulations, so far. One major obstacle consists of how to include both acoustic interaction and mechanical contact forces in a rigorous way. Our work is both experimental and numerical. Experiments are carried out with spherical glass and copolymer particles and alumina disks, showing the influence of material parameters and shape. We furthermore present a numerical method to solve these particle dynamics in acoustofluidics, effectively including acoustic inter-particle forces and non-smooth mechanic contact laws.

Methods

In bulk acoustic wave technology, a piezoelectric transducer is used to transmit acoustic waves to the lab-on-a-chip device. If the frequency is well chosen a resonance of the water channel in the chip may be excited. This way it is possible to achieve high amplitude 1D acoustic standing waves experimentally. In this study we used one of our standard devices and frequencies around 1.5 MHz, which excited the λ mode.

In order to compute the complete trajectories of particles in acoustic fields numerically, the acoustic radiation force, Stokes drag and contact forces need to be known.

Fortunately the Stokes drag can readily be computed analytically for spherical particles or using COMSOL Multiphysics and does not pose a major problem.

Analytical solutions exist for the inter-particle forces only for spherical particles. Here Gröschl [2] presented a formula, combining both the acoustic interaction presented by Bjerknes (compressible, monopole based) and Nyborg (rigid, dipole based). The formula can easily be implemented, however, proves to be lacking in precision.

Silva et al [3]. presented a more general but also involved method. Using scattering theory they were able to find an expression for the radiation force, which is not limited by the inter-particle distance. As the calculation is not straight forward, they presented a number of simplifications for the most useful cases. Their method remains limited, as it can only be applied in combination with spherical particles and ignores multi-scattering events and no pearl chain modeling has been achieved so far.

The most general method to determine the acoustic radiation force is to use an FEM Software such as COMSOL Multiphysics. By solving the complete coupled acoustic and mechanical equations, this approach is not limited by the particle materials and shapes.

The contact laws can be implemented using different methods, an easy way is to include very stiff springs between the particles, enforcing the contacts. This has the disadvantages that for every spring defined in the problem a parameter fitting is required and the problem can become numerically stiff, furthermore it is difficult to guarantee positive contact distances.

We present a non-smooth method based on Moreau's time-stepping algorithm [4] and set-valued contact force. A drift correction step [5] is added at the end to enforce positive contact distances, this way it is possible to couple the algorithm with COMSOL Multiphysics. The algorithm can be expanded to include more general geometries, which will be done in consecutive work.

Results

The first results are shown in figure 1. Here we use our algorithm in multiple ways.

First we couple it with the analytical solutions presented by Silva et al. [3] and the Stokes drag approximation. This way the particle trajectories can be obtained numerically for a) glass and b) polystyrene particles. Comparing it to trajectories we obtained experimentally with Kisker glass and Kisker polystyrene particles c) d), it can be observed that line formation, experimentally and numerically, only occurs with the Kisker glass particles, but does not using the Kisker polystyrene particles. We show that this phenomenon actually is depending on the particle parameters. Moreover, we coupled the contact algorithm with a 2D COMSOL scattering simulation e), to show the robustness of the contact algorithm. In this case, using alumina particles, the patterning occurred also.

In order to show the versatility of our algorithm we also implemented the particle clump rotation, first performed experimentally by Schwarz et al. [6] for copolymer particles using amplitude modulation of two orthogonal standing waves, shown in f).

Conclusion

Using our non-smooth contact algorithm with both analytical and numerical calculations for the acoustic inter-particle forces, we were able for the first time to show the complete trajectories of many interacting particles in acoustic fields. As predicted theoretically by Silva et al. [3] we find the pearl chain formation, experimentally and numerically, to be depending on the particle parameters. Especially, particles having a positive contrast factor require a contrast in density in order to form the aforementioned lines.

Our numerical results are backed by experiments. Furthermore we show that the line formation does not only happen with spherical particles and prove that our contact algorithm is versatile and general, by using it to simulate particle clump rotation. The method is of great use in understanding and optimizing particle manipulation and particle assembly techniques.

References

- [1] WL Nyborg. *Ultrasound in Med. & Biol.* **15.2**, 93-99 (1989)
- [2] Gröschl Martin. *Acta Acustica united with Acustica* **84.3**, 432-447 (1998).
- [3] Glauber T. Silva and Henrik Bruus. *Phys. Rev. E* **90.6**, 063007 (2014).
- [4] Moreau J. *Unilateral Contact and dry friction in finite freedom dynamics*. Springer Vienna (1988).
- [5] Nützi Gabriel, Phd. Thesis. (unpublished) (2016).
- [6] Schwarz Thomas. Phd. Thesis. ETH No. 21572 (2013).

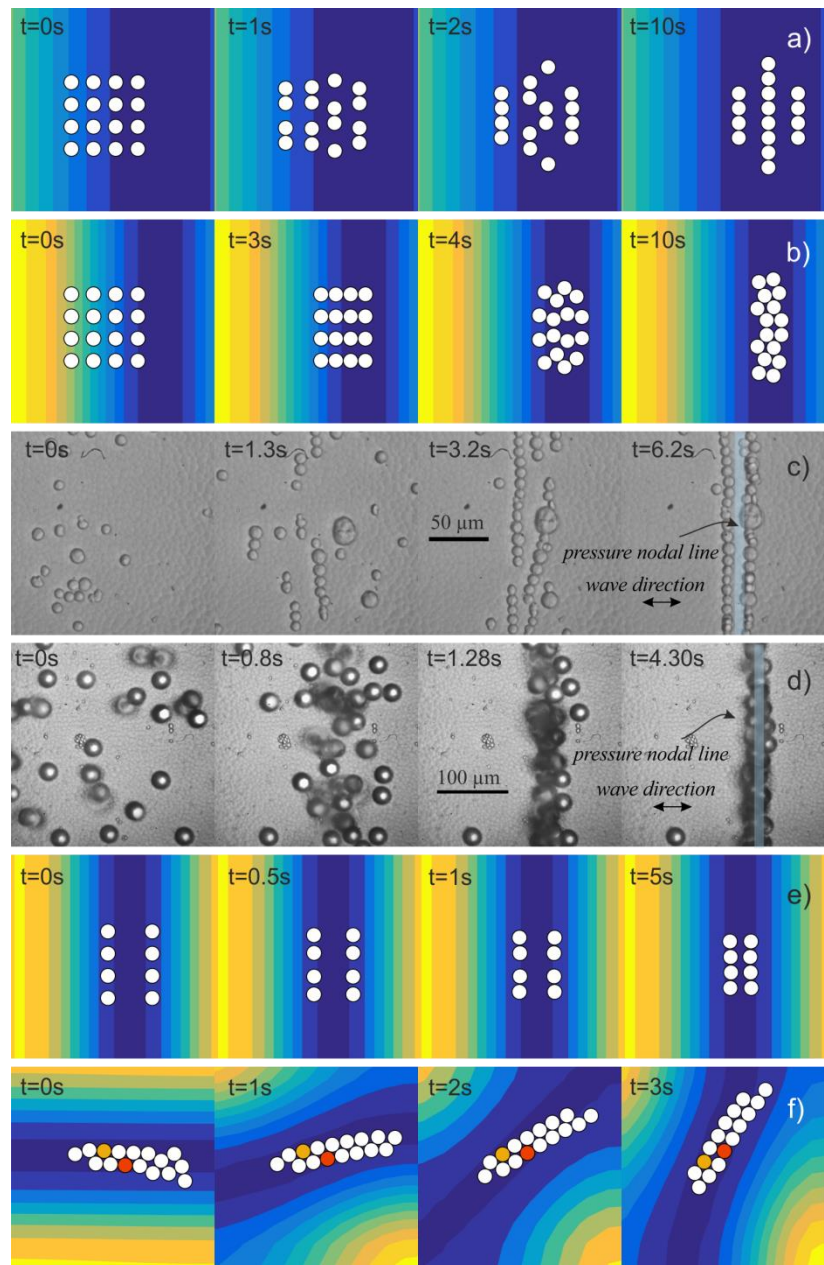


Figure 1 Simulations of glass particles a) and polystyrene particles b) of 10µm and 25µm diameter, respectively. Experiments with Kisker glass c) and polystyrene particles d) of 10µm and 25µm diameter, respectively. 2D Simulation using COMSOL, with 100 µm diameter particles e). Simulation of clump rotation for 100µm diameter copolymer particles f). Videos are available for a) b) c) d) e) and f).

The importance of travelling wave components in standing surface acoustic wave (SSAW) systems

Citsabehsan Devendran¹, Thomas Albrecht², Jason Brenker¹, Tuncay Alan¹ and Adrian Neild¹

¹Laboratory for Micro Systems, Department of Mechanical and Aerospace Engineering, Monash University, Clayton, Victoria 3800, Australia.

E-mail: saab.devendran@monash.edu, URL: www.labformicrosystems.com

²Department of Mechanical and Aerospace Engineering, Monash University, Clayton, Victoria 3800, Australia.

Introduction

The use of ultrasonic fields to manipulate particles, cells and droplets has become widespread in lab on a chip (LOC) systems. Two dominant actuation methods exist, namely bulk acoustic waves (BAW) or surface acoustic waves (SAW). The development of BAW actuated systems has been extensively studied leading to a strong link between the ultrasonic field and forces which can be generated. In this work, we examine this link for standing surface acoustic wave (SSAW) systems. We establish the boundary conditions required for accurate numerical modelling, describe the key resultant features of the pressure fields and the acoustic streaming fields which can be generated and finally we show that the relative importance of these two mechanisms is spatially dependant within a fluid chamber. The boundary condition used, models the SAW as two counter propagating travelling waves, rather than assuming a standing wave directly, this allows the accurate inclusion of the inherent energy decay as the SAW couples into the fluid chamber. As such, this previously neglected travelling wave component is a critical factor in the nature of the established streaming field, giving rise to strong streaming rolls at the channel walls, which we validate experimentally. These rolls result in the spatial variation in the dominant forces causing particle migration across the fluid domain.

Governing equation and acoustic forces

We employ perturbation theory as used in previous studies for BAW[1] systems, whereby the first-order solution are used to calculate the time-averaged second-order pressure field $\langle P_2 \rangle$ and steady-state acoustic streaming fields $\langle v_2 \rangle$. If we consider a particle of radius a much smaller than the acoustic wavelength λ (i.e. $a \ll \lambda$), the acoustic radiation forces (ARF) and acoustic streaming induced drag forces can be expressed analytically.[2] We propose a robust boundary condition that enables the omission of the piezoelectric domain with suitable velocity boundary conditions BC_{vel} , as described in Equation 1 which accommodate for the travelling wave components, the existence of some key features are identified.

Numerical Model

We use a finite element method to investigate the resultant pressure and streaming fields within a typical SSAW system. To obtain an appropriate velocity boundary condition for the bottom fluid boundary (i.e. the Lithium Niobate-fluid interface in Fig. 1 (a)), we differentiate the displacement profile of the x and y -components imposed by the SAW with time, which is similar to two counter-propagating travelling waves with the x -component shifted by a phase of $\pi/2$ and is given as follows

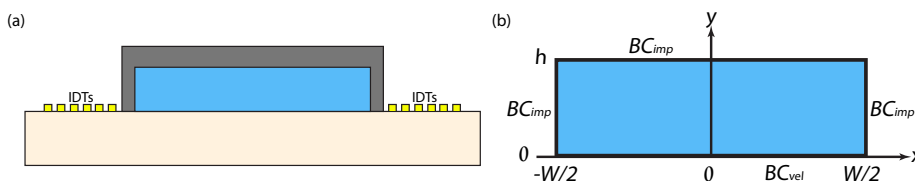


Figure 1: (a) Cross-sectional sketch of a typical SSAW driven acoustofluidic systems with PDMS bounded microchannels. (b) Sketch of the computational domain with a given width, W and height, h , along with acoustic impedance boundaries, BC_{imp} and velocity boundary condition, BC_{vel} .

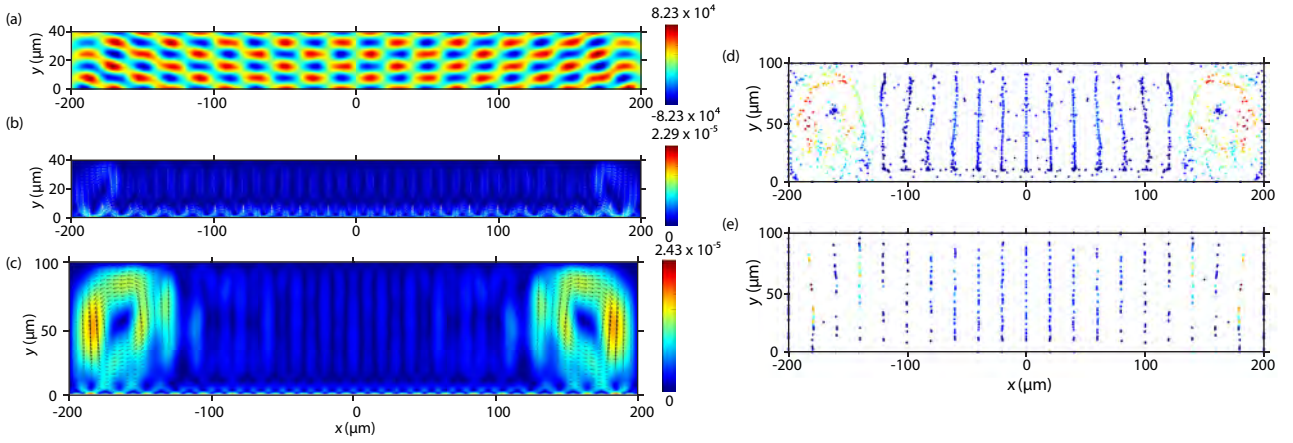


Figure 2: Surface plots of the resultant (a) first-order pressure fields, P_1 (b) streaming velocity field $\langle v_2 \rangle$ for a $h = 40 \mu\text{m}$ (i.e. $\lambda_{SAW} = 40 \mu\text{m}$) and (c) streaming velocity field $\langle v_2 \rangle$ for a $h = 100 \mu\text{m}$ (i.e. $2.5 \lambda_{SAW}$). Pressure surface plots have units of Pa and velocity surface plot have units of m/s. Velocity field vectors are depicted with white and black arrows respectively. (d) Acoustophoretic particle trajectory for given particle sizes (d) $2a = 0.5 \mu\text{m}$ (Particle velocity ranges from $0 \mu\text{m/s}$ (dark blue) to $17.3 \mu\text{m/s}$ (dark red)) and (e) $2a = 4 \mu\text{m}$ (Particle velocity ranges from $0 \mu\text{m/s}$ (dark blue) to $16.4 \mu\text{m/s}$ (dark red)) in a $W = 400 \mu\text{m}$ and $h = 100 \mu\text{m}$ channel.

$$\frac{u_x(x, t)}{e^{i\omega t}} = \zeta d_0 \omega \left[e^{-C_d(\frac{W}{2}-x)} e^{i[-k(\frac{W}{2}-x)]} + e^{-C_d(\frac{W}{2}+x)} e^{i[k(\frac{W}{2}-x)]} \right] \quad (1a)$$

$$\frac{u_y(x, t)}{e^{i\omega t}} = -d_0 \omega \left[e^{-C_d(\frac{W}{2}-x)} e^{i[-k(\frac{W}{2}-x)-\frac{\pi}{2}]} - e^{-C_d(\frac{W}{2}+x)} e^{i[k(\frac{W}{2}-x)-\frac{\pi}{2}]} \right] \quad (1b)$$

where, ω is the angular frequency of the propagating SAW $\omega = 2\pi f$, f is the excitation frequency, d_0 is the y -displacement amplitude of the SAW, $C_d = 2063 \text{ m}^{-1}$ is the SAW attenuation coefficient, $k = 2\pi/\lambda$ is the wavenumber and W is the width of the channel. $\zeta = A_x/A_y = 0.86$ is the proportion of the x -component's displacement amplitude A_x as compared to that of y -component. The channel walls and ceilings were imposed with an impedance boundary condition BC_{imp} . Herein, we investigate and demonstrate the effect of several geometrical (i.e. W and h), particle size dependency and channel wall impedance condition (i.e. water or poly-dimethylsiloxane (PDMS)) on the resultant time-averaged pressure and streaming fields. The numerical model was based on a $\lambda_{SAW} = 40 \mu\text{m}$ (i.e. $f_{SAW} = 99.85 \text{ MHz}$) and displacement amplitude $d_0 = 0.05 \text{ nm}$.

Results

Consideration of the inherent travelling wave component, specifically its effect on the acoustic streaming field results in relatively strong rolls near the channel walls (see Fig. 2 (b) and (c)) for typical SAW driven systems that span multiple λ_{SAW} . These streaming rolls are driven by the nature of SAW based acoustofluidics systems that observe an attenuation of the upwards propagating acoustic wave towards the channel ceiling at the Rayleigh angle coupled with acoustic lobing effects. In contrast to BAW systems, whereby, the bulk streaming field is driven by the boundary layer streaming (i.e. Schlichting streaming)[1], streaming fields within SAW systems are driven by the velocity gradient (i.e. Eckart streaming) resulting from the attenuation within the fluid. Thus, it is shown that as the height and width of the channel increases, the relative strength of the streaming roll increases as well. As a result, we demonstrate a size-dependent acoustophoretic particle migration of particles that consist of a width-wise spatial variation in dominant forcing mechanisms (see Fig. 2 (d) and (e)). These numerical results and predictions have been validated experimentally to show the key streaming features observed in typical SSAW based microfluidic systems.

Conclusion

We report a numerical approach using finite element analysis via COMSOL Multiphysics to accurately predict the acoustophoretic motion of suspended particles within a microchannel. It is demonstrated that the consideration of the travelling wave component within typical SSAW systems is critical to reveal important bulk flow features. Furthermore, consideration of the channel height and width is crucial to establish particle migration trajectory.

References

- [1] P. B. Muller, R. Barnkob, M.J.H. Jensen and H. Bruus. Lab on a Chip **12**, 4617-4627 (2012).
- [2] M. Settnes and H. Bruus Physical Review E **85**, 016327 (2012).



Imaging acoustic radiation forces and streaming with an optical trap

Andreas Lamprecht¹, Stefan Lakaemper¹, Iwan A.T. Schaap², and Jurg Dual¹

¹Institute for Mechanical Systems, ETH Zurich, 8092 Zurich, Switzerland.
E-mail: lamprecht@imes.mavt.ethz.ch, URL: <http://www.imes.ethz.ch>

²Institute of Biological Chemistry, Biophysics and Bioengineering, Heriot-Watt University, Edinburgh EH14 4AS, United Kingdom.

Introduction

A well formulated theoretical background and numerical simulations exists for the fundamental understanding of acoustofluidics inside micro fluidic channels. However, in lab-on-a-chip devices several environmental influences on the acoustic boundary conditions are present, which are so far inaccessible to be included in the numerical models: a.) They are difficult to quantify b.) The necessarily idealized models would get too complex. Therefore we use an optical trap [1,2] as a force sensor for acoustofluidic particle manipulation to close this characterization gap between ideal simulated and real fabricated devices.

Acoustic radiation force and streaming

The motion of particles within an acoustic separation device is driven by acoustic radiation and Stokes drag forces induced by acoustic streaming. The interacting radiation force on a particle was derived by Gorkov for a compressible particle in a non-viscous fluid [3]. Gorkov defined the time averaged acoustic radiation force as a potential force $\mathbf{F}_{ar} = -\nabla U$, where the acoustic potential U is defined as

$$U = 2\pi r_s^3 \rho_f \left(\frac{1}{3} \frac{\langle p^2 \rangle}{\rho_f^2 c_f^2} f_1 - \frac{1}{2} \langle \|\mathbf{u}\|^2 \rangle f_2 \right) \quad (1)$$

where r_s is the particle radius, p is the acoustic pressure, \mathbf{u} is the velocity with $\|\mathbf{u}\|^2 = u_x^2 + u_y^2 + u_z^2$, c is the speed of sound, and ρ is the density. The index “ f ” corresponds to the fluid and “ s ” to the particle specific properties. The expression $\langle \cdot \rangle$ indicates the time averaging over one wave period $T = \frac{2\pi}{\omega}$ with circular frequency ω . The compressibility factor f_1 and the density factor f_2 , are given as

$$f_1 = 1 - \frac{\rho_f c_f^2}{\rho_s c_s^2} \quad \text{and} \quad f_2 = \frac{2(\rho_s - \rho_f)}{2\rho_s + \rho_f} \quad (2)$$

The time harmonic acoustic field inside an acoustofluidic device initiates a continuous non-zero flow [4]. This time averaged nonlinear effect is called acoustic streaming and is formed in the acoustic boundary layer δ at the solid-liquid interfaces. The resultant force on a particle can be assumed as the viscous Stokes drag force, which is defined as

$$\mathbf{F}_{st} = 6\pi r_s \eta_f (\mathbf{u}_{st} - \mathbf{u}_s) \quad (3)$$

where η_f is the dynamic fluid viscosity and \mathbf{u}_{st} and \mathbf{u}_s are acoustic streaming and particle velocity, respectively. Muller *et al.* [5] have described the particle behavior under the action of radiation forces and streaming theoretically and experimentally for a rectangular shaped fluid channel.

Experimental setup

The concept of an optical trap provides the possibility to do direct and position dependent 3D acoustic force measurements on dielectric spheres [1,2]. In the experiment a device with a transparent fluid channel was used (Fig. 1), where a 120 μm mono crystalline silicon layer was bonded between a 1 mm and a 140 μm glass plate. The width of the fluid channel was 4 mm and its length was 76 mm. The orientation of the piezoelectric transducer (Ferropem, Pz26, $l \times w \times h = 8 \times 2 \times 0.5$ mm, Kvistgaard, Denmark) was parallel to the channel walls at the center of the channel length and it was glued by

conductive epoxy on the 140 μm cover-glass plate. In the experiments monodisperse silica beads (Microparticles GmbH, Berlin, Germany) of 2.06 μm and 4.39 μm diameter ($d = 2 \times r_s$) were diluted with water in the fluid channel at very low concentration (about 8 particles/ mm^3). The single-beam gradient trap of 786 nm wavelength was used to trap one single particle. The calibration of the linear trap stiffness, which defines the relation between the observed particle displacement and the total external force, for small displacements at 80 mW laser power was derived by observing the Brownian motion of the bead (equipartition theorem) [6]. Knowing the stiffness of the trap we subsequently monitored the 3D displacement of the particle from the trap center, due to acoustic radiation force and streaming, in dependence of its position in the channel.

Results

According to Eq. 1 and 3 the acoustic radiation force is proportional to the volume (r_s^3) of the particle, and the Stokes drag is proportional to the radius (r_s) of the particle. This property can be used to reach a separation between the two acoustic forces [2,4], \mathbf{F}_{ar} and \mathbf{F}_{st} . The measurement range inside one specific device has to be measured twice with two different sized particles. The force scaling laws proves all the necessary information and a comparison between the two measured total force fields ($\mathbf{F}_{ar} + \mathbf{F}_{st}$) leads to the two different force components. Fig. 1 shows the measured \mathbf{F}_{ar} in wave propagation direction on the 2.06 μm particle and acoustic streaming vectors for the upper half of the cross section of the channel. The spatial distribution of \mathbf{F}_{ar} and \mathbf{F}_{st} can be seen and it shows the complexity of such force fields inside acoustofluidic devices. The advantage here is that this method does not need specific information about global acoustic properties, e.g. acoustic energy density, thermal or viscous boundary layer thickness.

Conclusion

The 3D force data gave a detailed input to the global and local acoustic force and streaming field in function of frequency, particle size and channel dimensions. The measurement technique has a high force resolution of 12 fN and up to 700 single measurement points are realized, due to the high automation degree of the setup. The result shows a so far inaccessible picture of the 3D acoustic force and streaming field, which is spatially resolved for the specific 3D measurement region inside the acoustofluidic channel. This measurement technique can be further expanded to various fields in acoustofluidics, like the characterization of surface acoustic wave devices, transient force formation, non Newtonian fluids and interactions of a particle and a nearby wall.

References

- [1] S. Lakaemper, A. Lamprecht, I. A. T. Schaap, and J. Dual, Lab Chip, **15**, 290-300 (2015).
- [2] A. Lamprecht, S. Lakaemper, T. Baasch, I. A. T. Schaap, and J. Dual, Lab Chip (2016), DOI: 10.1039/c6lc00546b.
- [3] L. P. Gorkov, Solv. Phys. Dokl., **6**, 773-775 (1962).
- [4] R. Barnkob, P. Augustsson, T. Laurell, and H. Bruus, Phys. Rev. E, **86**, 056307 (2012).
- [5] B. Muller *et. al*, Phys. Rev. E, **88**, 023006 (2013).
- [6] K. Svoboda, and S. M. Block, Annu. Rev. Biophys. Biomol. Struct., **23**, 247-285 (1994).

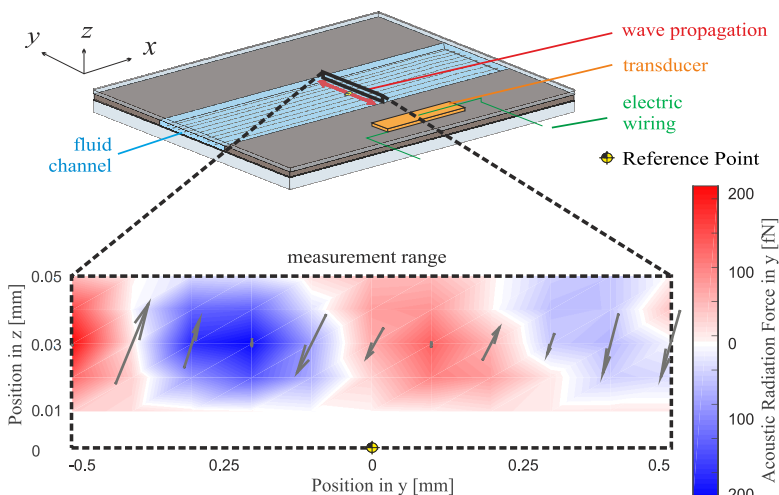


Figure 1: Schematic drawing of the acoustofluidic device and results within the chosen measurement range ($x = 0$, y : -0.5 to 0.5 mm, z : 0.01 to 0.05 mm, where $y, z = 0$ defines the center of the channel). Separation of the acoustic radiation force \mathbf{F}_{ar} on a 2.06 μm particle in y -direction (color bar) and Stokes drag force \mathbf{F}_{st} due to streaming (gray arrows, average 3D data between $z = 0.02$ to 0.04 mm at constant y , projection on yz -plane) by the optical trapping method. The longest arrow belongs to the maximum streaming velocity of 4.12 $\frac{\mu\text{m}}{\text{s}}$. An analysis of the acoustic radiation force field (-218 to 212 fN) shows an alternating pattern of positive and negative force in the wave propagation direction y at 3.82 MHz and 10 V_{pp} excitation amplitude. The streaming vortices have their center about 0.03 mm above the center plane, which is in agreement with the theory [4].



Numerical design and experimental evaluation of an acoustic separator for water treatment

H.J. Cappon^{1,2} and K. J. Keesman^{2,3}

¹HZ University of Applied Sciences, Vlissingen, the Netherlands
E-mail: hans.cappon@hz.nl, URL: <http://www.hz.nl/en>

²Dept. of Biobased Chemistry and Technology, Wageningen University, the Netherlands

³Wetsus Centre of Excellence of Sustainable Water Technology, Leeuwarden, the Netherlands

Introduction

Acoustic separation devices are able to separate water and particulate matter by means of ultrasound. They are especially interesting for recovery of particulate matter from suspensions without the use of additional chemicals and internals. Unfortunately, currently developed devices have a substantial energy demand, which needs improvement if large scale applications are pursued. The aim of the study was to demonstrate a multi-criteria numerical optimization approach on a basic design of an ultrasonic standing wave separator [1] with respect to separation efficiency, throughput and energy consumption. The numerical design was then built and evaluated, and the operational settings were optimized experimentally.

Methods

The numerical study involved over 350 finite element model simulations in which acoustics, flow characteristics, particle retention and energy demand were evaluated, while varying the geometrical properties of a basic separator design. The resulting device was then built and tested experimentally while varying the flow rate and determining the separation efficiency through turbidity measurements.

As the first part of the study mainly studied the geometrical design properties, a subsequent improvement of the efficiency seemed possible by optimizing the operational parameters. Three operational factors, namely the flow rate, on/off switching interval (between backwash and filtering mode) and applied electrical power, were investigated. A three level full-factorial design of experiments (DOE) was applied to evaluate the separation performance with insoluble starch. Turbidity measurements were shown to correlate well to particle concentration, so turbidity measurements of the stock suspension, the filtrate and the concentrate were used to determine the separation efficiency. The results were processed to formulate an algebraic model which described the effect of the three factors on the filtration efficiency. For this, the final prediction error (FPE) function [2] was used to determine the model which most accurately reflects the effect of each of the three factors. The resulting model, describing multiple response surfaces, was used to calculate the optimal settings for each factor to either obtain the most clarified filtrate or the most dense concentrate suspension. The operational settings found using the algebraic models were then tested in validation experiments.

Results

The methodology, using the design of experiments approach, showed that it was possible to obtain a theoretical separation efficiency of 100% with a laminar stable flow rate of 5 mL/s with 10 μm particles and optimized acoustic pressure and power (30 W). The resulting separator had inner dimensions of 70 mm length, 20 mm width and 28.5 mm height using two transducers perpendicular to the direction of flow and three parallel flow lanes with 9.5 mm height each and operated near 1.95 MHz. In the experimental evaluations of the prototype the input power was limited to 10 W only, due to amplifier constraints, resulting in a separation efficiency of suspended starch (1 - 100 μm) of 76% at a flow rate of 2 mL/s (Fig. 1).

The results of the experimental optimization showed that further improvement of efficiency was certainly possible. Moreover, the optimal operational settings for filtrate and concentrate were different. The response surfaces suggested that the optimal filtrate settings were found with a flow rate of 0.5 mL/s, a power setting of 12 W and a switching interval of 11 minutes and 40 seconds (with a backwash time of 20 seconds). This operational setting was already evaluated while constructing the response surface model. With this setting 350 mg of starch were processed per filter run, resulting in 17% remaining in the filtrate (83% clearance).

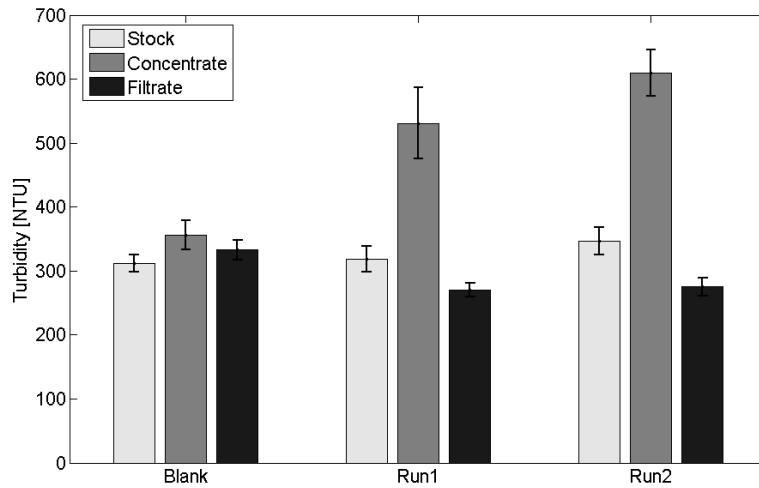


Figure 1: Experimental evaluation measuring particle concentration as turbidity at a flow rate of 2 mL/s. The error bars represent the 95% confidence interval.

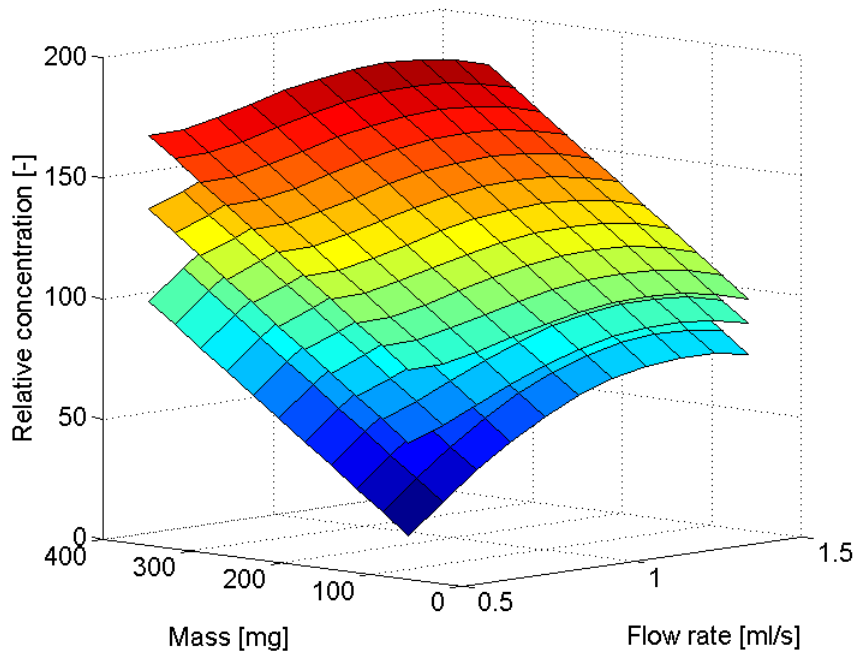


Figure 2: Best fit response surface models of concentrate turbidity versus flow rate and processed starch mass. The three stacked surfaces represent the influence of applied power of 3, 8 and 12 W; the higher the power the higher the concentrate turbidity.

For harvesting the largest amount of starch particles (in the tested range) the response surface (Fig. 2) indicated an optimal setting using a flow rate of 1.37 mL/s, a power setting of 12 W and a switching interval of 4 minutes and 15 seconds (with a backwash time of 20 seconds), also processing 350 mg of starch. Experimentally this resulted in an even higher concentration of starch particles (220%) than calculated via the response model (196%).

Conclusions and recommendations

The combination of a numerical and experimental approach to the design, evaluation and optimization of an ultrasonic particle filter showed that high filtration efficiencies could be obtained, concentrating up to 220%. Results showed that in fact two optimal operational settings were found: one for obtaining clarified water (filtrate) and the other for collecting suspended (starch) particles. Therefore, the aim of the separation is important for choosing the optimal settings.

The current setup was mainly limited by the power settings applied. Further research should focus on power settings beyond 12 W, which will also allow higher flow rates and efficiencies. A disadvantage of the starch used is the large range of particle sizes, between 1 and 100 μm . Therefore, also more uniformly sized suspended particles should be tested to verify the consistency of the procedure.

References

- [1] H.J. Cappon and K.J. Keesman *Proc IEEE UFFC IUS*, Prague 21-25 July 2013, pp 299-302.
- [2] K.J. Keesman. *System Identification: An Introduction*, Springer Verlag, London, 2011.

Acoustic nanofluidics: a novel platform for actuation and manipulation of nano-confined fluids and particles

Morteza Miansari¹, James Friend¹

¹Department of Mechanical and Aerospace Engineering, University of California-San Diego, San Diego, CA 92093, USA

E-mail: mmiansarigavzan@eng.ucsd.edu, miansari.83m@gmail.com, URL: <http://www.fysik.dtu.dk/Acoustofluidics2016>

Introduction

Controlled nanoscale manipulation of fluids and particle suspensions would serve to advance many fields—from energy conversion [1] and molecular biology [2] to water purification [3]—yet remains exceptionally difficult due to the dominance of surface and viscous forces. Though electrohydraulics [4], osmosis [5], and other such approaches have been used in nanofluidics, pressure-driven flow is most commonly used, despite the challenges of generating sufficient pressure to overcome fluidic resistance and capillary pressure in nanofluidics [6]. Recently, acoustic waves have been used in many microfluidics devices, overcoming such problems at those larger scales [7, 8]. Curiously, the use of acoustic waves in manipulating fluids and particles at the nanoscale remains unexplored. Here we show that 20 MHz surface acoustic waves (SAW) can effectively manipulate fluids, fluid droplets, and particles in 50–250 nm tall nanoslit channels. Such channels were formed in lithium niobate from a new room-temperature bonding process, and show the ability to increase the filling rate in the hydrophilic channel by 2–5 times with application of SAW in the same direction as the capillary filling direction, modeling it with a combination of the Washburn model of capillary filling and an approximate model for the SAW-driven bulk fluid drift.

As shown in Fig. 1, when applied in opposition to capillary filling, the SAW uniquely drains the channel, overcoming 1 MPa of capillary pressure. In drainage, we find a transition from simple to complex meniscus motion in nanoslit channels depending upon a ratio between the width of the channel and the wavelength of the SAW, demonstrating the unique absence of sound in the fluid itself due to the confined geometry. Furthermore, we demonstrate the ability to manipulate ~ 10 fl droplets of deionized

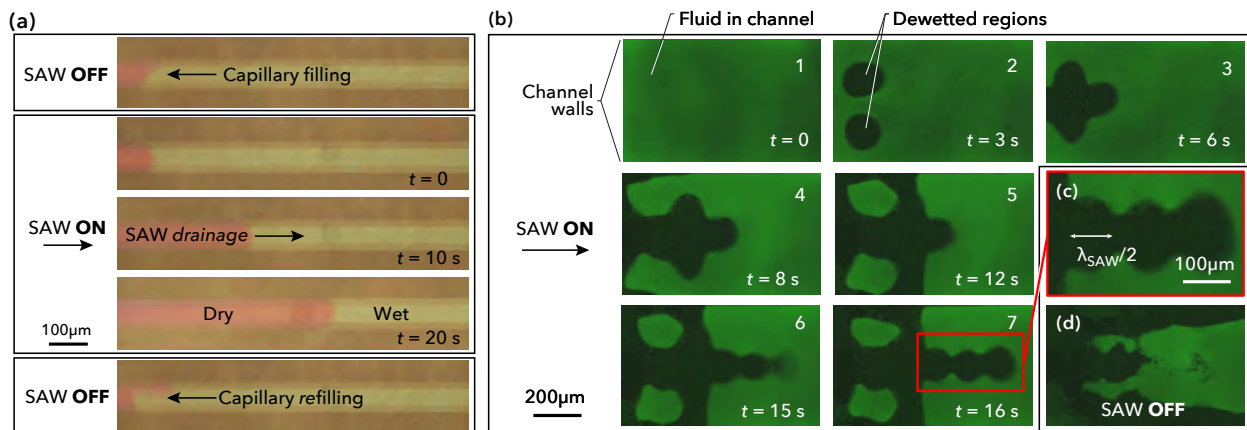


Figure 1: SAW can be used in *opposition* to the capillary filling in order to drain the fluid from a ~ 100 -nm nanoslit channel. With (a) channels of width $w = 60 \mu\text{m} < \lambda_{\text{SAW}}/2 = 100 \mu\text{m}$, the 1 W SAW-driven drainage is straightforward and complete. Note the capillary filling right-to-left of the dry (pink) channel while the SAW is off. This meniscus propagation is arrested upon turning on the SAW, driving the meniscus from left to right and in the direction of the SAW. When the SAW is turned off again, the channel refills with the meniscus propagating right-to-left. When the channel width $w = 400 \mu\text{m} > \lambda_{\text{SAW}}/2$, (b) the drainage is far more complex. Dewetted regions form in the channel, each (c) possessing a scale of $\sim \lambda_{\text{SAW}}/2$ and located laterally at positions $n\lambda_{\text{SAW}}/2$ (where $n = 1, 2, \dots$) from the channel walls (at the top and bottom of each image). These dewetted regions merge in a complex manner to progressively drain the channel left-to-right in the same direction as the SAW and against right-to-left capillary flow. Shutting the SAW off results in (d) the drained regions refilling under capillary action.

water between wide and narrow portions of the nanoslit by using SAW and the capillary pressure in opposition, indicating a possible means to manipulate and combine $f\ell$ fluid volumes. Finally, we show the ability to drive the entire volume of $10\ \mu\ell$ -order fluid droplet samples through the nanoslit to perform size exclusion separation: particles and molecules of the sample smaller than the nanoslit height are passed through the nanoslit and are retained at the nanoslit exit, meanwhile rejecting larger material at the entrance. We anticipate these results to represent fundamental tools to be used in an array of nanofluidic devices to come, overcoming the myriad and significant difficulties in fluid manipulation at such scales. For example, digital femtoliter fluidics for extremely small samples of analytes, size exclusion chromatography including a means to deagglomerate the molecules in the test sample, and continuous flow nanofluidics devices without a need for external pumping systems.

Conclusion

The first acoustic nanofluidics device was fabricated through a new but remarkably straightforward, room-temperature LN wafer bonding technique. The device produced non-laminar, irregular flow in $\sim 100\ \text{nm}$ nanoslits at exceptionally low Reynolds numbers ($\sim 10^{-5}$) via acoustic streaming induced by 20 MHz SAW, to our knowledge the first time such flow has been reported. The fluid flow within the hydrophilic nanoslit can be instantly controlled and the fluid can be drained from the channel using SAW applied in opposition to the capillary filling direction, overcoming the large capillary pressure formed within the nanochannel. The SAW furthermore was used to transport individual $\sim 10\ f\ell$ order droplets in concert with capillary forces in nanoslit channels of varying width.

A model taking into account the SAW-driven drift flow and the Washburn model of the capillary filling is proposed. Furthermore, the filling rate was found to increase with increases in the channel's height, SAW intensity, and the surface tension to viscosity ratio. Finally, rapid size separation of nanoparticles and large molecules was achieved by driving the liquid sample through the nanoslit channel using SAW.

References

- [1] S. Moghaddam, E. Pengwang, Y. B. Jiang, A. R. Garcia, D. J. Burnett, C. J. Brinker, R. I. Masel, and M. A. Shannon. *Nature Nanotechnology* **5**, 230-236 (2010).
- [2] E. C. Yusko, J. M. Johnson, S. Majd, P. Prangkio, R. C. Rollings, J. Li, J. Yang, and M. Mayer. *Nature Nano* **6**, 253-260 (2011).
- [3] D. K. Kim, C. Duan, Y. F. Chen, and A. Majumdar. *Microfluidics and nanofluidics* **9**, 1215-1224 (2010).
- [4] Y. Xue, J. Markmann, H. Duan, J. Weissmuller, and P. Huber. *Nature Communications* **5**, 4237 (2014).
- [5] L. Bocquet. *Nature Nanotechnology* **9**, 249-251 (2014).
- [6] J. O. Tegenfeldt, C. Prinz, H. Cao, R. L. Huang, R. H. Austin, S. Y. Chou, E. C. Cox, and J. C. Sturm. *Analytical and bioanalytical chemistry* **378**, 1678-1692 (2004).
- [7] J. R. Friend and L. Y. Yeo. *Reviews of Modern Physics* **83**, 647 (2011).
- [8] L. Y. Yeo and J. R. Friend. *Annual Review of Fluid Mechanics* **46**, 379-406 (2014).

Fast dimensional transition of Fe_3O_4 nanoparticles self-assembly through external magnetic force and surface acoustic wave

An Huang¹, Morteza Miansari², and James R. Friend²

¹Department of Materials Science and Engineering, University of California, San Diego, La Jolla, USA
E-mail: anh081@eng.ucsd.edu, URL: <http://www.fysik.dtu.dk/Acoustofluidics2016>

²Department of Mechanical and Aerospace Engineering, University of California, San Diego, La Jolla, USA

Introduction

There is a need in development of fast and low-cost method to form two-dimensional (2-D) films composed of magnetite (Fe_3O_4) nanoparticles (NP) due to its wide applicabilities, including magnetic recording device, sensor, biochip, targeted drug delivery, electronic devices, photonic crystals, and high-density data storage [1]. While soft or hard templates methods, lithography, spin coating, electrophoretic deposition, and laser interference lithography are useful for the 2-D Fe_3O_4 film formation, the processing complexity and high manufacturing cost make them unsuitable outside of a relatively small market niche [2-4]. Chip-based fluidic actuators using surface acoustic wave (SAW) have become popular among microfluidic practitioners who continue to explore new applications in acoustofluidic integration due to its great potential on controlling a small amount of fluid with the acoustic energy. And thus, it has been widely applied onto the drop handling, cell manipulation, and particle collection in microfluidics devices, offering extraordinary power density in a fingernail-sized device [5].

Here, we present a rapid and affordable technique to trigger rigid 2-D self-assembled films of magnetite (Fe_3O_4) NP. We have experimentally demonstrated that the round-like 2-D magnetite films formed with sufficient surface acoustic wave power and external magnetic force. A rapid dimensional transition happens, from 1-D chain to 2-D film of Fe_3O_4 NP, through external magnetic force (0.25-0.4 T) and surface acoustic wave (up to 115 mW). The scaling theory coupled with the experimental results was conducted to analyze the forces associated with the system to understand the mechanism of chain or film assembly processes.

Experimental method

In this study, a 100 MHz SAW device with travelling wave and 28 pairs Al/Cr bilayer interdigital transducer (IDT) on the 127.68° -Y rotated cut and X-propagating single-crystal lithium niobate (LN) substrate was fabricated. The power is applied over a wide range up to 115 mW. A $3 \mu\text{l}$ deionized water drop mixed with $0.1 \mu\text{l}$ Fe_3O_4 NP in toluene solution was placed on LN. The external magnetic fields were applied through magnets with different thickness but a fixed diameter of $3/8''$, producing magnetic field strengths from 0.2 to 0.4 Tesla. The motion of the droplet was recorded with

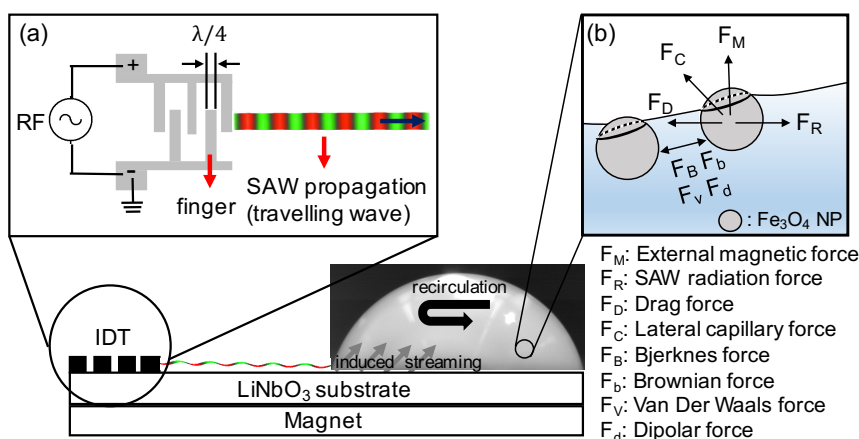


Figure 1: Schematic illustration of the experimental setup. A $3 \mu\text{l}$ DI water droplet with $0.1 \mu\text{l}$ Fe_3O_4 NP in toluene is placed on the LN surface. The enlarged plot (a) shows the SAW device with a resonant frequency of 100 MHz with λ of $40 \mu\text{m}$. The finger width and spacing is $10 \mu\text{m}$. The enlarged plot (b) shows the direction of the forces experienced by the Fe_3O_4 NP, including the external magnetic force, dipolar force, Brownian force, Van Der Waals force, lateral capillary force, SAW radiation force, drag force, and Bjerknes force.

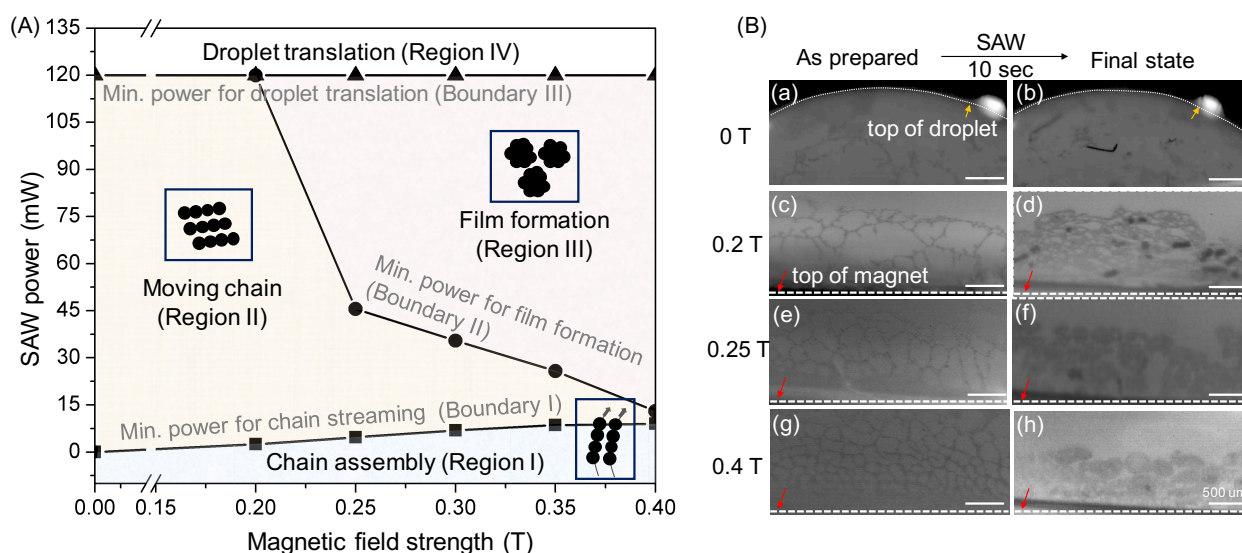


Figure 2: (A) Experimental phase diagram depicting the regions of chain assembly, chain movement, and film formation as a function of SAW power and magnetic field strength. Above 120 mW, the $3\mu\text{l}$ droplet translates across the LN surface, so represents the upper limit in applied power for our experiments. (B) The micro images obtained from high speed camera: (a), (c), (e), and (g) are the as-prepared samples under 0, 0.2, 0.25, and 0.4 T external magnetic field forces, respectively; (b), (d), (f), and (h) are the images obtained after 10 second SAW radiation under 0, 0.2, 0.25, and 0.4 T external magnetic field forces, respectively.

a high-speed camera. Images were analyzed through Matlab and ImageJ software.

Results and Discussion

The phase map in Figure 1(A) illustrates how the SAW power associates with the applied magnetic field strengths and leads to the Fe_3O_4 NP 1-D chain assembly and 2-D film formation on a $3\mu\text{l}$ sessile drop. The boundary I ($B \propto P_{SAW}$) represents the minimum SAW power required to detach the 1-D Fe_3O_4 chains from different external magnetic field strengths. While the boundary II ($B^{-1} \propto P_{SAW}$) describes the minimum SAW power needed to trigger the 2-D Fe_3O_4 NP films formation. The magnetic field strength shows inverse proportional to the SAW power at this boundary, which might be due to the local fields induced from the neighboring Fe_3O_4 NP is stronger with stronger magnets and its direction is the same as the attractive Bjerknnes force among the Fe_3O_4 NP [6]. Boundary III, shows the maximum SAW power above when the translation of the whole droplet starts [7].

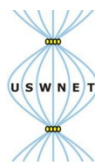
The representative microimages of the as-prepared and final states obtained under different external magnetic forces are shown in the Figure 1(B). A denser honey-comb like structure is formed with a stronger magnetic field at the as-prepared state [6]. While the round-like 2-D film, with average radius of 10^{-3} m, is formed when the magnetic field force is ≥ 0.25 T and after expose to 10 seconds of 115 mW SAW power. To understand the mechanism of the dimensional transition of our system, scaling theory was performed. It is found that the external magnetic force is the dominant force for the 1-D chain assembly, while the attractive Bjerknnes force among the Fe_3O_4 NP is the main force of the 2-D film assembly.

Conclusion

The rapid dimensional transition of self-assembled 1-D chain to 2-D film of Fe_3O_4 NP on a $3\mu\text{l}$ droplet through SAW and external magnetic force is shown experimentally. The scaling theory coupled with the experimental data on explaining the mechanism of the dimensional transition is discussed.

References

- [1] Y. Shaoo, M. Cheon, S. Wang, H. Lup, E. Furlani, and P. Prasad. The Journal of Physical Chemistry B **11**, 3380-3383 (2004).
- [2] M. Tanase, D. Silevitch, A. Hultgren, L. Bauer, P. Searson, G. Meyer, and D. Reich. Journal of applied physics **10**, 8549-8551(2002).
- [3] H. Niu, and Q. Chen, and H. Zhu, Y. Lin, and X. Zhang. Journal of Materials Chemistry **13**, 1803-1805 (2003).
- [4] J. Wang, Q. Chen, C. Zeng, and B. Hou. Advanced Materials **16**, 137-140 (2004).
- [5] J. Friend and Y. Lesile. Reviews of Modern Physics **83**, 647-704 (2011).
- [6] S. Singamaneni, and V. Bliznyuk, C. Binek, and E. Tsymbal. Journal of Materials Chemistry **21**, 16819-16845 (2011).
- [7] M. Tan, J. Friend, and Leslie Yeo. Lab on a Chip **7**, 618-625 (2007).



Ultrasound enhanced Process Analytical Technology (USe PAT) exploited in a model crystallization process

Stefan Radel^{1,2}, Stefan Tauber¹, Karin Wieland¹, Hamid Rasoulimehrabani¹ and Bernhard Lendl¹

¹Institute of Chemical Technologies and Analytics, Vienna University of Technology, Vienna, Austria
E-mail: stefan.radel@tuwien.ac.at

²Institute of Applied Physics, Vienna University of Technology, Vienna, Austria

Introduction

Within an ultrasonic standing wave (USW), so-called radiation forces are exerted on suspended particles directing them towards the pressure nodes, i.e. regions of vanishing sound pressure of the ultrasonic field. This technique is referred to as ultrasonic particle separation.

In case of monitoring reacting suspensions Raman spectroscopy holds great promise due to possible in-line measurement strategies. For instance crystallization processes, where real-time data of solute concentration and various qualities of the crystals are of interest. Furthermore, based on the Raman spectrum, polymorphs of a given substance during crystallization processes are potentially identified. This turns out to be difficult as Raman photons from the solid matter need to be discriminated from Raman signals originating from the pure liquid phase. This problem is of special relevance in case of low concentration of suspended particles.

Results

The combination of A USW for particle manipulation and Raman spectroscopy might be an interesting approach to increase selectivity and sensitivity of Raman measurements. This is because with the ultrasonic wave the crystals can be concentrated in the Raman measurement spot, thus allow to selectively and independently measuring the solid phase without strong influences from the liquid phase. In addition to that, an increase in sensitivity may be expected due to the local enrichment of the particles by means of the agglomeration by the USW resulting in an enhanced sensitivity of on-set detection of crystallization.

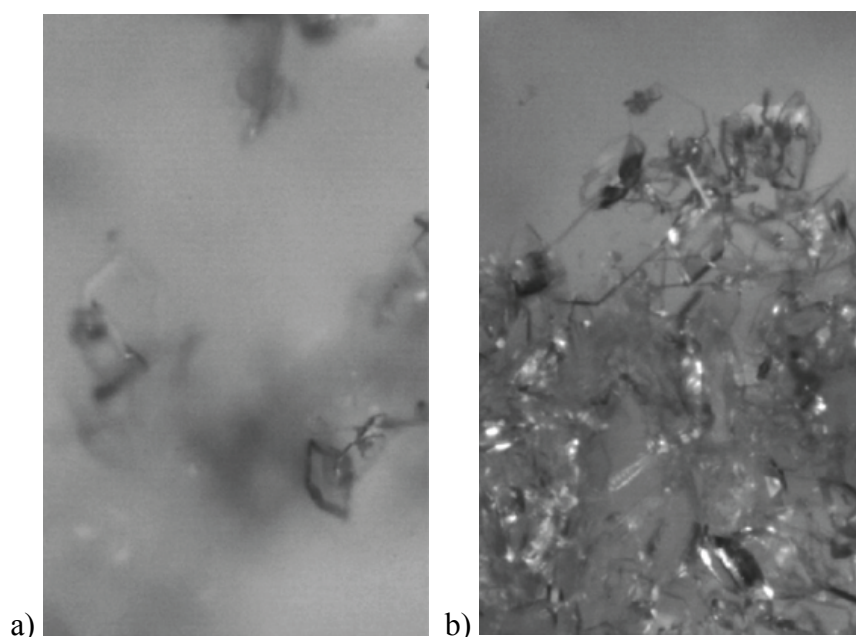


Figure 1: The USW is capable of concentrating particles at certain regions called the pressure nodes (for rigid, dense corpuscles as crystals). This leads to an increase spatial concentration and thus improves the SNR of the measurement. Pictures show crystals while forming in the experimental set-up during a decrease of temperature: (a) freely distributed crystals, (b) agglomerated by the USW.

We have already investigated the basic applicability when taking Raman spectra of theophylline crystals agglomerated by an ultrasonic standing wave in the focus of a confocal Raman microscope [1]. In this work we have gone on step further. The experiments were conducted with an in-line Raman spectroscopy probe

(Kaiser optical systems) in a bench-top crystallization set-up. The crystallization took place in a beaker equipped with a cooling jacket thus being temperature controlled. The model used was paracetamol in a 20% water-ETOH mixture. The ultrasonic field was emitted by a transducer positioned opposite of the probe tip, hence the USW was forming planes perpendicular to the probe axis.

Fig. 1 shows freely dispersed crystals while forming in the beaker compared to the agglomerate of crystals concentrated by the ultrasonic field. Clearly the advantages of applying an USW are visible: while the left picture shows a small number of crystals in focus, the picture at the right hand side shows the agglomerate of many crystals tightly packed. This is advantageous in two ways for the measurement of an Raman spectrum. On one hand Raman scattering is a rare process, hence the higher spatial concentration is leading to a stronger signal. On the other hand, this means at the same time that less Raman photons are scattered from molecules of the liquid. This can be concluded from the Raman spectra shown in Fig. 2. The measurements taken, when the USW was agglomerating the crystals and when the probe tip was put into the sediment crystals at the bottom of the beaker resemble each other strongly both in regard to the spectra and in respect to the Raman intensity (which is influenced by the spatial concentration of the analyte).

As predicted as well the influence of the carrier liquid is smaller. The inset shows the left part of the Raman spectrum, which is mainly influenced by the liquid present (water and ethanol). The graph stems from measurements taken when no crystals were yet formed (black) and when the crystals were freely dispersed (grey). In the latter case the influence of the liquid is decreased, but by far not to the extent when crystals were sedimented or agglomerated by the USW.

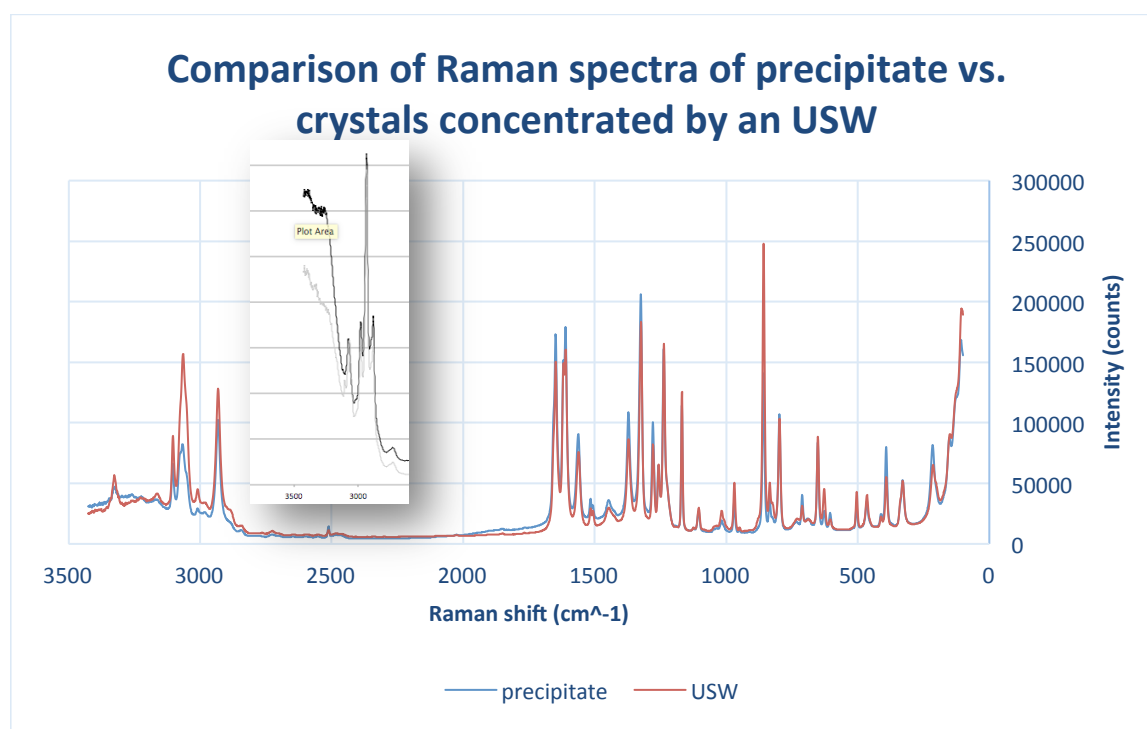


Figure 2: Raman spectra of an agglomerate of crystals in front of the probe tip compared to a measurement, where the probe was put into the crystal sediment at the bottom of the beaker. Inset shows the left part of the spectrum when pure solution without crystals were measured (black) and when crystals were measured freely distributed (grey).

Conclusion

It was shown, that in a crystallization suspension the crystals when agglomerated by the ultrasound are detected with much higher intensity than when freely dispersed at the same particle concentration. Moreover the Raman spectrum from the depleted region strongly resembles the result when a pure solution is measured. These results are promising in respect to the application of the Use PAT in industrial environments where in-line Raman spectroscopy is an increasingly use tool.

References

[1] S. Radel, J. Schnöller, A. Dominguez, B. Lendl, M. Gröschl, and E. Benes. *Elektrotechnik & Informationstechnik* **125**, 82–85 (2008). DOI 10.1007/s00502-008-0515-2

An examination of the limits of microparticle collection over a broad frequency range

Prashant Agrawal^{1,2,3}, Prasanna S. Gandhi³, Adrian Neild¹

¹Laboratory for Micro Systems, Department of Mechanical and Aerospace Engineering, Monash University, Clayton, Australia. E-mail: adrian.neild@monash.edu

²IITB Monash Research Academy, Indian Institute of Technology Bombay, Mumbai, India

³Suman Mashruwala Advanced Microengineering laboratory, Indian Institute of Technology Bombay, Mumbai, India

Introduction

Acoustic fields can be used to collect microparticles over a wide range of frequencies. Within the ultrasonic range acoustic radiation forces cause patterns of particles to form, typically along pressure nodes. At much lower frequencies (in the order of hundreds of Hertz) the collection mechanism is inertial in nature, a particle's inability to follow the fluid motion causes drag forces to act on the particle which are non-zero when integrated across a time cycle due to gradients in the flow field [1]. In both cases, however, the ability to collect particles is limited by acoustic streaming - the steady state fluid flow which results from gradients in the harmonic flow field. In this study, we examine the smallest particle size that can be collected as a function of frequency. For the low frequency vibration, an open fluid chamber is oscillated in the horizontal plane, these conditions are also applied to the ultrasonic case, and the acoustic energy is kept constant across frequencies. It is found that the minimum particle size can be collected at each end of the frequency scale.

Method

In both cases perturbation theory was used to model the oscillating and steady state (acoustic streaming) flow fields within Comsol Multiphysics². For low frequencies excitation, the dominant characteristic is a capillary wave at the water air interface, the fluid domain is modelled as experiencing incompressible laminar flow, and a moving mesh is used to handle the interface deformation, the model is transient in nature and run until a steady state is achieved. The contact line of the fluid air interface on the solid container is assumed to be at the upper edge of the container wall; as such a wide range of contact angles can be supported. A slightly concave interface is used, not because of the contact angle, but rather to avoid convergence issues which arise for a flat interface. The width of the chamber is fixed at one capillary wavelength. The boundary conditions are shown in Fig 1(a), prior to the application of a horizontal oscillation. In the ultrasonic system the fluid is modelled as being compressible and inviscid using the Helmholtz equation. To capture behavior near the walls of the chamber, the first order field is then modified to create a non-slip boundary condition^{2,3}. The boundary conditions for the ultrasonic case are given in Fig 1(b), it is assumed that the water/air interface the pressure fluctuations are zero. The ultrasonic system has a chamber which is constrained to be one ultrasonic wavelength long, though the symmetry of the system means that only half the chamber is modelled. In both cases once a first order flow field solution is obtained, the body forces acting on the fluid are calculated³ and applied to a viscous Navier-Stokes model to obtain the second order streaming fields. Subsequently particle tracing is performed for particles experiencing the combined first and second order fields^{1,2}.

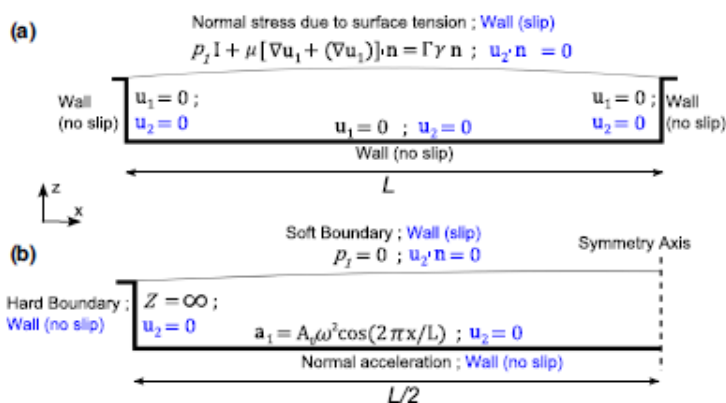


Figure 1: The boundary conditions for the first order flow field (black) and second order streaming field (blue) are shown for the two horizontally actuated fluid chambers. In (a), the low frequency system, the length, L , is one capillary wavelength, whilst in (b) the length is equated to an ultrasonic wavelength. The depth of the chamber, h , is fixed at $L/10$. The term Γ is the curvature of the interface and γ is the surface tension.

Results

In both cases there is a force acting to collect suspended particles at certain locations in the flow field. The strength of this force, the acoustic radiation force at ultrasonic frequencies and a net motion due to inertial effects at lower frequencies, is plotted in Figure 2 (a). At a fixed acoustic energy, the ultrasonic force increases with excitation frequency. The behavior in the low frequency domain is more complex, an optimum frequency exists. This is due to the nature of the origin of the force, when a particle fails to follow the flow field exactly due to its own inertia, it becomes exposed to other parts of the flow field. This means that in a flow field in which there is a spatial gradient, for part of the cycle in which the particle is moving one way it may be located in a slower flow, whilst for the rest of the cycle it may be in part of the flow field which is slightly higher in amplitude and moving in the other direction, as such there is a net motion over a cycle¹. Continuing the heavily simplified discussion, the size of this net displacement is related to the amount of lag the particle motion has compared to the fluid motion, so at low frequencies as the particle is better able to follow the flow (accelerations are slower and so inertia less significant) the lag is small and hence the exposure to flow gradients is reduced and the resulting displacement, or as plotted in Fig 2 the effective collection force, is also small. Whilst at too high frequencies the particle moves less due to the reduced time period and so again has less exposure to the fluid flow gradients. Hence there exists an optimal excitation frequency at which the collection forces are largest.

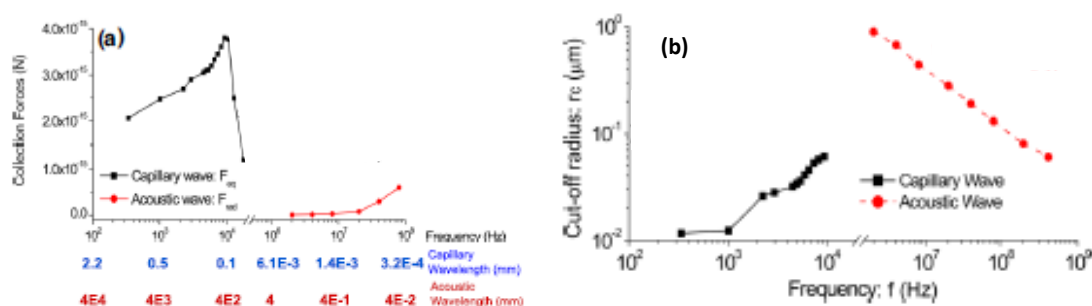


Figure 2: The collection force is compared (a) over a wide range of frequencies and shows that for ultrasonic excitation a higher force is generated at a higher frequency, however for capillary wave systems there is an optimal force at which inertia generated forces are greatest. When streaming is also considered there is a critical particle size below which the particles will follow the streaming field, and above which they can be collected, in (b) it is seen that the collection of the smallest particles occurs at either end of the frequency range considered.

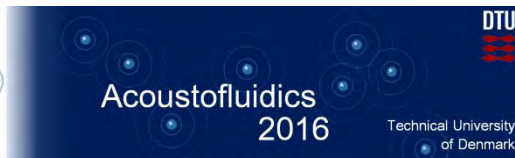
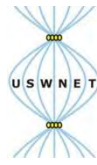
In Fig 2(b) the particle cut off size is shown. Below this size the particle behavior is dominated by the streaming flow, and so the particles follow a swirling trajectory. However, for particles larger than this size the collection forces dominate and so the trajectory leads the particles into stable locations. This arises as both collection force mechanisms are related to the radius by a higher power than one, whilst the drag force arising from acoustic streaming is related to the radius to the first power, hence at larger sizes the collection force becomes relatively more significant. It can be seen that a low frequency is best for the capillary waves, though it must also be noted that collection times can be expected to be very long as the collection force is weak at these frequencies

Conclusion

The minimum size of particle that can be collected has been analysed over a very wide range of frequency of excitation encompassing two different collection regimes. In a capillary wave regime smaller particles can be collected, though collection times can be expected to be long as the optimum frequency for collection to dominate coincides with weak collection forces, whilst for the ultrasonic regime smaller particles can be collected at higher frequencies.

References

- [1] P. Agrawal, P. S. Gandhi, A. Neild, *Journal of Applied Physics*, **114**, 114904 (2013).
- [2] P. Agrawal, P. S. Gandhi, A. Neild, *Microfluid Nanofluid*, **19**, 1209–1219 (2015).
- [3] W. L. M. Nyborg, *Physical acoustics IIB*. Academic Press, New York (1965).



Acoustofluidic manipulation of polystyrene, poly(methyl methacrylate) and fused silica particles using surface acoustic waves

Husnain Ahmed, Ghulam Destgeer, Jinsoo Park, Jin Ho Jung, and Hyung Jin Sung*

Flow Control Laboratory, Department of Mechanical Engineering, KAIST, Daejeon, 34141, South Korea.
Email: husnain@kaist.ac.kr, hjsung@kaist.ac.kr, URL: <http://flow.kaist.ac.kr/>

Introduction

We report on a microfluidic particle manipulation mechanism for continuous, label-free and contactless handling of polystyrene (PS), polymethylmethacrylate (PMMA) and fused silica (FS) microspheres based on their acoustic impedances using travelling surface acoustic waves (TSAWs). Previously, the size-dependent manipulation (focusing, trapping, separation, etc.) of microspheres have been demonstrated by TSAWs [1] and size- as well as density-dependent manipulation by standing surface acoustic waves (SSAWs) [2]. Here, we report a TSAW-based particle handling mechanism, first of its kind, using the differences in the acoustic impedances of two particle materials. The acoustic impedance (Z) of a material is defined as a product of density (ρ_p) and speed of sound (c_p) in the material; it combines two properties (ρ_p, c_p), that were previously dealt separately, into one parameter. Moreover, a theoretical estimation of the acoustic radiation force (ARF) acting on elastic microspheres is provided using the theoretical model of Hasegawa et al. [3]. In this work, we have tried to validate the theoretical estimation of the ARF by experimentally measuring the lateral deflection distance of the PS, PMMA, and FS particles.

The acoustofluidics particle manipulation device is composed of a piezoelectric (lithium niobate, LN) substrate with an interdigitated transducer (IDT) deposited on top of it, and a polydimethylsiloxane (PDMS) microchannel bonded to the substrate (Fig. 1(a)). A particle mixture is pumped through the microchannel along with two sheath flows to focus the particles close to the left wall. The particles are deflected by the TSAWs originating from the IDT, travelling in the rightward direction through the PDMS wall, and leaking into the fluid. The acoustic wave propagating through the fluid is scattered off the microparticle surface, which in turn induced a radiation pressure on the elastic microparticle. The radiation pressure is integrated over the surface of the microparticle to estimate a net ARF exerted in the direction of wave propagation. The microparticles are deflected from their original streamlines if the acoustic scattering is sufficiently asymmetric, creating a pressure difference between the front and rear face of the particle, to realize a strong ARF. The ARF and lateral deflection distance travelled by the particles is strongly dependent on the elastic particle properties (ρ_p, c_p), the acoustic wave frequency (f), the particle diameter (d), and the fluid properties (ρ_f, c_f). In the present work, the difference in the properties of fluid and particle is used to demonstrate the separation of particles (experimentation in progress).

Results

The ARF estimated, using the work of Hasegawa et al. [3], for PS ($Z = 2.5 \times 10^6 \text{ Pa} \cdot \text{s/m}$), PMMA ($Z = 3.3 \times 10^6 \text{ Pa} \cdot \text{s/m}$) and FS ($Z = 13.1 \times 10^6 \text{ Pa} \cdot \text{s/m}$) microspheres is plotted against κ (Fig. 1(c)). The κ ($= \pi f d / c_f$) factor is a dimensionless parameter that combines the TSAW-frequency and particle-diameter. A series of peaks and troughs observed in ARF plot (most prominent for PS particles) indicate the resonance between the elastic particle's vibration and the incident sound wave. The separation of PS particles of diameter 10 μm from PMMA 5 μm is achieved when exposed to 129 MHz of TSAWs as the PS particles are deflected further than the PMMA particles (see Fig. 1(b)). The deflection of polystyrene particles having diameter 5.8 μm , 7.0 μm , 12 μm , and 15 μm , and fused silica particles having diameter 4.8 μm , 5.0 μm , 6.1 μm , 6.46 μm and 10 μm is demonstrated inside the microchannel when exposed to 90 MHz frequency (see Fig. 2(a,d)). All of the particles except 7.0 μm (a NIST standard particle with narrow size distribution) are deflected over a wide region due to a larger variation in their size.

The initial and final positions of the particles after deflection are recorded, and plotted against microchannel width (see Fig. 2 (b, e); plots (b) and (e) corresponds to cases 4 (PS 15 μm) and 9 (FS 10 μm) in (a) and (d), respectively). The net deflection distance is calculated by taking a difference between the final and initial position of the particles, and is plotted against κ (see Fig. 2 (c, f)). The polystyrene particles show a varying trend corresponding to the ARF change with κ value (as depicted in Fig. 1(c)), while the fused silica particles show a uniform increase in deflection which also matches with the theoretical prediction. However, to further assure the validation of experimental results with the theoretical prediction, we are in the process of conducting additional experiments to obtain sufficient data points that would be mapped on to the theoretical estimation of ARF.

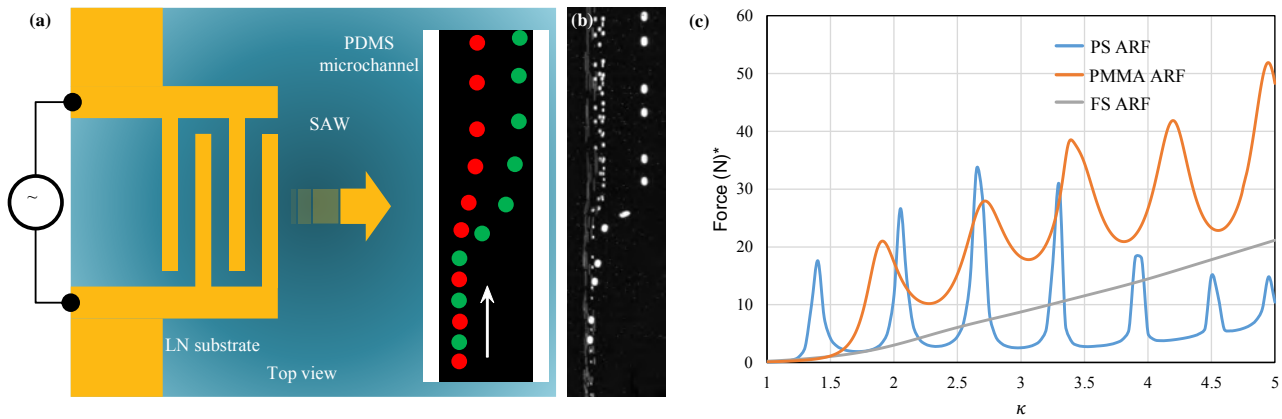


Figure 1: (a) A schematic of acoustic impedance based particle separation device. Separation of green and red microparticles, having similar diameters but different acoustic impedances, is shown. (b) Experimental image shows the separation of 10 μm PS particle from 5 μm PMMA particle. (c) Estimated ARF is plotted against κ for PS, PMMA and FS microspheres. (It is a qualitative plot as the force is normalized by the amplitude of velocity potential function.)

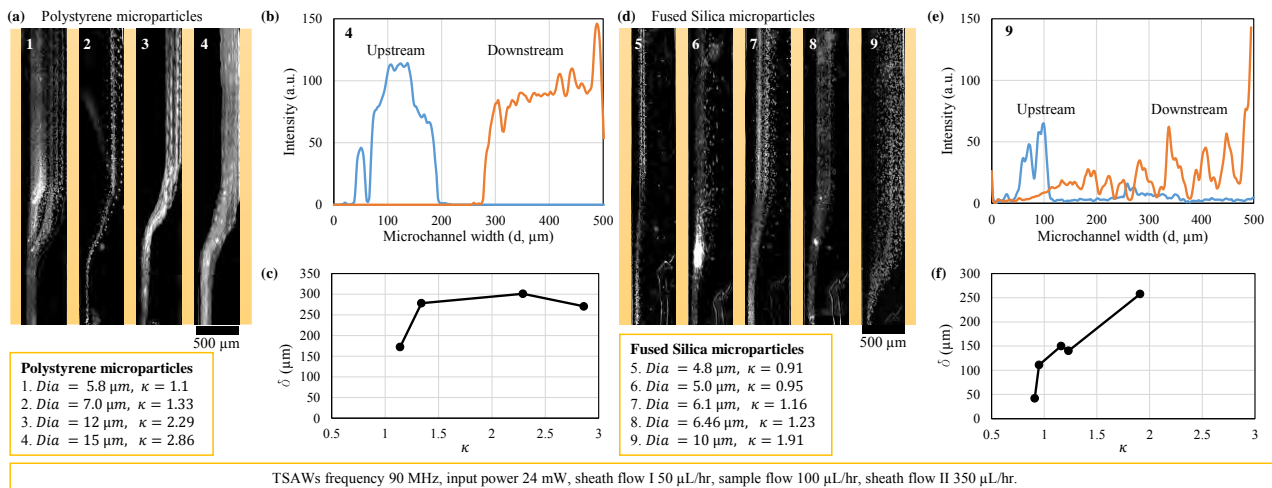


Figure 2: (a, d) Experimental images showed the deflection of microspheres when exposed to TSAWs with 90 MHz frequency. PS particles with 3 and 9 μm diameters showed a higher deflection, and deflection of fused silica particles gradually increases with diameter of the particles. (b, e) The plots indicate the particles location inside the microchannel before and after deflection by TSAWs. (c, f) The net deflection distance is plotted against kappa for PS and FS microparticles, respectively.

Conclusion

We have currently separated two different material, PS and PMMA, particles having different diameter and acoustic impedances. Moreover, we have analyzed the deflection behavior of PS and FS particles with a range of different diameters exposed to a single frequency (90 MHz) TSAWs. However, we are working on enriching the experimental data by using additional frequencies of ~ 130 , 150, and 190 MHz to validate the theoretical predictions of ARF acting on various particles. Our future focus is to separate the same diameter particle of different materials based on their acoustic impedances.

References

- [1] Destgeer *et al.*, Lab Chip **13**, 4210-4216 (2013).
- [2] Shi *et al.*, Lab Chip **9**, 3354-3359 (2009).
- [3] Hasegawa *et al.*, J. Acoust. Soc. Am. **46**, 1139-1143 (1969).

A simple acoustofluidic chip for microscale manipulation using evanescent Scholte waves

Vivian Aubert¹, Régis Wunenburger², Tony Valier-Brasier², David Rabaud¹, Jean-Philippe Kleman³ and Cédric Poulain¹

¹Univ. Grenoble Alpes, F-38000 Grenoble, France
CEA LETI MINATEC Campus, F-38054 Grenoble France.
Tel: +33 04 3878 9067; E-mail: vivian.aubert@cea.fr

²Sorbonne Universités, UPMC Univ Paris 06, CNRS, UMR 7190, Institut Jean Le Rond d'Alembert, F-75005 Paris, France.

³Univ. Grenoble Alpes, IBS, F-38044 Grenoble, France
CNRS, IBS, F-38044 Grenoble France
CEA, IBS, F-38044 Grenoble France.

Introduction

To date, most acoustic techniques for microscale manipulation rely on the use of waves propagating in the fluid and its associated radiation force or streaming flow. Here, we will present a new approach based on the use of an evanescent acoustic field above a substrate [2] to manipulate cells or particle in the near field region. This field is obtained by means of subsonic interfacial waves giving rise to a well-defined standing wave pattern of evanescent waves: We will show experimentally that these interfacial waves are guided waves known as quasi-Scholte acoustic waves. Scholte waves confine the acoustic energy to the vicinity of the surface. They are nearly lossless and thus can propagate over long distances along the substrate. With a very simple and low-cost device we show several examples of applications ranging from cell patterning to individual cell spinning by acoustorotation.

Theoretical description of Scholte waves

We consider a homogeneous, isotropic, elastic plate with thickness d delimited by surfaces $z = \pm d/2$ with longitudinal and transverse bulk wave speeds c_L and c_T and density ρ . The propagation of harmonic guided waves along the (Ox) axis with pulsation $\omega = 2\pi f$ and wavenumber k_x .

Assuming the plate to be surrounded by vacuum, the stress-free boundary conditions on both sides of the plate lead to two distinct dispersion equations for guided waves :

$$D_S = 4k_x^2 k_{Lz} k_{Tz} \tan\left(\frac{k_{Lz}d}{2}\right) + (k_{Tz}^2 - k_x^2)^2 \tan\left(\frac{k_{Tz}d}{2}\right) = 0, \quad (1)$$

$$D_A = 4k_x^2 k_{Lz} k_{Tz} \tan\left(\frac{k_{Tz}d}{2}\right) + (k_{Tz}^2 - k_x^2)^2 \tan\left(\frac{k_{Lz}d}{2}\right) = 0, \quad (2)$$

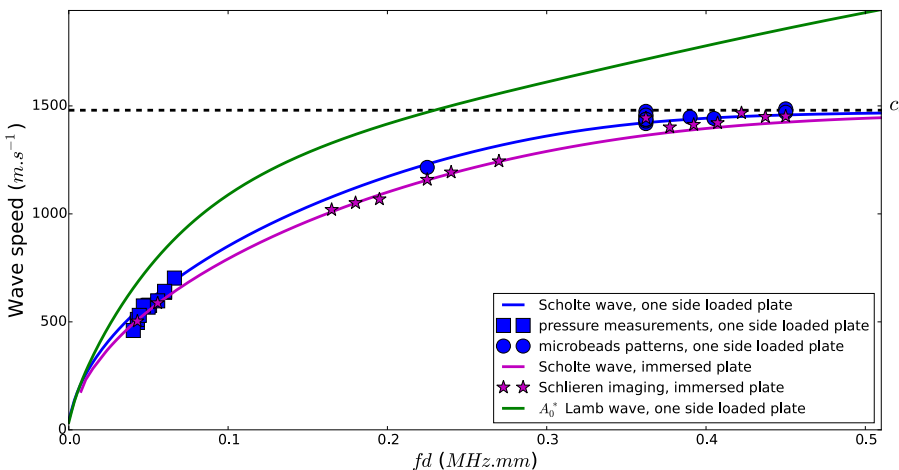


Figure 1: Theoretical predictions (solid lines) of the fd -dependent velocity of A_0^* Lamb and Scholte waves are compared to the experimental determination of wave velocity from wavelength measurements (symbols) in order to identify the nature of the standing surface wave set up along plates loaded on one or both sides with water. Quantitative agreement between measurements and the predicted Scholte velocity in both cases demonstrate the Scholte nature of the surface wave obtained experimentally.

with $k_{Lz}^2 = k_L^2 - k_x^2$, $k_{Tz}^2 = k_T^2 - k_x^2$, $k_L = \omega/c_L$ and $k_T = \omega/c_T$. Equation 1 (respectively 2) is the dispersion equation of the set of Lamb waves S_i (respectively A_i) (i being positive integer) characterised by a displacement field symmetric (respectively antisymmetric) with respect to the plate mid-plane.

Now assuming the plate to be loaded on one side by a semi-infinite, inviscid liquid with mass density ρ_0 and sound speed c_0 , the dispersion equation can be concisely written as :

$$D_S D_A = \frac{\rho_0 k_T^4 k_{Lz}}{\rho 2jk_{0z}} \left[\tan\left(\frac{k_{Lz}d}{2}\right) \tan\left(\frac{k_{Tz}d}{2}\right) D_A - D_S \right] \quad (3)$$

with $k_{0z}^2 = k_0^2 - k_x^2$, $k_0 = \omega/c_0$. Numerical resolution of equation 3 in the particular case of glass plate loaded with liquid water on one side, reveals two sets of waves (Fig. 1): (i) two sets of modes, labelled S_i^* and A_i^* , which identify respectively with the S_i and A_i sets of Lamb waves in the $\rho_0/\rho \rightarrow 0$ limit, and called Lamb waves in the following, (ii) a quasi-Scholte mode which identifies in the $k_x d \rightarrow \infty$ limit with a Scholte wave.

Assessment of the dispersion equation of Scholte waves

The measurement of the dispersion equation is performed by measuring the distance between pressure nodes (or antinodes) as a function of frequency. Two complementary techniques have been implemented: acoustic pressure measurements and tracers. The device consists in a $10 \text{ mm} \times 5 \text{ mm} \times 0.66 \text{ mm}$ piezo-transducer (*Noliac* NCE51) simply glued onto the bottom side of a $60 \text{ mm} \times 24 \text{ mm} \times 150 \text{ }\mu\text{m}$ glass plate with a chamber filled with water.

The evolution of the surface wave speed $c_x = \lambda f$ deduced from these wavelength measurements as function of fd is displayed in Fig. 1 together with the theoretical dispersion curves. Quantitative agreement between the dispersion curve of the Scholte wave and measurements is observed, which demonstrates that the acoustic field measured in water is associated to Scholte waves and not to loaded Lamb waves.

Microfluidic applications of Scholte waves

We will show how to use this Scholte-chip for achieving several key-operations in microfluidic such as pattern, concentrate flowing cell suspensions in a microchannel, or even trap and rotate single cell. Finally, we will also show that it is possible to form plasma-enriched regions in whole blood. All these devices are simply made of tape, standard glass plates and commercial piezo-transducer.

Conclusion

We have shown that a thin plate on which a piezo-transducer is glued consists in a very simple Scholte wave emitter capable to exert strong and well defined force or torque fields upon microparticles or cells. In particular, use of evanescent waves present interesting features namely because: it can operate at relatively low frequency with relatively high acoustic forces, operates in the near field and in the vicinity of the plate, and is easy to manufacture out of clean room conditions.

References

- [1] J. Friend and L.Y. Yeo. *Rev. Mod. Phys.* **83**, 647-704 (2011).
- [2] V. Aubert, R. Wunenburger, T. Valier-Brasier, D. Rabaud, J.P. Kleman and C. Poulain. *Lab Chip* **12**, 4617-4627 (2016).

A definition of acoustophoretic mobility and the optimization of acoustic SPLIT transport-Thin fractionation, SPLITT

Mauricio Hoyos¹, Michel Martin¹, Salomé Gutiérrez^{1,2}, and P. Stephen Williams³

¹CNRS UMR7636 Ecole Supérieure de Physique et Chimie Industrielles (ESPCI-ParisTech),
Laboratoire de Physique et Mécanique des Milieux Hétérogènes, Paris, France

E-mail: mauricio.hoyos@espci.fr. URL: www.pmmh.espci.fr/?-People-

²Cinvestav, Monterrey, Mexico

³Cambrian Technologies Inc., 1772 Saratoga Avenue, Cleveland, OH 44109, USA

A post-dead line contribution

Abstract

The mechanism of the split-flow thin channel fractionation (SPLITT) technique has similarities to that of field-flow fractionation (FFF), where a transverse field is applied across a thin channel in order to generate selectivity and separation. In separation sciences the parameter of choice for quantifying continuous separation is the mobility: electrophoretic mobility, magnetophoretic mobility, etc. In SPLITT Fractionation the most common cross field is the gravitational field in which the relevant mobility is the sedimentation coefficient. We are developing acoustic SPLITT Fractionation which utilizes transverse ultrasonic standing waves for separating species as a function of their acoustic physico-chemical characteristics. We also have defined the acoustophoretic mobility. Equations for predicting optimum flow conditions for separation when species interact with both, gravitational and acoustic fields are presented.

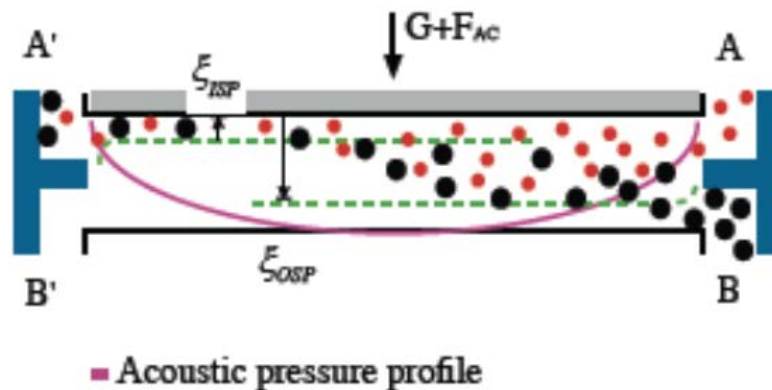


Figure 1: Schematic view of the SPLITT fractionation separation chamber. Particles are continuously separated by introducing at A' the suspension and through inlet B' is introduced clear fluid. Species interacting with the cross field force while driven along the channel. Species migrate at different transversal velocities. Species of different acoustophoretic mobility are continuously separated by the coupling of gravitational and acoustic forces.

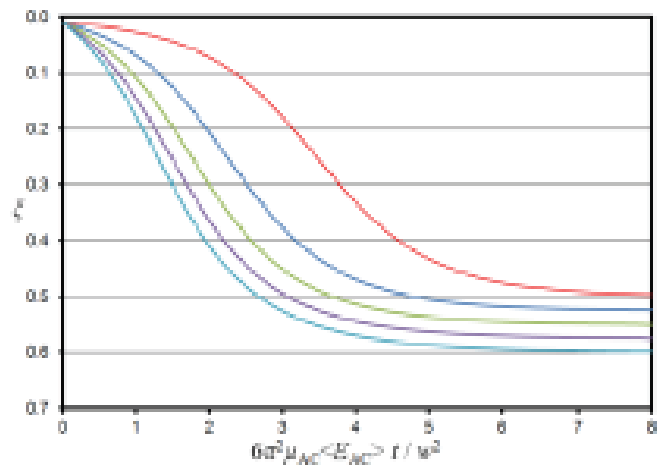


Figure 2: Trajectories of specie of different acoustophoretic mobilities along the SPLITTchannel.

A two-element acoustic tractor beam for microparticle manipulation

Amanda Franklin¹, Asier Marzo¹ and Bruce Drinkwater¹

¹Department of Mechanical Engineering, University of Bristol, Bristol, United Kingdom
E-mail: amandacfranklin@gmail.com

Introduction

Acoustic manipulation devices have been primed as an alternative to optical tweezers ever since researchers created standing waves inside chambers allowing the trapping of particles in their nodes. Ultrasound offers a less expensive and safer alternative to laser trapping with an applicability to a wider range of materials. In standing wave devices, changing the frequency and/or phase of the ultrasonic transducers allows movement of the trap position; however these devices do not provide the precise single-beam manipulation that is demanded for a viable technology in micro-scale manufacturing and chemical or medical research [1]. Single-beam acoustic manipulation (i.e. tractor beams) have been realised recently using phased arrays by Marzo et al. [2] and Baresch et al. [3] demonstrating dexterous manipulation in air and water respectively. However, these devices require complex electronics and multi-element arrays hindering their wide scale applicability. Microbeam devices created by Lee et al. [4] can trap particles on a surface using a single element transducer but they work in the Mie-scattering regime requiring ultra-high frequencies (>100 MHz) thus making them difficult and expensive to manufacture.

Here, we build a simple single-beam manipulator that requires a minimum of elements and uses a single driving signal, drastically reducing the cost of the system. The paper proposes a tractor beam device that uses a single input signal used to drive two transducer elements out of phase to create a tweezer-shaped trap (termed a twin trap [2]). This is achieved by using a piezoceramic disk with two sets of electrodes, a solid prefocussed lens and a shape-changing liquid lens. The arrangement, shown in Fig 1(a), is submerged in water to smoothly manipulate particles with a spatial resolution of the order of $\lambda/10$. In our device the wavelength is significantly greater than the particle size and so our device operates in the Rayleigh-scattering regime.

Methods

We generate an ultrasonic beam shaped as a twin trap with the combination of a PZT disk divided into two elements and a lens. A twin trap is the most stable Rayleigh regime acoustic tractor beam demonstrated so far [3]. Using a phased array, it is created by focusing the array at the target point and adding a π phase offset to half of the array.

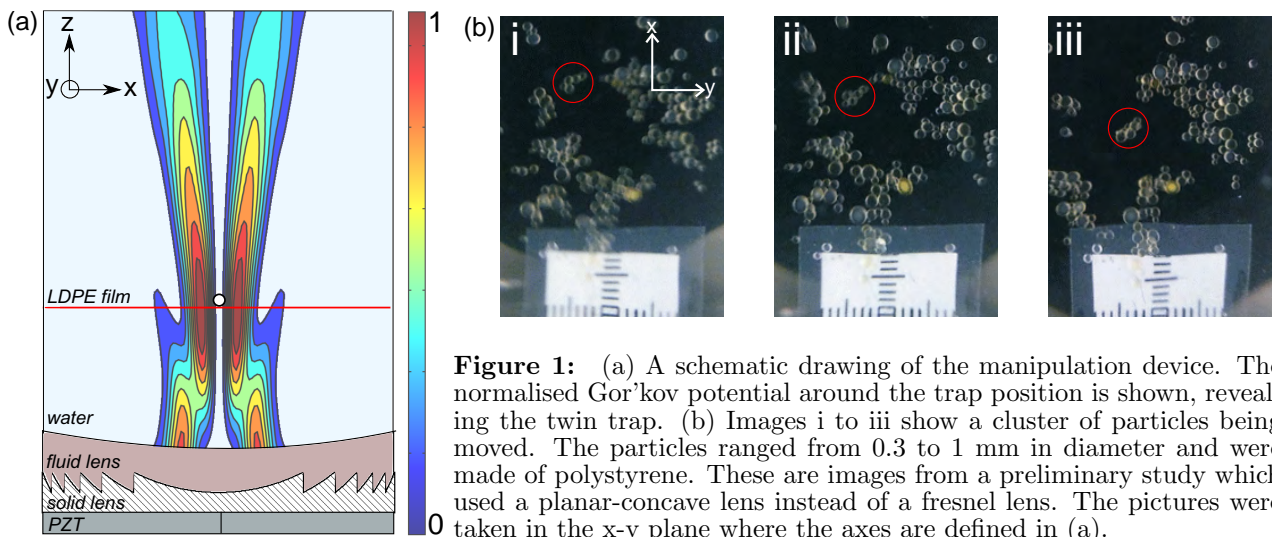


Figure 1: (a) A schematic drawing of the manipulation device. The normalised Gor'kov potential around the trap position is shown, revealing the twin trap. (b) Images i to iii show a cluster of particles being moved. The particles ranged from 0.3 to 1 mm in diameter and were made of polystyrene. These are images from a preliminary study which used a planar-concave lens instead of a fresnel lens. The pictures were taken in the x-y plane where the axes are defined in (a).

For generating a twin trap, we etched away a thin strip of the conducting electrodes of a PZT disk to create two elements. The same driving signal was applied to both halves of the disk but with reversed polarity in order to create a π phase difference. As the PZT disk remained monolithic this is termed a kerfless array. Then, we added a physical lens on top of the disk to focus the acoustic beam.

The device was submerged in a water tank and an angled Perspex plate was placed at the top of the tank to avoid the formation of standing waves between the device and the water surface. The plate deviated the sound away from the trap position and preserved the integrity of the pressure field around the twin trap. The driving frequency was 1.16 MHz which represents a wavelength of 1.5 mm in water. The manipulated particles were 300 μm polystyrene and 100 μm silica beads.

For dynamic trap positioning, we explore a shape-changing lens made of a cavity filled with glycerine. The cavity has a membrane on the top and by adjusting the volume of glycerine inside the curvature of the membrane can be varied and thus its focal point. This allows the refocussing the twin trap at different positions, moving the particles that are trapped without physically translating the device. To reduce the extent to which energy is lost through attenuation in the solid lens, a fresnel lens has been designed. This also makes the device more compact accomodating for the possibility of miniaturising trapping devices.

Modelling

The simulation shown in Fig 1(a) was modelled in COMSOL Multiphysics 5.0. Combining the structural mechanics and pressure acoustics modules to explore different lens designs (i.e. planar-concave and planar-fresnel) as well as lens curvature, material and thickness. The performance of the kerfless array design was also explored.

The surface velocity of the kerfless disk was measured at its resonance frequency using laser vibrometry. The velocity was used as an input parameter in the model thus ensuring the accuracy of the pressure field simulation. Knowing the correct velocity of the fluid medium at the transducer surface allows the quantitative calculation of the pressure.

The sound pressure field from the model was then used to predict the acoustic radiation force potential using the analytic approximation described by Gor'kov [5]. With the potential field obtained around the trap, we calculated the lateral and axial strength of the traps on various particles.

Results

Fig 1(a) shows the Gor'kov potential around the trap, the gradient of which determines the force exerted on the particle. The steep gradients on either side of the trapping point show that particles will be pushed towards the centre. The models of the pressure and the derived potential suggest that the lenses are able to produce a focus with sharp potential gradients that are sufficient for trapping in the x-y plane.

The manipulation of various particles over the surface of a low density polyethylene (LDPE) film is shown in Fig 1(b). These particles are trapped at the minimum of the Gor'kov potential field. The device used in the experiment had a large aperture (40 λ), and the resulting twin trap is elliptical in shape. Individual large particles can be manipulated, as can smaller particles which tend to form elliptically shaped clusters.

Conclusion

We have presented a two-element device that can generate acoustic tractor beams for the manipulation of microparticles. It would be possible to increase the frequency and/or reduce its size to enable the manipulation of smaller particles such as cells or microbubbles. The simplicity of the design reduces the cost, promoting the simultaneous use of multiple devices to execute parallel protocols in lab-on-a-chip scenarios or in a contactless production process.

References

- [1] Drinkwater, B. W. Lab Chip. In press. (2016). 10.1039/C6LC00502K
- [2] Marzo, A. et al. Nature Communications, **6**, 8661. (2015). 10.1038/ncomms9661
- [3] Baresch, D. et al. Physical Review Letters. **116**, 024301. (2016). 10.1103/PhysRevLett.116.024301
- [4] Lee, J. et al. Applied Physics Letters, **95**, 073701. (2009). 10.1063/1.3206910
- [5] Gor'kov, L.P. Sov. Phys. Dokl., **6**, 773. (1962).

Optimising particle manipulation via acoustofluidics at low frequency

Pierre-Yves Gires¹, Cedric Poulain¹

¹Université Grenoble Alpes, F-38000 Grenoble, France and
CEA LETI MINATEC Campus, F-38054 Grenoble, France
E-mail: cedric.poulain@cea.fr

Introduction

Manipulation of nano or microparticles, contrast agents, living cells or bacteria to mention but a few plays a key-role in many technological processes for health and care applications. Their efficient and flexible manipulation remains challenging because of their tiny size. Use of acoustofluidic effects a promising tool [1,2], which can be optimised in order for instance to improve power consumption. In this talk, we will present a system which combines successive overlapping resonances in the low ultrasonic domain (presently 45 kHz), using a thin plate and a bubble resonances. The separate effects of both resonators have shown separately the ability to concentrate particles at plate antinodes [1], and to capture beads at bubble surfaces [2]. Here we will show that used together, a repulsion phenomenon occurs and that this system can be used to either trap and concentrate, or repulse.

System dimensioning and experimental setup

Because of their higher inner pressure due to surface tension forces, gas bubbles tend to dissolve in a liquid. We considered H₂ electrolysed bubbles in water, with a radius above a few tenth of microns, for which this process doesn't affect significantly the bubble size on the time scale of the experiment (a few minutes). As the resonance frequency of a bubble scales as the inverse of its diameter, being about 60 kHz for a bubble of 100 micron diameter [3], in order to couple efficiently the piezoelectric emitter with the liquid, we used a thin enough glass plate, taking advantage of the strong dependence of the bending modulus with the thickness (third power), the more flexible a membrane being, the lower its resonance frequencies. In order that the piezoelectric resonates at such a low frequency range, we also used an annular massive one, with 4 mm thickness, and 17 (33) mm internal (external) diameters. The choice of such geometry allows observation by transmission under a microscope, as shown in our complete setup presented on Fig. 1a).

As sketched on Fig. 1b), the acoustofluidic device consists in a thin glass plate (150 μm thickness, 2 cm diameter), taped on an annular piezoelectric. A drop of suspension of particles is deposited, and a bubble can be generated in the center of the plate by electrolysis. The system is then confined at a given height by an upper removable PMMA disk (8 mm diameter), which position and orientation can be fully controlled via translation and goniometer stages, and a rotation mount. The crystal is excited at its 45 kHz thickness resonance which also matches an axisymmetrical resonance mode of the thin plate. The drop volume is adjusted to fill the cavity at the desired height. The recording can be done via a wide field (2048x2048 pixels) or a high speed camera (Photron, SA1.1.), to resolve long

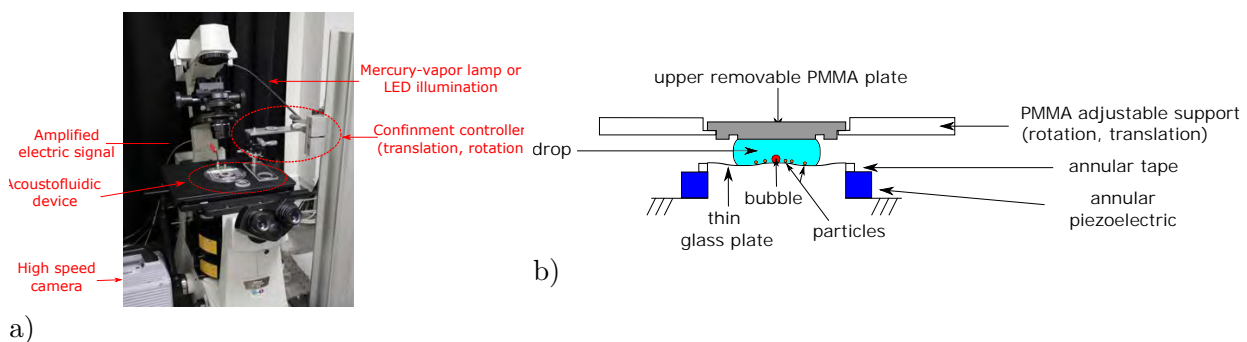


Figure 1: (a) Complete setup. (b) Sketch of the acoustofluidic device.

range migrations or the bubble dynamics. Polystyrene particles of 10 μm diameter, and HELA cells, have been used.

Without bubble

On Fig. 2a), we present the results obtained in a cavity of 500 μm height, with a 20 V input voltage on the piezoelectric. We find an attraction of the particles towards the membrane vibrational antinodes, in its center. The radial velocity v_r has also been plotted as a function of the distance to the plate center, from the center to 400 μm , via automatic tracking of some particles (Trackmate, Imagej) for which a roughly linear dependence is observed.

The migration speed can be tuned by the imposed voltage: the migration velocity increases to about a factor 10 when the imposed voltage is doubled. We also found a similar increase when the gap size is reduced to 250 μm : both results are presented on Fig. 2b). As explained in [1], we expect that this attraction towards motionless plate regions is related to streaming loops that converge to these areas, the particles remaining there because the streaming drag force does not overcome their reduced weight.

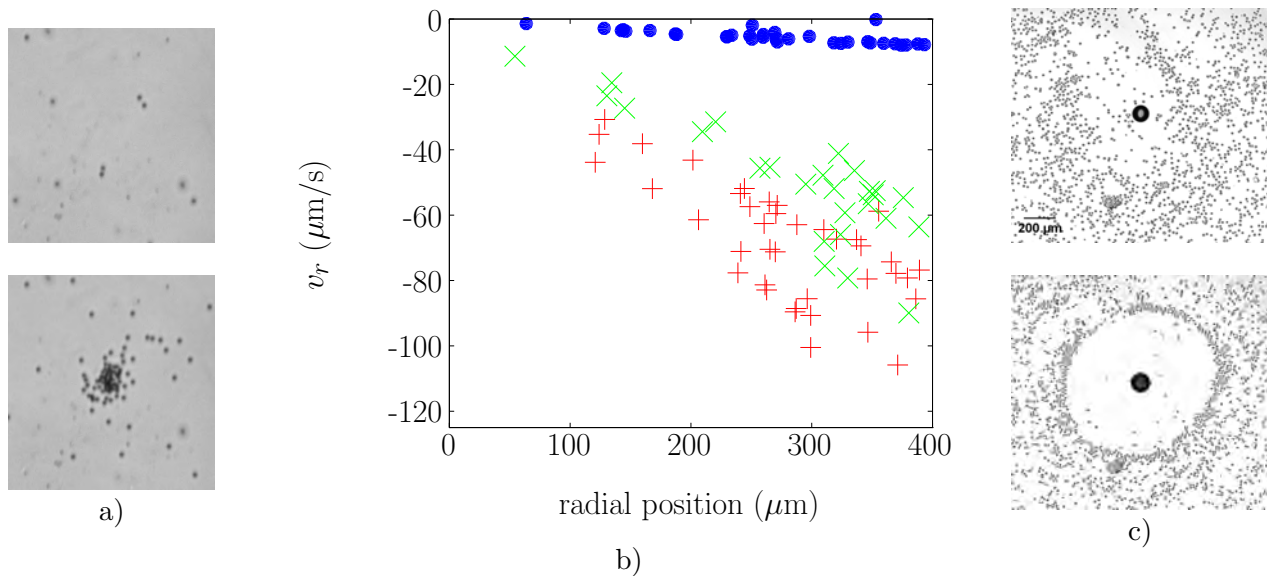


Figure 2: a) *without bubble*: Top: Initial repartition of the 10 μm polystyrene beads at the center of a 500 μm cavity. Bottom: Evolution after 151 s, under 20 V. b) *without bubble*: Influence of the imposed voltage and the gap height on the radial velocity v_r . Blue disks: 500 μm , 20 V; red crosses: 500 μm , 40 V; green crosses: 250 μm , 20 V. c) *with bubble*: Top: Initial position of HELA cells in a 500 μm cavity. Bottom: Position after 28 s, under 5 V.

With a bubble

When a bubble is present in the center of the cavity, with a 500 μm gap and 5 v voltage, the behaviour of the particles is opposite as shown on Fig 2c). We are currently analysing our observations and an attempt for modelling this behaviour will be presented.

Conclusion

We present a system that allows to combine a plate and a bubble resonance in order to optimise acoustofluidic effects at low frequency. Significant particle migrations are measured, with speeds as high as 100 $\mu\text{m/s}$. Without bubble, the depth of confinement turns out to be an important parameter, and the effect a bubble addition can have an effect as strong as to reverse the particle migration.

References

- [1] J.-G. Vuillermet, P.-Y. Gires, F. Casset and C. Poulain. Phys. Rev. Letters **116**, 184501 (2016).
- [2] Y. Xie, C. Zhao, Y. Zhao, S. Li, J. Rufo, Sh. Yang, F. Guob and T. Huang. Lab on Chip **13**, 1772 (2013).
- [3] M. Minnaert. Phil. Mag. **16**, 235-248 (1933)

Influence of rheological properties of blood samples on acoustic plasmapheresis

Itziar González, Pilar Carreras

¹Department of Sensors and Ultrasonic Systems, Spanish National Research Council, Madrid, Spain
 E-mail: icier.gonzalez@csic.es, URL: <http://www.itefi.csic.es/en/research-departments/sensors-ultrasonic-systems/group-of-ultrasonic-resonators-for-micromanipulation-and-cavitation/>

Introduction

The objective of this work was the study of reliability and efficiency of the use of Ultrasounds to perform plasma separation based in the concept of Blood as a non-Newtonian fluid whose viscosity and other rheological properties (such as cell aggregation) are defined by parameters associated to their hydrodynamics. Three important features of the suspension flow were analyzed under the action of the ultrasounds, (i) the effect of the blood cell spacing given by the blood dilution, (ii) the effect of the flow velocity and (iii) the effect of the cell–cell interaction (formation of roleaux) intrinsically related to the others but also influenced by the ultrasounds.

Ultrasounds also have been used to perform plasma separation [1-4]. The ability to manipulate particles using ultrasound arises due to non-linear interaction between the incident wave and that one scattered by each cell, giving rise to a steady Radiation Force.

Experimental setup

A square glass capillary (700 μ m x700 μ m x10cm) was used as the channel to perform the tests. Silicone tubing was attached to the inlet and outlet of the capillary tube. A 2MHz piezoceramic square transducer (PZ26, Ferroperm Piezoceramics, Kvistgard, Denmark (30mmx30mmx1mm) was coupled to the capillary together using a hydrogel (Aquasonic Clear Ultrasound Gel, Parker Laboratories Inc., Fairfield, NJ). Figure 1.

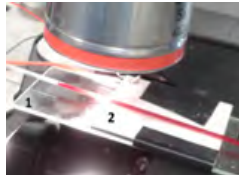


Figure 1: Setup to perform the plasmapheresis by ultrasounds, based on a blood cell enrichment process induced in a capillary tube under the ultrasonic actuation

Heparin treated blood samples were obtained from healthy individuals via the donor center of Hospital La Princesa (Madrid). blood was diluted in PBS (Sigma Aldrich, España) at different volumetric concentrations: $C_v = 5\%$, 10% , 20% and 50% respectively..

Microscopic effects on the red blood cells

Once applied the acoustic field, the cells collect at the central axis of the channel driven by the radiation force of Eq. (1), leaving areas of plasma free of cells around it and closer to the sidewalls of the capillary. The non-spherical RBCs become partially tilted during their flow motion before the application of the ultrasounds according at flow rates $Q=40\mu\text{L}/\text{min}$, increasing their angle of orientation with the flow velocity. When the cells are exposed to the ultrasounds, they adapt their motion to the standing wave according to both, hydrodynamic and acoustic focusing forces combined.(Figure 2). During their drift motion, the RBCs reorientate their biconcave shapes, becoming almost horizontal along the axis of collection,

Cell aggregation was also observed in the experiments. The application of ultrasounds during various seconds favored the formation of RBCs roleaux in the area of cell collection. Figure 2 shows three images filmed at $Q=40\mu\text{L}/\text{min}$. Several of these aggregates formed stratified chains of roleaux parallel to the central

axis, keeping a distance of equilibrium between them, of the order of their size. They showed reversibility in the experiments, disappearing after the acoustic treatment.

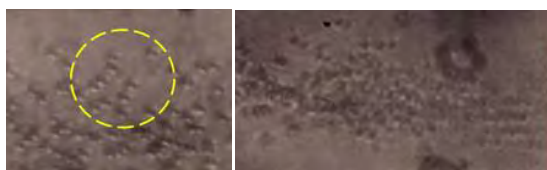


Figure 2: formation of Rouleaux during the RBC drift motion and collection at the pressure node along the central axis of the capillary. These rouleaux frequently formed stratified chains parallel to this axis.

Macroscopic effects of the ultrasounds on the blood samples

The cell collection achieved during the acoustic actuation generated a volume of plasma circulating clean of cells off the central axis after a certain time of treatment. At the end of the capillary this plasma was recovered through two lateral outlets separated from the enriched cells leaving the channel through a central outlet. So, the cell enrichment was used as a preconditioning method to perform the plasmapheresis at the end of the capillary. The samples required different times for this process, depending on their level of dilution and hydrodynamic conditions, defined by their flow rates. Figure 3 shows different times required by the samples to reach clearance percentages over 80% depending on the flow rate and blood dilutions. The most diluted blood samples ($C_v=5\%$) show the strongest dependence on the flow rate conditions to perform cell-plasma separation processes, reaching a maximal efficiency at $Q=40\mu\text{L}/\text{min}$. After the acoustic cell collection the samples were extracted at the end of the capillary through three different outlets. The enriched cells left through a central outlet, while the purified plasma was extracted through two symmetrical lateral outlets, viable for later biomolecular or other analysis. It was collected using Silicone tubing (Fisher scientific, UK) attached to the capillary ends as shown in Figure 5. Majority of the blood cells and plasma slightly colored by red cells entrained were collected in different sinks.

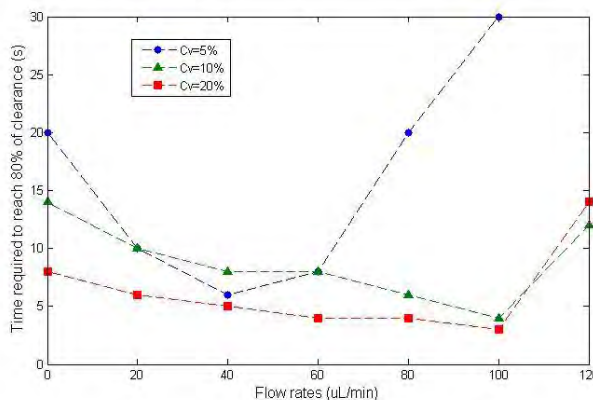


Figure 4: Time of acoustic treatment required to reach transparency levels of plasma over 80% versus the flow rate

These results evidence the influence of the hematocrit levels on the ability of the ultrasounds to perform suitable acoustic plasmapheresis. Specific hydrodynamic conditions of the samples should be applied to achieve optimal efficiencies. In consequence, different plasma clearance percentages were achieved on the blood samples applying the acoustic waves at a frequency $f=1153\text{ kHz}$ and fixed voltage of $V=48\text{ volts}$ for the five sample dilutions. According to these experimental results of the study, it can be concluded that the hydrodynamic conditions on processes of plasmapheresis by ultrasounds must be taken into account and carefully analysed for different blood sample dilution and hematocrit levels.

References

- [1] Harris N. R., Hill, M., Beeby, S., Shen, Y., White, N. M., Hawkes, J. J., Coakley, W. T. *Sens. Actuators, B: Chemical* 95, 425–434 (2003).
- [2] Hawkes, J. J., Barber, R. W., Emerson, D. R., Coakley, W. T. *Lab Chip*, 4, 446–452 (2004).
- [3] T. Laurell, F. Petterson, A. Nilsson, A. *Chem. Soc. Rev.* 36,492-506 (2007).
- [4] I.González, P. Carreras, O. Ahumada. *Physics Procedia* 70, 72-75, Int Congress on Ultrasonics, ICU (Metz,2015).



Investigation of polymer-shelled microbubbles motions in acoustophoresis

Dmitry Grishenkov¹, Satya Kothapalli¹, Martin Wiklund², Birgitta Janerot-Sjoberg³

¹Department of Medical Engineering, KTH Royal Institute of Technology, Stockholm, Sweden.

E-mail:dmitryg@kth.se

²Department of Applied Physics, KTH Royal Institute of Technology, Stockholm, Sweden

³Department of Clinical Science, Intervention and Technology, Karolinska Institute, Stockholm, Sweden.

Introduction.

The objective of this study is to explore the trajectory motion of polymer-shelled microbubbles by the radiation force in standing wave acoustic fields.

Materials and Methods.

The experimental set-up consists of microfluidic chip coupled to a piezoelectric crystal (PZT) having a resonance frequency of about 2.8 MHz. The microfluidic channel includes a rectangular chamber with the width, w , corresponding to one wavelength. This in turn corresponds to one full wave ultrasound standing wave pattern with two pressure nodes at $w/4$ and $3w/4$, and three anti-nodes at 0 , $w/2$, and w respectively.

The peak-to-peak amplitude of electrical potential over the PZT was varied between 1 and 10 Volts.

Results and Discussion.

From Gorkov's potential equation, the acoustic contrast factor, Φ , for the polymer-shelled microbubbles was calculated to about -100. Experimental results demonstrate that the polymer-shelled microbubbles are translated and accumulated at the pressure anti-nodal planes. First the primary radiation forces dragged polymer-shelled microbubbles into close proximity to each other at the pressure anti-nodal planes, then the secondary radiation force causing them to aggregate at different clusters along the channel. Experiments were performed at flow varied from 0 to 100 ul/min. Worth noting that the relocation time for polymer-shelled microbubbles is 40 times shorter than for solid polyamide microbeads of the same size. Furthermore, the polymer-shelled microbubbles can be actuated even at a driving voltage as low as 1 Volt (pressure amplitude below 50 kPa, acoustic energy density below 0.5 J/m^3), which is not the case for solid microbeads.

Conclusion.

In a conclusion, the polymer-shelled microbubbles demonstrate the behavior attributed to the negative acoustic contrast factor particles and thus can be trapped at the anti-nodal plane. This phenomenon could be utilized to explore in future applications, such as bio-assay, bio-affinity, and cell interaction studies *in vitro* in controlled environment.

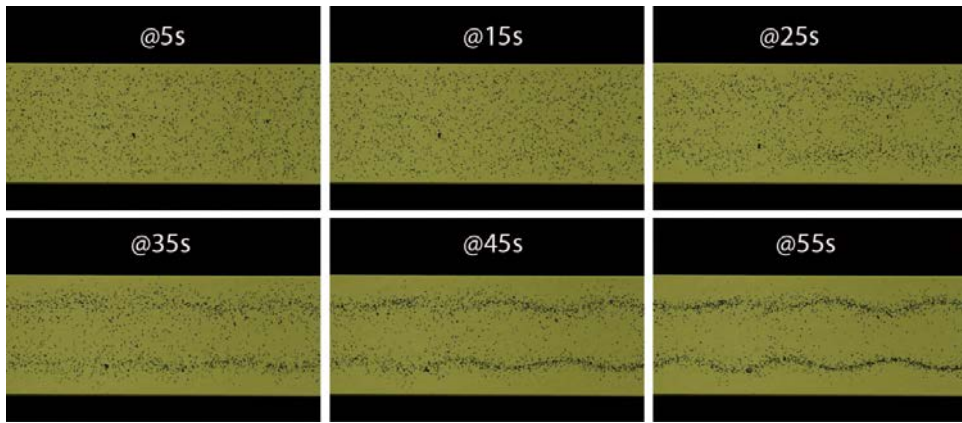


Figure 1. The microscopic images of 5 μm solid polyamide microbeads (represented in black dots) at different time intervals. Microbeads are positioned at pressure nodes.

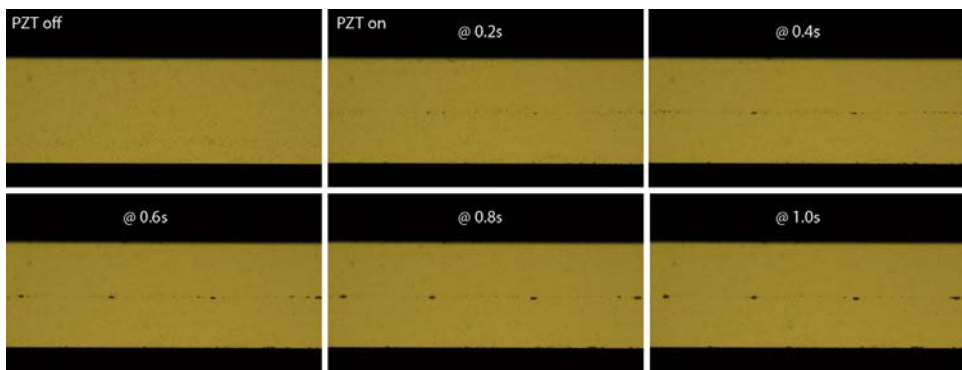


Figure 2. The microscopic images of polymer-shelled microbubbles (represented in black dots) at different time intervals. Microbubbles are positioned at pressure antinodes.

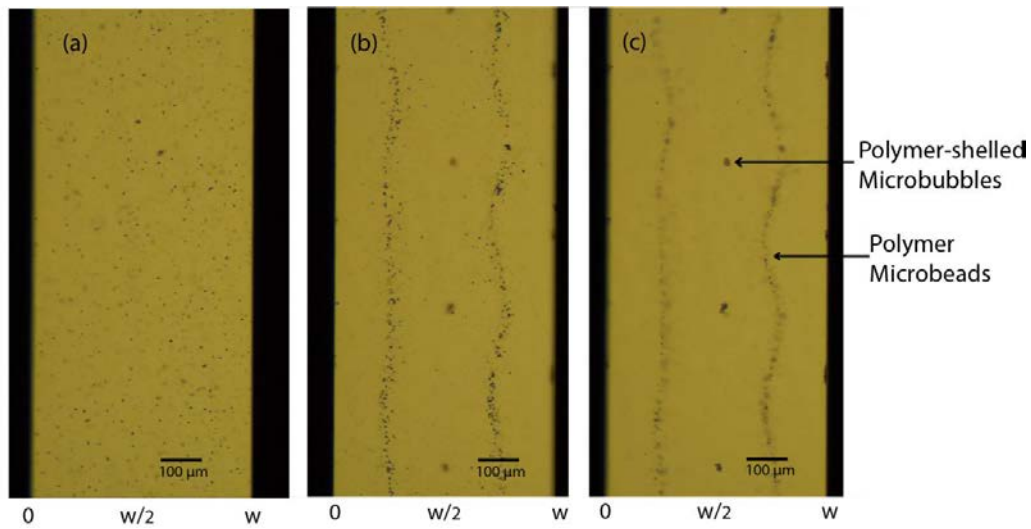


Figure 3. Microscopic images of combined polymer-shelled microbubbles and microbeads suspension in the microchip (a) before and (b) after subjected to standing wave acoustic fields.

Ultrasound filtration and manipulation of yeast using a fogger

Jeremy J. Hawkes¹, Bart Lipkens²

¹Acoustic Machines, Liverpool L25 4TQ, UK JeremyJHawkes@gmail.com

²FloDesign Sonics, 380 Main St Wilbraham, MA 01095, USA

Introduction

Ultrasound filter chambers are often small and some are low cost but the equipment used to produce the sound is typically very large and high cost, this excludes ultrasound filtration from many applications.

The reason high cost broadband ultrasonic amplifiers are currently used is: High Q MHz chambers have resonances only a few kHz wide. In many systems it is necessary to know the number of half wavelengths in the chamber. To maintain resonance with a chosen number of half wavelengths while factors such as temperature or particle concentration are changing the resonant peak needs to be actively tracked and to avoid signal loss flat response (broadband) amplifiers are selected. However in some multiwavelength and agglutination systems a good resonance is required but the number of half-wavelengths (nodes) is not critical to the operation.

Here we show that for applications where the number of wavelength in the chamber is not critical an ultrasonic Fogger device (shown in figure 1) can be used. These are sold for producing mist and provide a very low cost ultrasound source. Foggers adjust their operating frequency to achieve water resonance therefore in well coupled liquid systems with many resonances they bring the whole system to resonance. Two applications where the number of wavelengths in the chamber is non critical are multiwavelength enhanced sedimentation filters and ultrasonic agglutination devices, .

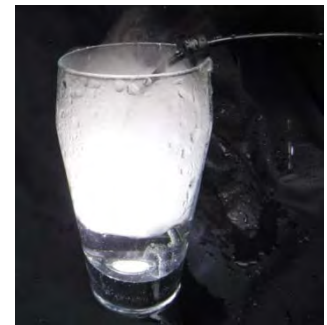


Figure 1: Fogger 30 mm below water in a glass.

Equipment and Methods

Ultrasound Foggers produce ultrasound in the region of 1.8 MHz, measured with a microphone comprising a 1 MHz PZT. The waveform depends on the reflected wave, when producing fog the surface of the water and the wave are constantly changing but when a reflector is present the wave becomes stable, the FFT in figure 2 shows that this includes the harmonics 3.6 and 5.4 MHz.

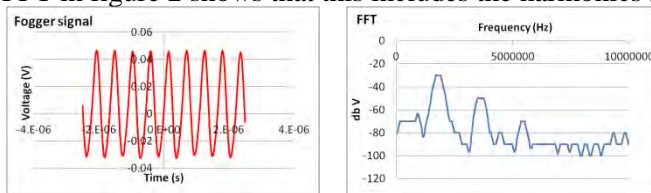


Figure 2: a) Fogger signal.
b) FFT spectrum

Fogger chamber: Foggers operate submersed in water this helps dissipate the 15 W of heat they typically produced. 15 W is enough to rise the temperature of 100 ml water by 10 °C in 5 min and cause significant disruption to a resonance. To remove the heat the fogger is placed in a chamber with cooling water flowing at 1 ml s⁻¹. The chamber is connected to the resonant section through a sound transparent window (thin glass or plastic).

Resonant filtration chamber: The chamber was based on previous enhanced sedimentation filter [1] designs where particles sediment against the incoming flow, but in this case the chamber was formed by additive printing in ABS and Tango black (shore hardness 27A) for rubber seals. Reflectors made of glass or thin polystyrene gave similar filtration efficiencies. Internal cross section 24.1x16 mm.

Agglutination tube: A 1 mm ID glass capillary was filled with a suspension of yeast in water[2,3]. Sound was guided to the tube through cooked spaghetti.

Filtration results

Yeast forms stable patterns of bands when the sound is turned on. At low concentrations the patterns remained stable as more cells flowed into the sound field (Figure 3 a and b). At higher input concentrations the stable pattern was increasingly disrupted as the clumps became overloaded. At high concentrations the clump pattern flitted from one pattern to another figure 3 c, d and e shows the clump number changing from 2 to 4 stacks.

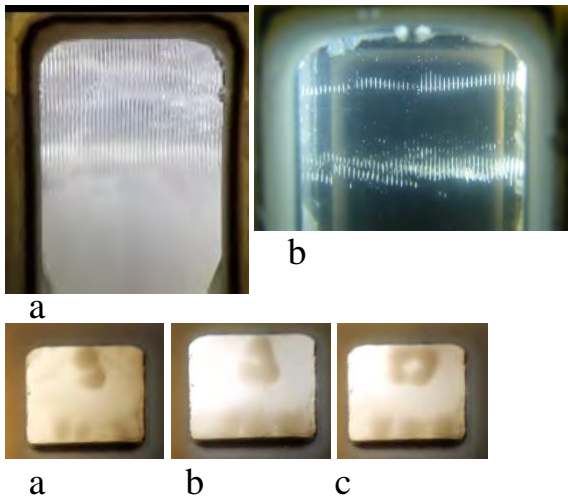


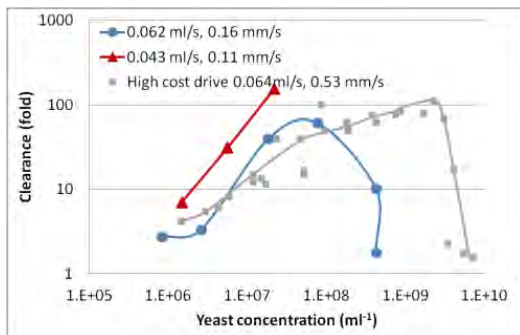
Figure 3: a) 10^7 ml⁻¹ Yeast moved to standing wave nodes as the suspension flows up into the sound field. b) 10^6 ml⁻¹ after a few seconds the cells form clumps.

c, d, e) Clump stacks viewed towards the drive unit. 10^8 ml⁻¹, at this concentration the number of clump stacks changes from 2 to 3 to 4 depending on the yeast load.

Stacks of clumps which occur help enhance the sedimentation process [4]. At high particle concentrations many cells sediment when the modes change (shown in figure 3 c, d and e). This mode change does not occur at lower concentration where a stable equilibrium is achieved between cells arriving and clumps sedimenting.

The clearance of yeast from suspension exceeds 100 fold at a low flow rate (see figure 4). This is similar to the clearance achieved with broad band amplifiers.

Figure 4: Log-log plot of the dependence of filtration (clearance) of yeast on the input concentration of yeast, at two flow rates. High cost drive results from ref 1.



In Figure 4 the chamber for the high cost ultrasound drive (data from [1]) had a smaller cross section (10 x12 mm) than the chamber presented here, therefore turbulence produced for example by falling clumps, would have been lower. This lower turbulence probably gives more advantage than the quality of the ultrasound source.

The sudden efficiency drop at high concentrations indicates the absence of space between the hydrated cells, this packed condition was also disrupted by turbulence in the current chamber.

Agglutination tube results

By using a waveguide (a strand of cooked spaghetti)[3] to carry sound from the fogger it is possible to take sound to any device without the need for purpose built chambers as shown in figure 5. This may have applications for microsystems where low power is sufficient since there are losses associated with waveguides.

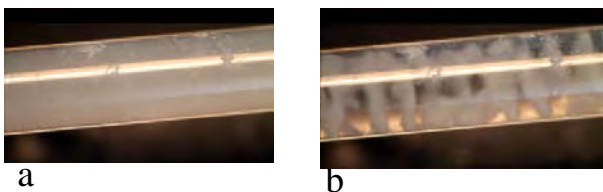


Figure 5: Yeast suspension in a glass capillary tube. Sound was transferred from the fogger to the capillary through a waveguide. a) Sound off. b) Sound on.

Conclusion

- For enhanced sedimentation reactions the position of clumps is not critical and therefore this is well suited to a fogger type drive unit.
- For agglutination reactions the position of clumps is not critical and therefore this is well suited to a fogger type drive unit.
- The unit is not an energy efficient source of ultrasound, cooling water was used to maintain a constant temperature.
- The unit provides sufficient power for both micro acoustofluidic devices and units with several mls of fluid.
- The low cost, ease of use and rugged design of Fogger devices should allow ultrasonic filtration to start taking place in laboratories and other locations which are not primarily dedicated to ultrasound research.

Acknowledgements

This work was partly funded by FloDesign Sonics.

References

- [1] J.J. Hawkes and W.T. Coakley. *Enzyme Microbial Tech.* **19**, 57-62 (1996).
- [2] M. Wiklund, J.J. Hawkes and S. Radel. *Lab Chip* **13** 25-39 (2013)
- [3] J.J. Hawkes. Youtube. Some Acoustic properties of cooked spaghetti (2014).
- [4] K.C. Chitale, B. Lipkens, W. Presz, O. Desjardins *Proc Acoust Soc Am* **23** 045004 (2015)

Tuning the Music: Acoustic Force Spectroscopy (AFS) 2.0

Douwe Kamsma^{1,2}, Ramon Creyghton³, Gerrit Sitters^{1,2,4}, Gijs J.L. Wuite^{1,2} and Erwin J.G. Peterman^{1,2}

[1] Department of Physics and Astronomy, Vrije Universiteit Amsterdam, Amsterdam, The Netherlands
 [2] LaserLaB Amsterdam, Vrije Universiteit Amsterdam, Amsterdam, The Netherlands
 [3] Department of Physics and Astronomy, University of Amsterdam, Amsterdam, The Netherlands
 [4] LUMICKS B.V., Amsterdam, The Netherlands

Introduction

AFS is a recently introduced high-throughput single-molecule technique that allows studying structural and mechanochemical properties of many biomolecules in parallel [1]. AFS is a Lab-on-a-chip device consisting of a flow cell with a piezo element glued on top. It uses acoustic force to stretch multiple molecules individually tethered between a surface and a microsphere. It distinguishes itself from other single-molecule techniques by a high experimental throughput, a wide force range and an unmatched range of force-loading rates. AFS experiments are highly parallel, allowing the simultaneous measurement of thousands of biomolecules simultaneously, in a single field of view. Here we present new technical developments which make AFS more accessible for a wider range of applications [2].

Transparent piezo

In the original AFS setup, a PZ26 opaque piezo element was used to generate the acoustic wave [1]. This made the implementation of bright-field microscopy impossible and a more complicated epillumination method had to be used. Here we introduce the use of transparent piezo elements as developed by Brodie et al. [3]. These transparent piezos are made of lithium niobate crystals with indium tin oxide electrodes. This piezo transmits 55% of the light with a wave length of 455 nm. With these piezos, bright-field illumination (Fig.1) can be implemented resulting in a more homogenous illumination. This yields a higher tracking accuracy and a larger field of view in which tethers can be tracked. Furthermore, this makes it possible to integrate AFS in most existing microscopes.

Optimizing layer thicknesses

An AFS sample chamber can be brought in acoustic resonance using only a specific set of frequencies, depending on chamber geometry and materials used. To optimize the sample chamber, we developed a MATLAB program that can calculate the resonance frequencies of a chamber geometry and the corresponding force profiles in the fluid layer. A single configuration can be calculated within 5 ms and therefore a large set of configurations can be computed to find the optimal dimensions for our system. Specifically, we used the model to optimize layer thicknesses with the goal to apply a force at the bottom fluid layer with a minimal force gradient. From the example shown in figure 2 it can be concluded that a thicker matching layer results in a lower quality number (QN), which represents the force at a specific height in fluid channel divided by the electrical input power. Furthermore, the acoustic power is almost constant between 100 and 1000 μm .

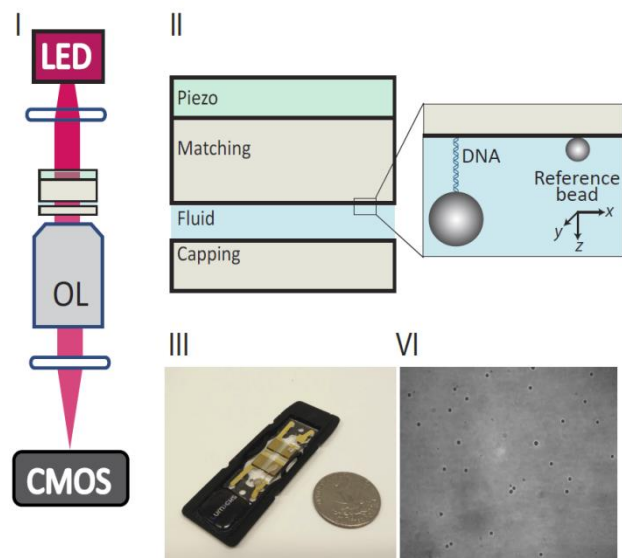


Figure 1: Illustration of the AFS setup. (I) The AFS chip is imaged using an inverted microscope with objective lens (OL), a digital CMOS camera and LED light source (455 nm). (II) The flow cell consists of two glass plates with a fluid chamber in between. A transparent piezo element is attached to the upper glass slide. Using an overhang the piezo is electronically connected. (III) A picture of the AFS chip (IV) and a digital camera image.

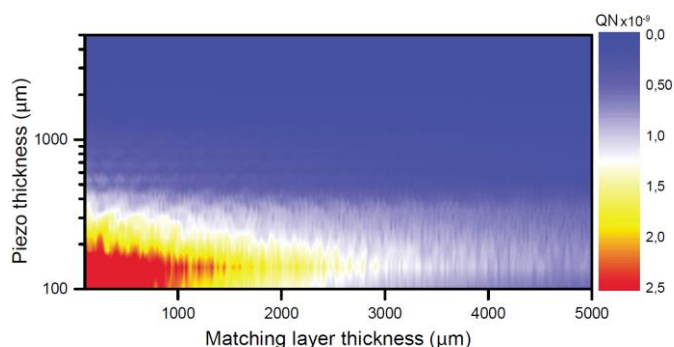


Figure 2: A contour plot of the QN (N/W) $3 \mu\text{m}$ above the capping layer with the force directed towards the fluid layer for a $4.5 \mu\text{m}$ polystyrene bead. Combination of piezo and matching layer thickness, the fluid and capping thickness ranging between $10\text{--}300$ and $50\text{--}300 \mu\text{m}$, respectively, with of $10 \mu\text{m}$ steps.

Direct measurement of the force profile

Our model allows us to predict the force profile along the fluid channel of the flow cell. To validate and calibrate the predicted resonance frequencies, we track the free movement of particles ($6.84 \mu\text{m}$ diameter silica) driven by the acoustic force. After switching on the acoustic force, particles are pushed away from the surface in the direction of a node of the acoustic standing wave. After switching off the force, particles sink to the bottom with a constant speed until they reach the surface. The forces acting on such a suspended particle are the gravitational force, buoyancy, the Stokes drag and the acoustic radiation force. For a particle moving at constant velocity these forces cancel out. The gravitational force and buoyancy are constant, while the drag force is directly related to the particle's velocity, meaning that from the particle velocity the drag force can directly be calculated. In Kamsma et al. [2] we demonstrate that this method to validate and quantify the acoustic force profile, is straightforward and quick, and can be used to calibrate any layered acoustic resonator comprising a fluid layer.

Optimizing the acoustic-force profile

With our force-profile calibration method we demonstrated that two resonance frequencies can be applied at the same time to change the shape of the force profile within the device [2]. Shaping force profiles can be used to create a more homogeneous force field, which is beneficial when the biomolecules studied undergo large length changes. By doing the opposite, and measure at a location in the force profile where the force gradient is very high, AFS can be transformed into a distance clamp. A distance clamp is better for probing multiple rupture events on a single construct.

Conclusion

AFS is a recently developed technique with much room for improvements. Each of the new AFS developments presented here can open the doors for increasingly diverse measurement opportunities on massively parallel single-molecule systems.

References

- [1] G. Sitters, D. Kamsma, G. Thalhammer, M. Ritsch-Martel, E.J.G. Peterman, G.J.L. Wuite, Acoustic force spectroscopy, *Nat. Methods*, 12 (1) (2014), pp. 47–50
- [2] Douwe Kamsma, Ramon Creyghton, Gerrit Sitters, Gijs J.L. Wuite, Erwin J.G. Peterman, Tuning the Music: Acoustic Force Spectroscopy (AFS) 2.0, *Methods*, Accepted 4 May 2016, Available online 6 May 2016
- [3] G.W.J. Brodie, Y. Qiu, S. Cochran, G.C. Spalding, M.P. MacDonald, Optically transparent piezoelectric transducer for ultrasonic particle manipulation, *IEEE Trans. Ultrason. Ferroelectr. Freq. Control*, 61 (3) (2014), pp. 389–391



Comparison between acoustic streaming induced fluid flow in 3D-simulation and experiment

Florian Kiebert¹, Stefan Wege¹, Jörg König¹, Robert Weser¹, Hagen Schmidt¹

¹Leibniz Institute for Solid State and Materials Research Dresden, D-01171 Dresden, Germany
E-mail: f.kiebert@ifw-dresden.de

Introduction

In acoustofluidics, the simulation of the acoustic streaming is an important part of the understanding of both particle focussing and mixing in a microchannel. By now there are in principle two ways to deal with this simulation task. One way is the 2D simulation of the problem including the wave field [1] and the second way to use the volume force [2] to simulate in 3D [3]. We adopted the second approach, used so far for droplets for the microchannel. Indeed the main difference is now given by the damping of the PDMS, so the amplitude of the SAW on the surface couldn't be calculated following Franke et al. 2003 [4]. Besides we replaced the damping perpendicular to the substrate proposed by Shiokawa by the damping following Stokes' law of sound attenuation. Furthermore we conducted vibrometer measurements to determine the SAW amplitude profile in reality. With this measured amplitude the simulation could be compared with flow measurements we recently performed. So for the first time a quantitative comparison between measurement and simulation in 3D will be given.

Simulation and experiment

We used a typical setup consisting of a piezoelectric LiNbO₃ chip (128° rotated Y cut, X-propagation direction) and a monolithic PDMS microchannel. The fluid flow induced in the PDMS microchannel by the SAW-device was measured using a μ Astigmatism Particle Tracking Velocimetry system [5].

For the simulation of the acoustic induced fluid flow in a PDMS-microchannel we solved the Navier-Stokes-equation for the special case of the Stuart streaming [5] utilising COMSOL Multiphysics. The volume force f used for the simulation reads according to [2]

$$f_{\text{Shiokawa}} = \rho_0(1 + \alpha_L^2)^{3/2} u_1^2 \omega^2 \alpha \exp(2\alpha x + \alpha_L \alpha z) \quad (1)$$

with $\alpha_l = \sqrt{\left(\frac{c_{\text{SAW}}}{c_{\text{Fl}}}\right)^2 - 1}$ and c the phase velocity of the SAW and the speed of sound in the fluid, respectively. With our replacement using Stokes' law of sound attenuation the volume force becomes

$$f = \rho_0 \omega^2 u_1^2 \exp(-2(\alpha x - \cos(\vartheta_R) \beta z)) \beta \begin{pmatrix} \sin(\vartheta_R) \\ 0 \\ \cos(\vartheta_R) \end{pmatrix} \quad (2)$$

whereby ρ_0 is the density of the fluid, ω the angular frequency, u_1 the amplitude of the SAW and α and β the damping coefficient of the SAW and the BAW, respectively. Here the only unknown quantity is the amplitude of the SAW. In contrast to Alghane et al. We didn't calculate the amplitude of the SAW, instead we performed a measurement for the determination providing comparable results to our setup.

For the determination of the amplitude profile of the acting SAW we used an vibrometer from Polytec. To get an estimation of the damping caused by the PDMS wall we measured the SAW device without channel and with a half channel bounded to the surface. With this measurements we determined a damping constant for the PDMS wall. For the simulation we assumed that the amplitude of the SAW is constant over the IDT aperture and given by the product of damping factor and the average amplitude over the IDT aperture for the SAW-device without channel.

Results

The measured wave profiles of a SAW-device (wavelength 30 μm) in front and behind the PDMS wall are depicted in fig. 1. From this measurements the damping factor for a 500 μm thick PDMS wall

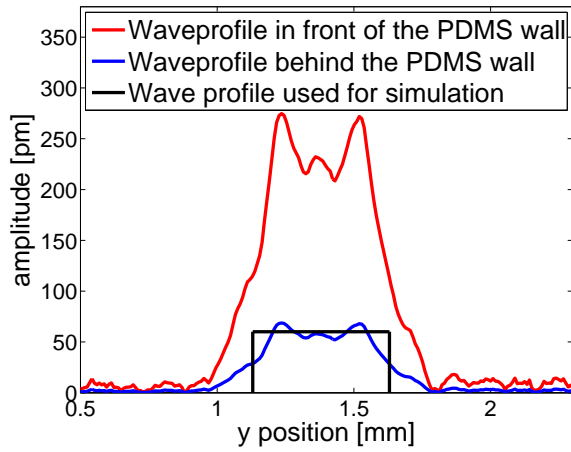


Figure 1: Measured wave profile in front of the PDMS wall (red) and behind the PDMS wall (blue). The black rectangular function is the product of damping factor and the average amplitude over the IDT aperture and used for the simulations.

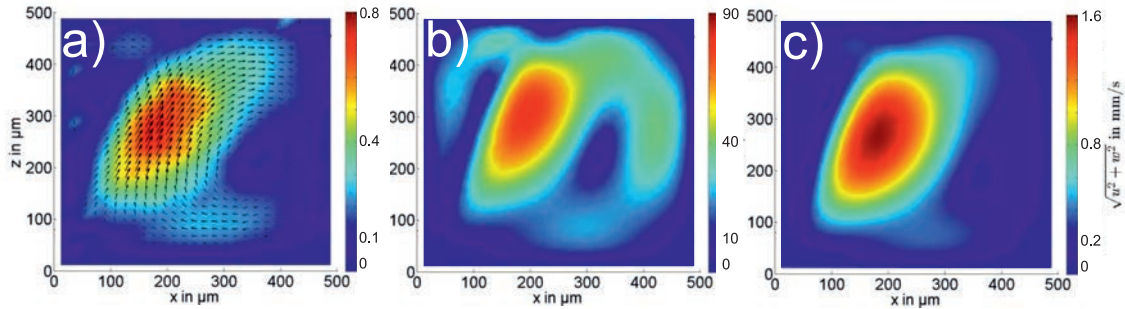


Figure 2: Figures of the fluid velocity in experiment and simulation in a 500 µm PDMS microchannel. a) Measurement; b) Simulation following Shiokawa; c) Simulation in consideration of Stoke's law of sound attenuation.

was determined to 4. This is in good comparison to the damping reported so far determined by transmission measurements [6].

The comparison between the simulations and the measurement of the fluid flow inside the channel is shown in fig. 2. The shape of the fluid flow is for both simulations comparable to the measurement. For our equation the shape fits even better to the measurement. Beyond the speed of the fluid flow in the simulation differs strongly from the experiment. For the volume force proposed by Shiokawa the fluid flow is much too strong. For our new equation the velocity is still a factor two to fast. This could be caused by a wrong determination of the amplitude of the SAW. As described above we measured the amplitude behind a PDMS wall but in an unloaded state. In the experiment the surface is additionally loaded with water. This will lead to a decreased amplitude on the surface and hence to a smaller velocity in the simulation.

Conclusion

We have shown that at least for a PDMS microchannel the volume force proposed by Shiokawa isn't applicable. The equation derived by us fits much better, but still has a distinction of factor 2 to the measurement. This could be caused by an incorrect measurement of the amplitude of the SAW. A second reason could be the neglect of the damping of the BAW perpendicular to the wave vector. We assumed a damping only in propagation direction. This additional damping would also lead to decreased fluid velocity in the simulation. Further investigations have to deal with this facts to improve the accordance between simulation and experiment.

References

- [1] J. Vanneste and O. Bühler. Proc. R. Soc. A **467**, 1779-1800 (2011).
- [2] S. Shiokawa and Y. Matsui. MRS Proceedings **360**, 53-64 (1994).
- [3] M. Alghane, Y. Q. Fu, B. X. Chen. Microfluidics and Nanofluidics **13**, 919-927 (2012).
- [4] K. Franke, M. Ross-Messemer, A. Menck, F. S. Hoeller, H. Schmidt and M. Weihnacht. IEEE Transactions on Ultrasonics, Ferroelectrics, and Frequency Control, **50**, 77-80 (2003).
- [5] C. Cierpka, R. Segura, R. Hain and C. J. Kähler. Measurement Science and Technology, **21**, 1-13 (2010).
- [6] A. Winkler, R. Brünig, C. Faust, R. Weser and H. Schmidt. Sensors and Actuators A: Physical, In press (06/2016).

Financial support by German BMBF (InnoProfile-Transfer grant 03IPT610A) is gratefully acknowledged.



Optical and acoustic sensing in dual phononic and photonic crystal

Rayisa P. Moiseyenko¹, Samira Amoudache^{2,3}, Yan Pennec², and Bahram Djafari-Rouhani²

¹Department of Physics, Technical University of Denmark, Denmark

E-mail: raymoi@fysik.dtu.dk, URL: <http://www.fysik.dtu.dk/microfluidics>

²Institut d'Electronique, de Microélectronique et de Nanotechnologie, Université Lille 1, France

³Laboratoire de Physique et Chimie Quantique, Université Mouloud Mammeri, Algeria

Introduction

The ability to precisely sort, move and mix individual microparticles, cells or droplets, sensing components in mixtures in suspension is of interest for various chemical and biological applications, ranging from basic cell biology to clinical diagnosis such as cancer cell detection, drug screening, and tissue engineering. Rapid processing is often a crucial factor in diagnostics and treatment. Thus, simple and efficient particle separation methods are fundamentally important. We discuss theoretical study of the use of periodic structures for sensing analyte's properties.

Currently, many biologists employ optic, magnetic or electric tweezers for single-cell manipulation due to their excellent precision and versatility.[1] However, they have their disadvantages. Optic tweezers may damage cells by heating and the system itself is large and expensive. Recently, there has been growing interest in on-chip microchannel acoustophoresis for biological applications, which allows label-free separation based on the size, density and compressibility of particles [2, 3]. Acoustophoresis is notably advantageous because it requires no pretreatment of the particles, label free and can be applied to virtually all kinds of particles, regardless of optical or charge properties. It is based on the bulk acoustic resonances in water, where the resonance frequency is governed by the width of the fluid channel, to create a standing wave field. Silicon and glass are conventional materials for such purpose. We present alternative method of sensing involving phoxonic crystals [4, 5] using simultaneous phononic and photonic band gaps, i.e. frequency regions where propagation of acoustic and electromagnetic waves through the structures are forbidden.

Geometry and numerical results

The structure is composed of a silicon crystal plate drilled with air holes (Figure. 1). The whole device is immersed in a liquid [9]. The goal is to define a phoxonic sensor sensitive simultaneously to the optical and acoustic index of refraction of the fluid. Calculation of the photonic and phononic transmission coefficient is performed using the finite difference time domain (FDTD) method.

The crystal is constituted of cylindrical inclusions of finite height along the z direction, arranged periodically on a square lattice in the (x, y) plane. The lattice is periodically infinite along x and y . The input signal is launched from the left of the unit cell, perpendicularly to the plate. The transmitted signal is then recorded at the end of the second homogeneous region and integrated along the (x, y) plane. To yield the transmission coefficient, the outgoing signal, recorded as a function of time, is Fourier transformed and normalized to the Fourier transform of a signal propagating through a homogeneous liquid.

The introduction of defects inside dual photonic and phononic crystals gave the opportunity to trap both phonons and photons in the same cavity for the purpose of enhancing their optomechanical interaction. The purpose of the presentation is to estimate the potentiality of a phoxonic crystal plates to be an efficient tool for sensing simultaneously the light and sound velocities of liquids in a same structure. From the point of view of sensing applications, some authors have studied the normal transmission of optical waves through a plate perforated periodically with holes and measured the shift of a well-defined feature in the spectrum with the refractive index of the embedding liquid.[6] Phononic crystals plates have recently been introduced as a new sensor platform featuring a liquid filling air inclusions or cavity defect.[7,8]

Sensing (refractive index of analyte for photonics, sound velocity of analyte for phononics) is achieved by using asymmetric peaks in the phononic and photonic transmission spectra (Fano-like resonances). In photonics, the origin comes from guided modes in the photonic plate while in phononics we show that it comes from the excitation of standing waves confined inside the cavity coming from the deformation of the water/silicon edges of the cylindrical inclusion.

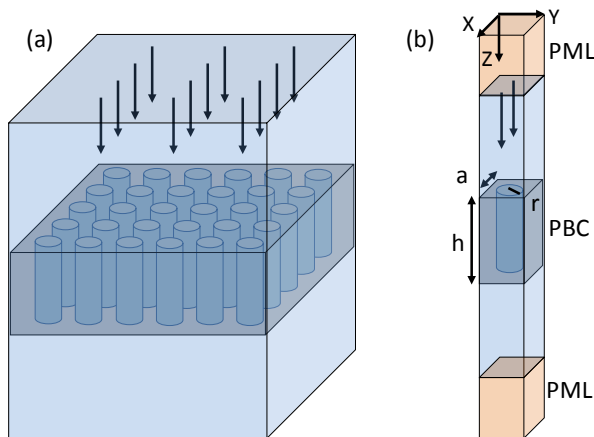


Figure 1: (a) Three-dimensional geometry of a normal transmission through a silicon periodic plate embedded in a liquid. (b) Elementary unit cell used for FDTD calculation of the photonic and phononic transmission. On each y-boundaries of the unit cell, perfect matching layers are applied while on the x-boundaries periodic boundary conditions insure the periodicity of the crystal. The phononic/photonic crystal plate of thickness h has a lattice parameter a and a radius r . [9]

Conclusion

This contribution shows the dual existence of optical and acoustic enhanced resonances inside silicon phononic and photonic (phoxonic) crystal plate under normal incidence of light and sound. Such ultra-compact structure then represents a label-free, affinity-based acoustic and optical nanosensor, useful for biosensing applications. Finally such structures can also open the way to enhance the phonon-photon interactions with the simultaneous confinement of the phononic and photonic waves. Through the confinement and the interaction between optical and acoustic waves inside mixed phoXonic crystals, we expect the enhancement of the properties of dual sensors.

References

- [1] D. Grier, *Nature*, **424**, 810–816 (2003)
- [2] M. Antfolk, P. B. Muller, P. Augustsson, H. Bruus and T. Laurell, *Lab Chip*, **14**, 2791–2799 (2014)
- [3] A. Lenshof, C. Magnusson and T. Laurell, *Lab Chip*, **12**, 1210–1223 (2012)
- [4] S. Mohammadi, A. A. Eftekhar, A. Khelif, and A. Adibi, *Opt. Express* **18**, 9164 (2010).
- [5] Y. Pennec, B. Djafari-Rouhani, E. H. El Boudouti, C. Li, Y. El Hassouani, J. O. Vasseur, N. Papanikolaou, S. Benchabane, V. Laude, and A. Martinez, *Opt. Express* **18**, 14301 (2010).
- [6] R. Gordon, D. Sinton, K. L. Kavanagh, and A. G. Brolo, *Acc. Chem. Res.* **41**, 1049 (2008).
- [7] A. Sato, Y. Pennec, T. Yanagishita, H. Masuda, W. Knoll, B. Djafari-Rouhani, and G. Fytas, *New J. Phys.* **14**, 113032 (2012);
- [8] R. Lucklum, M. Ke, and M. Zubtsov, *Sens. Actuators, B* 171–172, **271** (2012).
- [9] S. Amoudache, R. Moiseyenko, Y. Pennec, B. Djafari-Rouhani, A. Khater, R. Lucklum, and R. Tigrine *J. Appl. Phys.* **119**, 114502 (2016)

Label-free separation of neuroblastoma cells from mononuclear cells using an acoustophoresis-based microfluidic chip

Franziska Olm¹, Anke Urbansky², Thomas Laurell², Stefan Scheduling¹

¹Laboratory Medicine, Lund University, Lund, Sweden

E-mail: franziska.olm@med.lu.se

²Biomedical Engineering, Lund University, Lund, Sweden

Introduction

The established treatment for children with high risk neuroblastoma is high dose chemotherapy and the transplantation of autologous peripheral blood progenitor cells (PBPC). Survival rates are poor because of relapses, which might occur partly due to graft-contaminating tumor cells. Current methods to remove tumor cells from the graft (“purging”) are time and labor consuming or expensive. We established an acoustophoretic microfluidic chip-based technology for efficient and gentle cell separation. An acoustic standing wave generated in the microfluidic channel manipulates cells differently depending on their acoustophysical-properties, including size, density and compressibility. Acoustophoresis was used to efficiently remove platelets from PBSC products [1] and for sorting of bead-marked lymphocytes [2]. Furthermore, the label-free isolation of prostate cancer cells from blood was realized [3]. Based on this work, we started to develop acoustophoresis as an effective, label-free and non-contact purging technology for neuroblastoma cell-contaminated PBSC products by showing proof-of-principle evidence by successfully separating neuroblastoma cell line cells (NBCs) from mononuclear cells isolated from whole blood (MNCs).

Study design and methods

For the acoustophoretic separation, NBCs were spiked into MNCs, under defined conditions. A microfluidic chip, as shown in Figure 1, was used. Sample was infused in the channel through the sample inlet and after entering the channel, cells got aligned in the pre-focusing field generated by a 5 MHz resonant transducer. Infused buffer supported the separation by ensuring laminar flow. Size-based separation took place in the second acoustic field (2 MHz transducer). NBCs were collected in the center outlet and MNCs in the side outlet, respectively. Following separation, fractions were analyzed for separation efficiency, purity and viability of MNCs and NBCs, respectively. The influence of different voltages applied on the main separation transducer on the separation outcome of the different cell types, as well as different cell concentrations and tumor cell/MNC ratios on separation efficiency were investigated. A T-cell proliferation assay was performed to investigate a possible impact of the acoustic separation on T-cell function.

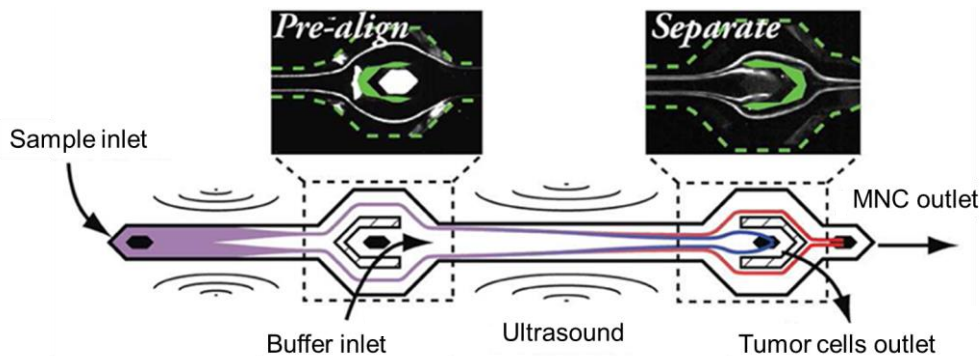


Figure 1: Schematic overview of the used microchip. The sample is infused into the chip through the sample inlet and reaches the pre-alignment channel with the 5 MHz transducer, where the cells are pre-focused. Washing buffer as central inlet fluid supports the separation. The pre-aligned cells enter the second acoustic field in the separation channel, generated by the 2 MHz transducer, and move according to their acoustic properties leading to a separation. The NBCs move into the central outlet and the MNCs to the side outlet. The drawing is not in full-scale, adapted with changes from Augustsson et al. 2012 [3].

Results

Using a concentration of 1×10^6 cells/ml and NBC/MNC ratio of 1:1, $92 \pm 3.5\%$ of MNCs were recovered, while tumor cells were depleted by nearly 2 logs ($97.4 \pm 3.8\%$) (Figure 2 A, B). At a NBC/MNC ratio of 1:1000, 87.9% of the MNCs could be recovered, while depleting tumor cells to undetectable levels (Figure 2 C). Cell type distribution analysis after separation showed that especially lymphocytes were recovered in the target side fraction, while granulocytes and monocytes tended to be collected in the central waste fraction outlet together with the tumor cells. T-cell assays showed that the proliferation capacity of sorted lymphocytes was not affected by the acoustic sorting.

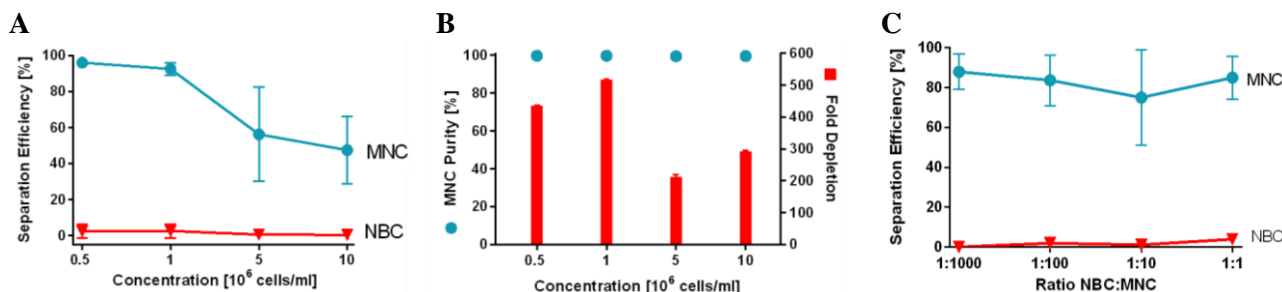


Figure 2: Testing of different cell concentration and NBC/MNC ratios on cell separation efficiency. MNCs and NBCs were mixed 1:1 for concentration tests and the concentration of the samples was set to 0.5×10^6 , 1×10^6 , 5×10^6 and 10×10^6 cells/ml. For ratio tests the sample concentration was chosen as 1×10^6 cells/ml and cells were mixed in ratios of 1:1, 1:10, 1:100, and 1:1000, respectively. Shown are: A) separation efficiency [%], B) MNC purity [%] and fold depletion of NBC/MNC in the target fraction.

Conclusion

These results provide proof-of-principle evidence that neuroblastoma tumor cells can be separated from MNC preparations with high efficiency and purity. Thus, acoustophoresis is a promising technology for PBPC processing, which provides the basis to develop label-free, non-contact and improved tumor cells purging procedures for future clinical use.

Disclosure

These results were recently presented at the 31st Congress of the International Society for Advancement of Cytometry and will be presented with a poster on the Microfluidics 2016 EMBL Conference in July.

References

- [1] J. Dykes, A. Lenshof, I. Åstrand-Grundström, T. Laurell, S. Scheduling, and M. Rojas. *PLoS ONE* **6** (8). e23074 (2012).
- [2] A. Lenshof, A. Jamal, J. Dykes, A. Urbansky, I. Åstrand-Grundström, T. Laurell, and S. Scheduling. *Cytometry, Part A* **85** (11), 933-941 (2014)
- [3] P. Augustsson, C. Magnusson, M. Nordin, H. Lilja, and T. Laurell. *Anal. Chem.* **84** (18), 7954–7962 (2012)

Acoustophoretic manipulation for use in particle detection

Filip Plazonic, Dario Carugo, Martyn Hill, and Peter Glynne-Jones

Mechatronics, Faculty of Engineering and the Environment, University of Southampton, Southampton, United Kingdom
E-mail: fp3g10@soton.ac.uk

Introduction

Poor water quality is estimated to be a cause of 3.1% of deaths worldwide and is a considerable cost in healthcare [1]. It can also compromise product quality in several diverse industries (food, pharmaceutical, chemical, textile, etc.) [2]. Monitoring the quality of the water used in those industries, as well as healthcare services, is of utmost importance. Current methods have high enough detection sensitivity, but lack the speed needed for a quick response in case of microbiological contamination [3,4].

A device that combines an antibody biosensor to capture pathogens with acoustic manipulation from ultrasonic standing waves (USWs) was further developed from a previous design [5] in order to reduce the time of analysis and even provide real-time data readouts. The device was targeted to detect a concentration of 300 CFU/ml in a 10 minute assay, as well as being robust enough to be assembled easily and insensitive to manufacturing variations. Preliminary data for this new device architecture show that such detection is possible at a conservative flow rate of 30 ml/hr, with capture rates of approximately 90-95 %.

Device schematic

The device is a combination of a half-wave and a thin-reflector layered resonator, and its design was optimized using a 1-D transfer impedance model. It consists of a PZT transducer glued onto a 1 mm stainless steel carrier layer. The fluid channel is 130 μm thick and is separated from the 170 μm glass coverslip reflector by a PDMS gasket and a cellulose acetate spacer. The design shows significant improvement over the previous Macor ceramic design [3], which may be due to material properties of the stainless steel carrier being more conducive to a stronger resonance in this system. The device is also shown to tolerate variation in the carrier layer thickness of up to 0.1 mm, resulting in only a small decrease in radiation force (3%).

The device has two transducers. The first one, over the first half of the channel (in the lengthwise direction) is tuned to set up a half-wave (HW) field, while the second one is tuned to set up a thin-reflector (TR) mode. As the spores/bacteria flow within the US field, they are first concentrated in the central plane of the channel and then pushed towards the reflector layer on which an antibody coating has been applied to capture them. Figure 1 shows the device in its constitutive layers (a) and fully assembled (b).

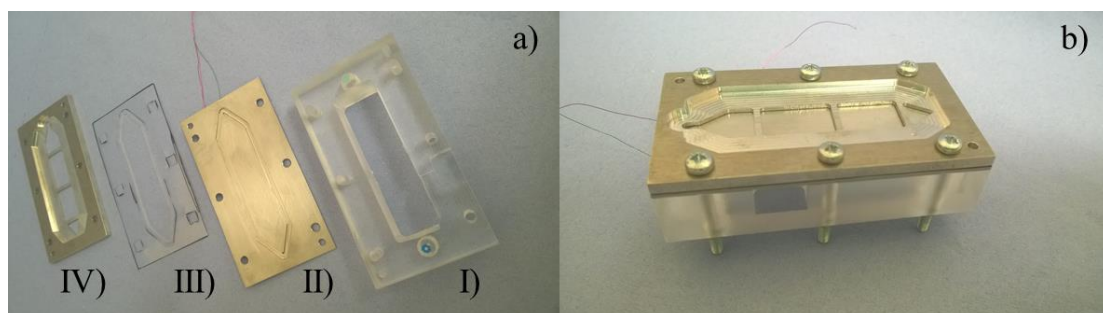


Figure 1: The device a) disassembled with components I) PMMA manifold, II) carrier layer with transducers on bottom, III) spacer and gasket, and IV) metal clamp and reflector layer glass coverslip underneath; and b) assembled

Results and discussion

To assess the robustness of device operation, in this preliminary stage, two devices were assembled and disassembled multiple times to determine potential deviations in the resonant frequency. Figure 2 shows a composite admittance plot of multiple tests done to show how the resonant frequency is stable over multiple uses.

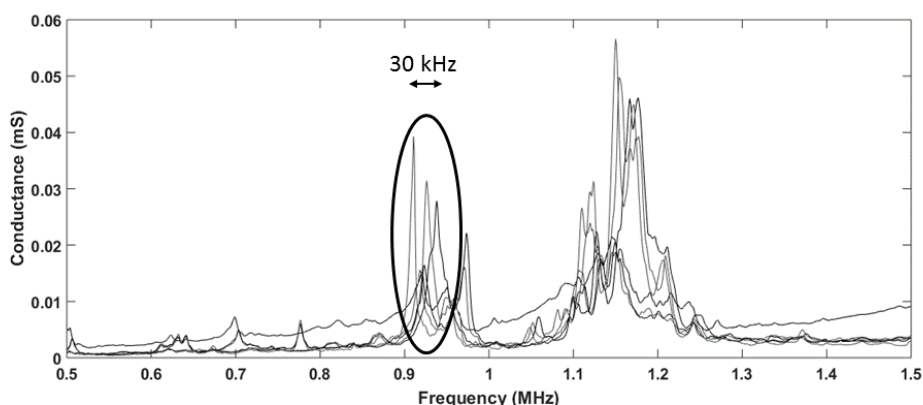


Figure 2: Conductance plot showing the resonant frequencies of two devices during multiple assemblies, and their small spread (30 kHz)

To characterize the device 1 μm beads were flown into the device, and after a duration of activity a cross-section of the channel was imaged with the microscope, using a z-scan technique. Figure 3 shows the distribution of 1 μm diameter beads (in the z-direction) imaged in a region just after the second transducer when i) only the TR transducer is used, and ii) both the HW and TR transducers are turned on. Even with just the TR transducer, 90% of the beads are pushed towards the reflector layer, while with both transducers this number increases to 95%. It is believed that, with a 100 μm fluid channel (the next generation device), and an easier-to-use manifold, the capture rate is likely to increase further. The figure omits the first image, taken on the reflector layer itself, as the scaling obscures the results as well as not being relevant itself (the number of beads is cumulative so the further into the experiment the more beads there are).

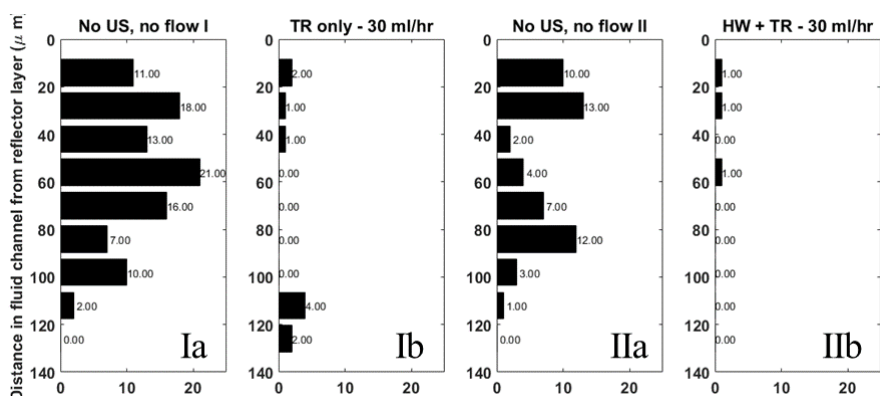


Figure 3: From left to right – Ia) shows the 1 μm diameter bead distribution in the channel before any flow or acoustic manipulation is applied; Ib) shows the subsequent distribution after 1 minute of 30 ml/hr flow as well as an acoustic excitation from just the TR transducer at 30 Vpp at 930 kHz; IIa) shows the initial particle distribution for the second experiment; and IIb) shows the end-point distribution, after 1 min of 30 ml/hr flow with both the TR and HW transducers activated

Conclusion

The device developed in this study is set to be a robust and cheaper alternative to the more established detection methods. It can be easily assembled and reassembled, and is insensitive to small variations in device geometry, with the resonant frequencies stable to ± 10 kHz, and with very good capture rates of around 95%. In the future, this capture rate should increase as the fluid channel is reduced further (to ~ 100 μm) and the assembly procedure is further simplified.

References

- [1] W.H.O., 2012. Burden of disease and cost-effectiveness estimates. http://www.who.int/water_sanitation_health/diseases/burden/en
- [2] Kneese, A.V., Bower, B.T., 1984. Managing water quality: economics, technology, institutions, Rff Press
- [3] Lazcka, O., Del Campo, F.J., Munoz F.X., 2007. Biosens Bioelectron, 22, pp. 1205-1217
- [4] Ivnitcki, D., Abdel-Hamid, I., Atanasov, P., Wilkins, E., 1999. Biosens Bioelectron, 14, pp. 599-624
- [5] Carugo D., Octon, T. Messaoudi, W. Fisher, A.L., Carboni, M., Harris, N.R., Hill, M. Glynne-Jones, P. 2014, Lab Chip, 14, pp. 3830-3842

Feasibility of High Throughput Particle Separation Using the Continuous Phase Modulation in Standing Surface Acoustic Wave

Chanryeol Rhyou¹, Junseok Lee¹, Byungjun Kang¹, and Hyungsuk Lee¹

¹School of Mechanical Engineering, Yonsei University, Seoul, Korea
E-mail: hyungsuk@yonsei.ac.kr, URL: <http://leelab.yonsei.ac.kr>

Introduction

This work includes theoretical analysis and experiments for development of particle separation technique using the standing surface acoustic waves (SSAW). Although several particle manipulation techniques using SSAW have been presented [1-4], a separation that can be applied to a channel as wide as multiple pressure nodes (MPN) has not been developed explored as yet. In this paper, we demonstrate the feasibility of the particle separation technique in MPN, so called the continuous phase modulation (CPM).

Theory

In acoustofluidics, commonly characterized with low Reynolds number, Acoustic Radiation Force (ARF) generated by the external RF input signal and the viscous force play key roles in determining particle motion, because the inertial term can be neglected in the equation of motion.[5]

Particles trapped at pressure nodes in SSAW can be displaced by phase shift. If the phase is shifted by $\pi/2$, the particle will be displaced by an eighth of wavelength ($\lambda/8$). Phase shift at a constant rate, i.e. the continuous phase modulation, can be achieved by changing the frequency of RF input signal. In this case, the change of frequency should be very small compared to the original frequency. [6] Movement of particle during continuous phase modulation depends on the rate of frequency change and particle's dimension. Our theoretical analysis seek an optimal frequency change Δf_{opt} at which particle follow the translation of pressure nodes without oscillatory motion. The optimal frequency change Δf_{opt} is proportional to the volume (radius³) of particle. We applied this technique to separate particles with a reference radius R from others smaller than R .

Experiment

We perform experiment to apply the theoretical analysis to develop a method of particle separation. Two sizes of fluorescent particles, 6 μm and 15 μm diameters, are mixed. The mixture of beads are infused into a microfluidic channel of PDMS at a constant flow rate (3 $\mu\text{l/s}$) using a syringe pump system. Fluorescent beads are imaged at 25 fps and their locations are identified using ImageJ software. As shown in Fig. 2, both 6 μm

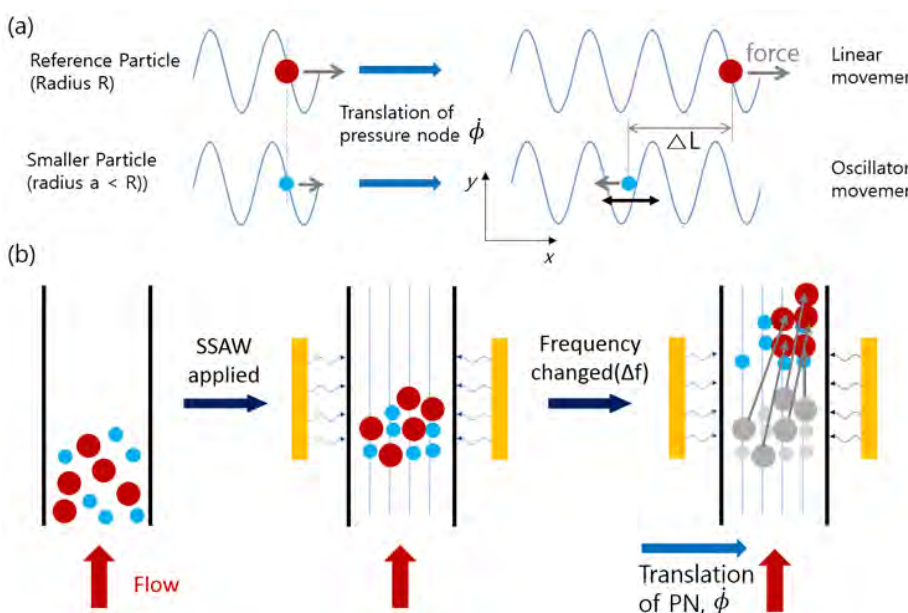


Figure 1: (a) Different movements of particles depending on their sizes. As a wave (Gor'kov potentials) propagates, particle with the reference size R can be modulated to be always forced maximally. On the other hand, a smaller particle lags behind the wave propagation and can be subject to the force to the opposite direction, leading to an oscillatory movement. Difference in displacement, ΔL , can be used for separating and sorting particles. (b) Sequences of particle separation with the continuous phase modulation. Initially, particles under SSAW will be trapped at pressure nodes. Displacement of particles in response to the frequency change (Δf) during continuous phase modulation depends on their sizes

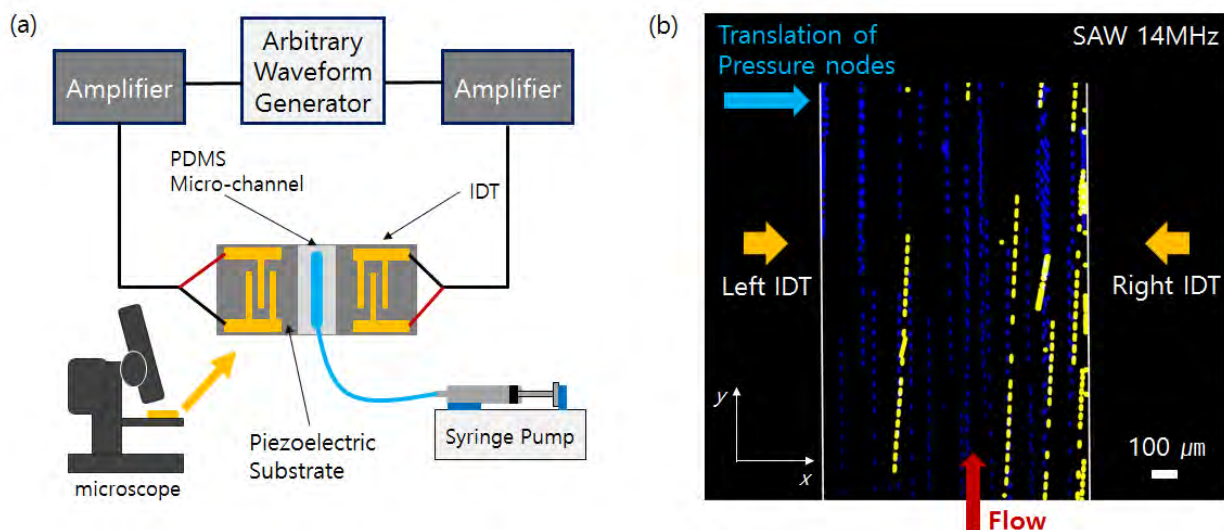


Figure 2: (a) Schematic of experimental setup (b) Stacked images of particles with a radius of $6\ \mu\text{m}$ (blue) and $15\ \mu\text{m}$ (yellow) in a microfluidic channel with y -directional flow. Due to the continuous phase modulation along x -direction, larger particles ($15\ \mu\text{m}$) are displaced to the right while smaller ones do not show any x -directional movement.

and $15\ \mu\text{m}$ beads are displaced along the y -direction due to the flow in a channel. However, in x -direction, the larger beads are displaced to the right by the continuous phase modulation while smaller one remains at the same position. It is expected that such a size-dependent response to CPM-SSAW can be developed into a method of high-throughput particle separation if incorporated with sheath flow.

Materials and methods

PDMS micro-channel (23mm length) was prepared with using SU8 mold provided by the manufacturer via conventional soft lithography. PDMS mixture of prepolymer (Sylgrad® 128) and curing agent at a ratio of 10:1 by volume were mixed over the SU8 mold inside the petri dish ($\Phi = 150\ \text{mm}$) and cured at $60\ ^\circ\text{C}$ in the drying oven overnight. The width and height of the main channel are $1050\ \mu\text{m}$ and $80\ \mu\text{m}$ respectively. The piezoelectric substrate is a 128° rotated Y -cut X -propagating Lithium Niobate (LiNbO_3). A sinusoidal RF input was generated by an arbitrary waveform generator (Keysight, HP33522). The RF input signal was amplified by the power amplifier (Mini-Circuits, LZY-22+). The particles are $6\ \mu\text{m}$ (Polyscience BioMag®, Bright Blue) and $15\ \mu\text{m}$ (Molecular Probe FluoSphere®, Orange) respectively. The particle mixture was infused by using the syringe pump (Fusion 200T) and observed at 4x magnification via both brightfield and fluorescence microscopy (Nikon Eclipse Ni-U)

Conclusion

We develop a technique of particle manipulation by modulating phase of SSAW continuously. Theoretically, we calculate the optimal rate of phase change to displace particles without lag compared with the wave propagation. Experimentally, we demonstrate to separate the particle with a specific size from others. Our technique can overcome the limitation of existing techniques using SSAW because it can be applied to a channel wider than the wavelength of SAW.

References

- [1] Shi, J., Huang, H., Stratton, Z., Huang, Y., and Huang, T. J. *Lab on a Chip*, 9(23), 3354-3359 (2009).
- [2] Destgeer, G., Lee, K. H., Jung, J. H., Alazzam, A., and Sung, H. J. *Lab on a Chip*, 13(21), 4210-4216 (2013).
- [3] Ding, X., Peng, Z., ... and Huang, T. J. *Proceedings of the National Academy of Sciences*, 111(36), 12992-12997. (2014).
- [4] Destgeer, G., Ha, B. H., ... and Sung, H. J. *Analytical chemistry*, 87(9), 4627-4632. (2015).
- [5] Nama, N., Barnkob, R., Mao, Z., Kähler, C. J., Costanzo, F., and Huang, T. J. *Lab on a Chip*, 15(12), 2700-2709. (2015).
- [6] Tran, S. B. Q., Philippe Marmottant, and Pierre Thibault. *Applied Physics Letters* 101.11: 114103 (2012).

Boundary conditions in numeric modelling of solid-fluid interactions in acoustofluidic microdevices

Nils R. Skov and Henrik Bruus

Department of Physics, Technical University of Denmark, DK-2800 Kongens Lyngby, Denmark
E-mail: nilsre@fysik.dtu.dk URL: <http://www.fysik.dtu.dk/microfluidics>

Introduction

Exact modelling of acoustofluidic microdevices is of increasing importance to guide proper device design. In the literature, microdevice modelling is often performed using simplified, approximate boundary conditions of the interaction between microchannel wall and device [1,2,3], to reduce computational requirements by excluding the microchannel walls from simulations. While these simplifications may be valid to a good approximation for the stiff and dense channel walls, e.g. made of borosilicate glass, they fail when approximating soft and light channel walls, e.g. made of PDMS, using the so-called lossy-wall boundary condition.

Model

A numeric model 2D model is set up in COMSOL Multiphysics. The model consists of a fluid domain (the channel) bounded to the sides and upwards by a solid domain (the channel walls) as shown in Fig. 1. Both domains are bounded downwards by a piezoelectric substrate, which in the model is replaced by a boundary condition. Additionally, reduced versions of the model are generated in which the interaction of fluid and solid along interfaces are replaced by boundary conditions as a comparison basis.

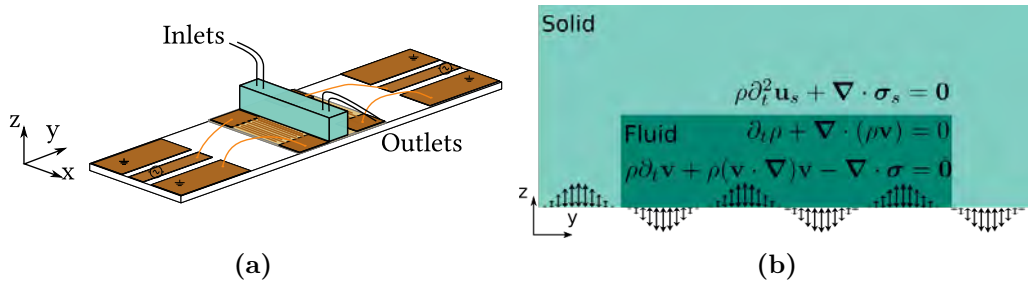


Figure 1: (a) A sketch of the actual physical system; solid wall defines a fluid-filled microchannel in three directions. The walls and the channel are resting on a piezoelectric substrate along which surface acoustic waves propagate. (b) The system is modelled two-dimensionally, with the motion of the piezoelectric substrate approximated by a harmonic sine function. The solid and fluid are modelled as separate domains, with separate governing equations, interacting along interfaces.

The problem is formulated using perturbation theory [4]. In the fluid domain of the model, the governing equations are first-order mass and momentum conservation, with temperature assumed constant, while the solid material is governed by linear elasticity. Along the lower boundary of the system, a harmonic expression is added to emulate the motion of the piezoelectric substrate. In order to couple the fluid and solid motions, velocity continuity is imposed from the solid to the fluid, while stress continuity is imposed from the fluid to the solid,

$$\mathbf{v} = \partial_t \mathbf{u}_s = -i\omega \mathbf{u}_s, \quad (1a)$$

$$\mathbf{n}_s \cdot \boldsymbol{\sigma}_s = \mathbf{n}_s \cdot \boldsymbol{\sigma}_f. \quad (1b)$$

Simplified boundary conditions

To lower computational requirements and model complexity, many numerical models in the literature solely model the fluid domain and replace the coupling outlined above with simplified boundary conditions to emulate the interactions. Depending on the interfacing material one of two conditions are usually applied; hard -all or lossy-wall, as shown in the reduced-model boundary conditions Eqs. (2) and (3).

The boundary conditions imposed, are designed to approximate different materials. The hard-wall condition Eq. (2) is intended to approximate hard and dense materials, e.g. borosilicate glass, by assuming the material does not move at all in the normal direction,

$$\mathbf{n} \cdot \mathbf{v}_1 = 0 \quad \text{or} \quad \mathbf{n} \cdot \nabla p_1 = 0, \quad \text{hard-wall along the fluid solid interface.} \quad (2)$$

The lossy-wall condition Eq. (3) approximates a wall through which there are radiative acoustic losses in the normal direction. The condition approximates wall motion based on the fluid pressure and the acoustic impedance of the surrounding material;

$$\mathbf{n} \cdot \mathbf{v}_1 = \frac{1}{\rho_s c_s} p_1 \quad \text{or} \quad \mathbf{n} \cdot \nabla p_1 = \frac{i \rho_0 \omega}{c_s \rho_s} p_1, \quad \text{lossy-wall along the fluid solid interface.} \quad (3)$$

Results

A selection of pressure plots of the fluid domain are shown. Comparisons are made between the reduced models and the full models. The reduced hard-wall model Eq. (2) is compared to a full model where the mechanical properties of borosilicate glass are used in the solid wall with varying wall thickness, while the reduced lossy-wall model Eq. (3) is compared to a full model where PDMS properties are used in the solid wall with varying thickness.

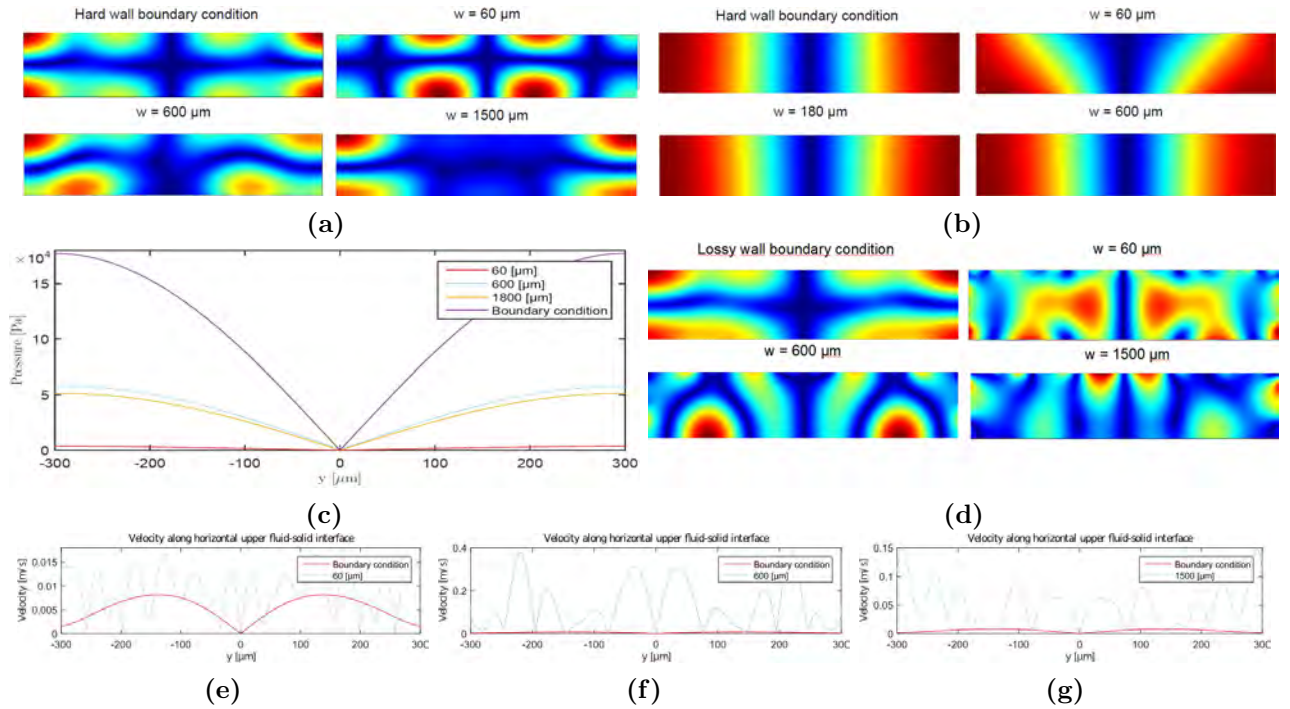


Figure 2: Colour plots of the first-order pressure fields for the reduced and full models. (a) For off-resonance actuation, the reduced hard-wall model is compared to the full borosilicate model for three wall thicknesses. (b) For on-resonance actuation, the reduced hard-wall model is compared to the full borosilicate model for three wall thicknesses. (c) Pressure profile of $|p_1|$ along the horizontal centre-line for the reduced hard-wall model and the full borosilicate model for three wall thicknesses. (d) For on-resonance actuation, the reduced lossy-wall model is compared to the full PDMS model for three wall thicknesses. (e-g) Comparison of the velocity solid-fluid interface along reduced lossy-wall model and the full PDMS model for three wall thicknesses.

Conclusion

The hard-wall model approximates borosilicate glass channels with thick walls ($1500 \mu\text{m}$ or above) fairly well when actuated at off-resonance frequencies. At resonant frequencies of the fluid, channel walls as thin as $180 \mu\text{m}$ are approximated fairly well using the hard-wall model. However, if exact values are desired the surrounding material should be modelled. The lossy-wall model does not approximate a PDMS channel well, regardless of PDMS width. This is also reflected in the clear mismatch between actual fluid motion along interface compared to the one predicted by the lossy-wall condition.

References

- [1] N. Nama, R. Barnkob, Z. Mao, C. J. Kähler, F. Costanzo, and T. J. Huang, *Lab Chip* **15**, 2700-2709 (2015).
- [2] P. B. Muller, R. Barnkob, M. J. H. Jensen and H. Bruus, *Lab Chip* **12**, 4617-4627 (2012)
- [3] Z. Mao *et al.* *Lab Chip* **16** 515-524 (2016)
- [4] H. Bruus, (2012). *Lab Chip* **12**, 20-28 (2012).

Acoustophoretic separation of mononuclear cells from red blood cells using optimized buffer conditions

Anke Urbansky¹, Andreas Lenshof¹, Pelle Ohlsson¹, Stefan Scheduling^{2,3} and Thomas Laurell¹

¹Department of Biomedical Engineering, Lund University, Lund, Sweden

E-mail: anke.urbansky@bme.lth.se

²Department of Laboratory Medicine, Lund Stem Cell Center, Lund University, Lund, Sweden

³Department of Hematology, University Hospital Skåne, Lund, Sweden

Introduction

Mononuclear cells (MNC) play an important role in the immune system and are widely used in research as well as in clinical applications. Collection of MNC can be challenging due to their low abundance in the blood. Standard separation technologies are either performed in a batch process, require labeling of the cells or require pre-processing of the sample such as red blood cell (RBC) lysis. Especially in cytometry, where a major part of research is done on MNCs, a simple method for eliminating RBCs would have a high impact on the analysis of MNCs. Here, we investigated the performance of acoustophoresis for enriching MNCs from peripheral blood in a label free and continuous manner, which is not possible with current standard methods.

By applying an acoustic standing wave field in a micro channel, cells passing through the wave field can be separated depending on their physical properties such as size and density in relation to the surrounding medium. Despite the size difference between red blood cells (RBC) and MNC are these two cell types in blood plasma or standard buffer systems too similar in their acoustophoretic mobilities to allow for an effective separation in a free flow acoustophoretic set-up. To address this bottleneck we have therefore developed novel buffer protocols and optimized the acoustophoretic conditions.

Study design and methods

Whole blood samples were obtained from healthy volunteers (n=3). After labeling the blood cells with fluorescent antibodies against CD45 and CD61, samples were diluted 20 times and processed through an acoustophoresis microchip consisting of a sample inlet, a pre-focusing zone, a central buffer inlet, the main separation channel and a waste outlet in the center of the channel as well as a target outlet at the side (Figure 1).

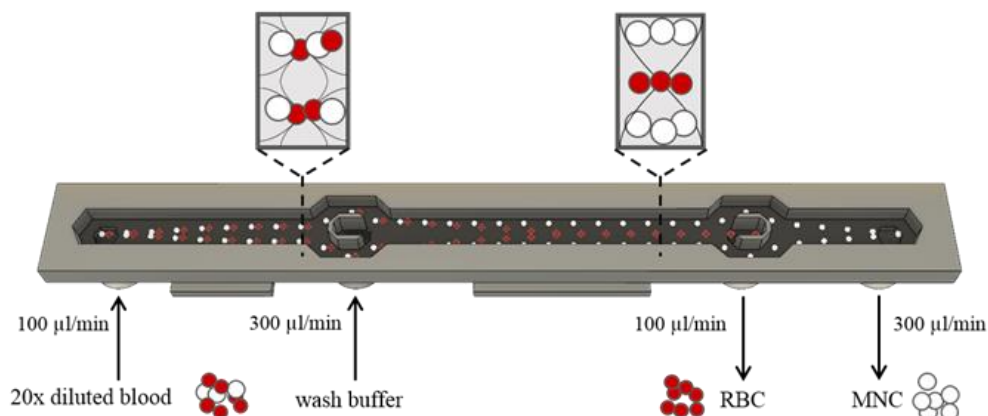


Figure 1: Schematic drawing of the acoustophoretic platform. Diluted blood is injected through the sample inlet and pre-focused into two parallel bands. Following the flow direction, the sample is bifurcated to each side of the wash buffer inlet and enters the main separation channel. Due to their higher acoustic mobility RBCs move faster in the acoustic standing wave field and can be collected at the center outlet (RBC outlet) while MNCs are less affected and stay close to the channel wall where they are collected in the side outlet.

Different buffer compositions, having different densities and speed of sound, were tested at a set constant flow rate of 100 $\mu\text{l}/\text{min}$ sample flow and the amplitude of the acoustic field was varied to obtain optimal separation conditions. Both target and waste outlet were analyzed for cell separation efficiency as well as enrichment by flow cytometry.

Results

Due to the similar acoustic properties of MNC and RBC it is not possible to separate these two cell types from each other in standard PBS buffer. At low amplitude the separation efficiency of MNC was 99.9%, while no RBC were removed, whereas high amplitude moved the MNC (96%) as well as the RBC (98%) to the waste fraction. By changing the buffer composition, such as density and speed of sound of the buffer, and thereby changing the acoustic forces acting on the cells, it was possible to enable the separation of MNCs from red blood cells (RBC) in diluted whole blood. A log 3.28 relative enrichment was achieved for MNCs in the target fraction as compared to the starting sample. The separation efficiency of the MNCs was 99.03 % while 99.93 % of the RBC were removed to the waste outlet.

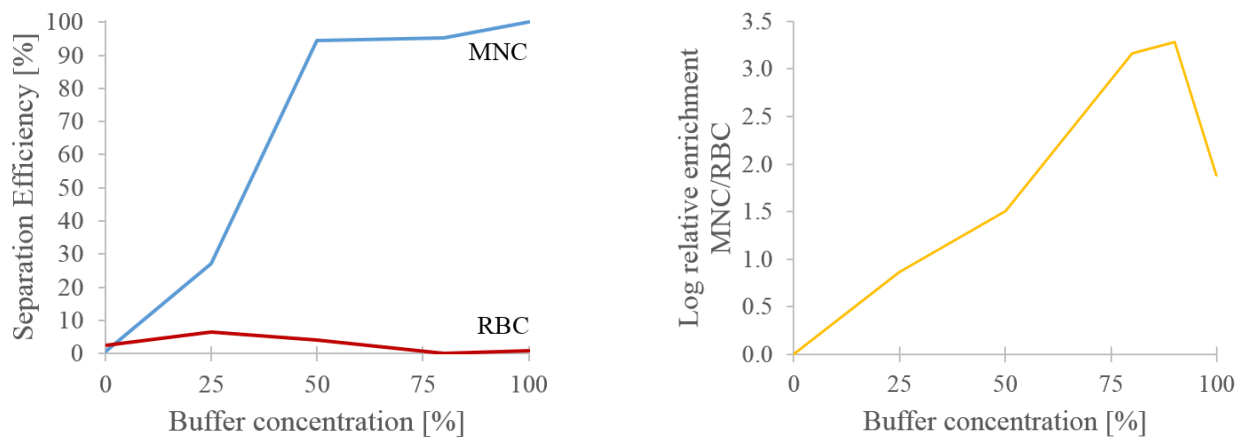


Figure 2: Buffer concentration affects the acoustic mobility of the different blood cells. Shown is the separation efficiency of MNC and RBC in the side outlet in relation to the buffer concentration used in the experiment (left). By increasing the buffer concentration, the acoustic mobility of the cells is changes such as MNCs are slowed down in the acoustic field and can be collected at the side outlet while RBC still move to the center and can be depleted from the sample. Also, the logarithmic relative enrichment of MNC to RBC in the target fraction as compared to the sample input is shown for different buffer conditions (right).

Conclusion

Acoustophoresis can be used to enrich MNCs from peripheral blood with high separation efficiency and low RBC contamination and offers the advantage of continuous separation as compared to standard density gradient centrifugation. Using acoustic separation of MNCs reduces pre-processing steps for flow cytometric analysis such as lysing of RBCs and washing protocols.

Disclosure

This work has been presented recently at the 31st Congress of the International Society for Advancement of Cytometry (Cyto 2016).

Controlled nanoparticle release through microbubble acoustofluidics: physical insight and applications.

Guillaume Lajoinie¹, Ying Luan², Erik Gelderblom¹, Benjamin Dollet³, Heleen Dewitte⁴, Ine Lentacker⁴, Nico de Jong², and Michel Versluis¹

1 - Physics of Fluids Group, MIRA Institute for Biomedical Technology and Technical Medicine and MESA+ Institute for Nanotechnology, University of Twente, P.O. Box 217, 7500 AE Enschede, The Netherlands

2 - Biomedical Engineering, Thoraxcenter, Erasmus MC, P.O. Box 2040, 3000 CA Rotterdam, The Netherlands

3 - Institut de Physique de Rennes, UMR 6251 CNRS/Universite Rennes 1, Campus Beaulieu, Batiment 11A, 35042 Rennes cedex, France

4 - Ghent Research Group on Nanomedicines, Lab of General Biochemistry and Physical Pharmacy, Faculty of Pharmaceutical Sciences, Ghent University, Ghent, Belgium

Abstract

Microbubbles driven by ultrasound are used in a number of applications including surface cleaning, ultrasound imaging, and as a vehicle for local drug delivery. To prolong the microbubble lifetime, its gas core is coated with a stabilizing shell, typically consisting of phospholipids. The coating can also be used to attach a payload or functional nanoparticles. Interestingly, upon ultrasound irradiation at several hundreds of kPa, the payload was observed to be released in a highly controlled way. This release carries great potential for using microbubbles as drug delivery agents in the context of personalized medical therapy. However, until now, limited experimental observations of the phenomenon are available. Here, we study using ultra high-speed and fluorescence imaging techniques in top and in side-view the underlying mechanisms of the release. We also developed a model on the basis of a Rayleigh-Plesset-type equation that reveals that non-spherical bubble behavior is key to the release mechanism. We also quantified the streamlines and acoustic streaming velocity responsible for the microfluidic transport of the material and propose for the first time a complete description of the controlled release of ultrasound actuated microbubbles.

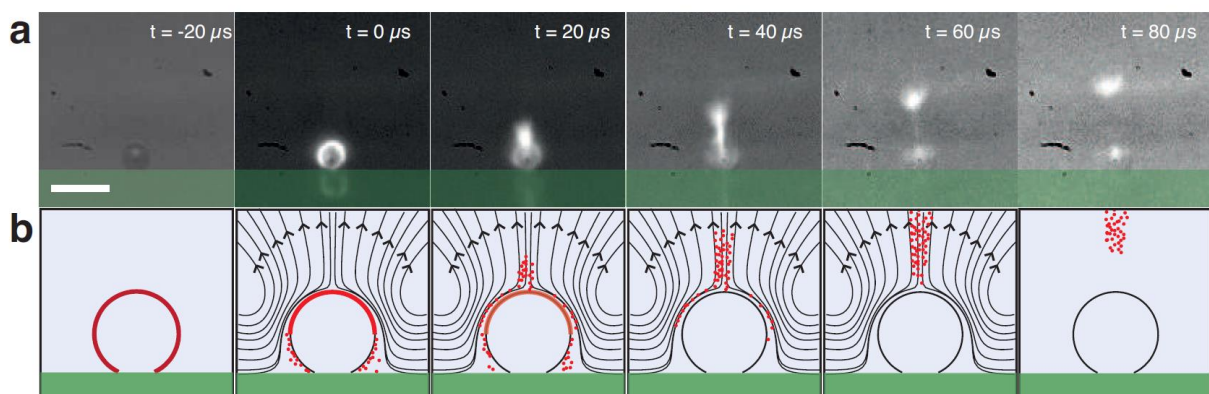


Figure 1: Experimental evidence of streaming. a. Release of the fluorescent material from an oscillating microbubble showing a clear transport away from the membrane. b. Schematics of the shedding process seen at 50 kfps, including the theoretically calculated streamlines (solid black lines).

Size-dependent particle migration in bubble-driven acoustic streaming

Andreas Volk, Massimiliano Rossi, Christian J. Kähler, and Alvaro Marin

Institute of Fluid Mechanics and Aerodynamics, Bundeswehr University Munich, Neubiberg, Germany
E-mail: andreas.volk@unibw.de

Introduction

When a microbubble's interface is actuated at frequencies in the kHz-regime, it creates an oscillating velocity field in the surrounding liquid. At longer time scales (seconds), a net flow can be observed which is commonly known as steady streaming or in this particular case *bubble-driven acoustic streaming* [1]. The use of semi-cylindrical bubbles for microfluidic applications is particularly interesting in medicine and chemistry, because it is suitable to manipulate flows and particles on small scales [2-3]. Previous studies assumed that the streaming flow in the vicinity of a semi-cylindrical bubble is essentially two dimensional. Recently, Marin *et al.* [4] revealed that the confinement along the bubble's axis gives rise to an unpredicted three-dimensional flow (see Fig. 1). In this work we show that the particle size in such a complex flow field is an important parameter leading to different but highly reproducible three-dimensional migration of particles towards the vicinity of the bubble. Our results have important consequences for bubble-driven microfluidic applications such as trapping, sorting and resuspension of particles [2-3].

Experiments

The microfluidic channel used in the experiments is made of polydimethylsiloxane (PDMS), has a height $h = 72 \mu\text{m}$, width $W = 1000 \mu\text{m}$, and total length L of about 3 cm (see Fig. 1(a)). A blind side channel of width $w = 80 \mu\text{m}$ and depth $d = 350 \mu\text{m}$ is situated perpendicular to the main channel. The PDMS device is bonded to a glass slide on which a piezoacoustic transducer is attached with epoxy. As the device is filled with a neutrally buoyant particle solution (fluorescent polystyrene (PS)-particles in 21% glycerol, 79% water w/w), a semi cylindrical bubble is left at the blind side channel. In order to keep the experimental conditions stable, the bubble radius r_{bub} was stabilized by a method that controls the hydrostatic pressure within the microchannel, taking advantage of the fact that PDMS is porous to gaseous substances [5]. By actuating the system with the transducer at a frequency $f = 20 \text{kHz}$ and a peak to peak voltage $U_{\text{pp}} = 40 \text{V}$, the gas-to-liquid interface oscillates and generates a steady streaming flow consisting of counter-rotating vortex pairs as shown in Fig. 1(b). We use an epifluorescent microscope to visualize the particle trajectories within the vortical flow structures. Since such flow structures are three-dimensional, the full particle motion is obtained using a single-camera approach based on particle defocusing [6].

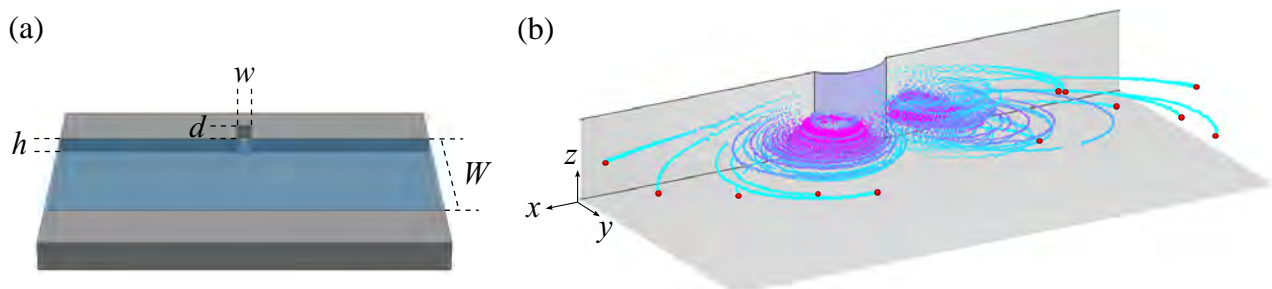


Figure 1: (a) Sketch of the microfluidic PDMS-channel: $h = 72 \mu\text{m}$, $W = 1000 \mu\text{m}$, $w = 80 \mu\text{m}$ and $d = 350 \mu\text{m}$ (b) Three-dimensional trajectories of $5\text{-}\mu\text{m}$ -diameter particles in bubble-driven acoustic streaming vortices. Color code is related with time: particles start the experiment (in cyan) homogeneously distributed over the channel and end up in smaller orbits at the end of the experiment (in magenta). The particle trajectories have a well-defined orbit and z -position, which is maintained as long as the bubble is acoustically actuated.

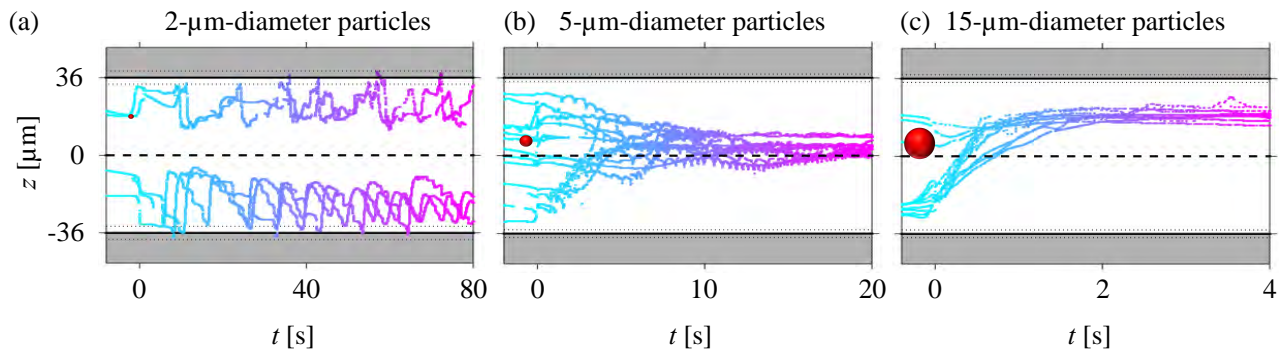


Figure 2: Vertical position z of 2-, 5- and 15- μm -diameter particles as a function of time t , as they migrate inside a bubble streaming vortex. The red dots illustrate the size of the particles. (a) 2- μm -diameter particles: no migration towards a specific z -location. (b) 5- μm -diameter particles: migration to $z = (5 \pm 5) \mu\text{m}$ within ~ 10 seconds. (c) 15- μm -diameter particles: migration to $z = (20 \pm 5) \mu\text{m}$ within ~ 2 seconds.

Results

The experiments are performed using PS particles with diameters of 2, 5, and 15 μm , which correspond to particle-to-bubble diameter ratios 1/40, 1/16, and 1/6, respectively. Figure 1(b) shows the typical vortical structures that particles follow, with their initial position depicted as a red sphere. The trajectory's color transforms from cyan to magenta over time. Streaming velocities in the xy -plane decay with increasing distance from the bubble and yield $\sim 10 \text{ mm/s}$ at the perigee (closest position to the bubble's interface) and $5 \mu\text{m/s}$ at a distance of $10 r_{\text{bub}}$. Typical streaming speeds in the vertical direction z are one order of magnitude slower. In order to characterize the migration more clearly, we display the z -component of the particle position in time. The results are shown in Fig. 2 where $t = 0$ is the time at which the particles pass the perigee for the first time. In Fig. 2(a) we see that 2- μm -diameter particles practically behave as passive tracers (within our experimental observation time) and follow the known toroidal trajectories [4]. A new and interesting result is that such toroidal structures are typically confined within the top or bottom halves of the microchannel, separated by the midplane at $z = 0$ (see Fig. 2(a)). No migration towards a specific z -location is observed for 2- μm -diameter particles. In contrast, 5- μm -diameter particles migrate on a typical time scale of ~ 10 seconds towards $z = (5 \pm 5) \mu\text{m}$, close to the midplane, while still orbiting in the xy -plane. This is clearly observed in Fig. 1(b). An even more pronounced migration is observed by increasing the particle diameter further up to 15 μm . In this case, the particle migration occurs at a typical time scale of ~ 2 seconds towards $z = (20 \pm 5) \mu\text{m}$ in the present experiment. Such a pronounced asymmetry of the final particle location might be caused by small defects in channel manufacturing and reveal that the trajectories of large particles are highly sensitive to the way the bubble anchors to the channel wall since this is crucial for the gas-to-liquid interface shape. However, small particles are not affected by this effect. The typical orbit radius of 15- μm -diameter particles in the xy -projection shrinks down to zero, such that large particles migrate to a stable position in the three-dimensional space.

Conclusions

Acoustically-actuated cylindrical microbubbles in PDMS microchannels induce a three-dimensional flow field in which particles migrate with a strong dependence on their size. Small particles basically behave as passive tracers and show characteristic toroidal trajectories. In contrast, large particles change the streamlines and focus in the vicinity of the bubble. The larger the particles are, the faster and more pronounced the particle focusing appears. As streaming velocity and focusing speed can be tuned by the actuation voltage of the piezo transducer, the described system is a promising tool to be applied in medical and chemical applications, such as size-sensitive sorting or trapping. The role of steric, hydrodynamic, and acoustic forces on the particle migration will be outlined during the presentation.

References

- [1] N. Riley. *Annu Rev Fluid Mech* **33**, 43-65 (2001).
- [2] C. Wang, S. V. Jalikop and S. Hilgenfeldt. *Appl Phys Lett* **99**, 034101 (2011).
- [3] C. Wang, S. V. Jalikop and S. Hilgenfeldt. *Biomicrofluidics* **6**, 012801 (2012).
- [4] A. Marin, M. Rossi, B. Rallabandi, C. Wang, S. Hilgenfeldt, and C. J. Kähler. *Phys Rev Appl* **3**, 041001-5 (2012).
- [5] A. Volk, M. Rossi, C. J. Kähler, S. Hilgenfeldt, and A. Marin. *Lab Chip* **15**, 4607-4613 (2015).
- [6] R. Barnkob, C. J. Kähler, and M. Rossi. *Lab Chip* **15**, 3556-3560 (2015).